THE UNIVERSITY OF SHEFFIELD

DEPARTMENT OF CIVIL AND STRUCTURAL ENGINEERING

PHD THESIS

Formalisation of a novel finite element design method based on the combined use of Gradient Elasticity and the Theory of Critical Distances

Cristian Bagni

Supervisors:
Prof. Harm ASKES
Prof. Luca SUSMEL

28 February 2017

To my Dad. . .

"Quelli che s'innamorano di pratica senza scienza son come il nocchiere, che entra in naviglio senza timone o bussola, che mai ha certezza dove si vada."

("Those who love practice without theory are like the sailor who boards ship without a rudder and compass and never know where they are going.")

Leonardo da Vinci

Abstract

The present research work is dedicated to the development, implementation and validation of a unified finite element methodology based on the combination of gradient elasticity and the Theory of Critical Distances, for the static and high-cycle fatigue assessment of notched engineering components. The proposed methodology, developed for plane, axisymmetric and three-dimensional problems, takes full advantage of both the TCD's accuracy in estimating static and high-cycle fatigue strength of notched components and of the computational efficiency of gradient elasticity in determining non-local stress fields whose distribution fully depends on the value of the adopted length scale parameter. In particular, the developed methodology, due to the ability of gradient elasticity to smooth stress fields in the vicinity of notch tips, has the great advantage of allowing accurate and reliable static and fatigue assessments of notched components by directly considering the relevant gradient-enriched stresses at the hot-spot on the surface of the component, in contrast to existing conventional approaches that require the knowledge of the failure location into the material a priori. This advantage, together with the fact that the proposed methodology can be easily implemented in commercial finite element software, makes the developed methodology a powerful and easy-to-use tool for the static and fatigue design/assessment of notched components. The developed methodology is accompanied by an accurate investigation of the best integration rules to be used as well as a comprehensive convergence study both in absence and presence of cracks, leading to a practical guideline on optimum element size. The proposed gradient-enriched methodology has been validated against a large number of problems involving notched components subject to both static and fatigue loading, covering a wide range of materials, geometries and loading conditions, clearly showing its accuracy and versatility. The developed gradient-enriched methodology has also been extended to the study of the dynamic behaviour of visco-elastic materials subject to vibration.

Acknowledgements

Contents

List of Figures

List of Tables

Chapter 1

Introduction

1.1 Problem statement

Due to ethical, environmental and economical reasons, engineers and designers are constantly facing the challenge of designing structures with increasing levels of safety and reliability by reducing at the same time costs (in terms of materials, production and maintenance), energy usage and polluting emissions. In order to achieve this goal, modern engineering structures/components tend to present slender and more complex geometries, often characterised by the presence of geometrical features producing stress concentrations that make structures potentially more vulnerable (if not properly designed and assessed) to both static and fatigue loading.

From the engineering point of view, the mechanical behaviour of materials is traditionally described through continuum mechanics models such as the conventional linear-elasticity theory that in the following of this thesis will be referred to as *classical elasticity*. These models allow an accurate description of complex variations of relevant state variables such as stress, strain and energy, but they are not able to take into account the effect of the microstructure on the macroscopic behaviour of a given material.

The simplicity of classical elasticity along with its accuracy in studying simple, traditional engineering structures, made it the favourite theory amongst engineers. Furthermore, its popularity increased even more with the advent of finite element (FE) software, since classical elasticity is easily implementable in a FE framework and computationally efficient. However, as previously mentioned, modern engineering components have complex geometries and classical elasticity is not always able to accurately describe all the problems introduced by these new geometries. For example, when dealing with engineering components presenting notches it is still common practice to use standard linear-elastic FE analyses due to their simplicity. Nevertheless, in this scenario, linear-elastic FE analyses result in high levels of conservatism (that increase with the sharpness of the stress riser), leading to oversized structures that obviously are against the aforementioned economic and environmental principles.

Furthermore, classical elasticity presents other limitations; in particular, it fails in capturing size effects and produces strain and stress singularities in correspondence of
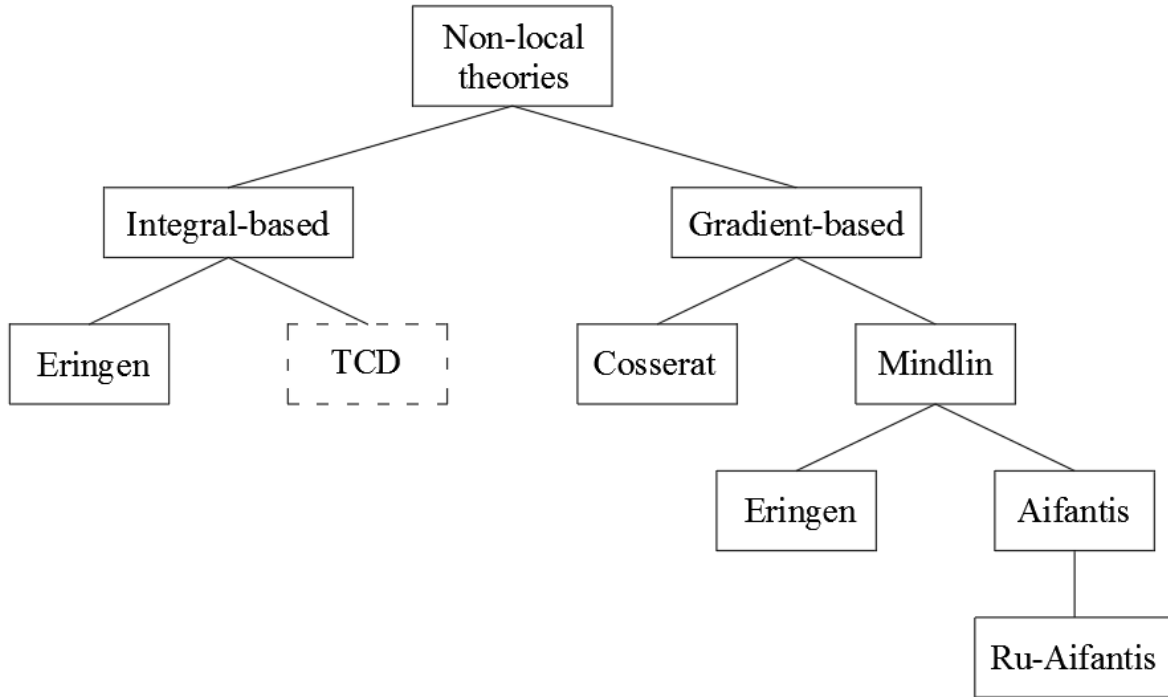
Fig. 1.1. Family tree of the main non-local theories.

dislocation lines and crack tips.

The aforementioned limitations of classical elasticity are mainly due to the fact that it considers materials as homogeneous continua, without considering the influence of the microstructure. It is clear then, that different theories need to be used in order to properly design and assess new engineering components and in particular a multiscale approach (able to take into account the different material behaviours at different size scales) would be extremely beneficial.

In the literature, a series of theories including information about the material microstructure have been proposed to overcome the limitations of classical elasticity. All these theories belong to the well-known family of *non-local* theories that consider the behaviour at any point of a given body depending also on the state of all the other points within a certain distance from the considered location.

Non-local theories, as schematically shown in Fig. 1.1, can be subdivided into two main sub-families:

- **integral-based non-local theories** where the governing equations contain integrals of relevant state variables accompanied by weighting functions depending on an internal characteristic length;

- **gradient-based non-local theories** where the constitutive equations of classical elasticity are enriched through higher-order gradients of relevant state variables, pre-multiplied by one or more intrinsic length parameters.

Amongst the integral-based non-local theories, the most famous is the one proposed by Eringen in 1972 [48, 49] (see Chapter 3). Also the Theory of Critical Distances (TCD), originally proposed to study the fatigue failure of notched metallic components, can be considered an integral-based non-local theory, and in particular, as will be explained in Chapter 3, it can be obtained from Eringen's theory through an appropriate definition of the weight function.

Regarding the gradient-based non-local theories, although their father can be considered Cauchy, who in the early 1850s proposed to enrich the equations of classical elasticity with higher-order spatial gradients to study more accurately the behaviour of discrete lattice models [35–37], they saw a significant development mainly thanks to the Cosserat brothers first, at the beginning of the 20th century [40], and Mindlin then, in the 1960s [95]. While in Mindlin's theory both kinetic and deformation energy density are defined also in terms of micro-strains, Cosserat theory includes three micro-rotations other than the usual three displacement components into the governing equations. Note that for the purpose of the present work, focused on stress/strength analysis, micropolar theories such as Cosserat theory are not of significant interest and therefore they will not be considered.

Starting from Mindlin's theory, in the last two decades of the 20th century, simpler Laplacian-based theories characterised by just one intrinsic length parameter have been proposed. In particular, the two worth mentioning are the gradient-type Eringen theory [50] and the Aifantis theory of gradient elasticity [3] (or *GradEla* as Aifantis himself prefers to call it). One of the main issues related to these theories (which is also the main reason why they have not found great success in practical applications yet) is that they require the solution of either fourth-order partial differential equations (p.d.e.) in one variable, which requires higher continuity, or second-order p.d.e. in two or more variables, which leads to a so-called "mixed formulation" (see §3.2.3 for a more in-depth discussion of the implementational intricacies). In both cases the implementation in finite element frameworks is non-trivial. In this context, the main advantage of *GradEla* over the gradient-type Eringen theory is that in 1993 it has been further modified by Ru and Aifantis [108], who proposed an operator split allowing the solution of the system of fourth-order p.d.e. as an un-coupled sequence of two systems of second-order p.d.e., decreasing the continuity requirements from $\mathcal{C}^1$ to $\mathcal{C}^0$ and therefore making the finite element implementation of the theory easier.

Despite the ability of the Ru-Aifantis theory to overcome the aforementioned limitations of classical elasticity and its relatively easy implementability into a finite element framework, as far as the author is aware, no unified gradient-enriched finite element methodology based on the aforementioned theory have been proposed yet. Nevertheless, a unified gradient elastic finite element methodology that, overcoming the aforementioned limitation of classical elasticity, allows more accurate static and fatigue assessments of engineering components presenting stress concentration features would be extremely beneficial.

The present thesis, as described in the next section, aims to fill this gap by proposing and validating a comprehensive gradient-enriched finite element methodology for plane,

axisymmetric and three-dimensional problems, able to accurately assess notched components.

1.2   Aim and objectives

The aim of the present research work is to propose a unified gradient elastic finite element methodology for the static and high-cycle fatigue assessment of notched engineering components, with the ambition of bringing gradient elasticity from a more mathematical dimension to engineering applications. In particular, the proposed methodology will provide engineers with an accurate and easy-to-use tool that allows to overcome the aforementioned deficiencies of classical elasticity with limited additional computational efforts respect to traditional approaches.

Based on the considerations described in the previous section, the natural choice was to base the proposed methodology on the Ru-Aifantis theory. However, TCD's accuracy in estimating static and high-cycle fatigue strength of notched components as well as its similarities with the Ru-Aifantis theory, led to the conclusion that the best option would have been to combine the Ru-Aifantis theory and the TCD into a unique finite element framework, in order to take advantage of the qualities of both the theories.

In particular the following objectives were set:

- Development and implementation of the gradient-elastic finite element methodology for both linear and quadratic plane (triangles and quadrilaterals), axisymmetric (triangles and quadrilaterals) and three-dimensional (tetrahedrons and bricks) elements.

- Identification of the most suitable integration rules for each implemented element.

- Convergence study of the implemented elements in the absence of cracks.

- Convergence study of the implemented elements in the presence of cracks and formulation of optimum element size recommendations.

- Application of the proposed methodology to simple plane, axisymmetric and three-dimensional problems to show its ability to remove stress singularities.

- Evaluation of the accuracy and reliability of the proposed methodology in estimating both static and high-cycle fatigue strength of notched components. This evaluation was carried out by analysing with the proposed methodology a wide range of experimental results obtained by testing notched components subject to both static and high-cycle fatigue loading. In particular, a wide range of geometries, materials and loading conditions were investigated.

Finally, in addition to the main objectives listed above a more explorative objective was set, that is the extension of the proposed gradient-elastic finite element methodology to visco-elastic problems.

1.3 Thesis outline

The present thesis is organised as follows. **Chapter 2** provides the theoretical background of the main problem that this thesis aims to address, i.e. the accurate and effective static and fatigue assessment on notched components. In particular, the fundamental aspects of traditional static assessment as well as fatigue and fracture mechanics are described, with particular emphasis on two theories that represents two key-aspects of the present research work, namely the Modified Wöhler Curve Method (MWCM) and the Theory of Critical Distances (TCD). **Chapter 3**, in turn, consists of a concise overview of a class of methodologies (non-local theories) able to efficiently address the aforementioned problem. In particular, it briefly retraces the key events in the history of gradient elasticity, from its origins to its modern developments. Particular attention has been paid to the Ru-Aifantis theory [3, 108], which represents the basis of the present research work. Comprehensive discussions about the boundary conditions as well as the identification of the length scale parameter characterising the Ru-Aifnatis theory are also provided. **Chapter 4** represents the "bridge" amongst *GradEla*, the TCD and the MWCM. In particular, it explains how the length scale parameters characterising *GradEla* and the TCD can be efficiently related and how, taking advantage of this relation, *GradEla* can be effectively applied to static and both uniaxial and multiaxial (incorporating also the MWCM) fatigue problems.

Chapter 5 is the core of the present thesis, where the Ru-Aifantis theory is implemented in an effective $\mathcal{C}^0$ finite element methodology for plane, axisymmetric and three-dimensional problems. An accurate discussion about the best integration rules to be used as well as a comprehensive convergence study are also provided. In particular, an extensive error estimation has been performed by analysing benchmark problems without cracks, followed by a convergence study of problems characterised by the presence of cracks, which allowed the formulation of recommendations on optimum element size. The ability of the developed methodology to remove stress singularities is also demonstrated through a series of plane, axisymmetric and three-dimensional examples containing geometrical singularities such as sharp cracks and 90° corners. The next three chapters contain different applications of the gradient-enriched methodology developed in Chapter 5, demonstrating its accuracy, reliability and versatility.

In **Chapter 6** the proposed methodology is applied to estimate the static and the high-cycle fatigue strength of notched components subject to various loading conditions. In these two chapters a wide range of geometry (plates, bars, U-nothes, V-notches, fillets,etc.) and materials (metals and polymers) have been investigated. In **Chapter 7**, instead, the proposed methodology is used to estimate the high-cycle fatigue strength of notched plain concrete.

Finally, the following chapter has a more explorative nature and it aims to show the versatility of the proposed gradient-enriched methodology investigating new possible applications in order to expand its spectrum of applicability. In particular, in **Chapter 8** the gradient elastic methodology presented in Chapter 5 is extended to visco-elastic problems with the main aim of accurately describing the dynamic behaviour of visco-elastic materials subject to vibrations, by taking into account the effect of both microstructure and

viscosity. This might lead, for example, to ambitious future applications in bio-mechanics, such as the study of bone regeneration in presence of vibrations.

1.4   Journal publications to date

The research work presented in this thesis has led to the following international journal publications, as also stated in the heading of the relevant chapter title pages:

- Bagni, C., and Askes, H. Unified finite element methodology for gradient elasticity. *Computers and Structures* 160 (2015), 100–110.

- Bagni, C., Gitman, I., and Askes, H. A micro-inertia gradient visco-elastic motivation for proportional damping. *Journal of Sound and Vibration* 347 (2015), 115–125.

- Jadallah, O., Bagni, C., Askes, H., and Susmel, L. Microstructural length scale parameters to model the high-cycle fatigue behaviour of notched plain concrete. *International Journal of Fatigue* 82 (2016), 708–720.

- Bagni, C., Askes, H., and Susmel, L. Gradient elasticity: a transformative stress analysis tool to design notched components against uniaxial/multiaxial high-cycle fatigue. *Fatigue and Fracture of Engineering Materials and Structures* 39(8) (2016), 1012–1029.

- Bagni, C., Askes, H., and Aifantis, E. C. Gradient-enriched finite element methodology for axisymmetric problems. *Acta Mechanica* (2017).

Chapter 2

Fracture and fatigue

In service engineering materials can be subject to a wide range of loading both static and dynamic. The main task of an engineer is to properly design and assess engineering components in order to ensure a good level of safety as well as cost effectiveness. The situation becomes even more delicate if we consider that real engineering components often present complex shapes, characterised by stress concentrators that facilitate the initiation of cracks. Both static and fatigue assessments of engineering components are therefore important tasks to carry out when designing any sort of structures in order to avoid catastrophic failures.

2.1   Static assessment

The static mechanical characterisation of metals is usually performed through uniaxial tensile tests, which allow to build the well-known stress-strain (or $\sigma - \varepsilon$) curves (Fig. 2.1). These curves are characterised by a first linear elastic branch, whose slope represents the Young's modulus, E, that in multi-dimensional problems is accompanied by other two material constants, namely the shear modulus, G, and the Poisson's ratio, ν (only two of these three material constants are independent (see for example [155])). This first linear elastic branch is followed by a more or less pronounced plateau, in correspondence of the yield stress, σ_y, that represents the transition from linear elastic to plastic behaviour. This third plastic region, as shown in Fig. 2.1a can assume two different shapes. The difference between the two curves is related to a phenomenon called *necking* (Fig. 2.2), consisting in a significant reduction of the cross-sectional area of the specimen when subject to high stress values. In particular the red curve, also called engineering $\sigma - \varepsilon$ curve is obtained by plotting the so-called engineering stress, determined dividing the applied load by the initial cross-sectional area (before necking). The blue one, instead, also called true $\sigma - \varepsilon$ curve is obtained by plotting the so-called true stress, determined as the ratio between the applied load and the actual cross-sectional area.

Although the engineering $\sigma - \varepsilon$ curves are not able to accurately describe the mechanical behaviour of materials in case of non-homogeneous deformations, they have the great
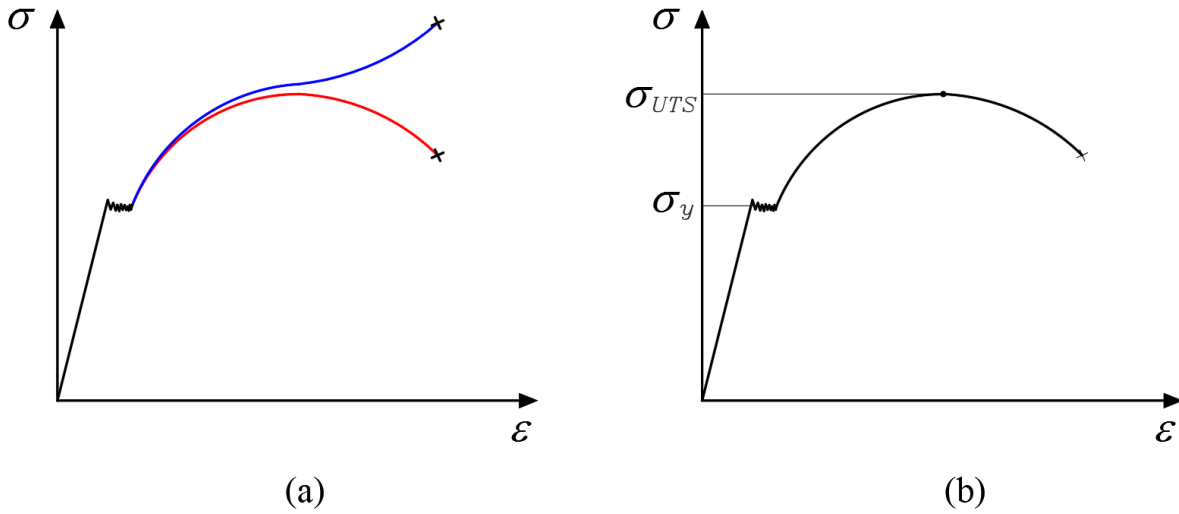
Fig. 2.1. Stress-strain curve: (a) engineering (red) and true (blue) stress-strain curve, (b) definition of σ_{UTS} and σ_y.
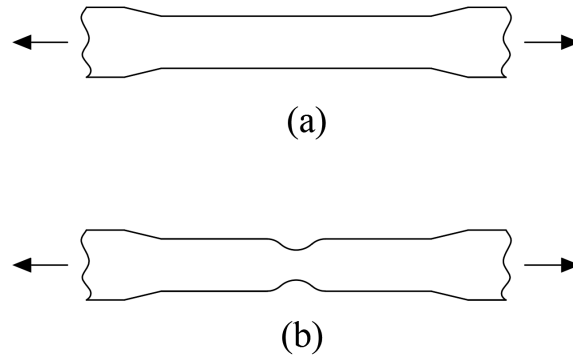
Fig. 2.2. Metal specimen pre (a) and post (b) necking.

advantage that they can be easily determined without the need of keeping track of the actual cross-sectional dimensions.

Considering now the engineering $\sigma - \varepsilon$ curve (Fig. 2.1b), it is possible to identify two characteristic stress values, usually considered as limit stresses, σ_L, to be used as reference values in the static assessments. In particular, σ_y is the previously defined yield stress, while σ_{UTS} is the ultimate tensile strength, corresponding to the maximum value of the engineering stress. Traditional static assessment approaches generally consider σ_y as limit stress for ductile materials and σ_{UTS} for brittle materials.

The previous concepts are valid only in the case of either uniform stress state or brittle material. In fact, when dealing with ductile materials subject to non-uniform stress state the previous assessment approach is often too conservative.

Consider for example the case of a beam made of a ductile material under pure bend-

ing (producing a linear distribution of the normal stress on the cross-section of the beam) and assume to reach σ_y in correspondence of the most stressed fibres. If the load is further increased, the beam does not fail thanks to a phenomenon known as *stress redistribution*. According to this, the stress in the yielded fibres remain constant and the load increment is taken by the other fibres still in the elastic state. Due to this, a portion of fibres next to the yielded ones reaches σ_y. By constantly increasing the applied load, due to the stress redistribution, the portion of yielded material in the beam progressively increases until the beam fails when the whole cross-section is subject to a stress equal to σ_y.

A similar but more delicate situation is the case of components presenting notches, leading to local stress concentrations. Let us consider a body made of a homogeneous, isotropic, linear-elastic material, presenting stress concentration features, such as the one shown in Fig. 2.3a. For simple geometries it is always possible to distinguish two different reference nominal stresses (Fig. 2.3a):

- gross nominal stress, σ_{gross}: referred to the gross cross-section;

- net nominal stress, σ_{net}: referred to the net cross-section.

As it is well known, the profile of the first linear-elastic principal stress in a component like the one of Fig. 2.3a, shows a peak value, σ_{ep}, in correspondence of the notch tip (Fig. 2.3b). The stress field then decreases along the notch bisector, moving towards the centre of the specimen, reaching eventually σ_{net} if the net section is sufficiently wide.

In 1974, Peterson [104], based on the aforementioned quantities, defined the so-called *stress concentration factor*, K_t, as the ratio between the linear-elastic peak stress and the relevant nominal stress:

$$K_{t,gross} = \frac{\sigma_{ep}}{\sigma_{gross}} \tag{2.1}$$

$$K_{t,net} = \frac{\sigma_{ep}}{\sigma_{net}} \tag{2.2}$$

It is worth highlighting that K_t depends only on the shape of the considered component and not on its size.

When dealing with notched components, due to the nature of the problem to be addressed, it is usual practice to refer to the net nominal stress, σ_{net}. Hence, in the following of this chapter, for notational simplicity, we will refer to the net stress concentration factor $K_{t,net}$, with the general notation K_t.

If the considered material is brittle, the static assessment is traditionally performed considering the elastic peak stress:

$$\sigma_{ep} = \sigma_{net} K_t \leq \sigma_L \tag{2.3}$$

since the material does not become plastic and therefore the peak stress does not redistribute.
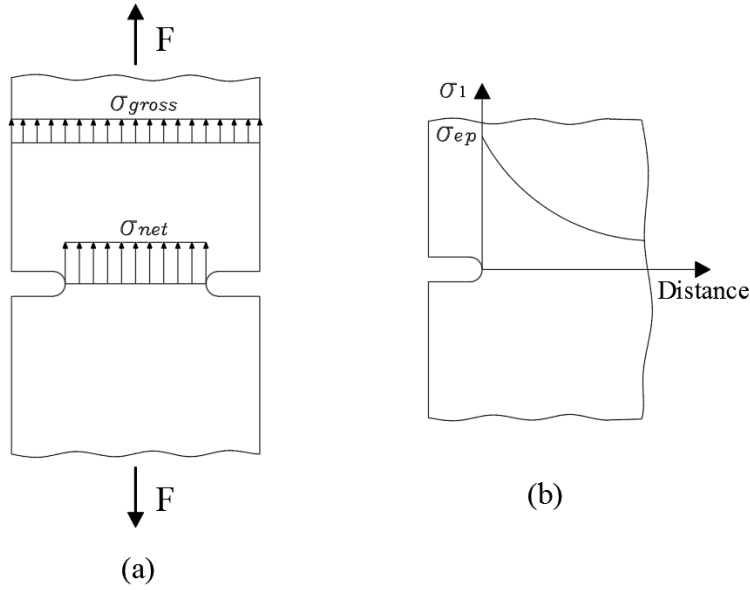
Fig. 2.3. Notched specimen: definition of gross, σ_{gross}, and net, σ_{net}, nominal stress (a) and elastic peak stress σ_{ep} (b).

If the material is ductile, instead, the static assessment is usually carried out considering directly σ_{net}, without taking into account K_t:

$$\sigma_{net} \leq \sigma_L \tag{2.4}$$

This is because when σ_{ep} becomes higher than σ_y, the material starts behaving plastically and stress redistribution occurs (dashed stress profile in Fig. 2.4), leading to a uniform stress distribution, $\sigma_{net} = \sigma_y$, (dash-dotted line in Fig. 2.4) at failure condition (see for example [24]). Therefore, as long as $\sigma_{net} < \sigma_y$ the net section is not fully plastic and part of it can still resist a load increase. The brittle and ductile cases discussed above, however, represent just the two extremes of a broad range of material behaviours. A large number of real materials, in fact, show intermediate behaviours (for example quasi-brittle materials) and in these cases a careful selection of the most suitable model to describe the behaviour of the considered material is needed.

In the previous analysis, only simple uniaxial stress state have been considered. However, engineering components are often subject to complex multiaxial stress states that need to be compared to the simple stress states characteristic of the experimental tests used for the mechanical characterisation of engineering materials.

For this purpose, different failure criteria were proposed in the past to determine an equivalent stress directly comparable with the limit stress in the static assessments. Amongst these criteria two deserve particular attention:

- **Tresca criterion**: the failure of the considered material is attributed to the maximum shear stress. The equivalent stress proposed by Tresca reads:

$$\sigma_{\mathrm{T}} = \max\{|\sigma_1 - \sigma_2|, |\sigma_1 - \sigma_3|, |\sigma_2 - \sigma_3|\} \tag{2.5}$$
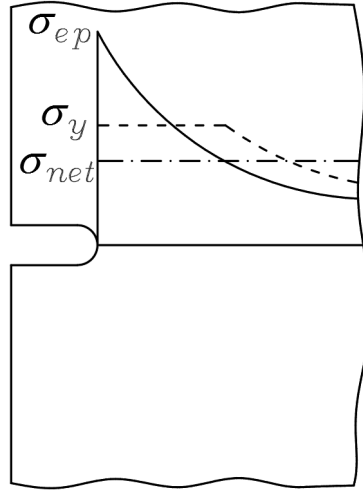
Fig. 2.4. Variation of the stress state in a notched ductile material for increasing applied load.

- **Von Mises criterion**: the failure of the considered material is attributed not to the total deformation work, but to the portion of deformation energy not associated to the hydrostatic stress state (changes in volume). The equivalent stress proposed by Von Mises reads:

$$\sigma_{\text{VM}} = \sqrt{\frac{1}{2}\left[(\sigma_1 - \sigma_2)^2 + (\sigma_1 - \sigma_3)^2 + (\sigma_2 - \sigma_3)^2\right]} \tag{2.6}$$

where $\sigma_1 \geq \sigma_2 \geq \sigma_3$ are the three principal stresses.

To conclude this section, it is worth mentioning that the main issue related to the static assessment of notched components is that for complex geometries and loading conditions, the determination of the nominal net stress is not a trivial task and, furthermore, obtaining it from FE results requires complicated post-processing. Therefore, adopting traditional assessment techniques, one option is to solve the given problem through a simple linear elastic FE analysis, which leads however to unphysically high local peak stresses, potentially resulting in oversized structures. A second option, instead, in particular for ductile materials, would be to adopt elasto-plastic FE analyses that are much more complex and expensive. It is clear then, that traditional techniques do not allow accurate and simple assessments of real engineering components and that different approaches need to be used (as we will see in the following of this chapter, the same applies also to fatigue problems).

2.2 Fatigue assessment

When engineering materials are subject to cyclic loadings, they undergo a weakening phenomenon well-known under the name *fatigue*. Due to fatigue, engineering components
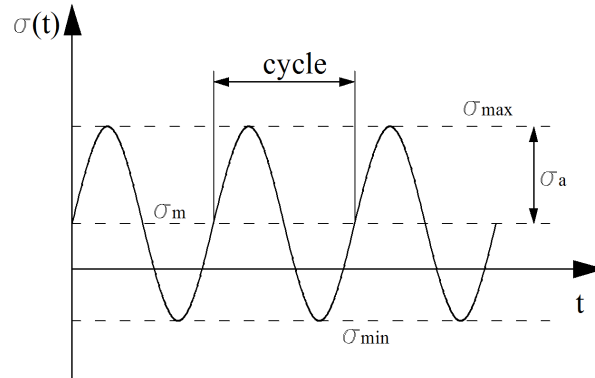
Fig. 2.5. Definition of the quantities characterising cyclic loading.

can fail even if subject to time-variable loads whose maximum value is well below the static strength of the considered material. The dangerous aspect about fatigue is the fact that fatigue failures can be unexpected, e.g. when showing no evident precursory signs, such as large scale deformations.

2.2.1   Constant amplitude cyclic loading

Before analysing the fatigue problem in more detail, it is worth introducing the concept of cyclic loading and the quantities defining time-variable signals.

By definition, a cyclic loading is the recurrence of a given load cycle, defined as a series of successive states, whose initial and final values are identical (Fig. 2.5). A cyclic load is characterised by different quantities, that will be defined in the following of this section. For sake of simplicity, let's consider the body shown in Fig. 2.6 subject to a system of periodical external forces creating, at the generic point P, a uniaxial sinusoidal stress state defined as:

$$\sigma(t) = \sigma_m + \sigma_a \sin(\omega t) \tag{2.7}$$

where subscripts a and m denote, respectively, the amplitude and the mean value of the relevant stress component, ω is the angular frequency and t is time. It is worth specifying at this point that, even if for simplicity a sinusoidal path has been considered, what follows holds true independently of the shape of the signal as long as the load is cyclic.

From Fig. 2.5 it is easy to observe that the maximum and minimum value of the periodic stress component can be defined as:

$$\sigma_{max} = \sigma_m + \sigma_a \tag{2.8}$$

$$\sigma_{min} = \sigma_m - \sigma_a \tag{2.9}$$
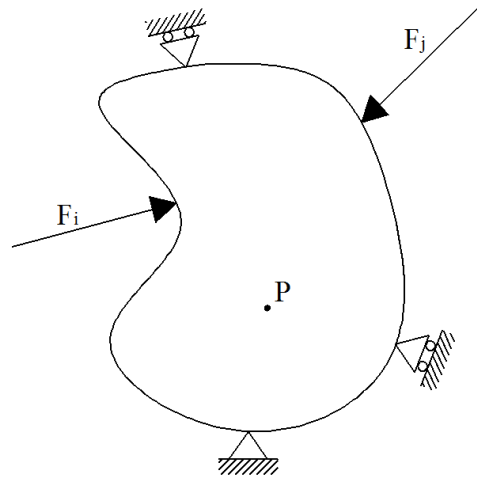
Fig. 2.6. Generic body subject to an external system of forces.

or alternatively σ_a and σ_m can be expressed as follows:

$$\sigma_a = \frac{\sigma_{max} - \sigma_{min}}{2} \tag{2.10}$$

$$\sigma_m = \frac{\sigma_{max} + \sigma_{min}}{2} \tag{2.11}$$

while the stress range is given by:

$$\Delta\sigma = \sigma_{max} - \sigma_{min} = 2\sigma_a \tag{2.12}$$

Finally another important parameter to take into account when dealing with fatigue problems is the so-called load ratio R defined as:

$$R = \frac{\sigma_{min}}{\sigma_{max}} = \frac{\sigma_m - \sigma_a}{\sigma_m + \sigma_a} \tag{2.13}$$

Considering Eq. (2.13) along with Eqs. (2.8) and (2.9), providing that $\sigma_{max} > 0$, it is possible to say that cyclic loading characterised by a load ratio $R = -1$ (fully-reversed loading) have zero mean stress (Fig. 2.7a), while cyclic load histories with $R > -1$ (Fig. 2.7b) are characterised by positive (traction) mean stress values and, of course, for $R < -1$ (Fig. 2.7c) the mean stress results to be negative (compression).

The uniaxial case just considered is clearly the simplest situation; however, real struc-
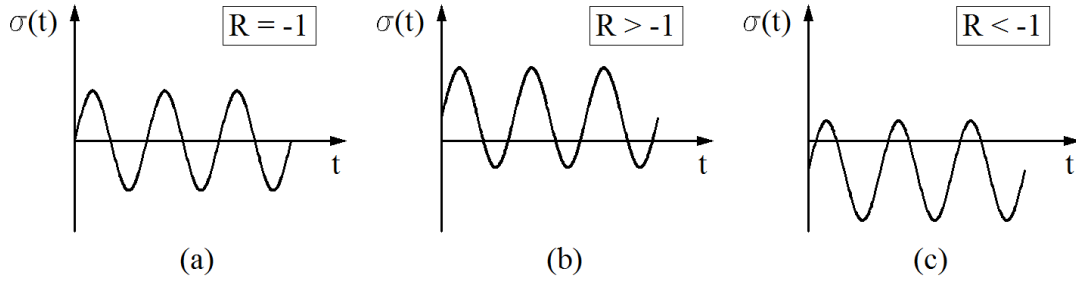
Fig. 2.7. Cyclic loading characterised by different values of R.

tures can be subject to more complex multiaxial stress states where the considered component is subject to different stress components acting in different directions, that in the most general case can be defined as:

$$\boldsymbol{\sigma}(t) = \begin{bmatrix} \sigma_x(t) & \tau_{xy}(t) & \tau_{xz}(t) \\ \tau_{xy}(t) & \sigma_y(t) & \tau_{yz}(t) \\ \tau_{xz}(t) & \tau_{yz}(t) & \sigma_z(t) \end{bmatrix} \tag{2.14}$$

where each of the stress components is considered to vary independently.

Since to perform an accurate assessment of the fatigue behaviour of engineering components subject to multiaxial cyclic loading the simultaneous effect of each stress component must be properly considered, it is clear that this represents undoubtedly the most complex scenario to deal with in practical situations. The multiaxial high-cycle fatigue problem will be analysed in more detail in §2.2.4.

2.2.2   Fatigue in metals

From a microscopic point of view, it is well-known that metals are made of crystals (also called grains), that are ideally considered as groups of atoms linked together by interatomic forces and arranged in order to minimise the potential energy of each single grain. However, real metallic crystals are not perfect, but they contain different types of defects; in particular, dislocations are the defects presenting the strongest influence on the overall behaviour of grains subject to stress or strain states. A dislocation can be considered, from a continuum point of view, as an additional half plane of atoms, resulting in a distortion of the atoms' arrangement in the crystal [12], see for example Fig. 2.8.

As explained in [123], when crystals are subject to cyclic stress/strain states, dislocations can move along the so-called easy glide directions on the correspondent easy glide plane. In particular, the dislocations' motion is caused by cyclic shear forces acting on the aforementioned easy glide plane, resulting in plastic deformations of the grains and the formation of the so-called persistent slip bands (PSBs). The formation of these PSBs results in irregular grain profiles, characterised by alternating peaks and valleys (Fig. 2.9), where the most pronounced intrusions as well as the interfaces between PSBs
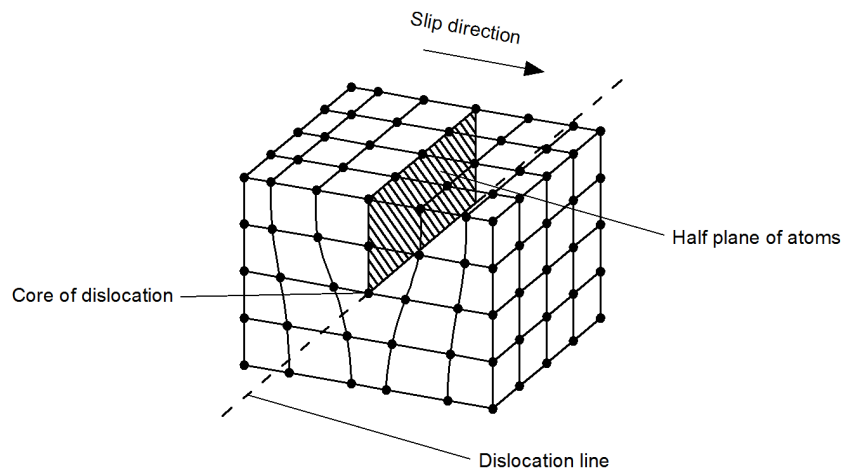
Fig. 2.8. Dislocation and re-arrangement of the atoms.

and the grain matrix represent the most critical locations for micro-cracks initiation, due to micro-stress concentration phenomena, which then propagate within the crystal as a result of plastic de-cohesion of the slip bands.

Even if this is a simplistic description of the much more complex reality, it can be still considered as a good representation of the basic mechanisms resulting in the initiation of micro-cracks in real fatigued grains.

2.2.3 Basics of uniaxial fatigue assessment

After this brief overview about cyclic loading and the microscopic mechanisms resulting in the initiation and propagation of fatigue cracks in metals, it is possible to address more in depth the fatigue problem starting from the simpler case of engineering components subject to cyclic uniaxial stress states.

For this purpose, it is worth considering the standard plain specimen shown in Fig. 2.10a subject to fully-reversed ($R = -1$) axial loading. It is well-known that the specimen will break due to fatigue after a certain number of cycles, which depends on the material fatigue properties as well as the amplitude of the applied cyclic loading. The fatigue performance of a material can be schematically represented by the so-called Wöhler curve (or S-N curve), obtained by testing several specimens subject to various stress amplitudes and plotting in a bi-logarithmic diagram the amplitude of the applied stress, σ_a, against the correspondent number of cycles to failure, N_f (Fig. 2.10b). Obviously, fatigue results, due to their experimental nature, are affected by a physiological scattering that makes necessary an accurate statistical post-processing of the experimental data in order to define the most appropriate fatigue curve.

Before mathematically defining the Wöhler curve, it is worth introducing the concepts of *fatigue limit* and *endurance limit*. In particular, ferrous metals tested in laboratory show the fatigue behaviour schematically represented in Fig. 2.11a, characterised by a plateau in correspondence of a certain stress amplitude σ_0, called fatigue limit, that correspond to
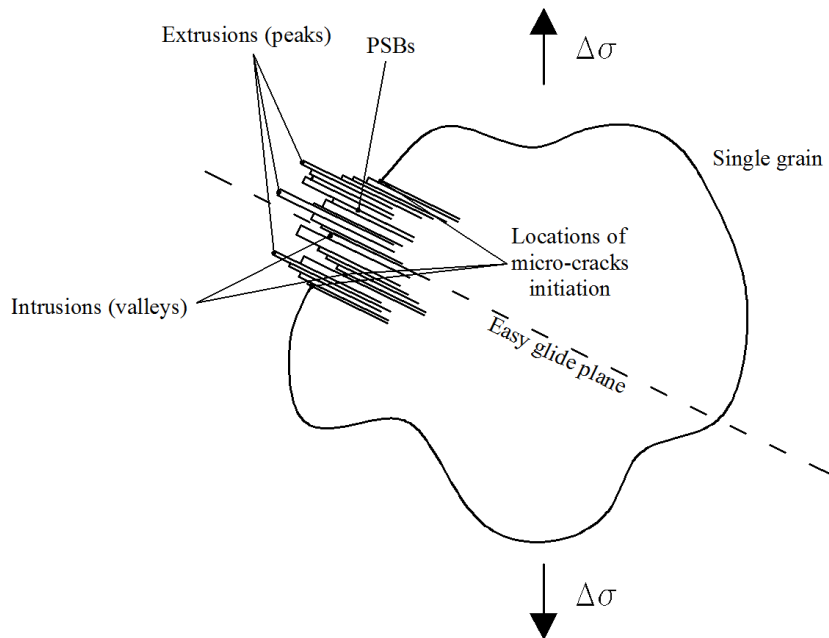
Fig. 2.9. PSBs resulting in irregular grain profile and potential micro-crack initiation locations.
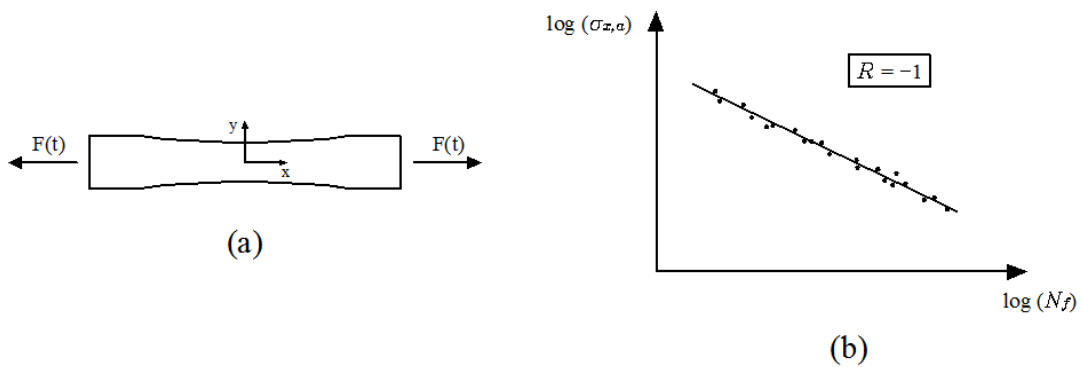
Fig. 2.10. Plain specimen subject to cyclic axial loading (a) and Wöhler curve obtained from experimental results (b).
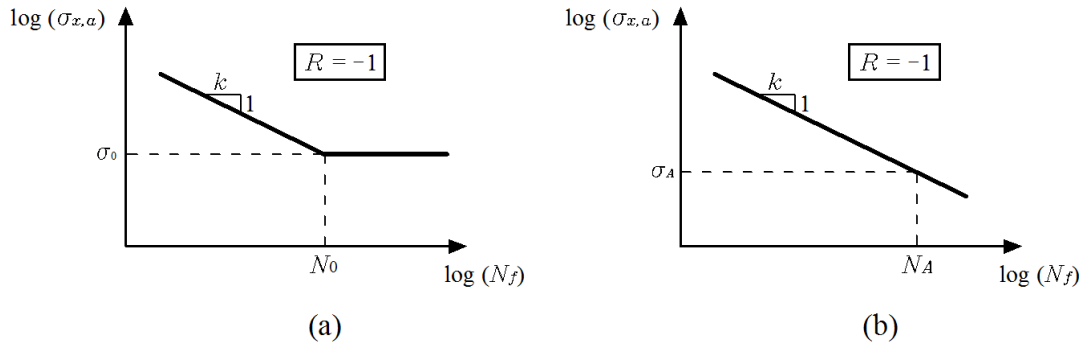
Fig. 2.11. Typical Wöhler curves for ferrous (a) and non-ferrous (b) metals.

the threshold value of stress amplitude, below which the fatigue life of the considered component is theoretically infinite. Non-ferrous metals, instead, must always be designed for finite fatigue life, due to the fact that it is impossible to define a fatigue limit, since their fatigue behaviour (Fig. 2.11b) does not exhibit any plateau. In this case, it is common practice to consider a so-called endurance limit, σ_A, corresponding to the stress amplitude determined at a certain number of cycles to failure in the high-cycle regime, N_A, ranging between 10^6 and 10^8.

However, the Wöhler curves, for all ferrous metals as well as most of the materials not exhibiting any fatigue limit, can be defined by the following mathematical expression (Wöhler equation):

$$\sigma_a^k N_f = \text{constant} \tag{2.15}$$

where k is the negative inverse slope, as shown in Fig. 2.11.

Since in a bi-logarithmic diagram the fatigue experimental results can be accurately approximated by straight lines, the Wöhler curves are commonly obtained by means of a least squares linear regression, along with the assumption that the number of cycles to failure is characterised by a log-normal distribution at any stress amplitude level [110]. For a probability of survival $P_S = 50\%$ the linear regression equation allowing the estimation of the S-N curve from experimental results reads as follows:

$$\log(N_f) = C_0 + C_1 \log(\sigma_a) \tag{2.16}$$

where C_0 and C_1 are two constants that, according to the least squares linear regression, are defined as follows [85]:

$$C_1 = \frac{\sum\limits_{i=1}^{n}(x_i - x_m)(y_i - y_m)}{\sum\limits_{i=1}^{n}(x_i - x_m)^2} \tag{2.17}$$

$$C_0 = y_m - C_1 x_m \tag{2.18}$$

where

$$x_m = \frac{\sum\limits_{i=1}^{n} x_i}{n} \tag{2.19}$$

$$y_m = \frac{\sum\limits_{i=1}^{n} y_i}{n} \tag{2.20}$$

while x_i and y_i are the logarithms of, respectively, the stress amplitude, $\log(\sigma_{a,i})$, and the corresponding number of cycles to failure, $\log(N_{f,i})$, for the i-th tested specimen (with $i = 1, \ldots, n$).

Comparing now Eq. (2.16) with Eq. (2.15) it is easy to find that the negative inverse slope, k, and the endurance limit, σ_A, (the same holds true in terms of fatigue limit) of the considered S-N curve having $P_S = 50\%$ can be defined, respectively, as:

$$k = -C_1 \tag{2.21}$$

$$\sigma_A = \left(\frac{10^{C_0}}{N_A}\right)^{1/k} \tag{2.22}$$

Finally, the design fatigue curve having a given probability of survival $P_S = P\%$ different from 50%, can be defined as [85]:

$$\log(N_f) = C_0 + C_1 \log(\sigma_a) - q \cdot s \tag{2.23}$$

and at the endurance limit:

$$\log(N_A) = C_0 + C_1 \log(\sigma_{A,P\%}) - q \cdot s \tag{2.24}$$

Substituting C_0 and C_1, obtained from Eqs. (2.21) and (2.22), into Eq. (2.24) the endurance limit of the fatigue curve having $P_S = P\%$ takes the following form:

$$\sigma_{A,P\%} = \sigma_A \left[\frac{N_A}{10^{\log(N_A)+q \cdot s}} \right]^{1/k} \tag{2.25}$$

where q is a coefficient that varies according to probability of survival, number of tested specimens as well as confidence level [85], whereas s is the sample standard error of the n experimental results, defined as:

$$s = \sqrt{\frac{\sum\limits_{i=1}^{n} [y_i - y(x_i)]^2}{n-2}} = \sqrt{\frac{\sum\limits_{i=1}^{n} \left\{ \log(N_{f,i}) - \log\left[N_A \left(\frac{\sigma_A}{\sigma_{a,i}} \right)^k \right] \right\}^2}{n-2}} \tag{2.26}$$

2.2.3.1 Factors affecting the fatigue behaviour of metals

Standard S-N curves, as those discussed above, are generally obtained by testing in laboratory conditions (controlled environment) and under fully-reversed loading, small, plain specimens whose surface has been previously polished, in order to remove any superficial defect. Clearly, this situation is quite far from real in-service conditions: real components are usually bigger than the specimens generally used in tests, they are often characterised by rough surfaces and they can be subject to any kind of loading at completely different environmental conditions. Furthermore, due to their complex geometry they are often characterised by stress concentration features (e.g. notches). It is also worth highlighting, at this point, that the fatigue behaviour of metals, is strongly influenced by several factors (amongst which surface finishing, size effect, load type, mean stress effect, geometrical characteristics, etc.) that can significantly reduce the fatigue strength of a given material.

It is clear now that, when performing fatigue assessments of real engineering components, great attention must be paid to all these factors. In particular, due to their significant detrimental effects, two of the aforementioned factors will be discussed more in depth in the following of this section: *mean stress effect* and *notch effect*.

2.2.3.1.1 Mean stress effect

As explained in [123], positive mean stresses, or in other words, tensile superimposed static stresses, have a detrimental effect on the fatigue behaviour of metals. In particular, by increasing the load ratio R, the Wöhler curve of a given material shifts downwards, meaning a decrease of the material endurance limit.

As shown in Fig. 2.12, different metals can have a completely different sensitivity to the presence of mean stresses. This is the reason why, in the past, several rules have been

proposed for accurately taking into account the mean stress effect; most of these can be summarised, as proposed by Marin [90], by the following equation:

$$\left(\frac{\sigma_0}{\sigma_{0,R=-1}}\right)^n + \left(f\frac{\sigma_{x,m}}{\sigma_{UTS}}\right)^m = 1 \qquad (2.27)$$

where $\sigma_{0,R=-1}$ represents the fatigue limit determined under fully-reversed loading conditions, σ_{UTS} is the ultimate tensile strength, while n, m and f are constants defining different rules:

- Goodman's relationship: $n = m = f = 1$;

- Gerber's parabola: $n = f = 1$ and $m = 2$;

- Dietman's parabola: $n = 2$ and $m = f = 1$;

- elliptical relationship: $n = m = 2$ and $f = 1$.

Obviously, the best way to determine the effect of superimposed static tensile stresses on a specific metal is by running appropriate experimental tests. However, when this is not possible a conservative choice is to use Goodman's relationship.

2.2.3.1.2   Notch effect

Stress concentration phenomena have a strong damaging effect on the overall behaviour of engineering components, resulting in an important reduction of the fatigue strength. This is why fatigue in notched components has been a central problem in the last century. Today, thanks to the comprehensive studies carried out in the past, we can count on a wide range of criteria able to accurately account for the detrimental effect of stress concentrators on components subject to cyclic loading.

It is worth remembering at this point, as already mentioned in §2.1, that the notation K_t refers to the net stress concentration factor $K_{t,net}$, defined in Eq. (2.2).

As previously mentioned, the detrimental effect of notches produces a reduction of the fatigue strength of the considered material, resulting in the dashed Wöhler curve of Fig. 2.13. Therefore, the aforementioned damaging effect can be measured, as proposed by Peterson [103], by means of the so-called *fatigue strength reduction factor*, K_f:

$$K_f = \frac{\sigma_0}{\sigma_{0n}} \qquad (2.28)$$

where σ_{0n} is the notch fatigue limit, determined under the same experimental and loading conditions used for the evaluation of σ_0. Even if for sake of simplicity the fatigue limits
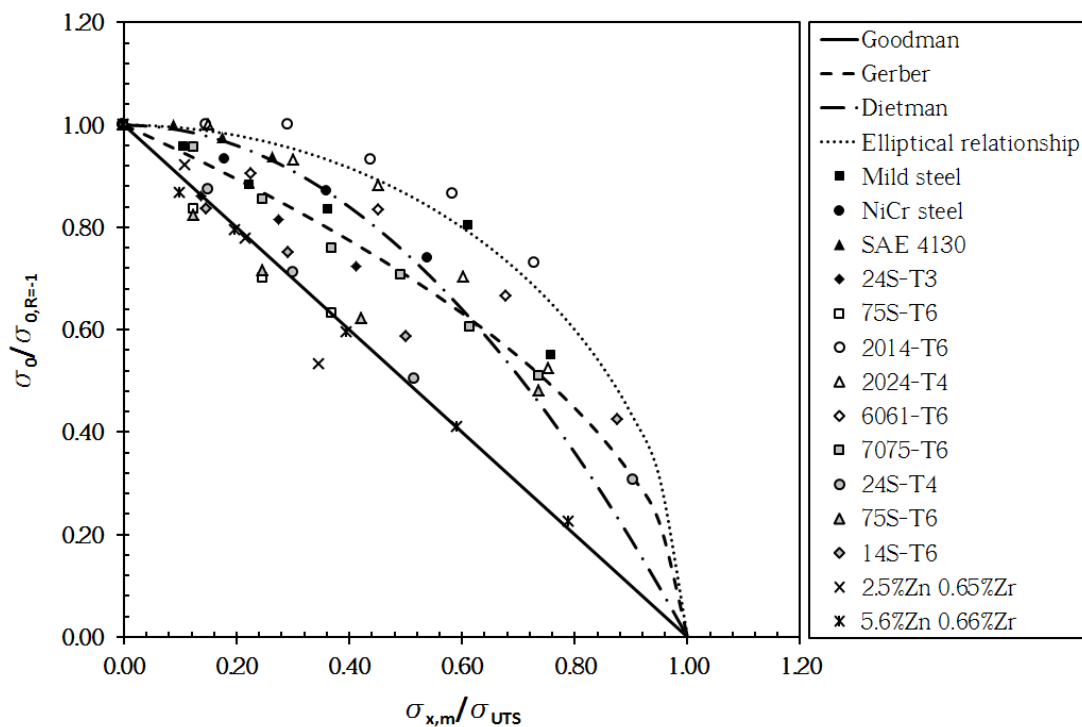
Fig. 2.12. Mean stress effect description provided by the different relationships under uniaxial fatigue loading (experimental data taken from [56]).
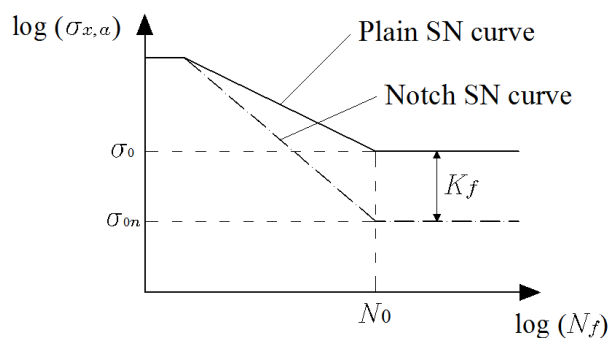
Fig. 2.13. Effect of notches on the Wöhler curve and definition of the fatigue strength reduction factor, K_f.

have been considered, this holds true also in terms of endurance limits.

Obviously, the most precise estimations of K_f are obtained by running appropriate tests. However, experiments can be expensive and time consuming and several times they do not represent a feasible solution. For this reason different formulas for an accurate estimation of K_f have been proposed; in particular, as presented by Peterson [103] K_f can be estimated through the following equation:

$$K_f = 1 + q(K_t - 1) \tag{2.29}$$

where q is the so-called *notch sensitivity factor* ranging between 0 and 1. In particular, Neuber [98] proposed to estimate q through the following expression:

$$q = \frac{1}{1 + \sqrt{\frac{a_N}{r_n}}} \tag{2.30}$$

where a_N is a constant depending on the ultimate tensile strength, σ_{UTS}, while r_n is the notch root radius, which is considered to be the most significant parameter defining the linear-elastic stress field in the vicinity of the notch.

The following year, Peterson [103] suggested an alternative formula to calculate q:

$$q = \frac{1}{1 + \frac{a_P}{r_n}} \tag{2.31}$$

where a_P is again a constant depending on σ_{UTS}.

Regarding the determination of the two aforementioned constants, a_N and a_P, Dowling [44] proposed to use the following empirical relations, respectively:

$$a_N = 10^{-\frac{\sigma_{UTS}-134}{586}} \quad [\text{mm}] \tag{2.32}$$

$$a_P = 0.0254 \left(\frac{2079}{\sigma_{UTS}} \right)^{1.8} \quad [\text{mm}] \tag{2.33}$$

2.2.3.2   Fatigue under torsional cyclic loading

Similarly to the case of cyclic uniaxial loading, the fatigue behaviour of engineering materials subject to torsional loading can be represented by Wöhler diagrams, like the one in
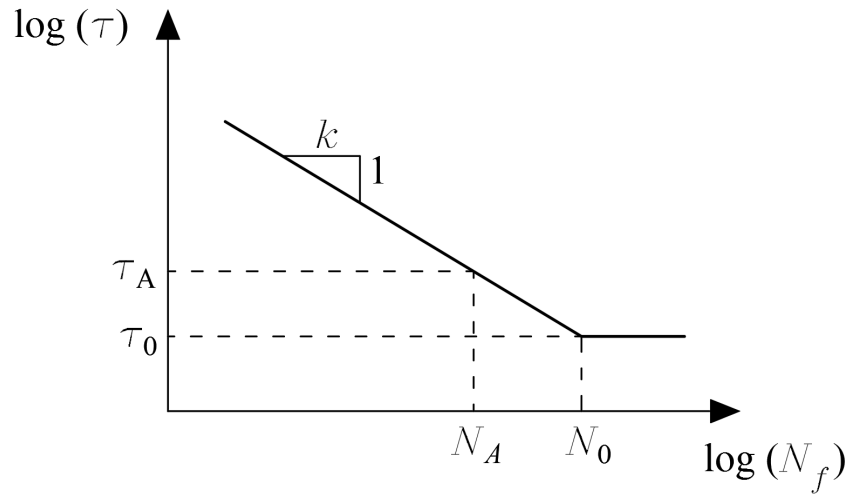
Fig. 2.14. Wöhler curve for torsional cyclic loading.

Fig. 2.14, where the amplitude of the shear stress is plotted against the number of cycle to failure, N_f. The aforementioned fatigue curves can be determined through statistical techniques, similar to those presented in the first part of this section and it is always possible to define a *torsional plain fatigue limit*, τ_0, at N_0 cycles to failure (or alternatively, a *torsional plain endurance limit*, τ_A, at N_A cycles to failure), for a chosen probability of survival P_s.

The fatigue behaviour of engineering materials subject to cyclic torsional loading, as it happens under uniaxial loading, is significantly influenced by several factors such as microstructure, surface finishing, size and geometry of the component, etc. However, even if these factors should be accurately taken into account when designing and assessing real components against fatigue, as mentioned in [123] no comprehensive investigations have been carried out in order to evaluate the effect of all the aforementioned factors on the torsional fatigue behaviour of engineering materials. This is why for practical reasons, even if not rigorously accurate, it is common practise to address the torsional problem using the same information valid for the uniaxial case. Also the torsional plain fatigue limit, τ_0, if it cannot be determined through appropriate tests, can be approximatively calculated, as suggested in [123] and according to the experimental investigations performed by Fukuda and Nisitani [57], from its uniaxial counterpart, σ_0, through Von Mises's criterion:

$$\tau_0 = \frac{\sigma_0}{\sqrt{3}} \tag{2.34}$$

Finally, in contrast to the case of uniaxial loading, it has been shown [42, 111] that the effect of superimposed static torsional stresses on the fatigue behaviour of engineering materials is generally very small and can be neglected, as long as the maximum torsional stress, τ_{max}, is lower than the material torsional yield stress, τ_y. This leads to significant advantages when the multiaxial fatigue assessment is performed by using certain criteria.
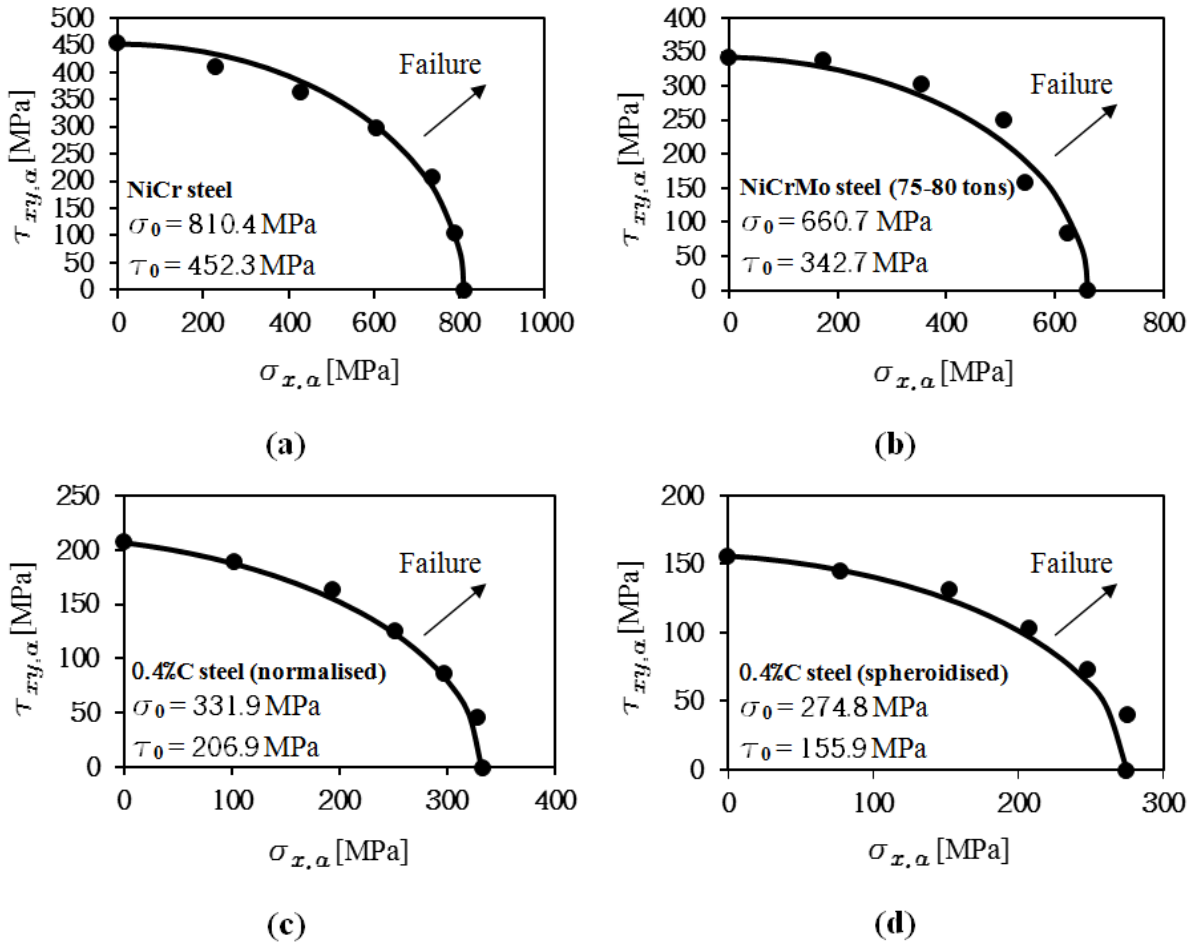
Fig. 2.15. Multiaxial fatigue behaviour of ductile (a, b) and brittle (c, d) materials according to Gough [65] (experimental data taken from [123]). Solid lines represent Eq. (2.35) (a, b) and Eq. (2.36) (c, d).

2.2.4   Multiaxial high-cycle fatigue

The observations made in §2.2.3 are valid for components subject to uniaxial cyclic loading. However, in situations of practical interest, engineering components are often subject to complex systems of cyclic loads, producing multiaxial stress states at elements' hotspots, where the hot-spot is defined as the point at a certain distance from the stress riser tip (to avoid plastic behaviour of the material) experiencing the maximum relevant stress. Hence, in order to accurately address the multiaxial fatigue assessment of structural components, appropriate engineering tools are needed.

According to Gough [65] fatigue limit conditions for steels (that he defined 'ductile'), subject to in-phase bending and torsion, can be expressed by the following relation (solid line in Figs. 2.15a and b):

$$\left(\frac{\sigma_{x,a}}{\sigma_0}\right)^2 + \left(\frac{\tau_{xy,a}}{\tau_0}\right)^2 = 1 \tag{2.35}$$

representing an ellipse quadrant. On the other hand, fatigue limit conditions of what he defined 'brittle' cast iron can be described by an arc of ellipse as follows (solid line in Figs. 2.15c and d):

$$\left(\frac{\tau_{xy,a}}{\tau_0}\right)^2 + \left(\frac{\sigma_{x,a}}{\sigma_0}\right)^2 \left(\frac{\sigma_0}{\tau_0} - 1\right) + \left(\frac{\sigma_{x,a}}{\sigma_0}\right) \left(2 - \frac{\sigma_0}{\tau_0}\right) = 1 \tag{2.36}$$

One of the most difficult aspects to appropriately take into consideration, when dealing with multiaxial problems, is the degree of non-proportionality of the considered stress state, produced by out-of-phase loadings. For a better understanding of this concept, it is worth considering the example presented in [160], where hollow cylinders are subject to two different loading systems producing the same maximum and minimum principal stresses at any time instant (Fig. 2.16). In particular, Case a corresponds to a hollow cylinder subject to fully-reversed axial stress and phase-shifted torsion (out-of-phase angle $\delta_{xy} = 90°$), whereas Case b consists of an identical hollow cylinder under in-phase pulsating internal and axial pressures. From Fig. 2.16 it is possible to observe that while in Case b the angle θ, between the first principal stress direction and the x-axis, remains constantly equal to zero during the load cycle (first principal stress direction coincides with the x-axis), in Case a θ varies in time. Hence, it is easy to understand that out-of-phase loadings produce non-proportional stress states characterised by principal stresses whose directions change during the load history.

Furthermore, it is worth mentioning that, as observed by Sonsino [114], engineering materials behave differently in presence of non-proportional stress states. In particular, while for some materials the presence of out-of-phase loadings has a damaging effect, for others it can have either a neutral or even a beneficial effect on the overall fatigue behaviour. This is due to the fact that fatigue damage is strongly influenced by the interaction between the ductility of the material and the periodic variation of the maximum principal stress directions [114, 115]. Therefore, it is evident that the effects of non-proportional loadings on the fatigue behaviour of a given material can be properly evaluated only through suitable experimental tests.

2.2.5 The Modified Wöhler Curve Method

The Modified Wöhler Curve Method (MWCM) [119] is a bi-parametric approach belonging to the family of the critical plane approaches. The MWCM is based on the idea that by modelling the nucleation as well as the initial propagation stage of micro/meso fatigue cracks, it is possible to accurately estimate the fatigue damage extent in homogeneous, isotropic materials under cyclic loading.

Case a

$\sigma_x(t) = \sigma_{x,a} \sin(\omega t)$

$\tau_{xy}(t) = \tau_{xy,a} \sin(\omega t - \delta_{xy})$

$\tau_{xy,a} = 0.5\sigma_{x,a}$

$\delta_{xy} = 90°$
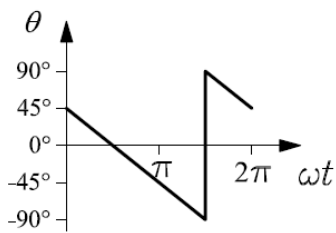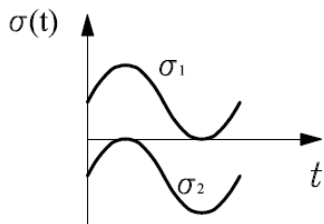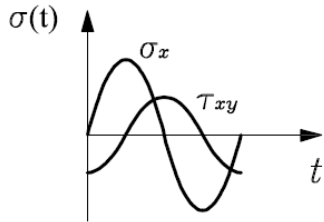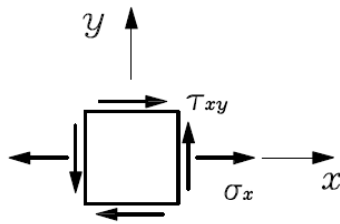
Case b

$\sigma_x(t) = \sigma_{x,m} + \sigma_{x,a} \sin(\omega t)$

$\sigma_y(t) = \sigma_{y,m} + \sigma_{y,a} \sin(\omega t)$

$\sigma_{y,m} = -\sigma_{x,m} \qquad \sigma_{y,a} = \sigma_{x,a}$

$\sigma_{x,m} = \sigma_{x,a}$
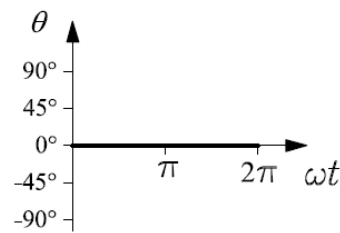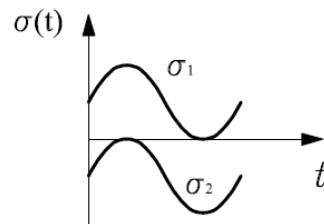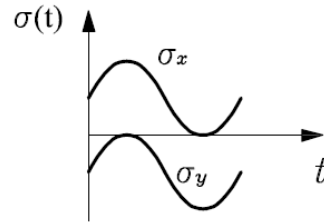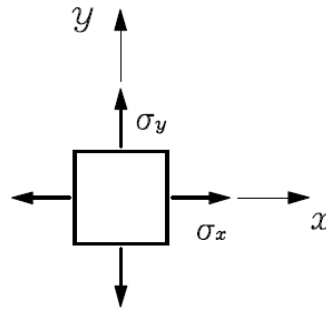
Fig. 2.16. Effect of out-of-phase angle, δ_{xy}, on the orientation, θ, of the first principal axis (example taken from [160]).
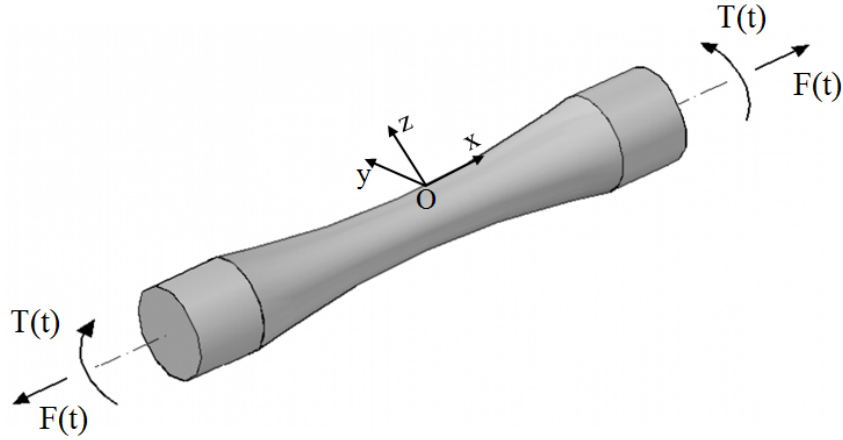
Fig. 2.17. Cylindrical specimen under combined axial and torsional loading.

As already mentioned in §2.2.2, shear stress is the main cause for the dislocations' motion, resulting in the formation of PSBs. In particular, as stated in [123], the MWCM is based on the assumption that, in the medium/high-cycle fatigue regime, both nucleation and initial propagation phenomena are driven by the shear stress damaging the process zone. Hence, for materials subject to multiaxial cyclic loadings, at the hot-spot, the plane experiencing the maximum fatigue damage (critical plane) is the one subject to the maximum shear stress amplitude, τ_a. However, shear stresses are not the only ones influencing crack formation and propagation. In particular, it has been shown that stress components normal to the crack initiation plane play also an important role in crack nucleation and propagation [112] as well as PSBs development [128]. In fact, it can be easily understood that normal compressive stresses have a beneficial effect, reducing, due to friction, the crack growth rate as well as the laminar movement of PSBs. On the contrary, normal tensile stresses have a detrimental effect favouring crack opening (and therefore propagation) and PSBs flow. Hence, as shown by Findley [51] and Matake [91], mean stress effects can be accurately considered by means of the maximum normal stress $\sigma_{n,max}$ (sum of both alternating and static superimposed normal stresses) related to the critical plane.

As described in §2.2.4 the fatigue behaviour of engineering materials subject to multiaxial loading is strongly influenced by the degree of non-proportionality of the applied loads. In order to accurately estimate the fatigue strength of a given material, the MWCM accounts for the aforementioned degree of non-proportionality through the following stress ratio [119]:

$$\rho_s = \frac{\sigma_{n,max}}{\tau_a} \tag{2.37}$$

which also allows to take into consideration the effects of non-zero mean stresses. Finally, it is worth remembering that $\sigma_{n,max}$ and τ_a are relative to the critical plane.

The characteristics of the stress ratio, ρ_s, can be highlighted by considering the problem presented in Fig. 2.17, consisting of a cylindrical specimen subject to combined

tension and torsion. For simplicity reasons, the generic point O, on the surface of the specimen, is considered to be subject to the following periodic bi-axial stress field:

$$\boldsymbol{\sigma}(t) = \begin{bmatrix} \sigma_x(t) & \tau_{xy}(t) & 0 \\ \tau_{xy}(t) & 0 & 0 \\ 0 & 0 & 0 \end{bmatrix} \tag{2.38}$$

with the stress components defined as:

$$\sigma_x(t) = \sigma_{x,m} + \sigma_{x,a} \sin(\omega t) \tag{2.39}$$

$$\tau_{xy}(t) = \tau_{xy,m} + \tau_{xy,a} \sin(\omega t - \delta_{xy,x}) \tag{2.40}$$

Considering the particular uniaxial case when τ_{xy} is equal to zero during the entire load history, it is easy to determine the expression for the stress ratio ρ_s under uniaxial fatigue loading. In particular, the stress components, determined with respect to the critical plane, can be expressed as:

$$\tau_a = \frac{\sigma_{x,a}}{2} = \frac{\sigma_{x,max}}{4}(1 - R) \tag{2.41}$$

$$\sigma_{n,max} = \sigma_{n,a} + \sigma_{n,m} = \frac{\sigma_{x,a}}{2} + \frac{\sigma_{x,m}}{2} = \frac{\sigma_{x,a} + \sigma_{x,m}}{2} = \frac{\sigma_{x,max}}{2} \tag{2.42}$$

where $\sigma_{n,a}$ and $\sigma_{n,m}$ are, respectively, the amplitude and the mean value of the stress component normal to the critical plane. By substituting Eqs. (2.41) and (2.42) into Eq. (2.37) the following expression for ρ_s is obtained:

$$\rho_s = \frac{\sigma_{n,max}}{\tau_a} = \frac{2}{1 - R} \tag{2.43}$$

From Eq. (2.43) it is possible to observe that, in case of uniaxial fatigue loading, ρ_s increases with the load ratio, R, tending to infinity for R approaching unity, while under fully-reversed loading $\rho_s = 1$.

Under pure torsional fatigue loading, instead, since the effect of non-zero mean torsional stresses on the fatigue behaviour of the considered material can be neglected in the high-cycle fatigue regime (see §2.2.3.2), ρ_s is not influenced by the presence of superimposed static shear stresses and it is invariably equal to zero. This is due to the fact that

under pure torsional loading $\tau_a = \tau_{xy,a}$, while $\sigma_{n,max} = 0$.

Furthermore, by testing the same cylindrical specimen, shown in Fig. 2.17, under combined tension and torsion shifted by different out-of-phase angles, $\delta_{xy,x}$, it has been shown that ρ_s is able to account not only for the mean-stress effect but also for the degree of non-proportionality of the applied loading [123].

The stress ratio, ρ_s, can be re-written in terms of an amplitude-related stress ratio, $\rho_{s,a}$, and a mean value-related stress ratio, $\rho_{s,m}$, as follows [121]:

$$\rho_s = \rho_{s,a} + \rho_{s,m} = \frac{\sigma_{n,a}}{\tau_a} + \frac{\sigma_{n,m}}{\tau_a} \qquad (2.44)$$

In particular, as shown in [123], $\rho_{s,m}$ is sensitive only to the mean value of the stress component normal to the critical plane, whereas $\rho_{s,a}$ allows to account for the degree of non-proportionality of the applied loading.

In order to more accurately take into consideration the damaging effect of non-zero mean stresses normal to the critical plane, Susmel [121] proposed to define the following effective stress ratio ρ_{eff}:

$$\rho_{\text{eff}} = \frac{\sigma_{n,a}}{\tau_a} + \frac{m\sigma_{n,m}}{\tau_a} \qquad (2.45)$$

where m is considered to be a material property to be determined experimentally, called *mean stress sensitivity index*, able to properly define the portion of $\sigma_{n,m}$ effectively contributing to the initiation and propagation phenomena.

This idea comes from Kaufman and Topper's findings [80] that when $\sigma_{n,m}$ exceeds a certain threshold value, an increase of the aforementioned stress does not produce any further detrimental effect on the fatigue strength of the considered material. This can be easily explained considering that as soon as $\sigma_{n,m}$ is greater than the aforementioned material limit, micro/meso cracks can be assumed to be fully opened and therefore the shear stresses are completely transmitted to the crack tip, resulting in Mode II propagation.

The mean stress sensitivity index, m, is assumed to vary in the range $0-1$. In particular $m = 0$ indicates that the considered material is not sensitive to superimposed static stresses acting perpendicularly to the critical plane, while a value of m equal to unity implies that the considered material is fully sensitive to the presence of non-zero mean stresses normal to the critical plane.

2.2.5.1 Modified Wöhler curves

The MWCM is based on the assumption that fatigue strength can be accurately estimated in terms of τ_a, on condition that the fatigue curves are conveniently corrected through the effective critical plane stress ratio, ρ_{eff}, in order to take into account the degree of multiaxiality of the stress state at the hot-spot.

As described in [123], the aforementioned corrected curves, usually called modified
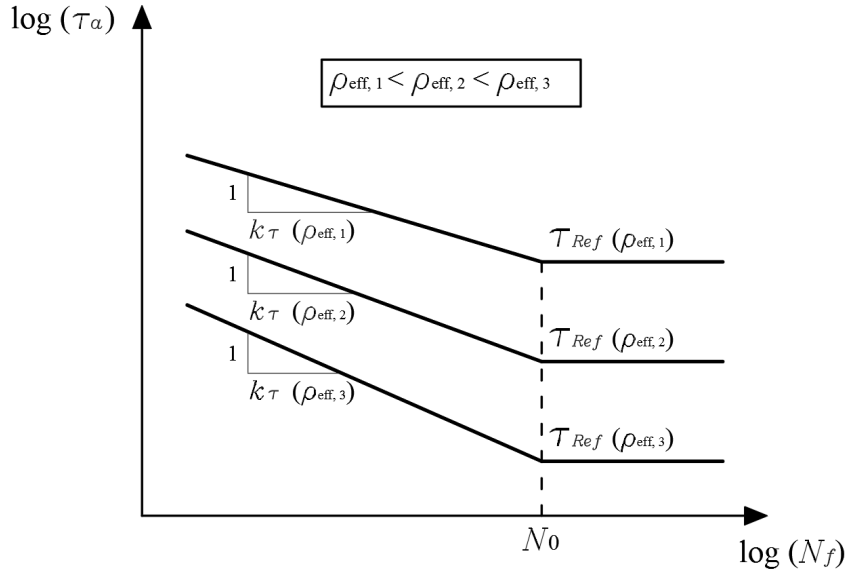
Fig. 2.18. Modified Wöhler curves and dependence on the critical plane stress ratio, ρ_{eff}.

Wöhler curves, consist in a log-log diagram plotting the shear stress amplitude acting on the critical plane, τ_a, versus the number of cycle to failure, N_f (Fig. 2.18). Furthermore, it has been shown (see [123] and references reported therein) that, for conventional engineering materials, the reference shear stress amplitude (either fatigue or endurance limit), $\tau_{Ref}(\rho_{\text{eff}})$, decreases as ρ_{eff} increases (Fig. 2.18). In particular, from Fig. 2.18 it is clear that, as also highlighted by Susmel and Lazzarin [128], a plain component is in fatigue limit conditions if the following inequality is satisfied:

$$\tau_a \leq \tau_{Ref}(\rho_{\text{eff}}) \tag{2.46}$$

Finally, the modified Wöhler diagrams can be accurately estimated, once both τ_{Ref} and the negative inverse slope k_τ are correctly related to ρ_{eff} and these relations properly calibrated through suitable experimental tests. By running an extensive experimental investigation, Susmel and co-workers [83, 119, 128, 129] proposed to perform the aforementioned calibrations through simple linear laws, which can be summarised as follows:

$$\tau_{Ref}(\rho_{\text{eff}}) = \alpha \cdot \rho_{\text{eff}} + \beta \tag{2.47}$$

$$k_\tau(\rho_{\text{eff}}) = a \cdot \rho_{\text{eff}} + b \tag{2.48}$$

where α, β, a and b are material constants to be estimated experimentally.

In particular, as reported in [123], the two parameters α and β can be expressed in

function of the corresponding fully-reversed uniaxial, σ_0, and torsional, τ_0, fatigue limits as follows:

$$\alpha = \frac{\sigma_0}{2} - \tau_0 \qquad (2.49)$$

$$\beta = \tau_0 \qquad (2.50)$$

and by substituting Eqs. (2.49) and (2.50) into Eq. (2.46), the fatigue limit condition can be reformulated as [121]:

$$\tau_{eq} = \tau_a + \left(\tau_0 - \frac{\sigma_0}{2} \right) \rho_{\text{eff}} \leq \tau_0 \qquad (2.51)$$

where τ_{eq} can be considered as an equivalent shear stress.

2.2.5.2 Validity of the Modified Wöhler Curve Method

Before concluding this section about the Modified Wöhler Curve Method, one last interesting aspect which deserves to be discussed is the range of applicability of the present method. The MWCM as formalised above is valid as long as the fatigue damaging process is driven by the amplitude of the shear stress referred to the critical plane (Mode II). As suggested in [123], when the stress component acting normally to the critical plane is much larger than the aforementioned shear stress amplitude, or in other words when ρ_{eff} is larger than a certain limit value ρ_{lim} defined as [83, 140]:

$$\rho_{\text{lim}} = \frac{\tau_0}{2\tau_0 - \sigma_0} \qquad (2.52)$$

the mechanisms leading to fatigue failure is not pure Mode II anymore. In these cases, the MWCM has been seen to produce excessively conservative results [140], making its use no longer appropriate. In order to overcome this issue and make the MWCM suitable to address also those problems characterised by high values of ρ_{eff}, Susmel [121] proposed to use Eq. (2.46) by setting $\rho_{\text{eff}} = \rho_{\text{lim}}$ when $\rho_{\text{eff}} > \rho_{\text{lim}}$.

2.3 Linear Elastic Fracture Mechanics

In the previous sections, the fatigue behaviour of components presenting stress risers characterised by finite root radii, r_n, has been analysed. However, for root radii approaching zero, linear elastic analyses produce stresses and, as a consequence of that, stress concentration factors tending to infinity in the vicinity of the stress concentrator tip. In case of stress risers with $r_n = 0$ (cracks), or in other words when singular stress fields are involved,

Mode I   Mode II   Mode III
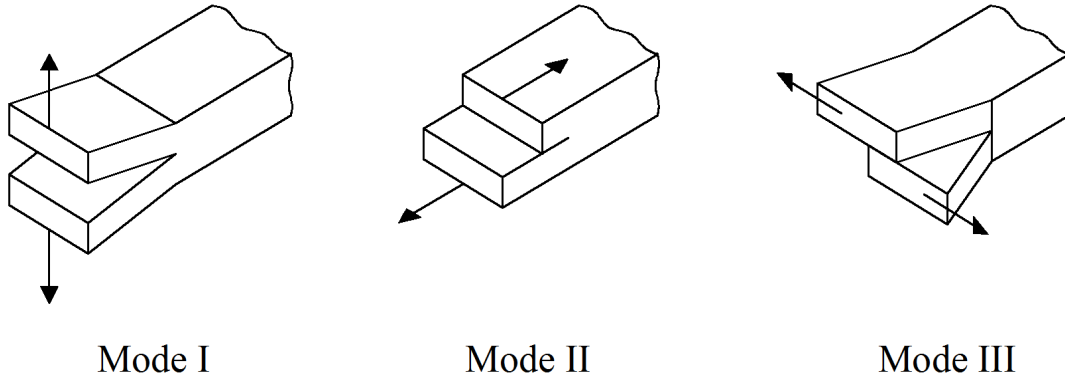
Fig. 2.19. Fundamental loading modes.

the previously described approach is thus no longer applicable and alternative techniques must be followed in order to address the fatigue assessment in the aforementioned cases, without renouncing the obvious advantages of using linear elasticity.

One possibility is to adopt an approach, that could be defined as *field approach*, where the stress field in a small region around the tip of the stress riser is considered, in contrast to the approach presented in § 2.2.3 (which can be defined as *point approach*), that is based on the peak stress experienced at the tip. The engineering field based on this approach is well-known as Linear Elastic Fracture Mechanics (LEFM).

Before analysing the stress field in the neighbourhood of a crack tip, it is worth mentioning that a crack can be subject to three different loading modes, as shown in Fig. 2.19: Mode I (opening mode), Mode II (in-plane shear mode) and Mode III (anti-plane shear mode).

According to Irwin [78, 141], the stress field in the vicinity of the tip of a crack loaded in Mode I can be expressed by the following relations (plane stress):

$$\sigma_{xx} = \frac{K_I}{\sqrt{2\pi r}} \cos\frac{\theta}{2} \left(1 - \sin\frac{\theta}{2} \sin\frac{3\theta}{2}\right) \tag{2.53}$$

$$\sigma_{yy} = \frac{K_I}{\sqrt{2\pi r}} \cos\frac{\theta}{2} \left(1 + \sin\frac{\theta}{2} \sin\frac{3\theta}{2}\right) \tag{2.54}$$

$$\tau_{xy} = \frac{K_I}{\sqrt{2\pi r}} \sin\frac{\theta}{2} \cos\frac{\theta}{2} \cos\frac{3\theta}{2} \tag{2.55}$$

and for plane strain:

$$\sigma_{zz} = \nu \left(\sigma_{xx} + \sigma_{yy}\right) \tag{2.56}$$
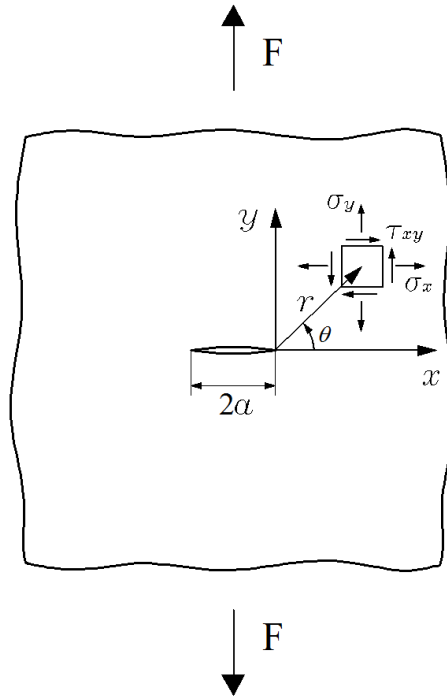
Fig. 2.20. Infinite plate with central crack subject to static tensile loading.

where K_I is the so-called Stress Intensity Factor (SIF) under Mode I, while r and θ are the polar coordinates of a generic point in the neighbourhood of the crack tip, as defined in Fig. 2.20. It is worth highlighting that the SIF is not a material property and provides information about the severity of the stress field in the neighbourhood of the crack tip. Furthermore, the SIF has unit of $\mathrm{Nm}^{-3/2}$, in contrast to the stress concentration factor K_t that is dimensionless. Eqs. (2.53 – 2.55) are valid only under all of the following conditions [8, 24]:

- Plane problems (either plane stress or plane strain)

- $r < \frac{1}{10}a$, where a represents half the crack length. This means that the distance from the crack tip must not be too large, since the stress field far from the crack tip tends to a constant value while the one described by Irwin's equations keeps changing with the same law

- $\sigma_g \leq 0.6\sigma_y$, where σ_g is the nominal gross stress and σ_y the yield stress of the material being assessed. This is to ensure that the plastic zone ahead of the crack tip is sufficiently small.

In a similar manner, the stress field in the vicinity of the crack tip can be related to the correspondent SIFs and polar coordinates also for Mode II and Mode III (see for example [141]).

The Stress Intensity Factor, K_I, is a parameter which gives an idea of the severity of

the stress field and for an infinite plate with a central crack (Fig. 2.20) it can be defined as follows:

$$K_I = \sigma_g \sqrt{\pi a} \tag{2.57}$$

while for a generic geometry Eq. (2.57) must be corrected through a shape factor F as [141]:

$$K_I = F \sigma_g \sqrt{\pi a} \tag{2.58}$$

2.3.1   Validity of Linear Elastic Fracture Mechanics

From Eq. (2.58) it is easy to understand that, for a given geometry, K_I increases as the gross nominal stress, σ_g, increases. Consider now to increase σ_g up to a value σ_f in correspondence of which the considered specimen fails statically. In this situation it is possible to define a new quantity, called *fracture toughness*, which is nothing but the value of the SIF at failure conditions:

$$K_{IC} = F \sigma_f \sqrt{\pi a} \tag{2.59}$$

From Eqs. (2.58) and (2.59), it can be noted that while K_I is characteristic of the problem under consideration and in particular of the stress field in the vicinity of the crack tip of the component being assessed, K_{IC} is a material property.

As can be seen from Eq. (2.59), if the length of the crack decreases the stress, σ_f, needed to statically break the considered component increases. However, for very small cracks, whose length is lower than a critical value a_0, LEFM leads to the wrong prediction that a specimen with a small crack will fail in correspondence of a stress value higher than the ultimate tensile stress, σ_{UTS}.

This consideration highlights the fact that LEFM is suitable only for the design of bodies containing cracks longer than a critical value defined as:

$$a_0 = \frac{1}{\pi} \left(\frac{K_{IC}}{\sigma_{UTS}} \right)^2 \tag{2.60}$$

If $a < a_0$, instead, the design must be performed according to continuum mechanics, neglecting the presence of cracks. This is due to the fact that, in these cases, cracks are so small that the material yields before failing due to the presence of cracks.
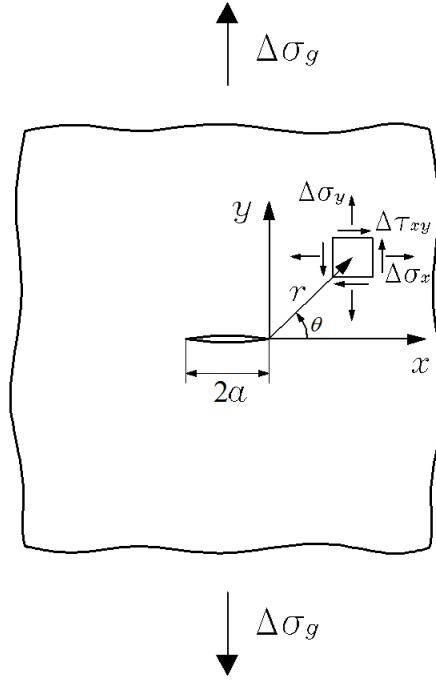
Fig. 2.21. Infinite plate with central crack subject to cyclic tensile loading.

2.3.2 Linear Elastic Fracture Mechanics to describe the fatigue behaviour of cracked bodies

Consider the cracked plate of Fig. 2.21 subject to cyclic uniaxial loading. The stress field in the neighbourhood of the crack tip can be defined by re-writing Eqs. (2.53 – 2.55) in terms of range quantities as

$$\Delta\sigma_{xx} = \frac{\Delta K_I}{\sqrt{2\pi r}} \cos\frac{\theta}{2} \left(1 - \sin\frac{\theta}{2}\sin\frac{3\theta}{2}\right) \tag{2.61}$$

$$\Delta\sigma_{yy} = \frac{\Delta K_I}{\sqrt{2\pi r}} \cos\frac{\theta}{2} \left(1 + \sin\frac{\theta}{2}\sin\frac{3\theta}{2}\right) \tag{2.62}$$

$$\Delta\tau_{xy} = \frac{\Delta K_I}{\sqrt{2\pi r}} \sin\frac{\theta}{2} \cos\frac{\theta}{2} \cos\frac{3\theta}{2} \tag{2.63}$$

where $\Delta K_I = F\Delta\sigma_g\sqrt{\pi a}$ is the SIF range.

From Eqs. (2.61 – 2.63) it is evident that ΔK_I is representative of the whole stress state acting in the vicinity of the crack tip, making it an effective tool to address crack growth problems. Considering again the problem presented in Fig. 2.21, and assuming
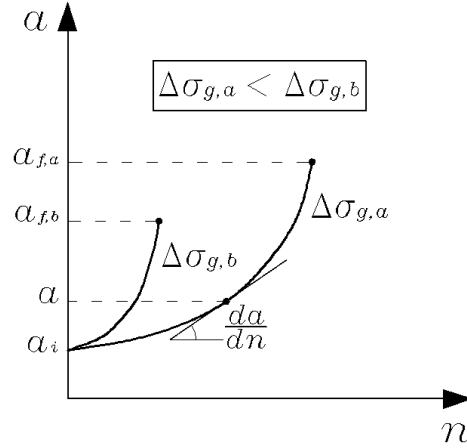
Fig. 2.22. Crack growth curve.

that both the initial semi-length of the crack, a_i and the range of the applied load allow crack propagation, it is possible to build the graph in Fig. 2.22 that shows how the semi-length of the crack, a, evolve with the number of cycle, n. In particular it is possible to observe that the semi-length of the crack increases as the number of cycles increases, with a profile that depends on the range of the applied loading, until it reaches a critical value, a_f, in correspondence of which the static failure of the sample occurs under the maximum value of the applied nominal stress, $\sigma_{g,max}$. Furthermore, from Fig. 2.22 it is easy to determine the crack growth rate, $\frac{da}{dn}$, after a given number of cycles to failure, as the slope of the tangent to the curve in correspondence of the wanted number of cycles.

The crack growth rate, $\frac{da}{dn}$, and the SIF range, ΔK_I, can be related in the well-known fatigue crack growth rate curve, also known as Paris diagram (Fig. 2.23). Classically, this diagram is subdivided in three regions [24, 123]:

- **Region I**, when ΔK_I is lower than a certain threshold value of the SIF range, ΔK_{th}. This situation occurs when an engineering component is subject to a low gross nominal stress range, $\Delta \sigma_g$, under which the crack propagation rate is null (no propagation). It is also worth pointing out that ΔK_{th} is a material property to be determined by following one of the procedures specified in the relevant codes (see for example [23]). In this region the cracking behaviour of the considered material depends on different factors, such as microstructure, environmental conditions and mean stress, but not on the thickness of the specimen used to evaluate ΔK_{th}.

- **Region II**, where crack propagation takes place. In this region the crack growth rate curve is defined by the well-known Paris law:

$$\frac{da}{dn} = C \left(\Delta K_I \right)^m \tag{2.64}$$
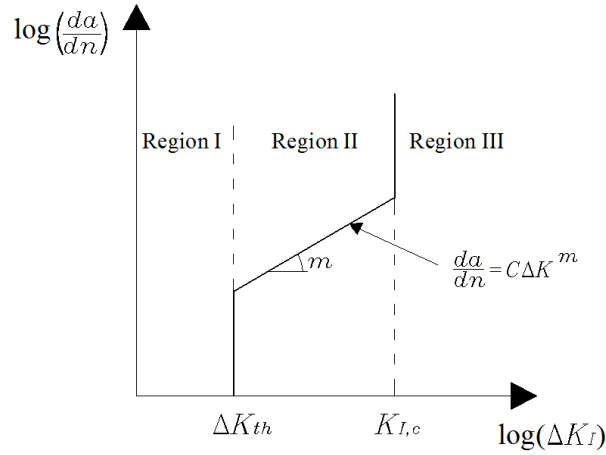
Fig. 2.23. Paris diagram.

where C and m are material constants to be determined through appropriate experimental tests and whose values depend on the load ratio R. In this region, also the thickness of the specimen used to evaluate ΔK_{th} influences the cracking behaviour of the material being assessed.

- **Region III**, where the crack propagation rate increases drastically, eventually resulting in the static breakage of the component for $\Delta K_I = K_{IC}$ (vertical asymptote). In this region the environmental conditions have a limited influence, except for the temperature.

2.3.3 Applicability of Linear Elastic Fracture Mechanics to fatigue problems

Similarly to the static case, also in the presence of fatigue loading it is possible to identify a critical crack length below which LEFM produces incorrect and non-conservative results.

At the threshold condition for crack propagation, ΔK_{th} can be defined as:

$$\Delta K_{th} = F\Delta\sigma_{0n}\sqrt{\pi a} \tag{2.65}$$

leading to:

$$\Delta\sigma_{0n} = \frac{\Delta K_{th}}{F\sqrt{\pi a}} \tag{2.66}$$

where $\Delta\sigma_{0n}$ represents the nominal fatigue limit range or, in other words, the value of the stress range below which a cracked specimen has infinite fatigue life.

From Eq. (2.66), it is possible to observe that for decreasing crack lengths, $\Delta\sigma_{0n}$
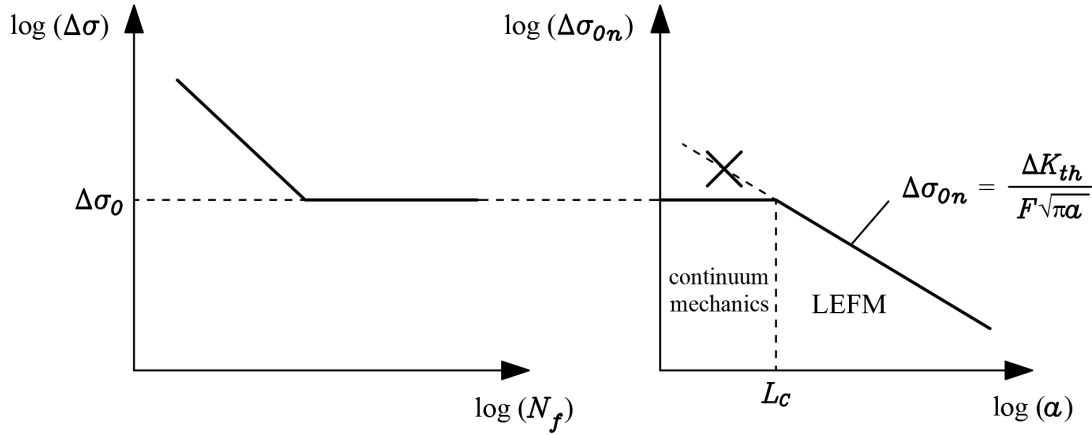
Fig. 2.24. Applicability of LEFM to fatigue problems.

increases and eventually, as also schematically shown in Fig. 2.24, for cracks shorter than a critical length, L_C, $\Delta\sigma_{0n}$ becomes larger than the fatigue limit, $\Delta\sigma_0$, of the plain material. This consideration makes it clear that for crack lengths smaller than a critical distance, L_C, defined as

$$L_C = \frac{1}{\pi}\left(\frac{\Delta K_{th}}{F\Delta\sigma_0}\right)^2 \tag{2.67}$$

LEFM leads to a wrong interpretation of the problem. This is due to the fact that when $a < L_C$ the crack is so small that the considered material does not fail for the propagation an the existing crack, but for nucleation and propagation of fatigue cracks. Hence, to conclude this section, while for $a > L_C$ LEFM is able to accurately describe the fatigue behaviour of cracked bodies, when $a < L_C$ the problem has to be addressed by applying continuum mechanics. However, experimental evidence showed that for values of $a \approx L_C$ neither continuum mechanics nor LEFM produce accurate results. This has been attributed to the fact that when the crack length approaches L_C the propagation phenomenon is strongly influenced by the local plasticity as well as the morphology of the material in the vicinity of the crack tip. In order to properly address this problem, Miller [94] proposed to study the behaviour of cracks with length approaching L_C by using elasto-plastic analyses. On the other hand, El-Haddad and co-workers [47] proposed to address this problem by using LEFM along with the following relationship:

$$\Delta\sigma_0 = \frac{\Delta K_{th}}{\sqrt{\pi(a + L_C)}} \tag{2.68}$$

In other words, according to El-Haddad and co-workers the fatigue behaviour of short cracks with length approaching L_C can be estimated through LEFM by considering an

imaginary crack of length $(a + L_C)$. However, despite the accurate estimates produced by this method, as pointed-out by Taylor [148] it is difficult to find a physical justification for Eq. (2.68).

2.4 The Theory of Critical Distances

As defined by Taylor [148], the Theory of Critical Distances (TCD) represents a family of methods, all characterised by the use of linear elastic analysis and a constant material characteristic length, commonly called critical distance L.

The TCD was originally proposed by two researchers: Neuber [98] in Germany and Peterson [103] in the United States. Both interested in the estimation of fatigue failure of notched metallic components, they proposed two slightly different critical distance methods.

Neuber started from the idea that classic continuum mechanics is not able to accurately describe the elastic stress field in areas characterised by high stress gradients, producing unphysically high stress values. To overcome this problem, he proposed to use as representative value σ_{eff} the average of the stresses, calculated according to classical elasticity, over a certain length d_L from the notch tip (Fig. 2.25c), inventing the now called Line Method (LM):

$$\sigma_{\text{eff}} = \frac{1}{d_L} \int\limits_{0}^{d_L} \sigma(r) dr \tag{2.69}$$

where $\sigma(r)$ and r are, respectively, the relevant linear elastic stress and the distance along the focus path, with the focus path defined as the straight line starting at the point of maximum stress (on the surface of the notch) and perpendicular to the surface at that point.

Peterson [103] instead, knowing Neuber's research work, decided to solve the same problem by adopting an even simpler approach. Instead of assuming a line-averaged stress, Peterson proposed to consider as reference quantity σ_{eff}, the linear elastic stress at a point distant d_P from the specimen surface along the focus path (Fig. 2.25b):

$$\sigma_{\text{eff}} = \sigma(d_P) \tag{2.70}$$

This represents the simplest version of the TCD and today is known as Point Method (PM).

Another important aspect to highlight is that the TCD considers cracked/notched specimens in their failure condition when

$$\sigma_{\text{eff}} = \sigma_0 \tag{2.71}$$
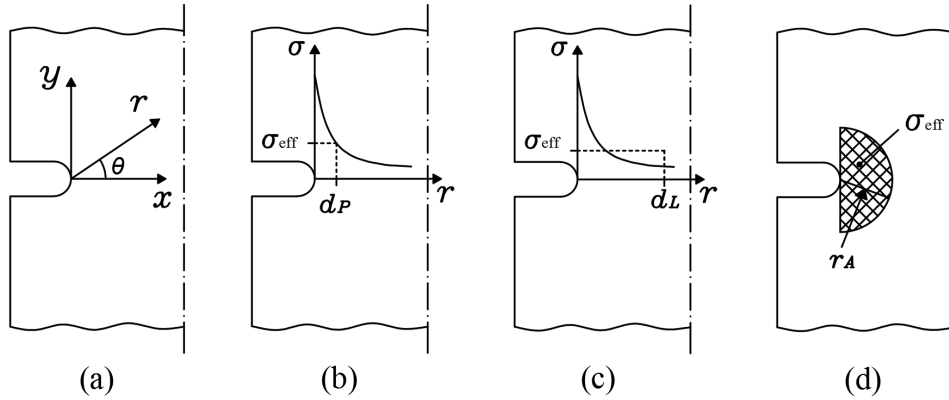
Fig. 2.25. Schematic representation of the different versions of the TCD: local reference system (a), Point Method (b), Line Method (c) and Area Method (d).

where σ_0 is the un-notched material strength, which has to be determined through appropriate experiments [148].

As explained in [148], the TCD can be easily related to LEFM. As described in §2.3, in sharp crack problems brittle fracture happens when the SIF, K_I (for simplicity Mode I problem is considered, however, the same holds true also for Mode II and III problems), equals the fracture toughness, K_{IC}. In particular, considering the infinite plate with central crack shown in Fig. 2.20, according to Eq. (2.59) the failure stress σ_f can be expressed as:

$$\sigma_f = \frac{K_{IC}}{\sqrt{\pi a}} \tag{2.72}$$

Furthermore, in the considered problem the stress of interest is $\sigma(r) = \sigma_{yy}(r)$ and according to Eqs. (2.54) and (2.57) along the crack bisector ($\theta = 0$ in Fig. 2.25a) at failure conditions it assumes the following expression:

$$\sigma(r) = \sigma_{yy}(r) = \sigma_f \sqrt{\frac{a}{2r}} \tag{2.73}$$

Substituting Eqs. (2.72) and (2.73) into Eq. (2.70), and remembering condition (2.71), distance d_P can be defined as:

$$d_P = \frac{1}{2\pi} \left(\frac{K_{IC}}{\sigma_0} \right)^2 \tag{2.74}$$

Considering now the LM (Eq. (2.69)) and following the same procedure previously used for the PM (Eq. (2.70)), distance d_L can be expressed as:

$$d_L = \frac{2}{\pi} \left(\frac{K_{IC}}{\sigma_0} \right)^2 \tag{2.75}$$

If the traditional expression for the critical distance L is assumed (see for example [148]):

$$L = \frac{1}{\pi} \left(\frac{K_{IC}}{\sigma_0} \right)^2 \tag{2.76}$$

it can be easily observed that both the PM and the LM can be expressed in terms of the same characteristic length; in particular, $d_P = L/2$ and $d_L = 2L$. Therefore, Eqs. (2.70) and (2.69) can be, respectively, re-written as:

$$\sigma_{\text{eff}} = \sigma(L/2) \tag{2.77}$$

$$\sigma_{\text{eff}} = \frac{1}{2L} \int_0^{2L} \sigma(r) dr \tag{2.78}$$

Based on Sheppard's intuition, two other versions of the TCD have been proposed. In particular, in 1999 Taylor [146] proposed the so-called Area Method (AM) that consists in calculating the effective stress, σ_{eff}, by averaging the relevant stress over a semi-circular area of radius r_A and centred at point of maximum stress as shown in Fig. 2.25d, leading to the following expression:

$$\sigma_{\text{eff}} = \frac{4}{\pi r_A^2} \int_0^{\pi/2} \int_0^{r_A} \sigma(r, \theta) r \, dr \, d\theta \tag{2.79}$$

Taylor [146] proposed to assume $r_A = L$ highlighting, however, the fact that this assumption leads to slightly conservative estimates of the inherent strength of the material. In a later work, Bellett and co-workers [31] found that to have exact correspondence between σ_{eff}, calculated according to Eq. (2.79), and σ_0 the radius of the semi-circular area must be $r_A = 1.32L$.

Finally, the fourth version of the TCD, commonly called Volume Method (VM), was proposed in 2005 by Bellett and co-workers [31] and it consists in calculating σ_{eff} by averaging the relevant stress over an hemispherical volume of radius $r_V = 1.54L$ and centred in the point of maximum stress.

For completeness, it is worth specifying that all the equations presented in this section
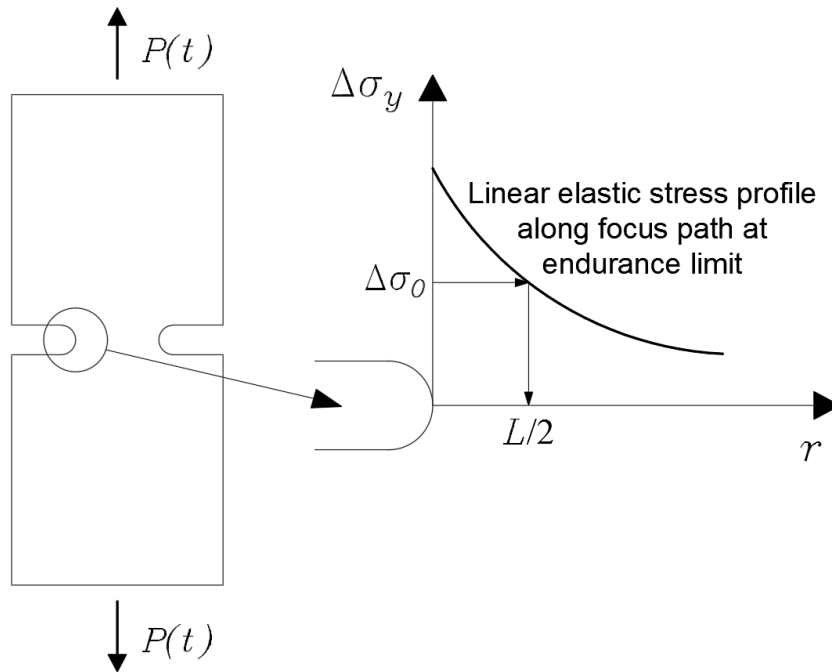
Fig. 2.26. Procedure to experimentally determine critical distance L.

for static problems hold true also for fatigue problems, provided that all the static quantities are replaced by the respective cyclic counterparts. In particular, the critical distance in fatigue problems is defined as:

$$L = \frac{1}{\pi}\left(\frac{\Delta K_{th}}{\Delta\sigma_0}\right)^2 \tag{2.80}$$

Alternatively, L can be experimentally determined by following the PM-based procedure presented in Fig. 2.26.

2.5　Final considerations

Concluding this chapter it is possible to state that several approaches are available to safely perform the static and fatigue assessment of cracked/notched components. Most of these methods have the great advantage of allowing the aforementioned static and fatigue assessments by means of classical linear elastic analyses, taking also into consideration several factors such as notch and mean stress effects, multiaxiality and non-proportionality of the loads, etc.

However, even if the possibility to use classical elastic analyses is undoubtedly a great advantage (avoiding the need of more complex elasto-plastic analyses), it presents also important drawbacks. In particular, it is well known that classical elasticity produces either

local stress singularities in correspondence of crack tips or unphysically high local stress concentrations at notch tips. Due to this, the aforementioned assessment approaches are characterised by high levels of conservatism (increasing with the sharpness of the stress concentration feature) resulting in oversized structures and therefore not complying with the environmental and economic principles described in Chapter 1.

In order to overcome the limitations of classical elasticity, as already mentioned in Chapter 1, several non-local theories were proposed in the past. In particular, amongst these the Theory of Critical Distances (that, as described in §3.2.1, can be easily obtained from the non-local integral-based Eringen theory [48, 49]) has been extensively applied to the static and fatigue assessment of cracked/notched components producing accurate results. However, also the TCD presents some disadvantages, in particular it requires the knowledge of the failure location inside the assessed component a priori. Furthermore, in the case of complex components the determination of the effective stress σ_{eff} requires complex and time consuming post-processing.

The research work presented in this thesis aims to solve all the aforementioned issues by proposing a novel finite element methodology, based on a non-local elastic theory known with the name of Ru-Aifantis theory (see §3.2.2). This methodology, easily implementable in any commercial software, allows straightforward and accurate static and fatigue assessments of notched components overcoming the limitations of classical elasticity (by effectively taking into account the effect of the microstructure through an internal length parameter) and avoiding the need of knowing the failure location inside the analysed component a priori.

Chapter 3

Gradient elasticity and the Ru-Aifantis theory

Nowadays, most of the fundamental engineering problems are addressed through classical continuum theories. Even if these theories have been originally devised to describe phenomena visible to the naked eye, they have been used to characterise a wider range of problems, from dislocations (atomistic scale) to planetary sciences (astronomic scale). Furthermore, classical elasticity has also been used to study micro- and nano-deformation problems.

However, experimental observations made it evident that classical continuum mechanics theories do not allow a precise and reliable description of micro- and nano-deformation phenomena. One of the most evident problems related to the use of classical continuum theories is the description of strain and stress fields in correspondence of stress concentration features and dislocation lines. In particular, classical elasticity produces singular strain/stress values in the vicinity of sharp crack tips as well as unphysically high stress level in the neighbourhood of stress concentration features such as notches. Furthermore, classical continuum mechanics theories fail in the description of size effects, even if their influence increases for decreasing size of the component being assessed.

The aforementioned limits of classical continuum theories can be ascribed to the absence of an intrinsic material length parameter (representative of the underlying microstructure of the considered material) in the constitutive laws. One possible solution to the deficiencies described above is to introduce, into the standard elastic constitutive equations, high-order gradients of relevant state variables (e.g. strains or stresses) multiplied by internal length parameters, representative of microstructural features of the considered material [14].

The idea of enriching the classical elastic constitutive relations with higher order gradients dates back to the early 1850s. Cauchy [35–37], during his studies of discrete lattice models, had the intuition of introducing higher order spatial gradients into the standard elastic equations. This new approach, where the size of the elementary volume was introduced as an additional constitutive parameter, allowed a more accurate description of the behaviour of discrete lattice models.

The objectives of these early studies were completely different form those of the fol-

lowing 20th century. In particular, while Cauchy's studies were aimed to describe and understand specific physical phenomena, in the 20th century researchers focused their efforts in formulating complete mathematical theories. A great contribution to the expansion of this research field came from the Cosserat brothers at the beginning of the 1900s [40]. However, the proposed theories were too complex to attract the attention of the engineering community and, as a result of this, the aforementioned research area remained mostly dormant until the 1960s when a significant number of studies started to appear. Part of these works aimed to extend the Cosserat theory into comprehensive and complex gradient theories, characterised by a large number of higher-order gradients. Owing to their complexity as well as their extremely large number of parameters, which need to be quantified, these theories found very limited practical applications. Nevertheless, amongst the 1960s studies, Mindlin's theory [95] deserves particular consideration.

3.1   Mindlin's theory

In 1964 Mindlin [95] proposed a linear elastic theory, containing microstructural information. In particular, he included in his theory the concept of unit cell, which can be considered as a microscopic feature of the material being assessed, for example a grain in the case of metals or a particle for a polymer. If the unit cell is considered rigid, the Cosserat theory [40] is retrieved.

Mindlin assumed that each particle of a given material of volume V is associated to a micro-volume V' in which it is possible to identify micro-quantities such as micro-displacements u_i' and micro-deformations ψ_{ij}, different from their macroscopic counterparts.

Based on this assumption, he defined the kinetic energy density $\mathcal{T}$ in terms of both micro- and macro-quantities as:

$$\mathcal{T} = \frac{1}{2}\rho \dot{u}_i \dot{u}_i + \frac{1}{2}\rho \ell_1^2 \dot{\psi}_{ij} \dot{\psi}_{ij} \tag{3.1}$$

where ρ is the material mass density (considered to be the same at both scale levels), ℓ_1 is an intrinsic length parameter, dependent on the size of the unit cell, while u_i are the macro-displacements. Superimposed dots represent time derivatives.

Furthermore, considering the same assumption, Mindlin proposed to express also the deformation energy density $\mathcal{W}$ in terms of both micro- and macro-quantities, resulting in the following definition:

$$\mathcal{W} = \frac{1}{2}C_{ijkl}\varepsilon_{ij}\varepsilon_{kl} + \frac{1}{2}B_{ijkl}\gamma_{ij}\gamma_{kl} + \frac{1}{2}A_{ijklmn}\kappa_{ijk}\kappa_{lmn} + D_{ijklm}\gamma_{ij}\kappa_{klm}+ \\ + F_{ijklm}\kappa_{ijk}\varepsilon_{lm} + G_{ijkl}\gamma_{ij}\varepsilon_{kl} \tag{3.2}$$

where $\varepsilon_{ij} = \frac{1}{2}(u_{i,j} + u_{j,i})$ is the macroscopic strain tensor, $\kappa_{ijk} = \psi_{jk,i}$ is the micro-deformation gradient, while $\gamma_{ij} = u_{i,j} - \psi_{ij}$ represents the relative deformation, that is the difference between macro- and micro-deformations. Regarding the tensors C_{ijkl}, B_{ijkl}, A_{ijklmn}, D_{ijklm}, F_{ijklm} and G_{ijkl}, they contains 903 independent coefficients over a total number of 1764 [95]. This figure drastically decreases to 18 in the case of isotropic materials, since D_{ijklm} and F_{ijklm} must be equal to zero (there are no odd-rank isotropic tensors), while the fourth-order tensors and the sixth-order tensor are linear, homogeneous functions of, respectively, three independent products of two Kronecker deltas, δ_{ij}, and fifteen independent products of three Kronecker deltas:

$$C_{ijkl} = \lambda\delta_{ij}\delta_{kl} + \mu_1\delta_{ik}\delta_{jl} + \mu_2\delta_{il}\delta_{jk} \tag{3.3}$$

$$B_{ijkl} = b_1\delta_{ij}\delta_{kl} + b_2\delta_{ik}\delta_{jl} + b_3\delta_{il}\delta_{jk} \tag{3.4}$$

$$G_{ijkl} = g_1\delta_{ij}\delta_{kl} + g_2\delta_{ik}\delta_{jl} + g_3\delta_{il}\delta_{jk} \tag{3.5}$$

$$
\begin{aligned}
A_{ijklmn} = {} & a_1\delta_{ij}\delta_{kl}\delta_{mn} + a_2\delta_{ij}\delta_{km}\delta_{nl} + a_3\delta_{ij}\delta_{kn}\delta_{lm} + \\
& + a_4\delta_{jk}\delta_{il}\delta_{mn} + a_5\delta_{jk}\delta_{im}\delta_{nl} + a_6\delta_{jk}\delta_{in}\delta_{lm} + \\
& + a_7\delta_{ki}\delta_{jl}\delta_{mn} + a_8\delta_{ki}\delta_{jm}\delta_{nl} + a_9\delta_{ki}\delta_{jn}\delta_{lm} + \\
& + a_{10}\delta_{il}\delta_{jm}\delta_{kn} + a_{11}\delta_{jl}\delta_{km}\delta_{in} + a_{12}\delta_{kl}\delta_{im}\delta_{jn} + \\
& + a_{13}\delta_{il}\delta_{jn}\delta_{km} + a_{14}\delta_{jl}\delta_{kn}\delta_{im} + a_{15}\delta_{kl}\delta_{in}\delta_{jm}
\end{aligned} \tag{3.6}
$$

Furthermore, the aforementioned tensors are characterised by the following relations:

$$C_{ijkl} = C_{klij} = C_{jikl}; \quad B_{ijkl} = B_{klij}; \quad G_{ijkl} = G_{ijlk}; \quad A_{ijklmn} = A_{lmnijk} \tag{3.7}$$

leading to the following conditions:

$$\mu_1 = \mu_2 = \mu; \quad g_2 = g_3; \quad a_1 = a_6; \quad a_2 = a_9; \quad a_5 = a_7; \quad a_{11} = a_{12} \tag{3.8}$$

leaving, as mentioned above, 18 independent coefficients. The deformation energy density $\mathcal{W}$ can be, therefore, re-written in the following simplified form:

$$
\begin{aligned}
\mathcal{W} = {} & \frac{1}{2}\lambda\varepsilon_{ii}\varepsilon_{jj} + \mu\varepsilon_{ij}\varepsilon_{ij} + \frac{1}{2}b_1\gamma_{ii}\gamma_{jj} + \frac{1}{2}b_2\gamma_{ij}\gamma_{ij} + \frac{1}{2}b_3\gamma_{ij}\gamma_{ji} + g_1\gamma_{ii}\varepsilon_{jj} + \\
& + g_2\left(\gamma_{ij} + \gamma_{ji}\right)\varepsilon_{ij} + a_1\kappa_{iik}\kappa_{kjj} + a_2\kappa_{iik}\kappa_{jkj} + \frac{1}{2}a_3\kappa_{iik}\kappa_{jjk} + \frac{1}{2}a_4\kappa_{ijj}\kappa_{ikk} + \\
& + a_5\kappa_{ijj}\kappa_{kik} + \frac{1}{2}a_8\kappa_{iji}\kappa_{kjk} + \frac{1}{2}a_{10}\kappa_{ijk}\kappa_{ijk} + a_{11}\kappa_{ijk}\kappa_{jki} + \frac{1}{2}a_{13}\kappa_{ijk}\kappa_{ikj} + \\
& + \frac{1}{2}a_{14}\kappa_{ijk}\kappa_{jik} + \frac{1}{2}a_{15}\kappa_{ijk}\kappa_{kji}
\end{aligned}
\tag{3.9}
$$

where λ and μ are the usual Lamé constants.

However, even if the number of coefficients to be quantified significantly decreases for isotropic materials, it still remains quite substantial, resulting in an excessive effort, from a practical point of view, for the estimation of the aforementioned coefficients. For this reason, Mindlin proposed even simpler, although less general, versions of his theory. In particular, he expressed the micro-deformation gradient κ_{ijk} in terms of a gradient function $\tilde{\kappa}_{ijk}$ only, the 18 components of which are independent linear combination of the second-gradient of the macro-displacements, $u_{k,ij}$. This enables the deformation energy density $\mathcal{W}$ to be expressed in terms of macro-displacements only. Mindlin [95] proposed three simplified version of his theory that differ for the definition of $\tilde{\kappa}_{ijk}$ and he called Form I, II and III:

- **Form I**: $\tilde{\kappa}_{ijk}$ is defined as the second-gradient of the macro-displacements, that is $\tilde{\kappa}_{ijk} = u_{k,ij} = \tilde{\kappa}_{jik}$.

- **Form II**: $\tilde{\kappa}_{ijk}$ is defined as $\tilde{\kappa}_{ijk} = \hat{\kappa}_{ijk} + \hat{\kappa}_{jki} - \hat{\kappa}_{kij}$, where $\hat{\kappa}_{ijk}$ is the first gradient of the macro-strain, i.e. $\hat{\kappa}_{ijk} = \varepsilon_{jk,i} = \frac{1}{2}\left(u_{k,ij} + u_{j,ik}\right) = \hat{\kappa}_{ikj}$.

- **Form III**: this version address the problem differently respect to the previous two Forms. In particular, as also explained in [14], the effects of the micro-deformations are separated into two components: the gradient of the macro-rotations $\bar{\kappa}_{ij} \equiv e_{jlm}\varepsilon_{mi,l} = \frac{1}{2}e_{jlm}u_{m,il}$ (e_{jlm} is the so-called Levi-Civita permutation tensor) and the symmetric part of the second gradient of the macro-displacements $\bar{\bar{\kappa}}_{ijk} = \frac{1}{3}(u_{k,ij} + u_{j,ki} + u_{i,jk})$.

The three versions presented above, even if theoretically different, lead to the same equations of motion in terms of the macroscopic displacements. Considering for example Form II, the deformation energy density takes the following simplified form:

$$
\hat{\mathcal{W}} = \frac{1}{2}\tilde{\lambda}\varepsilon_{ii}\varepsilon_{jj} + \tilde{\mu}\varepsilon_{ij}\varepsilon_{ij} + \hat{a}_1\hat{\kappa}_{iik}\hat{\kappa}_{kjj} + \hat{a}_2\hat{\kappa}_{ijj}\hat{\kappa}_{ikk} + \hat{a}_3\hat{\kappa}_{iik}\hat{\kappa}_{jjk} + \hat{a}_4\hat{\kappa}_{ijk}\hat{\kappa}_{ijk} + \hat{a}_5\hat{\kappa}_{ijk}\hat{\kappa}_{kji}
\tag{3.10}
$$

where [95]

$$\tilde{\lambda} + 2\tilde{\mu} = \lambda + 2\mu - \frac{8g_2^2}{3(b_2 + b_3)} - \frac{(3g_1 + 2g_2)^2}{3(3b_1 + b_2 + b_3)}$$

$$\tilde{\mu} = \mu - \frac{2g_2^2}{b_2 + b_3}$$

$$\hat{a}_1 = f(a_1, a_2, a_3, a_5, a_8, a_{11}, a_{14}, a_{15})$$

$$\hat{a}_2 = f(a_1, a_2, a_3, a_4, a_5, a_8, a_{10}, a_{11}, a_{13}, a_{14}, a_{15}) \qquad (3.11)$$

$$\hat{a}_3 = f(a_2, a_3, a_8)$$

$$\hat{a}_4 = f(a_{10}, a_{11}, a_{13}, a_{14}, a_{15})$$

$$\hat{a}_5 = f(a_{10}, a_{11}, a_{13}, a_{14}, a_{15})$$

Mindlin [95], as also stated in [14], proposed the following simplified definition of the kinetic energy density $\mathcal{T}$:

$$\mathcal{T} = \frac{1}{2}\rho \dot{u}_i \dot{u}_i + \frac{1}{2}\rho \ell_1^2 \dot{u}_{i,j} \dot{u}_{i,j} \qquad (3.12)$$

The simplified deformation and kinetic energy density (i.e. Eqs. (3.10) and (3.12)) lead to the following equations of motion:

$$(\lambda + \mu)\, u_{j,ij} + \mu u_{i,jj} - \frac{4\hat{a}_1 + \hat{a}_2 + 3\hat{a}_3 + 2\hat{a}_4 + 3\hat{a}_5}{2}u_{j,ijkk} -$$

$$(3.13)$$

$$- \frac{\hat{a}_3 + 2\hat{a}_4 + \hat{a}_5}{2}u_{i,jjkk} + b_i = \rho\left(\ddot{u}_i - \ell_1^2 \ddot{u}_{i,jj}\right)$$

where b_i are the body forces. Eq. (3.13) can be also written in the following form:

$$(\lambda + \mu)\left(1 - \ell_2^2 \frac{\partial^2}{\partial x_k^2}\right)u_{j,ij} + \mu\left(1 - \ell_3^2 \frac{\partial^2}{\partial x_k^2}\right)u_{i,jj} + b_i = \rho\left(1 - \ell_1^2 \frac{\partial^2}{\partial x_j^2}\right)\ddot{u}_i \qquad (3.14)$$

where the two parameters ℓ_2 and ℓ_3 have the dimension of length and are defined by the following expressions:

$$\ell_2 = \sqrt{\frac{4\hat{a}_1 + 4\hat{a}_2 + 3\hat{a}_3 + 2\hat{a}_4 + 3\hat{a}_5}{2(\lambda + \mu)}}$$

$$(3.15)$$

$$\ell_3 = \sqrt{\frac{\hat{a}_3 + 2\hat{a}_4 + \hat{a}_5}{2\mu}}$$

From Eq. (3.14) it is clear that now only three material length parameters (ℓ_1, ℓ_2 and ℓ_3) have to be quantified, making this simplified version of Mindlin theory much more tractable, from a practical point of view, with respect to the original one. Furthermore, from Eq. (3.14), as also pointed out in [14], it is possible to observe that, in both the stiffness and inertia components, the higher-order terms are nothing but the Laplacian of the corresponding lower-order terms.

As explained in [14], Laplace-type gradients are extremely versatile, since they appear in many physical processes and microstructural reasons of gradient-based theories. In the next section, more recent Laplacian-based non-local theories will be discussed in details.

3.2   Laplacian-based gradient theories and the Ru-Aifantis theory

From the 1980s onward we witness a new series of much simpler gradient-based theories characterised by few high-order terms, which obviously means a sensible reduction in the number of additional constitutive parameters to validate experimentally. In particular, Eringen's and Aifantis' theories deserve special attention and they will be discussed in more details in the following of this chapter. The guiding principle of these theories was to include only the high-order derivatives necessary to describe the physical phenomenon of interest.

While for non-linear problems the use of numerical methods is necessary, in the case of linear problem characterised by very simple geometries a willing person could solve it analytically, with some mathematical efforts. Unfortunately the number of this kind of problems is extremely low and for all other linear problems a numerical solution is needed.

For this reason, we are seeing a continuous increase in the use of numerical methods for simulations, which makes the implementation of gradient elasticity of central importance. However, finite element implementations of these theories is not trivial due to the more complex structure of the governing equations. Also for what concerns the implementation, we can find different schools of thought: on one hand some authors (see for example [7, 102, 109, 161]) have focussed their efforts on implementing the more complete theories of the 1960s, while on the other hands others have taken advantage of the simplicity offered by the Aifantis theory, developing notably straightforward finite element implementations [15, 18, 152].

3.2.1   Eringen theory

In 1983, Eringen [50] proposed an integral-based non-local elastic theory, where relevant state variables are averaged over volume. In terms of stresses, Eringen's theory postulates that the non-local stress tensor σ_{ij}^g at a given point $\mathbf{x}$ of a body is the weighted average of the local stress tensor σ_{ij}^c of all points $\mathbf{x}'$ into the body volume. In the cases when the effect of stresses in points different from $\mathbf{x}$ can be neglected, the standard local theory

of elasticity is retrieved. In particular, for elastic, homogeneous and isotropic bodies, the static equations of equilibrium are given by:

$$\sigma^g_{ij,j} + b_i = 0 \tag{3.16}$$

with the non-local stress tensor defined as:

$$\sigma^g_{ij}(\mathbf{x}) = \int_V \chi(|\mathbf{x}' - \mathbf{x}|, \epsilon) \sigma^c_{ij}(\mathbf{x}') dV \tag{3.17}$$

where the non-local weight function $\chi(|\mathbf{x}' - \mathbf{x}|, \epsilon)$ is related to an intrinsic internal length a (for example grain distance) and an external characteristic length l (such as the crack length) through the parameter ϵ defined as:

$$\epsilon = e_0 \frac{a}{l} \tag{3.18}$$

where e_0 is a material constant.

As pointed out by Eringen [50], the non-local weight function χ must obey a number of properties, in particular:

- χ reaches its maximum for $\mathbf{x}' = \mathbf{x}$ and decreases for increasing values of $|\mathbf{x}' - \mathbf{x}|$.

- To ensure that classical elasticity condition is considered for vanishing values of a, χ must take the shape of a Dirac delta function for $\epsilon \to 0$:

$$\lim_{\epsilon \to 0} \chi(|\mathbf{x}' - \mathbf{x}|, \epsilon) = \delta(|\mathbf{x}' - \mathbf{x}|) \tag{3.19}$$

- χ can be determined, for a considered material, by fitting dispersion curves of plane waves with experimental ones or those characteristic of atomic lattice dynamics. Several possible definitions of χ can be found in [50].

- If χ is taken as a Green's function of a linear differential operator, the integral-based non-local elastic theory described above is converted into a gradient-based non-local elastic theory, with significant simplifications. In particular Eringen [50] proposed to relate the non-local stress tensor σ^g_{ij} to its local counterpart σ^c_{ij} (or displacements u_k) through the following partial differential equation (p.d.e.):

$$\sigma^g_{ij} - \ell^2_E \sigma^g_{ij,kk} = \sigma^c_{ij} = C_{ijkl} u_{k,l} \tag{3.20}$$

where C_{ijkl} is the constitutive tensor and ℓ_E is an internal length parameter.

It is worth mentioning, as pointed out in [14], that both the mathematical procedure needed to pass from Eq. (3.17) to Eq. (3.20) and the correspondent approximation error depend on the definition of the non-local weight function χ.

Finally, one last interesting aspect emerging from a careful analysis of both the integral-based Eringen theory (Eq. (3.17)) and the TCD described in §2.4, is that the different versions of the TCD can be retrieved from the integral-based Eringen theory by appropriately defining the weight factor χ and in particular:

- the **PM** is obtained by considering $\chi = \delta(L/2, r)$, where δ is the Dirac function;

- the **LM**, instead, corresponds to Eq. (3.17) when the weight factor is defined as a combination of Heaviside functions: $\chi = H_0(r) - H_{2L}(r)$;

- while the **AM** is retrieved when the weight factor is taken as follows:

$$\chi = \begin{cases} 1 & \text{when} \quad 0 \le r \le r_A \\ 0 & \text{when} \quad r > r_A \end{cases} \tag{3.21}$$

with $-\pi/2 \le \theta \le \pi/2$. Similar considerations can be made for the **VM** where the domain is now half a sphere of radius r_A, instead of half a circle as for the AM.

3.2.2   Ru-Aifantis theory

At the beginning of the 1990s, Aifantis and coworkers, inspired by an earlier gradient-plasticity model developed for the determination of shear bands width [1, 2], proposed to enrich the constitutive relations of classical elasticity by means of the Laplacian of the strain as [3, 6, 108]

$$\sigma_{ij} = C_{ijkl}(\varepsilon_{kl} - \ell^2 \varepsilon_{kl,mm}) \tag{3.22}$$

where ℓ is a length scale parameter that, as suggested in [18] and references reported therein, can be related to microstructural features of the considered material (e.g. inter-particle distance for periodic lattices or representative volume element for heterogeneous media). This gradient-elastic model, characterised by just one internal length parameter, has the remarkable ability to remove singularities from the strain field in correspondence of sharp crack tips as well as dislocation lines [4–6, 18, 68, 70, 71, 108].

The previous constitutive relations (Eq. (3.22)) along with the following kinematic equations

$$\varepsilon_{kl} = \frac{1}{2}(u_{k,l} + u_{l,k}) \tag{3.23}$$

and the fact that for isotropic linear elastic materials $C_{ijkl} = \lambda\delta_{ij}\delta_{kl} + \mu\delta_{ik}\delta_{jl} + \mu\delta_{il}\delta_{jk}$ lead to the following equilibrium equations for homogeneous materials:

$$C_{ijkl}(u_{k,jl} - \ell^2 u_{k,jlmm}) + b_i = 0 \tag{3.24}$$

From a numerical point of view the solution of Eq. (3.24) presents some difficulties, making the Aifantis theory not very appealing for practical applications. In particular, its finite element implementation is non-trivial, mainly due to the fact that the solution of the fourth-order problem defined by Eq. (3.24) requires $\mathcal{C}^1$-continuous shape functions (e.g. those of meshless methods, see for instance [13, 145]), instead of the standard $\mathcal{C}^0$-continuous shape functions required by the second-order p.d.e. of classical elasticity.

At this point it is worth highlighting the fact that, as also explained in [14], Eq. (3.24) represents the particular case of Mindlin's theory (Eq. (3.14)) when the condition $\ell_2 = \ell_3 = \ell$ is imposed. Having said that, the Aifantis theory could seem to be a mere simplification of Mindlin's theory, however the condition $\ell_2 = \ell_3 = \ell$ is the only one that allows, as described next, to solve Eq. (3.24) as a decoupled sequence of two second-order p.d.e. systems, with significant simplifications from the finite element implementation point of view.

In particular, in 1993 Ru and Aifantis [108] observed that by changing the derivation order, Eq. (3.24) can be written as:

$$C_{ijkl}u_{k,jl}^c + b_i = 0 \tag{3.25}$$

where the classical (or local) displacements u_k^c are related to the gradient-enriched (or non-local) counterpart u_k^g through the following relationship:

$$u_k^g - \ell^2 u_{k,mm}^g = u_k^c \tag{3.26}$$

It is worth noticing that if Eq. (3.26) is substituted into Eq. (3.25) the original fourth-order p.d.e. system (Eq. (3.24)) is obtained. However, both analytical and numerical advantages of the Ru-Aifantis formulation compared to the original fourth-order theory (Eq. 3.24) are evident. In fact, once the local displacements u_k^c are determined through classical elasticity (Eq. (3.25)), the non-local displacements u_k^g can be easily calculated by solving the second-order Helmholtz equations given by Eq. (3.26), where just $\mathcal{C}^0$-continuity is required for the discretisation of u_k^g.

As suggested in [18, 69, 70], Eq. (3.26) can be re-written in terms of strains through simple differentiation as:

$$\varepsilon_{kl}^g - \ell^2 \varepsilon_{kl,mm}^g = \varepsilon_{kl}^c \tag{3.27}$$

where ε_{kl}^c and ε_{kl}^g are, respectively, the local and non-local strain tensor.

The strain-based Ru-Aifantis formulation consists in determining the non-local strain tensor ε_{kl}^g from Eq. (3.27), where ε_{kl}^c is determined through Eq. (3.23) once the local displacements u_k^c are known from the solution of Eq. (3.25).

As pointed out in [18], in the absence of external boundaries Eqs. (3.26) and (3.27) are equivalent if the displacement field is sufficiently smooth and ℓ is constant throughout the domain.

Finally, if the local and non-local stress tensors are defined, respectively, as $\sigma_{ij}^c = C_{ijkl}\varepsilon_{kl}^c$ and $\sigma_{ij}^g = C_{ijkl}\varepsilon_{kl}^g$, Eq. (3.27) can be re-written in terms of stresses, obtaining the so-called stress-based Ru-Aifantis formulation (see also [14, 18] and references reported therein):

$$\sigma_{ij}^g - \ell^2 \sigma_{ij,mm}^g = C_{ijkl} u_{k,l}^c \qquad (3.28)$$

The non-local stress tensor σ_{ij}^g can be easily calculated by solving Eq. (3.28), where u_k^c are again the local displacements obeying the equations of classical elasticity (Eq. (3.25)).

It is also worth mentioning two aspects:

- The different versions of the Ru-Aifantis theorem (i.e. Eqs. (3.26), (3.27) and (3.28)) requires different variationally consistent boundary conditions, as explained in §3.3.

- The negative sign in front of the higher-order terms is needed to guarantee uniqueness and stability of the solution [19]. However, other formulations containing a positive sign have been proposed in the literature to describe dispersion and wave propagation in granular materials [38, 96, 117, 118]. A detailed comparison between the two different formulations in both statics and dynamics can be found in [19].

3.2.3   Differences between Eringen and Ru-Aifantis theories

Even if Eqs. (3.20) and (3.28) describe the same gradient dependence, the Eringen and the Ru-Aifantis theories present a fundamental difference resulting in important implications on the numerical implementation of the two theories. In particular, in Eringen's theory the equilibrium equations are written in terms of non-local stresses σ_{ij}^g as:

$$\sigma_{ij,j}^g + b_i = 0 \qquad (3.29)$$

Therefore Eq. (3.29) is coupled with Eq. (3.20) and their solution needs to be simultaneous, drastically reducing the possibilities of developing a straightforward implementation of Eringen's theory. For example, Askes and Gutiérrez [16] proposed a possible implementation of the Eringen theory similar to the one described in §3.2.1, with the only difference that the unknown are displacements and non-local strains (instead of stresses). In their work, Askes and Gutiérrez [16] showed that, in order to avoid oscillations, the displacements must be interpolated with lower-order polynomials, compared to those needed for

the non-local strains. However, the implementation of finite elements characterised by different interpolation functions for displacements and stresses has been shown to be rather complicated (see for instance [11, 34]) due to the inf-sup condition (also known as Babuška-Brezzi condition) (see for example [74]).

In the Ru-Aifantis formulation, instead, the equilibrium is defined in terms of local stresses σ_{ij}^c, which are directly related to the local displacements u_i^c, allowing the solution of the problem as a sequence of two decoupled sets of equations (Eq. (3.25) followed by Eq. (3.28)), as described in §3.2.2. Obviously, this leads to an higher number of degrees of freedom per element. Nevertheless, the decoupled nature of Eqs. (3.25) and (3.28) reduces the computational costs and allows a straightforward and effective numerical implementation of the Ru-Aifantis formulation as shown in Chapter 5.

3.3 Boundary conditions

From §3.2.3 it is clear that the Ru-Aifantis formulation is more appealing than the Eringen theory from the numerical implementation point of view. However, the definition of the most suitable boundary conditions is a problem that needs to be properly addressed.

As described in §3.2.2, the Aifantis theory can be considered as either a system of fourth-order p.d.e. (Eq. (3.24)) with the displacements as only unknown, or two decoupled sets of second-order p.d.e. (Ru-Aifantis formulation), with displacements as unknowns of the first set (Eq. (3.25)) and an additional variable for the second step (Eq. (3.26), (3.27) or (3.28)).

As described in [18] the variationally consistent boundary conditions for the Aifantis theory in its fourth-order format (Eq. (3.24)) are set in terms of displacements and their first derivative in what concerns the essential boundary conditions. In particular the standard essential boundary conditions read

$$u_i = \bar{u}_i \tag{3.30}$$

where $\bar{u}_i$ are the displacements prescribed on the boundary. The higher-order essential boundary conditions, instead, are defined as:

$$\frac{\partial u_i}{\partial x_j} n_j = \bar{\eta}_i \tag{3.31}$$

where n is the outward normal vector to the boundary, while $\bar{\eta}_i$ are the prescribed values for the normal derivative of the displacements.

The natural boundary conditions, on the other hand, are written in terms of standard, t, and higher-order, m, tractions as

$$t_i = n_j \left[\sigma_{ij} + n_k \tau_{ijk} \left(\delta_{lm} - n_l n_m \right) \frac{\partial n_l}{\partial x_m} \right] - \left(\delta_{km} - n_k n_m \right) \frac{\partial n_j \tau_{ijk}}{\partial x_m} = \bar{t}_i \qquad (3.32)$$

$$m_i = n_j n_k \tau_{ijk} = \bar{m}_i \qquad (3.33)$$

where the higher-order stresses are defined as $\tau_{ijk} = \ell^2 C_{ijkl} \varepsilon^c_{kl,m}$, whereas $\bar{t}_i$ and $\bar{m}_i$ are the tractions prescribed on the boundary.

Since the field equations of the Ru-Aifantis theory differ from those of the fourth-order Aifanits theory, also the correspondent boundary conditions are different. First of all, the first step of all the different formulations of the staggered Ru-Aifantis formulation consists in Eq. (3.25) and therefore they share the same standard boundary conditions in terms of either displacements:

$$u_i^c = \bar{u}_i^c \qquad (3.34)$$

where $\bar{u}_i^c$ are the local displacements prescribed on the boundary, or standard tractions:

$$t_i = n_j \sigma_{ij}^c = \bar{t}_i \qquad (3.35)$$

To analyse the higher-order boundary conditions accompanying the three different formulations of the second step, instead, it is worth considering the weak form of the second step:

$$\int_\Omega \delta s \left(s^g - \ell^2 s^g_{,ii} \right) d\Omega = \int_\Omega \delta s \ s^c d\Omega \qquad (3.36)$$

where s is a generic variable (either displacements, strains or stresses), δs is a test function and Ω is the considered domain. After integration by parts, Eq. (3.36) reads:

$$\int_\Omega \delta s \ s^g d\Omega + \int_\Omega \delta s_{,i} \ \ell^2 s^g_{,i} d\Omega = \int_\Omega \delta s \ s^c d\Omega + \oint_\Gamma \delta s \ \ell^2 n_i s^g_{,i} d\Gamma \qquad (3.37)$$

where Γ is the boundary of the domain Ω.

From the second term on the right-hand side of Eq. (3.37) it is possible to observe that the natural boundary conditions are expressed in terms of first derivatives of the relevant gradient-enriched variables (either displacements, strains or stresses).

As shown in [18], the displacement-based Ru-Aifantis theory (Eq. (3.26)) is not able to remove all singularities from the strain field of cracked specimens subject to Mode I loading; hence this version of the Ru-Aifantis theory will not be discussed any further.

On the other hand, the Ru-Aifantis formulation applied in terms of strains is able to

remove all singularities from the strain field. However, as shown in [18], this method is not able to describe stiffness jumps such as those occurring at the interface of bi-materials. This difference with respect to the original fourth-order Aifantis theory (Eq. (3.24)) is due to the different higher-order boundary conditions. In fact, unlike the higher-order traction m accompanying Eq. (3.24), the higher-order natural boundary conditions accompanying Eq. (3.27) are expressed in terms of the first derivative of the gradient-enriched strains and therefore no stiffness effects are considered.

The stress-based Ru-Aifantis theory (Eq. (3.28)), instead, is characterised by natural boundary conditions of the dynamic type, i.e expressed in terms of (gradient-enriched) stresses, similarly to those accompanying Eq. (3.24), allowing for the description of stiffness jump phenomena [14, 18]:

$$n_m \ell^2 \sigma_{ij,m}^g = 0 \tag{3.38}$$

This feature along with the ability to remove all singularities from the stress field make the stress-based Ru-Aifnatis theory more versatile and therefore preferable to the displacements- and strain-based versions.

3.4 Length scale parameters

One last aspect that needs to be discussed more in depth is the identification of the internal length parameter ℓ.

As mentioned in the incipit of this chapter, the intrinsic length parameter ℓ is usually assumed to be somehow related to microstructural features of the material being assessed and, in particular, to the size of the prevailing source of microstructural heterogeneity [14]. However, a clear and widely accepted identification of the length scale parameters remains an open problem.

Some researchers proposed to relate the length scale to the size of the Representative Volume Element (RVE), defined at a microscopic level as a cell large enough to allow a statistically homogeneous response (see [14] for a synthetic yet exhaustive overview). In particular, it has been found that the length scale ℓ can be related to the size of the RVE, L_{RVE}, through the following relation [61, 81]:

$$\ell^2 = \frac{1}{12} L_{RVE}^2 \tag{3.39}$$

As described in [14], other researchers proposed to derive the length scale parameters as closed-form solutions from the constitutive properties of discrete periodic lattices or composite materials.

In what concerns discrete lattices, the length scale parameters are generally a function of the inter-particle distance (see for instance [92, 93]).

Studying the dispersive behaviour of laminated materials, instead, Fish and co-workers

[39, 52, 53] proposed to define the intrinsic length parameters not only in terms of geometrical features such as volume fraction and unit cell size, but also of the properties of the involved materials (Young's modulus and mass density). The results of Fish and co-workers have also been used to determine the length scale parameters of a dynamically consistent gradient elastic model [32] as well as the micro-inertia gradient visco-elastic methodology presented in Chapter 8 (see also [29]).

In 2013 Susmel and co-workers [127] mathematically derived an expression that relates the length scale ℓ of the Ru-Aifantis formulation to two fatigue material properties as described in Chapter 4. This relation, originally derived for cracked bodies subject to fatigue loading, has also been successfully applied to notched components subject to both static (Chapter 6.1) and fatigue (Chapters 6.2 and 7 as well as [28, 79]) loading.

Furthermore, in Chapter 7 an attempt to give ℓ a physical meaning is proposed (see also [79]). In particular, in the context of plain concrete notched beams subject to fatigue loading, the length scale ℓ has been taken equal to the average inter-aggregate distance, leading to extremely accurate results. This encouraging results further support the idea that ℓ must be directly related to geometrical features characterising the material microstructure.

Finally, even if beyond the scope of this thesis, it is worth mentioning that another group of studies can be found in the literature (for a comprehensive overview see [14]). These works aim to numerically quantify the length scale parameters (through either experimental validations or nanoscale numerical simulations), instead of relating them to geometrical or constitutive material properties as the previous formulations.

Chapter 4

Combining Gradient elasticity, the Theory of Critical Distances and the Modified Wöhler Curve Method

It is widely accepted that the length scale parameter ℓ is related to the size of the dominant source of microstructural heterogeneity [14]. However, examination of the state of the art suggests that the scientific community has yet to agree on a commonly accepted strategy suitable for estimating ℓ to use in situations of practical interest.

As to a possible way to determine length ℓ, the previous chapters should make it evident that gradient elasticity and the TCD share some important features. In particular, both approaches post-process the relevant stress fields by coupling linear-elasticity with an internal length scale parameter which is assumed to be an intrinsic material property. By taking as a starting point these similarities, it was recently proven that length ℓ from gradient elasticity can be directly linked to the TCD's critical distance L as follows [127]:

$$\ell \approx \frac{L}{2\sqrt{2}} = \frac{1}{2\sqrt{2}\pi}\left(\frac{\Delta K_{th}}{\Delta\sigma_0}\right)^2 \tag{4.1}$$

The above relationship was derived by considering a cracked plate subject to Mode I cyclic loading and post-processing the stress field in the vicinity of the crack tip through considerations based on local mechanics [127]. According to Eq. (4.1), length scale parameter ℓ can directly be estimated from the material plain fatigue limit range, $\Delta\sigma_0$, and the threshold value of the stress intensity factor range, ΔK_{th}. Since both $\Delta\sigma_0$ and ΔK_{th} are material properties, ℓ is an intrinsic characteristic length which is different for different materials and different load ratios. By post-processing a large number of experimental results taken from the literature, gradient elasticity, with ℓ defined as in Eq. (4.1), was seen to be capable of accurately describing, at fatigue limit condition, the transition from the short- to the long-crack regime [127]. Relation 4.1 holds true also for static problems, with the only difference that the critical distance L is now defined by Eq. (2.76), leading to:

$$\ell \approx \frac{L}{2\sqrt{2}} = \frac{1}{2\sqrt{2}\pi}\left(\frac{K_{IC}}{\sigma_0}\right)^2 \tag{4.2}$$

In the light of the encouraging results obtained by considering cracked materials, the next logical step in the development of this design approach is then verifying whether the length ℓ estimated via Eq. (4.1) is suitable also for assessing high-cycle fatigue strength in the presence of finite radius stress concentrators.

The way gradient elasticity determines the non-local stress fields according to the TCD (i.e. when ℓ is directly derived from L through Eq. (4.1)) is explained in Fig. 4.1a. As shown in Fig. 4.1a, gradient elasticity can simply be considered as an operator transferring the linear elastic stress state determined according to the PM onto the surface of the notch itself (Fig. 4.1a). According to this idea, high-cycle fatigue strength of notched components can be assessed by directly using the maximum gradient-enriched stress state determined at the apex of the geometrical feature being assessed.

To use gradient elasticity consistently, the second problem to address is the definition of appropriate reference un-notched fatigue (endurance) limits. Figs. 4.1b, c and d show the stress distributions in a smooth cylindrical shaft loaded in cyclic tension-compression (Fig. 4.1b), cyclic bending (Fig. 4.1c) and cyclic torsion (Fig. 4.1d). These three bars are assumed to be made of the same metallic material, so that length scale ℓ is the same independently of the type of applied load. In these sketches the symbols F_0, M_0 and T_0 are used to denote the amplitudes of the external forces and moments in the fatigue (endurance) limit condition. As shown in Figs. 4.1c and d, the gradient-enriched fatigue (endurance) limits on the surface of the shaft, σ_0^g and τ_0^g, are lower than the corresponding ones, σ_0 and τ_0, calculated according to continuum mechanics. This can be ascribed to the fact that in the presence of stress gradients the Ru-Aifantis formulation smooths the local stress fields via length scale parameter ℓ, irrespective of the source generating the stress gradients themselves. Gradient elasticity produces the same stress fields as those determined according to continuum mechanics, only in the absence of stress gradients as it happens, for instance, under cyclic axial loading (Fig. 4.1b). Therefore, to be rigorous, gradient elasticity should be used by adopting σ_0^g and τ_0^g as reference un-notched fatigue (endurance) limits [79]. However, it has to be said that, in general, under both cyclic bending and torsion the difference between conventional and gradient-enriched fatigue (endurance) limits is seen to be very little (on average, less than about 5%). This suggests that σ_0 and τ_0 can still be used as reference fatigue strengths, provided that a little loss of accuracy is acceptable when performing the high-cycle fatigue assessment.

Figs. 4.2a and b summarise the procedures which are suggested here as being followed to design notched components against uniaxial and multiaxial high-cycle fatigue, respectively.

For the sake of simplicity, attention can be initially focused on the simpler uniaxial fatigue problem. Consider then the notch sketched in Fig. 4.2a which is assumed to be subject to Mode I cyclic loading. According to the procedure summarised in Fig. 4.2a, the range of the gradient-enriched stress at the notch tip, $\Delta\sigma_y^g$, has to be determined by solving a linear gradient elasticity FE model with ℓ determined via Eq. (4.1). The
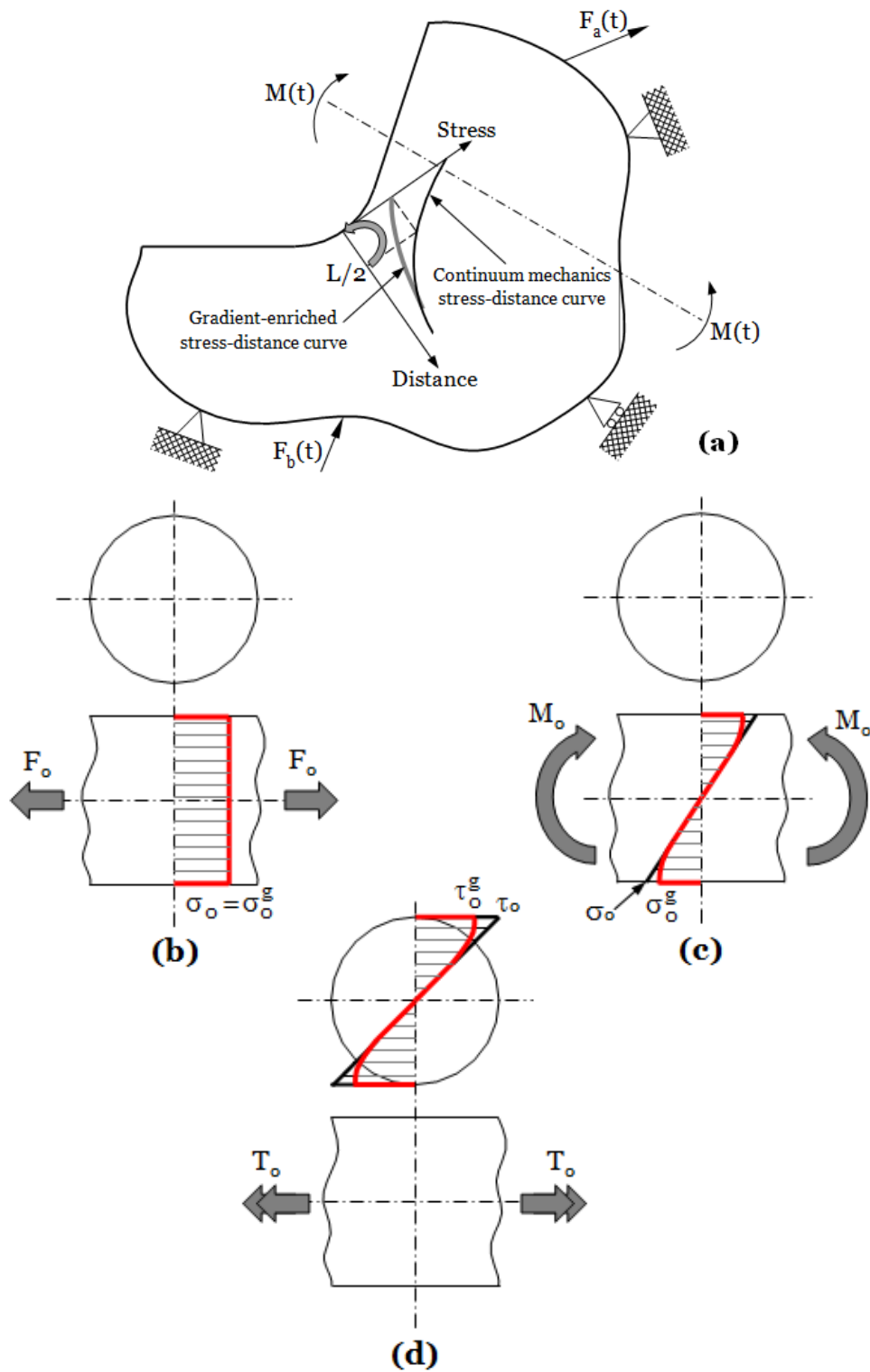
Fig. 4.1. Gradient-enriched notch tip stress vs. PM effective stress (a); conventional and gradient-enriched un-notched fatigue (endurance) limits under cyclic axial loading (b), cyclic bending (c) and cyclic torsion (d).

component being assessed is assumed to be at its fatigue (endurance) limit as long as the following condition is assured:

$$\Delta\sigma_y^g \leq \Delta\sigma_0^g \tag{4.3}$$

At this point, it is worth pointing out that, as postulated by the TCD, under Mode I cyclic loading both $\Delta\sigma_0^g$ and ℓ must be determined by post-processing experimental results generated under the same load ratio as the one characterising the load history that is applied to the component being assessed.

Turning to the multiaxial fatigue case, consider now the notched component of Fig. 4.2b which is assumed to be subject to a complex system of time-variable forces and moments. By post-processing the results obtained from a gradient elasticity FE model, the gradient-enriched linear-elastic stress state at the hot-spot can be expressed as follows (Fig. 4.2b):

$$\boldsymbol{\sigma}^g(t) = \begin{bmatrix} \sigma_x^g(t) & \tau_{xy}^g(t) & \tau_{xz}^g(t) \\ \tau_{xy}^g(t) & \sigma_y^g(t) & \tau_{yz}^g(t) \\ \tau_{xz}^g(t) & \tau_{yz}^g(t) & \sigma_z^g(t) \end{bmatrix} \tag{4.4}$$

where t is time. Due to the ability of the MWCM to directly take into account the effect of non-zero mean stresses in both uniaxial and multiaxial fatigue [123], it is recommended to use material fatigue properties determined under $R = -1$ to calculate ℓ according to Eq. (4.1). This is to ensure a consistent use of the MWCM in the post-processing of gradient-enriched stress tensor (4.4).

Turning back to the design procedure summarised in Fig. 4.2b, as soon as the stress tensor from expression (4.4) is known at any instant of the assessed load history, the maximum shear stress amplitude, τ_a^g, and the relevant stress components perpendicular to the critical plane (i.e. $\sigma_{n,m}^g$ and $\sigma_{n,a}^g$) can directly be calculated according to one of the available methods (for more details see [123] and references reported therein). Gradient-enriched stress components τ_a^g, $\sigma_{n,m}^g$ and $\sigma_{n,a}^g$ allow then the effective value of the critical plane stress ratio, ρ_{eff}^g, to be calculated as

$$\rho_{\text{eff}}^g = \frac{\sigma_{n,a}^g + m \cdot \sigma_{n,m}^g}{\tau_a^g} \tag{4.5}$$

Finally, the notched component being designed is assumed to be at its endurance limit as long as the following condition is assured:

$$\tau_{eq}^g = \tau_a^g - \left(\frac{\sigma_0^g}{2} - \tau_0^g\right)\rho_{\text{eff}}^g \leq \tau_0^g \quad \text{with} \quad \rho_{\text{eff}}^g = \rho_{\text{lim}}^g \quad \text{for} \quad \rho_{\text{eff}}^g > \rho_{\text{lim}}^g \tag{4.6}$$

$$\Delta\sigma_y^g \leq \Delta\sigma_0^g$$

(a) Gradient elasticity FE model with $\ell = \dfrac{L}{2\sqrt{2}}$

(b)

$$[\sigma^g(t)] = \begin{bmatrix} \sigma_x^g(t) & \tau_{xy}^g(t) & \tau_{xz}^g(t) \\ \tau_{xy}^g(t) & \sigma_y^g(t) & \tau_{yz}^g(t) \\ \tau_{xz}^g(t) & \tau_{yz}^g(t) & \sigma_z^g(t) \end{bmatrix}$$

$$\tau_a^g, \ \sigma_{n,m}^g, \ \sigma_{n,a}^g, \ \rho_{\text{eff}}^g$$

$$\tau_{eq}^g = \tau_a^g - \left(\frac{\sigma_0^g}{2} - \tau_0^g\right)\cdot\rho_{\text{eff}}^g \leq \tau_0^g$$
with $\rho_{\text{eff}}^g = \rho_{\text{lim}}^g$ for $\rho_{\text{eff}}^g > \rho_{\text{lim}}^g$

Gradient elasticity FE model with $\ell = \dfrac{L}{2\sqrt{2}}$
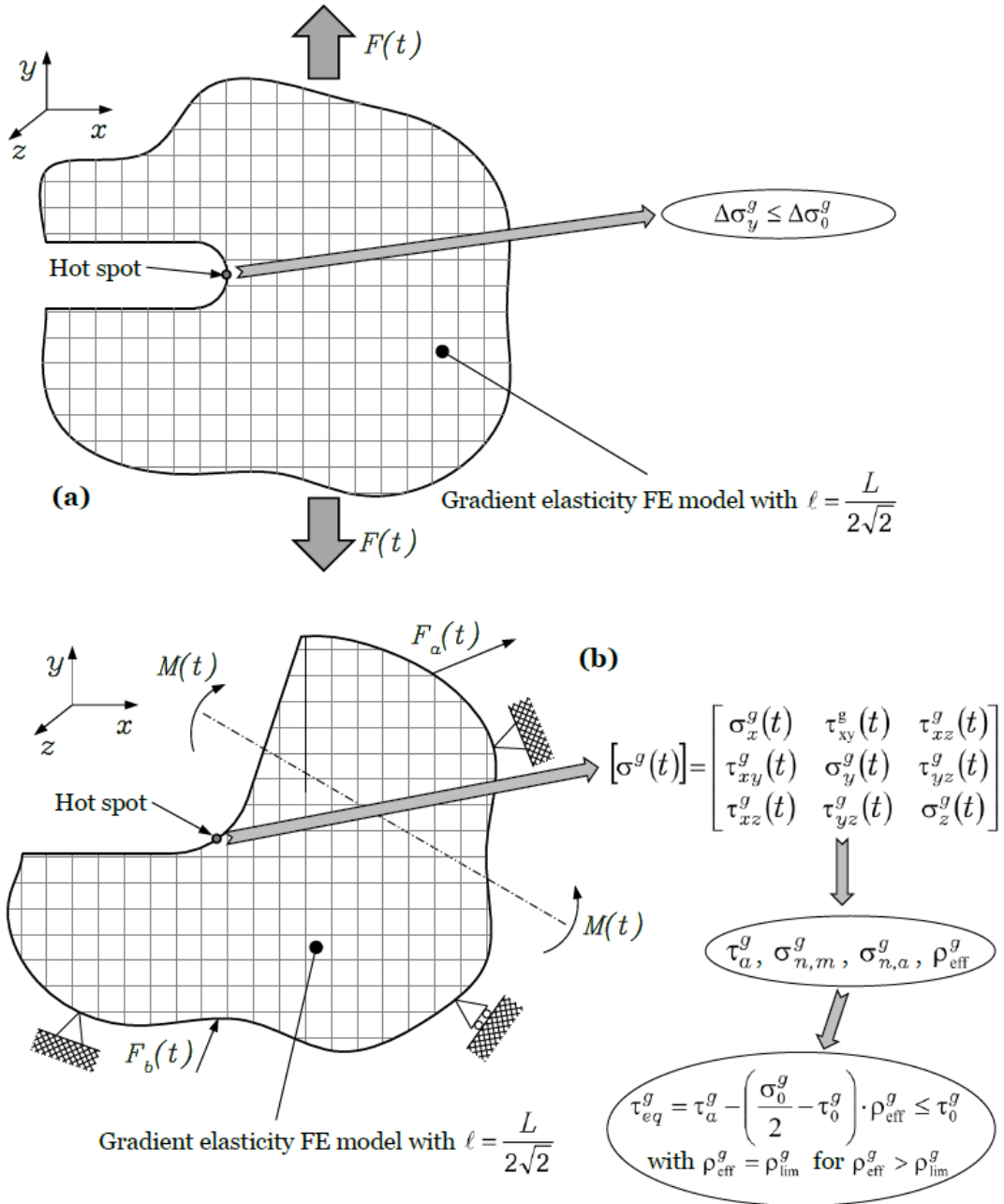
Fig. 4.2. In-field use of gradient elasticity to estimate notch fatigue (endurance) limits.

where

$$\rho_{\text{lim}}^g = \frac{\tau_0^g}{2\tau_0^g - \sigma_0^g} \tag{4.7}$$

Regarding the design procedure suggested to address multiaxial fatigue problems (Fig. 4.2b), under complex time-variable load histories, the gradient-enriched stress state resulting from every applied force/moment can be computed separately. By so doing, the total gradient-enriched stress tensor at the hot-spot, i.e. the material point experiencing the largest value of τ_{eq}^g calculated according to Eq. (4.6), can then be calculated *a posteriori* by employing the superposition principle. This can be done because the proposed approach makes use of linear-elastic gradient-enriched stresses. Finally, this methodology based on the superposition principle has to be used by paying attention to keep unchanged the synchronism amongst the different forces and moments being assessed. This simple and standard procedure allows the presence of superimposed static stresses as well as the degree of non-proportionality of the applied load history to be accurately taken into account during the design process as shown in Chapter 6.2. However, in order to be able to apply these concepts to more general geometries, it is necessary to develop a finite element framework. This will be discussed in detail in the next Chapter.

Chapter 5

Finite element implementation of the Ru-Aifantis theory

In this chapter, the stress-based Ru-Aifantis theorem presented in §3.2.2 is implemented in a finite element framework for plane stress/strain, axisymmetric and three-dimensional problems. Considerations about the best integration rules to be adopted, a comprehensive convergence study and recommendations about optimal element size are also provided. Furthermore, the ability of the proposed methodology to remove singularities will be shown through several examples. From now on matrix-vector notation is adopted, instead of the index notation used in §3.2.2.

5.1 Plane stress and plane strain

In both plane stress and plane strain problems, the displacements field is fully defined by the displacement components u_x and u_y in the two Cartesian directions x and y, respectively. The continuum displacements $\mathbf{u} = [u_x, u_y]^T$ can be discretised and expressed in terms of the nodal displacements $\mathbf{d} = [d_{1x}, d_{1y}, d_{2x}, d_{2y}, \ldots]^T$ through the relation

$$\mathbf{u} = \mathbf{N}_u \mathbf{d} \tag{5.1}$$

where $\mathbf{N}_u$ is the matrix containing the traditional shape functions N_i (see for instance [164]) and can be written as:

$$\mathbf{N}_u = \begin{bmatrix} N_1 & 0 & N_2 & 0 & \ldots \\ 0 & N_1 & 0 & N_2 & \ldots \end{bmatrix} \tag{5.2}$$

As explained in §3.2.2, the Ru-Aifantis theorem splits the original fourth-order partial differential equations (p.d.e.) into two sets of second-order p.d.e., which allows the

determination, in the first instance, of the local displacements $\mathbf{u}^c$ by solving the p.d.e. of classical elasticity:

$$\mathbf{L}^T\mathbf{C}\mathbf{L}\mathbf{u}^c + \mathbf{b} = 0 \tag{5.3}$$

where $\mathbf{b}$ are the body forces and $\mathbf{C}$ is the elasticity matrix, which, for isotropic materials, in the case of plane stress problems takes the form

$$\mathbf{C} = \frac{E}{1-\nu^2} \begin{bmatrix} 1 & \nu & 0 \\ \nu & 1 & 0 \\ 0 & 0 & (1-\nu)/2 \end{bmatrix} \tag{5.4}$$

while in plane strain conditions

$$\mathbf{C} = \frac{E}{(1+\nu)(1-2\nu)} \begin{bmatrix} 1-\nu & \nu & 0 \\ \nu & 1-\nu & 0 \\ 0 & 0 & (1-2\nu)/2 \end{bmatrix} \tag{5.5}$$

where E and ν are the Young's modulus and the Poisson's ratio, respectively.

Moreover, the derivative operator $\mathbf{L}$ is defined as

$$\mathbf{L} = \begin{bmatrix} \frac{\partial}{\partial x} & 0 \\ 0 & \frac{\partial}{\partial y} \\ \frac{\partial}{\partial y} & \frac{\partial}{\partial x} \end{bmatrix} \tag{5.6}$$

Taking now the weak form of Eq. (5.3), followed by integration by parts and using the finite element discretisation described above, Eq. (5.3) leads to

$$\int_\Omega \mathbf{B}_u^T\mathbf{C}\mathbf{B}_u d\Omega\, \mathbf{d}^c \equiv \mathbf{K}\mathbf{d}^c = \mathbf{f} \tag{5.7}$$

where $\mathbf{K} = \int_\Omega \mathbf{B}_u^T\mathbf{C}\mathbf{B}_u d\Omega$ is the stiffness matrix, $\mathbf{B}_u = \mathbf{L}\mathbf{N}_u$ is the strain-displacement matrix, $\mathbf{d}^c$ is the vector of the nodal local displacements and $\mathbf{f}$ is the force vector, that collects the contributions of both the body forces and the external tractions.

Then, from the second set of equations (second step) it is possible to evaluate the

gradient-enriched stress field, by introducing the local displacements $\mathbf{u}^c$ (obtained solving Eq. (5.3)) as source term in

$$(\boldsymbol{\sigma}^g - \ell^2 \nabla^2 \boldsymbol{\sigma}^g) = \mathbf{C}\mathbf{L}\mathbf{u}^c \tag{5.8}$$

where $\boldsymbol{\sigma}^g$ is the non-local (i.e. affected by the gradient enrichment) stress tensor and ∇^2 is the Laplace operator defined as

$$\nabla^2 \equiv \nabla^T \nabla \quad \text{with} \quad \nabla = \left\{ \begin{matrix} \frac{\partial}{\partial x} \\ \frac{\partial}{\partial y} \end{matrix} \right\} \tag{5.9}$$

Considering again the weak form of Eq. (5.8) and integrating by parts, we obtain

$$\begin{aligned} &\int_\Omega \left[\mathbf{w}^T \boldsymbol{\sigma}^g + \ell^2 \left(\frac{\partial \mathbf{w}^T}{\partial x} \frac{\partial \boldsymbol{\sigma}^g}{\partial x} + \frac{\partial \mathbf{w}^T}{\partial y} \frac{\partial \boldsymbol{\sigma}^g}{\partial y} \right) \right] d\Omega - \oint_\Gamma \mathbf{w}^T \ell^2 \left(\mathbf{n} \cdot \nabla \boldsymbol{\sigma}^g \right) d\Gamma = \\ &= \int_\Omega \mathbf{w}^T \mathbf{C}\mathbf{L}\mathbf{u}^c d\Omega \end{aligned} \tag{5.10}$$

where $\mathbf{n} = [n_x \ \ n_y]^T$ contains the components of the normal vector to the boundary Γ and $\mathbf{w}$ now contains three components.

In the case of plane stress all out-of-plane stress components are null; while in plane strain conditions the stress normal to the plane xy is not zero, but the strain in the same direction is zero by definition, which means that the aforementioned stress component does not contribute to the internal work and, if needed, it can be easily calculated using the three in-plane stress components.

Similar to the displacements, the continuum stress field $\boldsymbol{\sigma} = [\sigma_{xx} \ \ \sigma_{yy} \ \ \sigma_{xy}]^T$ can be discretised and expressed in terms of the nodal values $\mathbf{s} = [s_{1xx} \ \ s_{1yy} \ \ s_{1xy} \ \ s_{2xx} \ \ s_{2yy} \ \ s_{2xy} \ldots]^T$ through the relation

$$\boldsymbol{\sigma} = \mathbf{N}_\sigma \mathbf{s} \tag{5.11}$$

where $\mathbf{N}_\sigma$ is an expanded form of the shape function matrix $\mathbf{N}_u$ given in Eq. (5.2), in order to accommodate all three stress components. The shape functions $\mathbf{N}_\sigma$ can in principle be defined independently of $\mathbf{N}_u$, however, since the same finite element mesh can be used for both the first step, described above, and this second step, the same shape functions, previously used for the discretisation of the displacements, can also be adopted to discretise the stresses, making the solution of the problem much easier. This is permitted because of the de-coupled nature of the proposed formulation (this would not be possible for mixed formulations such as the Eringen theory presented in §3.2.1).

Finally, using the same shape functions $\mathbf{N}_\sigma$ to discretise the test function vector $\mathbf{w}$ and recalling that $\mathbf{u}^c = \mathbf{N}_u \mathbf{d}^c$, the resulting system of equations reads

$$\int_\Omega \left[\mathbf{N}_\sigma^T \mathbf{N}_\sigma + \ell^2 \left(\frac{\partial \mathbf{N}_\sigma^T}{\partial x} \frac{\partial \mathbf{N}_\sigma}{\partial x} + \frac{\partial \mathbf{N}_\sigma^T}{\partial y} \frac{\partial \mathbf{N}_\sigma}{\partial y} \right) \right] d\Omega \, \mathbf{s}^g = \int_\Omega \mathbf{N}_\sigma^T \mathbf{C} \mathbf{B}_u d\Omega \, \mathbf{d}^c \qquad (5.12)$$

where $\mathbf{s}^g$ is the vector of the nodal non-local stresses. As can be noted, in passing from Eq. (5.10) to Eq. (5.12) the boundary integral $\oint_\Gamma \delta\boldsymbol{\sigma}^{gT} \ell^2 \left(\mathbf{n} \cdot \nabla \boldsymbol{\sigma}^g \right) d\Gamma$ has disappeared. This is due to the fact that:

- if *essential* boundary conditions are used, $\boldsymbol{\sigma}^g$ is known (usually the condition $\boldsymbol{\sigma}^g = \boldsymbol{\sigma}^c$ is chosen), therefore $\delta\boldsymbol{\sigma}^g = 0$;

- if *natural* boundary conditions are used, the condition $\mathbf{n} \cdot \nabla \boldsymbol{\sigma}^g = 0$ is chosen.

Hence, either way the boundary integral cancels.

It is worth highlighting at this point that the de-coupled Ru-Aifantis theorem does not influence the field equations of the original fourth-order Aifantis theory (Eq. (3.24)) but influence the boundary conditions and therefore, it is not possible to exactly replicate the original boundary conditions expressed by Eqs. (3.32) and (3.33). The boundary conditions described above come directly from the boundary integral in Eq. (5.10). Finally, homogeneous higher-order natural boundary conditions are taken because they are easier to apply.

5.2   Axisymmetry

It is well known from the literature (see for example [164]) that in axisymmetric solids subject to axisymmetric loading, displacements, strains and stresses are all independent of the circumferential coordinate θ of the cylindrical coordinate system defined in Fig. 5.1. This characteristic allows the study of this kind of problems by simply considering the generic plane section of the solid along its axis of revolution z (shaded in Fig. 5.1), subject to in-plane loading.

The displacement field is described by two components only, since the circumferential component $u_\theta = 0$ for axisymmetry reasons, which are a function of the radial (r) and axial (z) coordinates only:

$$\mathbf{u}(r, z) = \{ u_r(r, z) \quad u_z(r, z) \}^T \qquad (5.13)$$

In what concerns the strains, they can be collected in the strain vector

$$\boldsymbol{\varepsilon}(r, z) = \{ \varepsilon_{rr}(r, z) \quad \varepsilon_{zz}(r, z) \quad \varepsilon_{\theta\theta}(r, z) \quad 2\varepsilon_{rz}(r, z) \}^T \qquad (5.14)$$

where (ignoring the spatial dependence for notational simplicity)
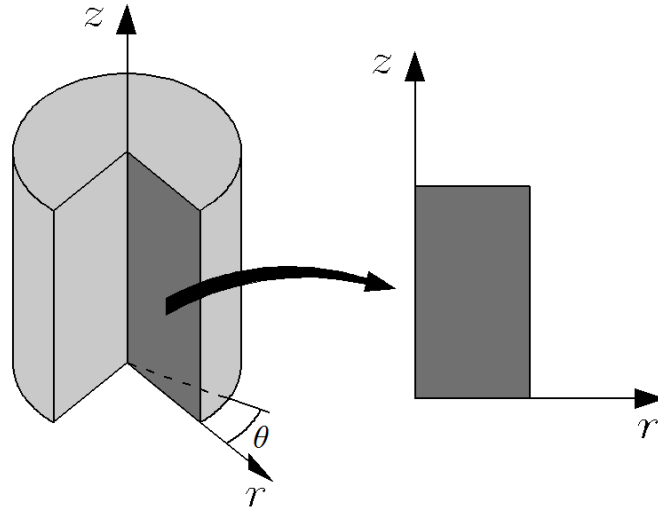
Fig. 5.1. Axisymmetric solid: cylindrical coordinate system and generic plane section of the solid to analyse.

$$\varepsilon_{rr} = \frac{\partial u_r}{\partial r}, \quad \varepsilon_{zz} = \frac{\partial u_z}{\partial z}, \quad \varepsilon_{\theta\theta} = \frac{u_r}{r}, \quad 2\varepsilon_{rz} = \frac{\partial u_z}{\partial r} + \frac{\partial u_r}{\partial z} \qquad (5.15)$$

Finally, in the case of linear elastic materials, the stress field is linked to the strain field through the following constitutive relation

$$\boldsymbol{\sigma} = \begin{Bmatrix} \sigma_{rr} \\ \sigma_{zz} \\ \sigma_{\theta\theta} \\ \sigma_{rz} \end{Bmatrix} = \mathbf{C}\boldsymbol{\varepsilon} = \frac{E}{(1+\nu)(1-2\nu)} \begin{bmatrix} 1-\nu & \nu & \nu & 0 \\ \nu & 1-\nu & \nu & 0 \\ \nu & \nu & 1-\nu & 0 \\ 0 & 0 & 0 & \frac{1-2\nu}{2} \end{bmatrix} \boldsymbol{\varepsilon} \qquad (5.16)$$

5.2.1 Non-axisymmetric loading

In the case of an axisymmetric solid subject to non-axisymmetric loads, the circumferential component of the displacements u_θ must be considered in addition to the radial and axial components. As a consequence of this, all the strain and stress components may assume non-zero values; in particular the strain field is described by the following vector (ignoring the spatial dependence for notational simplicity)

$$\boldsymbol{\varepsilon} = \{\varepsilon_{rr} \quad \varepsilon_{zz} \quad \varepsilon_{\theta\theta} \quad 2\varepsilon_{rz} \quad 2\varepsilon_{r\theta} \quad 2\varepsilon_{z\theta}\}^T \qquad (5.17)$$

where in addition to Eq. (5.15) we have

$$2\varepsilon_{r\theta} = \frac{1}{r}\left(\frac{\partial u_r}{\partial \theta} - u_\theta\right) + \frac{\partial u_\theta}{\partial r}, \qquad 2\varepsilon_{z\theta} = \frac{\partial u_\theta}{\partial z} + \frac{1}{r}\frac{\partial u_z}{\partial \theta} \tag{5.18}$$

and the stress vector is now defined as

$$\boldsymbol{\sigma} = \left\{\sigma_{rr} \quad \sigma_{zz} \quad \sigma_{\theta\theta} \quad \sigma_{rz} \quad \sigma_{r\theta} \quad \sigma_{z\theta}\right\}^T = \mathbf{C}^\star \boldsymbol{\varepsilon} =$$

$$= \frac{E}{(1+\nu)(1-2\nu)}\begin{bmatrix} 1-\nu & \nu & \nu & 0 & 0 & 0 \\ \nu & 1-\nu & \nu & 0 & 0 & 0 \\ \nu & \nu & 1-\nu & 0 & 0 & 0 \\ 0 & 0 & 0 & \frac{1-2\nu}{2} & 0 & 0 \\ 0 & 0 & 0 & 0 & \frac{1-2\nu}{2} & 0 \\ 0 & 0 & 0 & 0 & 0 & \frac{1-2\nu}{2} \end{bmatrix}\boldsymbol{\varepsilon} \tag{5.19}$$

However, by re-defining the load and displacement components through Fourier series, this problem can still be solved as a quasi-bidimensional problem (see for example [159, 165]).

5.2.2   Implementation aspects

In this section, a possible finite element implementation of the stress-based Ru-Aifantis theory described in §3.2.2 is proposed for the analysis of axisymmetric solids subject to both axisymmetric and non-axisymmetric loads.

5.2.2.1   Axisymmetric loads

The index notation used in §3.2.2 is valid in Cartesian coordinates, while axisymmetric problems are usually addressed in cylindrical coordinates as in the following of the present section. Therefore, in order to derive the finite element equations for axisymmetric problems unambiguously, we will now depart from the index notation used in §3.2.2, adopting a matrix-vector notation. Furthermore, two potential energy functionals, one for each of the two steps of the Ru-Aifantis theory, have been defined as follows

$$W_1 = \int_\Omega \frac{1}{2}\boldsymbol{\varepsilon}^{cT}\mathbf{C}\boldsymbol{\varepsilon}^c \, d\Omega - \int_\Omega \mathbf{u}^{cT}\mathbf{b} \, d\Omega - \int_{\Gamma_n} \mathbf{u}^{cT}\mathbf{t} \, d\Gamma_n \tag{5.20}$$

for the first step and

$$W_2 = \int_\Omega \frac{1}{2} \left[\boldsymbol{\sigma}^{gT} \mathbf{S} \boldsymbol{\sigma}^g + \ell^2 \left(\frac{\partial \boldsymbol{\sigma}^{gT}}{\partial r} \mathbf{S} \frac{\partial \boldsymbol{\sigma}^g}{\partial r} + \frac{\partial \boldsymbol{\sigma}^{gT}}{\partial z} \mathbf{S} \frac{\partial \boldsymbol{\sigma}^g}{\partial z} \right) \right] d\Omega - \int_\Omega \boldsymbol{\sigma}^{gT} \boldsymbol{\varepsilon}^c \, d\Omega \qquad (5.21)$$

for the second, where $\boldsymbol{\varepsilon}^c$ is the local strain vector, $\mathbf{C}$ is the constitutive matrix, defined in Eq. (5.16), $\mathbf{S} = \mathbf{C}^{-1}$ is the compliance matrix, $\mathbf{t}$ is the vector of the prescribed traction on the free portion Γ_n of the boundary.

Imposing the stationarity of the first functional, that is $\delta W_1 = 0$, the usual global system of standard elasticity equations is obtained:

$$\mathbf{K}\mathbf{d}^c - \mathbf{f} = 0 \qquad (5.22)$$

where $\mathbf{f} = \int_\Omega \mathbf{N}_u^T \mathbf{b} \, d\Omega + \int_{\Gamma_n} \mathbf{N}_u^T \mathbf{t} \, d\Gamma_n$ the force vector.

Repeating the same procedure for the second functional W_2 leads to

$$\int_\Omega \mathbf{N}_\sigma^T \mathbf{N}_\sigma + \ell^2 \left(\frac{\partial \mathbf{N}_\sigma^T}{\partial r} \frac{\partial \mathbf{N}_\sigma}{\partial r} + \frac{\partial \mathbf{N}_\sigma^T}{\partial z} \frac{\partial \mathbf{N}_\sigma}{\partial z} \right) d\Omega \, \mathbf{s}^g = \int_\Omega \mathbf{N}_\sigma^T \mathbf{C} \mathbf{B}_u \, d\Omega \, \mathbf{d}^c \qquad (5.23)$$

where $\mathbf{N}_\sigma$ is an expanded version of the shape function matrix $\mathbf{N}_u$ given in Eq. (5.2), in order to accommodate all four non-local stress components, so that $\boldsymbol{\sigma}^g = \mathbf{N}_\sigma \mathbf{s}^g$.

Next, solving Eq. (5.22) for $\mathbf{d}^c$, and using the result as source term in Eq. (5.23), the nodal values of the gradient-enriched stresses $\mathbf{s}^g$ can be easily obtained.

5.2.2.2 Non-axisymmetric loads

The finite element equations for the case of axisymmetric solids subject to non-axisymmetric loads can be determined by following the same process described in § 5.2.2.1. Regarding the first step of the Ru-Aifantis theory, the functional defined by Eq.(5.20) can be considered by taking into account that now the constitutive matrix is $\mathbf{C}^\star$ defined in Eq. (5.19) and the displacements (including now also the circumferential component) are described by means of Fourier series as

$$\mathbf{u}^c = \sum_{h=0}^m \boldsymbol{\Theta}_h^s \mathbf{N}_u \mathbf{d}_h^{c,s} + \sum_{h=0}^m \boldsymbol{\Theta}_h^a \mathbf{N}_u \mathbf{d}_h^{c,a} \qquad (5.24)$$

with

$$\boldsymbol{\Theta}_h^s = \begin{bmatrix} \cos(h\theta) & 0 & 0 \\ 0 & \cos(h\theta) & 0 \\ 0 & 0 & \sin(h\theta) \end{bmatrix} \quad \text{and} \quad \boldsymbol{\Theta}_h^a = \begin{bmatrix} \sin(h\theta) & 0 & 0 \\ 0 & \sin(h\theta) & 0 \\ 0 & 0 & \cos(h\theta) \end{bmatrix} \qquad (5.25)$$

where h is the order of the harmonic, while the superscripts s and a indicate, respectively, the symmetric and anti-symmetric components of the displacements (and of the loads) with respect to the $\theta = 0$ axis.

The local strains are defined as follows

$$\boldsymbol{\varepsilon}^c = \begin{Bmatrix} \varepsilon_{rr}^c \\ \varepsilon_{zz}^c \\ \varepsilon_{\theta\theta}^c \\ \varepsilon_{rz}^c \\ \varepsilon_{r\theta}^c \\ \varepsilon_{z\theta}^c \end{Bmatrix} = \mathbf{L}\mathbf{u}^c = \begin{bmatrix} \frac{\partial}{\partial r} & 0 & 0 \\ 0 & \frac{\partial}{\partial z} & 0 \\ \frac{1}{r} & 0 & \frac{1}{r}\frac{\partial}{\partial \theta} \\ \frac{\partial}{\partial z} & \frac{\partial}{\partial r} & 0 \\ \frac{1}{r}\frac{\partial}{\partial \theta} & 0 & \frac{\partial}{\partial r} - \frac{1}{r} \\ 0 & \frac{1}{r}\frac{\partial}{\partial \theta} & \frac{\partial}{\partial z} \end{bmatrix} \begin{Bmatrix} u_r^c \\ u_z^c \\ u_\theta^c \end{Bmatrix} \tag{5.26}$$

and substituting Eq. (5.24) into Eq. (5.26)

$$\boldsymbol{\varepsilon}^c = \sum_{h=0}^{m} \mathbf{B}_{u,h}^s \mathbf{d}_h^{c,s} + \sum_{h=0}^{m} \mathbf{B}_{u,h}^a \mathbf{d}_h^{c,a} \tag{5.27}$$

where $\mathbf{B}_{u,h}^s = \mathbf{L}\boldsymbol{\Theta}_h^s \mathbf{N}_u$ and $\mathbf{B}_{u,h}^a = \mathbf{L}\boldsymbol{\Theta}_h^a \mathbf{N}_u$ are the two strain-displacement matrices for symmetric and antisymmetric displacements/loads, respectively.

After these considerations, the first step of the Ru-Aifantis theory still consists in Eq. (5.22), with the difference that now also the nodal forces are expressed in terms of Fourier series as

$$\mathbf{f} = \begin{Bmatrix} f_r \\ f_z \\ f_\theta \end{Bmatrix} = \begin{Bmatrix} \sum_{h=0}^{m} f_{r,h}^s \cos(h\theta) + \sum_{h=0}^{m} f_{r,h}^a \sin(h\theta) \\ \sum_{h=0}^{m} f_{z,h}^s \cos(h\theta) + \sum_{h=0}^{m} f_{z,h}^a \sin(h\theta) \\ \sum_{h=0}^{m} f_{\theta,h}^s \sin(h\theta) + \sum_{h=0}^{m} f_{\theta,h}^a \cos(h\theta) \end{Bmatrix} \tag{5.28}$$

and the stiffness matrix is defined as

$$\mathbf{K} = \sum_{h=0}^{m} \sum_{l=0}^{m} \mathbf{k}_{hl} \tag{5.29}$$

where $\mathbf{k}_{hl}$ is the stiffness contribution of the hth and l^{th} harmonics, given by

$$\mathbf{k}_{hl} = \int\limits_V \mathbf{B}_{u,h}^T \mathbf{C}^\star \mathbf{B}_{u,l} dV = \int\limits_V \begin{bmatrix} \mathbf{B}_{u,h}^{sT} \\ \mathbf{B}_{u,h}^{aT} \end{bmatrix} \mathbf{C}^\star \begin{bmatrix} \mathbf{B}_{u,l}^s & \mathbf{B}_{u,l}^a \end{bmatrix} dV =$$

$$= \int\limits_V \begin{bmatrix} \mathbf{B}_{u,h}^{sT} \mathbf{C}^\star \mathbf{B}_{u,l}^s & \mathbf{B}_{u,h}^{sT} \mathbf{C}^\star \mathbf{B}_{u,l}^a \\ \mathbf{B}_{u,h}^{aT} \mathbf{C}^\star \mathbf{B}_{u,l}^s & \mathbf{B}_{u,h}^{aT} \mathbf{C}^\star \mathbf{B}_{u,l}^a \end{bmatrix} dV \qquad (5.30)$$

Considering that $dV = rdrdzd\theta = rd\theta dA$, it can be easily demonstrated that

$$\int\limits_A \int\limits_0^{2\pi} \mathbf{B}_{u,h}^{sT} \mathbf{C}^\star \mathbf{B}_{u,l}^a \, rd\theta dA = \int\limits_A \int\limits_0^{2\pi} \mathbf{B}_{u,h}^{aT} \mathbf{C}^\star \mathbf{B}_{u,l}^s \, rd\theta dA = [0] \qquad (5.31)$$

which means that the symmetric and anti-symmetric terms are decoupled, as it should be, given the orthogonality of the Fourier series. Furthermore, it can also be proven that

$$\int\limits_A \int\limits_0^{2\pi} \mathbf{B}_{u,h}^{sT} \mathbf{C}^\star \mathbf{B}_{u,l}^s \, rd\theta dA = \int\limits_A \int\limits_0^{2\pi} \mathbf{B}_{u,h}^{aT} \mathbf{C}^\star \mathbf{B}_{u,l}^a \, rd\theta dA = [0] \quad \text{when} \quad h \neq l \qquad (5.32)$$

Hence, the off-diagonal terms of the global stiffness matrix $\mathbf{K}$ are all null and each harmonic can be treated separately, allowing application of the principle of superposition to determine the final result.

In what concerns the second step of the Ru-Aifantis theory, considering for simplicity only the symmetric components, defining the following functional

$$\widetilde{W}_2 = \int\limits_V \frac{1}{2} \left\{ \left(\boldsymbol{\Theta}_{\sigma,h}^s \boldsymbol{\sigma}_h^{g,s} \right)^T \mathbf{S}^\star \left(\boldsymbol{\Theta}_{\sigma,h}^s \boldsymbol{\sigma}_h^{g,s} \right) + \right.$$

$$+ \ell^2 \left[\left(\boldsymbol{\Theta}_{\sigma,h}^s \frac{\partial \boldsymbol{\sigma}_h^{g,s}}{\partial r} \right)^T \mathbf{S}^\star \left(\boldsymbol{\Theta}_{\sigma,h}^s \frac{\partial \boldsymbol{\sigma}_h^{g,s}}{\partial r} \right) + \left(\boldsymbol{\Theta}_{\sigma,h}^s \frac{\partial \boldsymbol{\sigma}_h^{g,s}}{\partial z} \right)^T \mathbf{S}^\star \left(\boldsymbol{\Theta}_{\sigma,h}^s \frac{\partial \boldsymbol{\sigma}_h^{g,s}}{\partial z} \right) + \quad (5.33)$$

$$\left. + \frac{1}{r} \frac{\partial}{\partial \theta} \left(\boldsymbol{\Theta}_{\sigma,h}^s \boldsymbol{\sigma}_h^{g,s} \right)^T \mathbf{S}^\star \frac{1}{r} \frac{\partial}{\partial \theta} \left(\boldsymbol{\Theta}_{\sigma,h}^s \boldsymbol{\sigma}_h^{g,s} \right) \right] \right\} dV - \int\limits_V \left(\boldsymbol{\Theta}_{\sigma,h}^s \boldsymbol{\sigma}_h^{g,s} \right)^T \boldsymbol{\varepsilon}_h^{c,s} \, dV$$

where $\mathbf{S}^\star = \mathbf{C}^{\star-1}$, while $\boldsymbol{\Theta}_{\sigma,h}^s$ is defined as (see for example [159])

$$\Theta_{\sigma,h}^s = \begin{bmatrix} \cos(h\theta) & 0 & 0 & 0 & 0 & 0 \\ 0 & \cos(h\theta) & 0 & 0 & 0 & 0 \\ 0 & 0 & \cos(h\theta) & 0 & 0 & 0 \\ 0 & 0 & 0 & \cos(h\theta) & 0 & 0 \\ 0 & 0 & 0 & 0 & \sin(h\theta) & 0 \\ 0 & 0 & 0 & 0 & 0 & \sin(h\theta) \end{bmatrix} \tag{5.34}$$

and imposing the stationarity of $\widetilde{W}_2$, that is $\delta\widetilde{W}_2 = 0$, the following solving system of equations is obtained

$$\int_V \left[\mathbf{N}_\sigma^T \Theta_{\sigma,h}^{sT} \Theta_{\sigma,h}^s \mathbf{N}_\sigma + \ell^2 \left(\frac{\partial \mathbf{N}_\sigma^T}{\partial r} \Theta_{\sigma,h}^{sT} \Theta_{\sigma,h}^s \frac{\partial \mathbf{N}_\sigma}{\partial r} + \frac{\partial \mathbf{N}_\sigma^T}{\partial z} \Theta_{\sigma,h}^{sT} \Theta_{\sigma,h}^s \frac{\partial \mathbf{N}_\sigma}{\partial z} + \right. \right.$$
$$\left. \left. + \frac{1}{r^2} \mathbf{N}_\sigma^T \frac{\partial \Theta_{\sigma,h}^{sT}}{\partial \theta} \frac{\partial \Theta_{\sigma,h}^s}{\partial \theta} \mathbf{N}_\sigma \right) \right] dV \ \mathbf{s}_h^{g,s} = \int_V \mathbf{N}_\sigma^T \Theta_{\sigma,h}^{sT} \mathbf{C}^\star \mathbf{B}_{u,h}^s dV \ \mathbf{d}_h^{c,s} \tag{5.35}$$

which can be numerically solved for the non-local stress $\mathbf{s}_h^{g,s}$. The same system must also be solved for the anti-symmetric components (if needed). Finally, once the solutions for all the necessary harmonics are calculated, the global solution can be determined through superposition of the effects.

5.3   Three-dimensional problems

The displacements field in a three-dimensional problem is fully defined by the displacement components u_x, u_y and u_z in the three Cartesian directions x, y and z, respectively. The continuum displacements $\mathbf{u} = [u_x, u_y, u_z]^T$ can be discretised and expressed in terms of the nodal displacements $\mathbf{d} = [d_{1x}, d_{1y}, d_{1z}, d_{2x}, d_{2y}, , d_{2z} \ldots]^T$, as previously described in §5.1, through the usual shape functions N_i (see for instance [164]), collected in the following matrix:

$$\mathbf{N}_u = \begin{bmatrix} N_1 & 0 & 0 & N_2 & 0 & 0 & \ldots \\ 0 & N_1 & 0 & 0 & N_2 & 0 & \ldots \\ 0 & 0 & N_1 & 0 & 0 & N_2 & \ldots \end{bmatrix} \tag{5.36}$$

The nodal local displacements $\mathbf{d}^c$ can be determined by solving Eq. (5.7), where now the constitutive matrix $\mathbf{C}$ takes the same form of $\mathbf{C}^\star$ in Eq. (5.19), while the derivative operator $\mathbf{L}$ is defined as

$$\mathbf{L} = \begin{bmatrix} \frac{\partial}{\partial x} & 0 & 0 & \frac{\partial}{\partial y} & \frac{\partial}{\partial z} & 0 \\ 0 & \frac{\partial}{\partial y} & 0 & \frac{\partial}{\partial x} & 0 & \frac{\partial}{\partial z} \\ 0 & 0 & \frac{\partial}{\partial z} & 0 & \frac{\partial}{\partial x} & \frac{\partial}{\partial y} \end{bmatrix}^T \tag{5.37}$$

The nodal non-local stresses $\mathbf{s}^g$, instead, can be determined, knowing the local displacements $\mathbf{d}^c$ from the previous step, by solving the following second set of equations (second step):

$$\int_\Omega \left[\mathbf{N}_\sigma^T \mathbf{N}_\sigma + \ell^2 \left(\frac{\partial \mathbf{N}_\sigma^T}{\partial x} \frac{\partial \mathbf{N}_\sigma}{\partial x} + \frac{\partial \mathbf{N}_\sigma^T}{\partial y} \frac{\partial \mathbf{N}_\sigma}{\partial y} + \frac{\partial \mathbf{N}_\sigma^T}{\partial z} \frac{\partial \mathbf{N}_\sigma}{\partial z} \right) \right] d\Omega \, \mathbf{s}^g =$$
$$= \int_\Omega \mathbf{N}_\sigma^T \mathbf{C} \mathbf{B}_u d\Omega \, \mathbf{d}^c \tag{5.38}$$

obtained by following the same procedure used in §5.1 to derive Eq. (5.12), where the derivative operator ∇ is now defined as

$$\nabla = \left\{ \frac{\partial}{\partial x} \quad \frac{\partial}{\partial y} \quad \frac{\partial}{\partial z} \right\}^T \tag{5.39}$$

In Eq. (5.38) the boundary integral has been dropped for the same reasons pointed out in §5.1.

5.4 Numerical integration

To solve the two steps of the Ru-Aifantis theory, the Gauss quadrature rule has been adopted.

Since the first step of the Ru-Aifantis theory consists in the solution of the second-order p.d.e. of classical elasticity (5.7), for the numerical integration of the stiffness matrix $\mathbf{K}$, the usual number of integration points is used for each kind of implemented elements, as summarised in Table 5.1. It is noted that for the bi-quadratic serendipity quadrilateral and the tri-quadratic serendipity brick elements, under-integration is adopted. This allowed to save computational time as well as avoid potential stiffer behaviour of the elements (sometimes occurring in fully-integrated elements).

At this point, the most interesting aspect to investigate is the integration rule to use in the second step of the Ru-Aifantis theory and, in particular, for the numerical solution of the integral in the left side of Eqs. (5.12), (5.23), (5.35) and (5.38). From the implementational and computational point of view, the most desirable solution would be to use the same integration rule used in the first step of the Ru-Aifantis theory.

Table 5.1. Number of Gauss points used in the first step of the Ru-Aifantis theory.

Problem	Element type	Order	Gauss Points
Plane stress/strain	Triangles	Linear	1
		Quadratic	3
	Quadrilaterals	Bi-linear	2×2
		Bi-quadratic	2×2
Axisymmetric	Triangles	Linear	1
		Quadratic	3
	Quadrilaterals	Bi-linear	2×2
		Bi-quadratic	2×2
Three-dimensional	Tetrahedrons	Linear	1
		Quadratic	4
	Bricks	Tri-linear	$2 \times 2 \times 2$
		Tri-quadratic	$2 \times 2 \times 2$

However, the applicability of such a solution is not obvious and would need to be demonstrated. In fact, while for the first step of the Ru-Aifantis theory the order of the stiffness matrix (which has to be integrated) is two times the order of the derivative of the shape functions, in the second step the order of the integrand part (of the term in the left side of Eqs. (5.12), (5.23), (5.35) and (5.38)) is two times the order of the shape functions themselves; this means that for exact integration, higher order integration rules are needed as listed in Table 5.2. Hence, in other words, the problem is to prove if it is possible to under-integrate (i.e. use integration rules with a lower order than that necessary for the exact integration) the left part of Eqs. (5.12), (5.23), (5.35) and (5.38) for both $\ell = 0$ and $\ell \neq 0$. Unfortunately, this is not always possible, as described afterwards.

The investigation has been carried out through a study of the eigenvalues of the matrix $\mathbf{M} + \ell^2 \mathbf{F}$ when $\ell \neq 0$ and, obviously, of matrix $\mathbf{M}$ on its own when $\ell = 0$, where $\mathbf{M} = \int_\Omega \mathbf{N}_\sigma^T \mathbf{N}_\sigma \, d\Omega$ is the first matrix term of the left integral in Eqs. (5.12), (5.23), (5.35) and (5.38) similar to a mass matrix, while $\mathbf{F}$ is the second matrix term similar to a diffusivity matrix. In particular, to avoid rank deficiencies all the eigenvalues must be non-zero, which means that zero energy modes are not admitted.

From the performed studies it turned out that, when $\ell = 0$, it is possible to use the same integration rule only for the linear quadrilateral, tetrahedron and brick elements, while for the other five types of elements higher order integration rules are needed (the minimum number of integration points according to stability is given in Tab. 5.2, for each kind of element). On the contrary, for $\ell \neq 0$, thanks to the contribution of the matrix $\mathbf{F}$, it is possible to use the same integration rule, used in the first step, for every type of finite element.

Table 5.2. Number of Gauss points formally required in the second step of the Ru-Aifantis theory.

Problem	Element type	Order	Gauss Points
Plane stress/strain	Triangles	Linear	3
		Quadratic	6 (degree of precision 4)
	Quadrilaterals	Bi-linear	2×2
		Bi-quadratic	3×3
Axisymmetric	Triangles	Linear	3
		Quadratic	6 (degree of precision 4)
	Quadrilaterals	Bi-linear	2×2
		Bi-quadratic	3×3
Three-dimensional	Tetrahedrons	Linear	1
		Quadratic	11
	Bricks	Tri-linear	$2 \times 2 \times 2$
		Tri-quadratic	$3 \times 3 \times 3$

5.4.1 Shear locking

As well known, in the case of bending-dominant problems, especially for fully integrated linear elements, the numerical solution of the problem can be affected by shear locking, leading to an unphysically stiffer behaviour of the analysed component. To check the occurrence of this phenomenon, the proposed methodology has been applied to model a classical bending problem. The results of the aforementioned analysis have shown that the numerical solution of the second step of the Ru-Aifantis theory is not affected by locking effects, even in the case of fully integrated linear elements, while the usual selective integration rules (for example under-integrating the part of the stiffness matrix related to the shear strain and fully-integrating the part related to the normal strain) may be applied for the first step (Eq. (5.7)).

5.4.2 Axisymmetric benchmark problem – Internally pressurised hollow cylinder

The problem of a thick-walled hollow cylinder of inner radius $a = 0.5$ m, outer radius $b = 1.5$ m and length L = 8 m, subject to an internal pressure $p_i = 10$ MPa (Fig. 5.2) is considered. The material is characterised by a Young's modulus $E = 1000$ MPa, Poisson's ratio $\nu = 0.25$ and the length scale $\ell = 0.1$ m. In what concerns the boundary conditions, for the first step (Eq. 5.22) the cylinder is simply supported in the axial direction at both ends (Fig. 5.2), while for the second step (Eq. 5.23) homogeneous natural boundary conditions are taken throughout, since, as also described in [14], this choice is the most widely accepted amongst the scientific community when dealing with gradient elasticity.
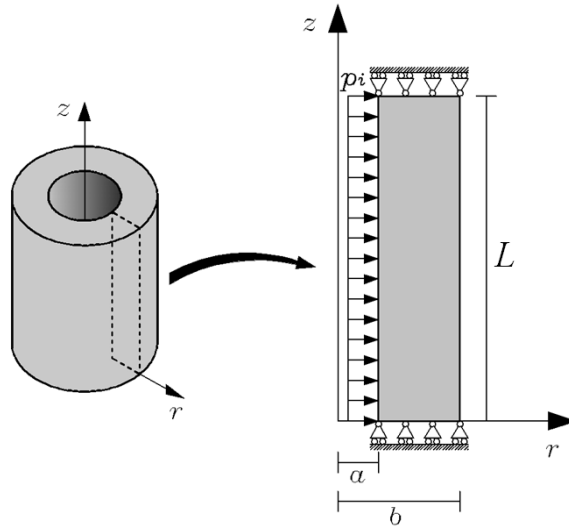
Fig. 5.2. Benchmark problem: geometry and boundary conditions.

For symmetry of the cylinder with respect to a plane normal to the z-axis only half of
the cross-section has been modelled using 16×64 bi-linear and bi-quadratic quadrilateral
elements, or twice as many linear and quadratic triangular elements (note that for triangu-
lar elements the meshes are obtained by subdividing each quadrilateral in two triangles).
Since the displacements determined according to the proposed methodology correspond
to the classical elastic displacements, the numerical solution for the displacements has
been compared with the following analytical solution of classical elasticity known from
the literature [155]:

$$u_r = \frac{p_i a^2 r}{E\,(b^2 - a^2)} \left[(1 - 2\nu)(1 + \nu) + \frac{(1 + \nu)b^2}{r^2} \right] \qquad (5.40)$$

From Fig. 5.3 it can be observed that the numerical estimation of the radial displace-
ments u_r (obtained by using bi-quadratic quadrilateral elements) perfectly matches the
corresponding analytical counterpart. Similar results have also been obtained with all the
other implemented elements.

Regarding the stresses, instead, the gradient-enriched stress fields numerically obtained
by applying the developed methodology must be compared to suitable gradient-enriched
analytical solutions. After a thorough literature review, the analytical solution proposed
by Gao and Park [58] was chosen as reference solution, since it was the only one addressing
the considered problem in a similar fashion as the proposed methodology. However, this
choice presents some limitations. In particular, the analytical solution proposed by Gao
and Park [58] is obtained through a displacement-based formulation, while the method-
ology presented in §5.2 is stress-based, this leading to different boundary conditions. In
particular, the displacement-based formulation used by Gao and Park [58] requires just
two higher-order boundary conditions (in particular they set homogeneous natural bound-
ary conditions of the radial stress at the inner and outer surfaces) while the stress-based
methodology proposed in §5.2 requires a larger number of higer-order boundary condi-

tions (homogeneous natural boundary conditions of *all the stress components* at the inner and outer surfaces have been taken). Furthermore, while in the proposed methodology the stress components are de-coupled, in the analytical solution proposed by Gao and Park [58] the stress components are coupled.

The aforementioned differences between the proposed methodology and the analytical solution obtained by Gao and Park will lead to both qualitative and quantitative differences of the stress profiles. In particular, from Fig. 5.3 it can be observed that both the numerical $\sigma_{\theta\theta}^g$ and σ_{zz}^g stress profiles present qualitative differences at the boundaries and only quantitative differences inside the domain if compared to their analytical counterparts. This is mainly due to the different applied boundary conditions. Moreover, it can be easily explained why σ_{zz}^g obtained by applying the proposed methodology should be constant. To do so, let us consider first the exact stress solutions of classical elasticity known from the literature [155]:

$$\sigma_{rr} = \frac{p_i a^2}{b^2 - a^2}\left(1 - \frac{b^2}{r^2}\right), \quad \sigma_{\theta\theta} = \frac{p_i a^2}{b^2 - a^2}\left(1 + \frac{b^2}{r^2}\right), \quad \sigma_{zz} = 2\nu\frac{p_i a^2}{b^2 - a^2} \tag{5.41}$$

In particular, it can be observed that σ_{zz} is constant along the radial coordinate and therefore, due to the way the proposed methodology post-processes the stress fields, the longitudinal stress component is not affected by any gradient enrichment, leading to $\sigma_{zz}^g = \sigma_{zz} = \text{const.}$

Only quantitative differences can be seen, instead, in the radial stress component. This is mainly due to the fact that, as mentioned above, while in the analytical solution proposed by Gao and Park the stress components are coupled, in the proposed methodology the stress components are de-coupled.

The fact that the results produced by the proposed methodology presents qualitative differences respect to Gao and Park's solution only at the boundaries (where different conditions are imposed), while inside the domain the differences are only quantitative and reasonably small, give confidence about the validity of the proposed methodology.

However, due to the aforementioned differences (although justified), the analytical solution proposed by Gao and Park cannot be used as benchmark solution for the convergence study performed in the following section where the reference solution will instead be approximated through second-order Richardson's extrapolation (see Appendix A and [107]). At this point it is worth highlighting that, in general, convergence towards a solution determined through Richardson's extrapolation does not necessarily mean that the numerical solution converges to the correct solution. However, since as previously discussed the comparison of the numerical solution produced by the proposed methodology with the analytical solution proposed by Gao and Park give confidence about the validity of the proposed methodology it is possible to reasonably assume that convergence to the right solution occurs.
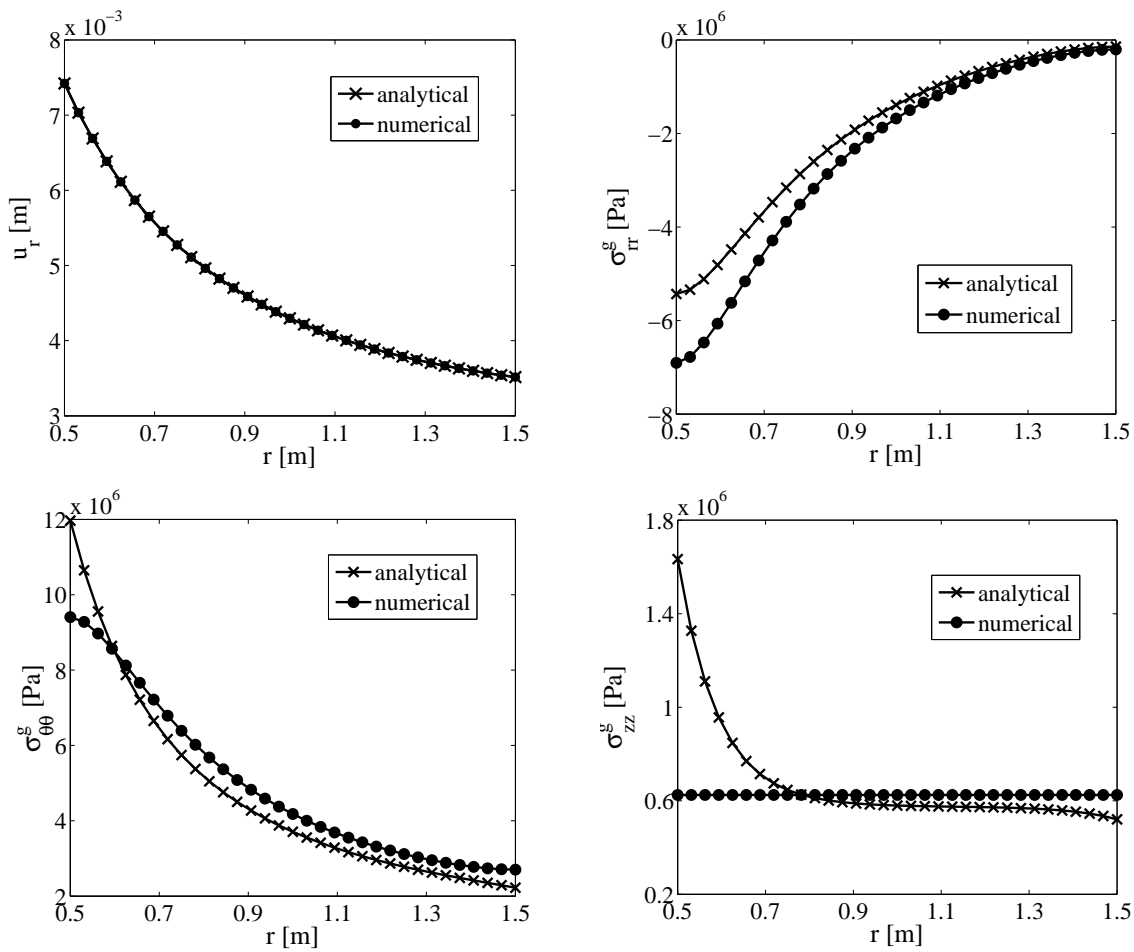
Fig. 5.3. Comparison between the numerical solutions obtained with bi-quadratic quadrilateral elements and their correspondent analytical counterparts. Similar results have also been obtained with all the other implemented elements.

5.5 Error estimation and convergence study

Now that the most suitable integration rules have been identified for each kind of finite element, the attention can be focused on the error estimation of the new methodology. In particular the convergence rate of the different finite elements has been studied for some simple problems.

To determine the convergence rate, the L2-norm error defined as

$$\|e\|_2 = \frac{\|\sigma_e - \sigma_c\|}{\|\sigma_e\|} \tag{5.42}$$

where σ_e and σ_c are, respectively, the exact and calculated values of the stresses, has been plotted against the number of degrees of freedom (nDoF).

From the theory [164] it is well known that the error on displacements is proportional to the nDoF as

$$e_u \simeq O(\text{nDoF})^{-\frac{p+1}{k}} = O(\text{nDoF})^{c_r} \tag{5.43}$$

where p is the polynomial order and $k = 2, 3$ for 2D and 3D problems, respectively.

In what concerns the stresses, in the proposed methodology they are calculated from Eq. (5.12), (5.23),(5.35) or (5.38) as primary variable, instead of secondary variable as it happens in standard finite element methodologies, based on classical elasticity. For this reason, the error in the stresses is still proportional to the nDoF, but with a different rate respect to classical elasticity. In particular, for a Helmholtz equation like Eqs. (5.12), (5.23),(5.35) and (5.38), the proportionality is given by [76]:

$$e_\sigma \simeq O(\text{nDoF})^{-\frac{p+1}{k}} = O(\text{nDoF})^{\bar{c}_r} \tag{5.44}$$

From Eqs. (5.43) and (5.44), it is clear that the $\|e\|_2$ – nDoF curve in a bi-logarithmic system of axes is a straight line, whose slope represents the convergence rate c_r of the numerical solution to the exact solution. The theoretical convergence rates are summarised in Table 5.3.

5.5.1 Plane elements – Internally pressurised hollow cylinder

To test the convergence rate of the bi-dimensional elements, a problem similar to the one considered in §5.4.2 has been analysed (see Fig. 5.4 for geometry and loading conditions). The geometrical and material parameters of the problem are $b = 4$ m, $a = 1$ m, $E = 1000$ MPa, $\nu = 0.25$ and $\ell = 0.1$ m. An internal pressure $p_i = 10$ MPa is applied.

Due to the symmetry of the problem only a quarter of the vessel has been modelled.

Table 5.3. Theoretical convergence rates in the determination of the displacements (c_r) and stresses ($\bar{c}_r$).

Problem	Order	c_r	$\bar{c}_r$
Two-dimensional	Linear	-1	-1
(plane stress/strain and axisymmetric)	Quadratic	-3/2	-3/2
Three-dimensional	Linear	-2/3	-2/3
	Quadratic	-1	-1
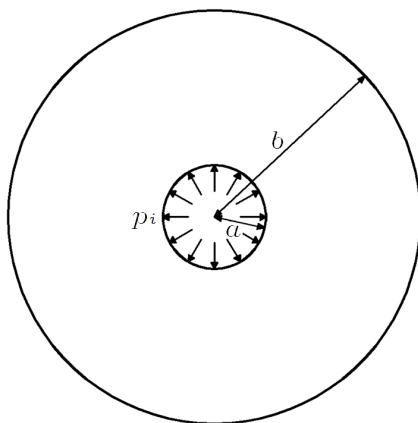
Fig. 5.4. Cylinder subject to an internal pressure: geometry and loading conditions.
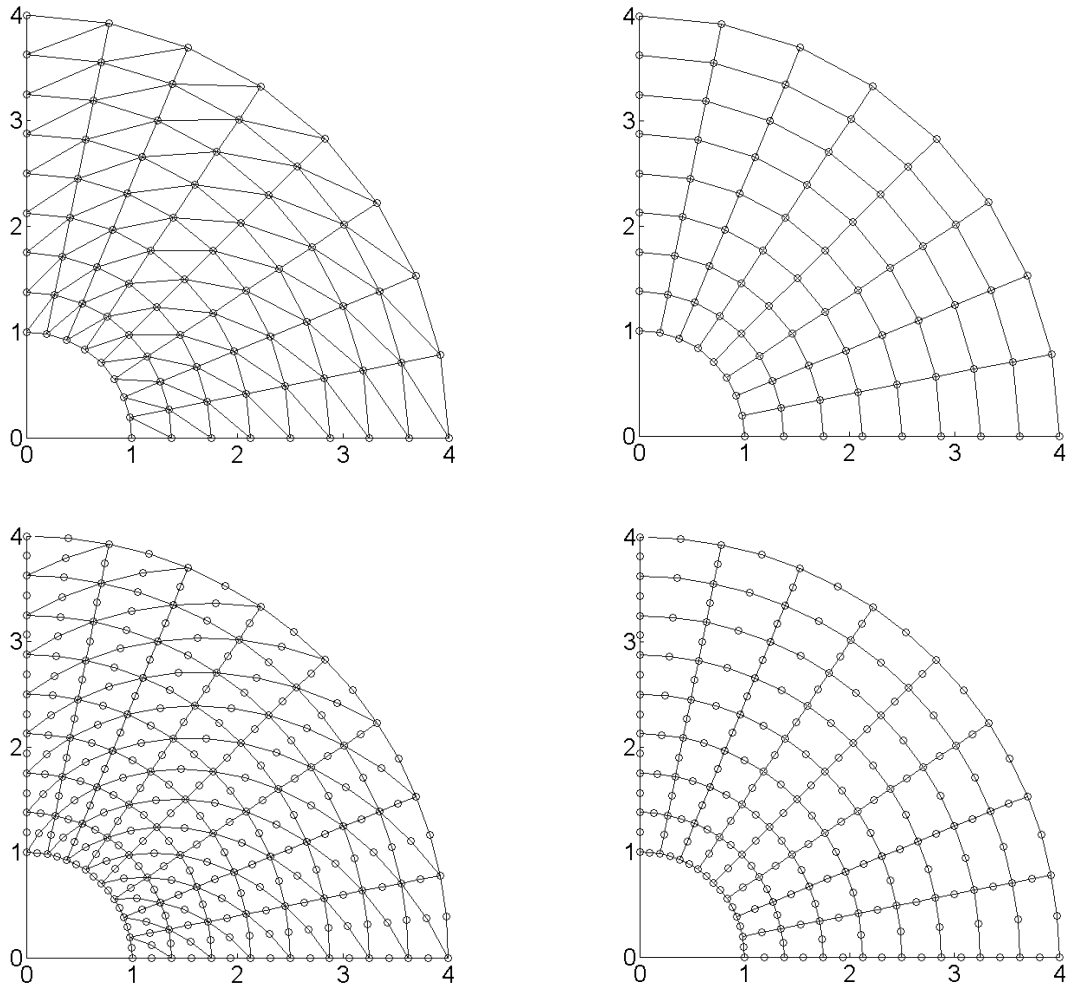
Fig. 5.5. Cylinder subject to an internal pressure: employed meshes for linear (top-left) and quadratic (bottom-left) triangular elements, bi-linear (top-right) and bi-quadratic (bottom-right) quadrilateral elements.

The domain has been modelled with all four types of implemented 2D finite elements, starting from a coarse mesh of 8×8 elements and performing then a mesh refinement by doubling the number of elements along each side until a mesh of 256×256 elements is obtained. All the employed meshes are shown in Fig. 5.5.

The boundary conditions accompanying Eq. (5.7) are taken as *homogeneous essential* so that the circumferential displacements u_θ are null along the two axes of symmetry, while those associated to Eq. (5.12) are chosen as *homogeneous natural* throughout, that is $\mathbf{n} \cdot \nabla \boldsymbol{\sigma}^g = 0$.

To define the error, the numerical solutions obtained using the new methodology have been compared with the reference solution approximated using second-order Richardson's extrapolation (see Appendix A and [107]).

In Fig. 5.6 the convergence behaviour of all the implemented bi-dimensional elements
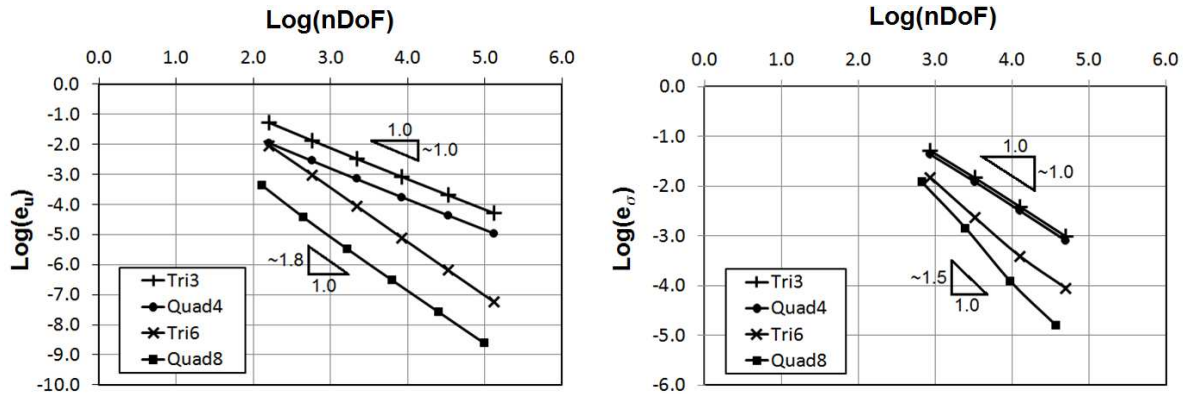
Fig. 5.6. Cylinder subject to an internal pressure: displacements error (left) and stresses error (right) versus number of Degrees of Freedom. The slope of the straight lines represent the convergence rate of the numerical solution to the exact solution.

is shown, for both displacements and stresses. It can be seen that the numerically obtained convergence rates are in good agreement with the theoretical predictions given in Table 5.3.

5.5.2   Plane elements – Cross-shape specimen

The second problem is the case of a cross-shape specimen subject to a uniform tensile state at the end of the arms as shown in Fig. 5.7. The geometrical and material parameters of the problem are $R = 1$ m, $L = 2$ m, $E = 1000$ MPa, $\nu = 0.25$ and $\ell = 0.1$ m. Distributed loads $q_x = q_y = 1000$ N/m are applied at the end of the arms.

Also in this case, for symmetry reasons, only a quarter of the specimens has been modelled using all the different types of implemented finite elements, starting also in this case with a coarse mesh as shown in Fig. 5.8. Afterwords, a mesh refinement has been performed, running four other meshes obtained by doubling the number of element, in both radial and circumferential directions, of the previous one.

The boundary conditions accompanying Eq. (5.7) are taken as *homogeneous essential* so that the displacements in x-direction u_x and in y-direction u_y are null along the vertical and horizontal axes of symmetry, respectively. In what concerns Eq. (5.12), instead, the boundary conditions are chosen as *homogeneous natural* throughout, like in the previous example.

To define the error, the numerical solutions obtained using the new methodology have been compared with the reference solution obtained by applying second-order Richardsons extrapolation.

Fig. 5.9 shows the convergence behaviour of all the implemented bi-dimensional elements in the determination of both displacements and stresses. Again, this is in line with the theoretical predictions.
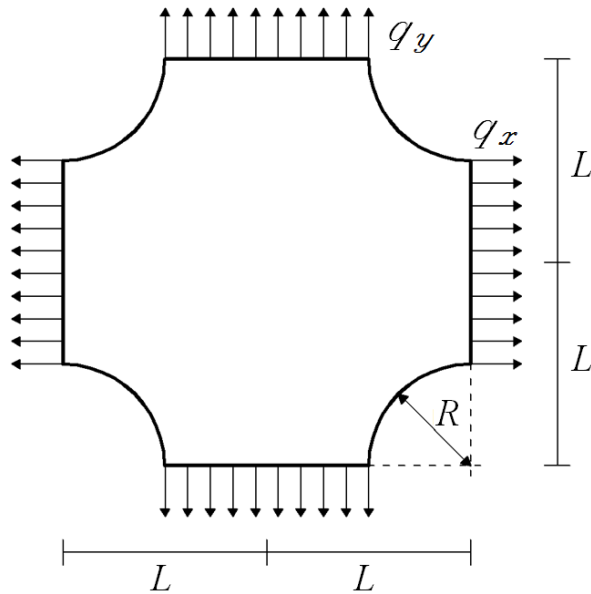
Fig. 5.7. Cross-shape specimen: geometry and loading conditions.

5.5.3 Axisymmetric elements

Regarding the case of axisymmetric solids subject to axisymmetric loads, the thick-walled hollow cylinder problem presented in §5.4 has been considered. The domain has been modelled by using all the implemented elements , starting from a 4×16 mesh and refining the mesh, by doubling the number of elements in both directions 4 times, up to a 64×256 mesh. The length parameter has been chosen as $\ell = 0.1$ m.

Regarding the case of axisymmetric solids subject to non-axisymmetric loads, two different problems have been considered. The first one consists of a cylindrical bar of radius $R = 1$ m and length $L = 8$ m, subject to a bending moment $M = 10^6$ Nm (Fig. 5.10 left); while the second one consists of the same cylinder subject now to a torsional moment $T = 10^6$ Nm (Fig. 5.10 right). In both cases, Young's modulus $E = 1000$ MPa, Poisson's ratio $\nu = 0.25$ and the length scale has been set as $\ell = 0.1$ m.

For symmetry of the cylinder respect to a plane normal to the z-axis, in both cases, only half of the cross-section has been modelled (Fig. 5.10). Also in this case all the implemented elements have been used to discretise the domain, starting from a 4×16 mesh and performing the same mesh refinement described in the case of axisymmetric loads. In what concerns the boundary conditions, in both problems, for the first step (Eq. (5.22) with **K** defined by Eq. (5.29)), homogeneous essential boundary conditions have been imposed, so that $u_z = 0$ (bending problem) and $u_z = u_\theta = 0$ (torsional problem) along the axis of symmetry (Fig. 5.10); while for the second step (Eq. (5.35)) homogeneous natural boundary conditions have been chosen, as in the previous cases.

Also in this case, the error has been defined by comparing the numerical solution obtained using the proposed methodology with the reference solution obtained through second-order Richardson's extrapolation.
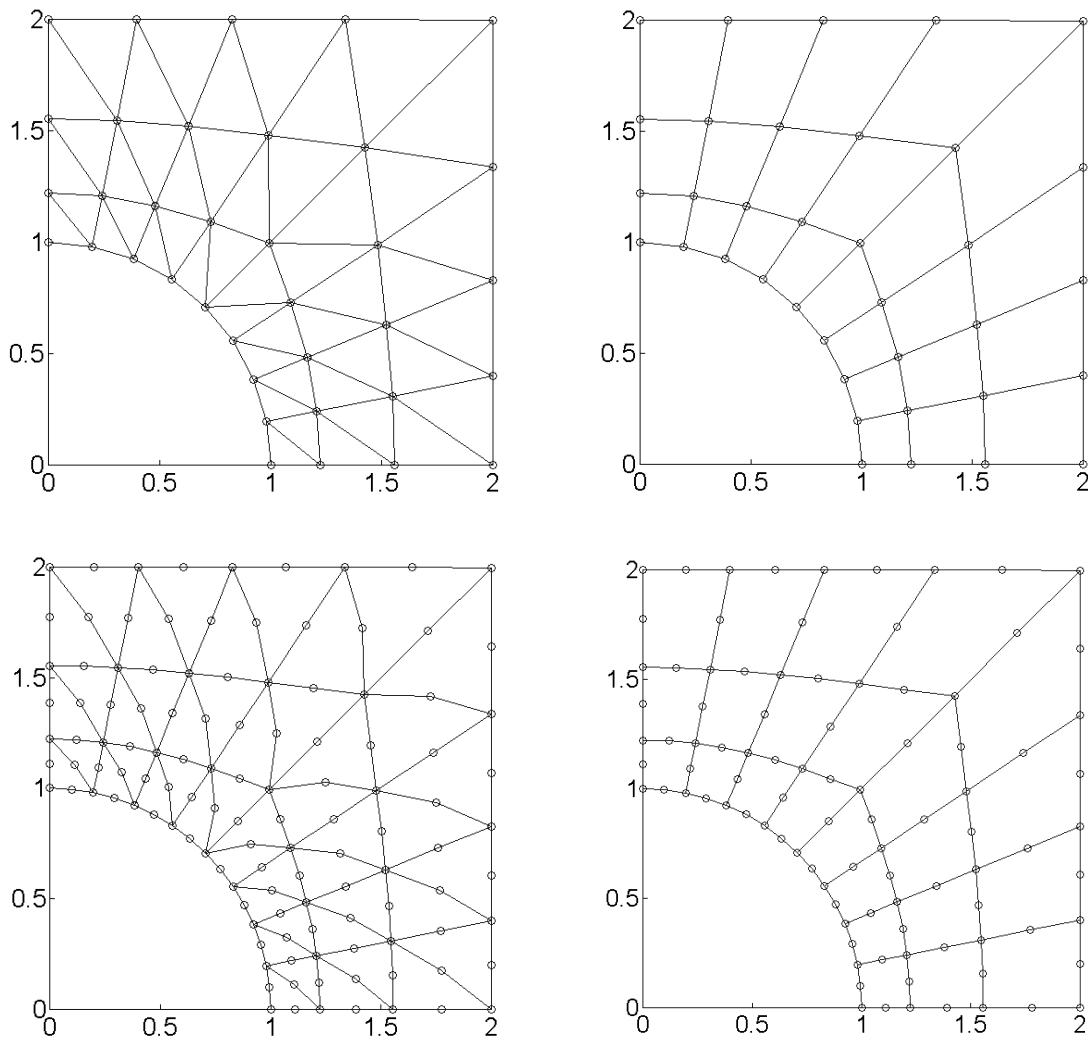
Fig. 5.8. Cross-shape specimen: employed meshes for linear (top-left) and quadratic (bottom-left) triangular elements, bi-linear (top-right) and bi-quadratic (bottom-right) quadrilateral elements.
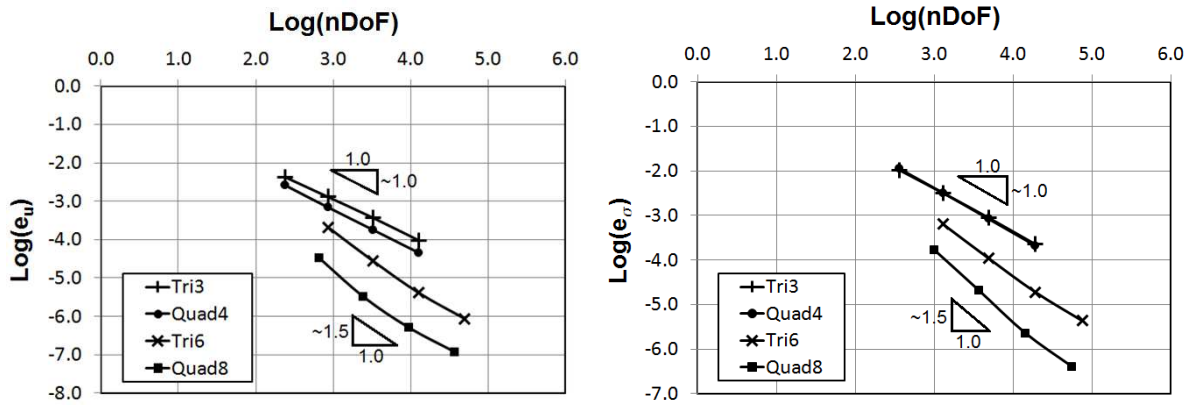
Fig. 5.9. Cross-shape specimen: displacements error (left) and stresses error (right) versus number of Degrees of Freedom. The slope of the straight lines represent the convergence rate.
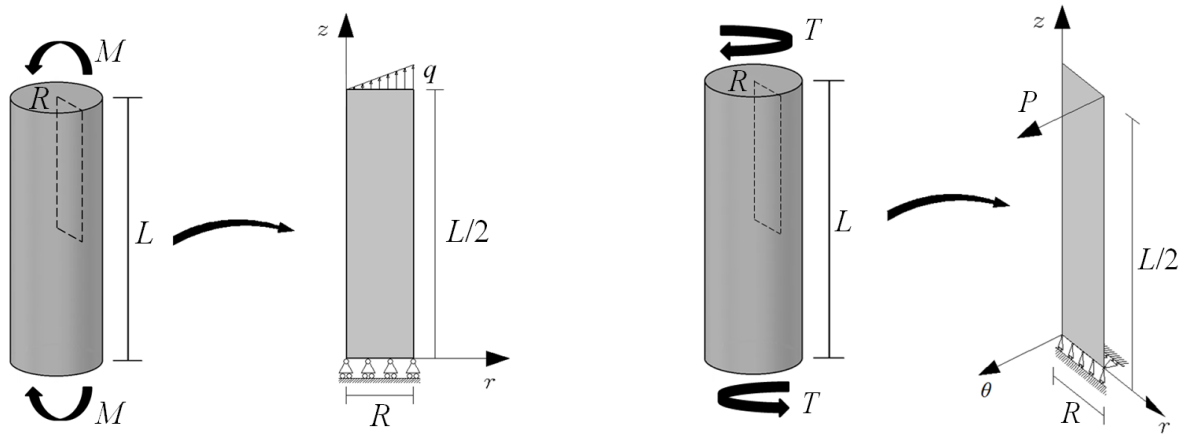
Fig. 5.10. Cylindrical bars under pure bending (left) and pure torsion (right): geometry and boundary conditions.

In Fig. 5.11 the L2-norm error is plotted against the nDoF in a bi-logarithmic system for the three analysed problems, which shows that all the implemented elements produce numerical solutions characterised by convergence rates in good agreement with the theoretical predictions also when applied to any kind of axisymmetric problem.

5.5.4 Three-dimensional elements – Internally pressurised hollow sphere

In what concerns the convergence rate of the three-dimensional elements, the problem of a sphere subject to an internal pressure p_i shown in Fig. 5.12 has been studied. The geometrical and material parameters of the problem are $b = 1$ m, $a = 0.5$ m, $E = 1000$ MPa, $\nu = 0.25$ and $\ell = 0.1$ m. An internal pressure $p_i = 10$ MPa is applied.

Due to the symmetry of the problem only an eighth of the sphere has been modelled.
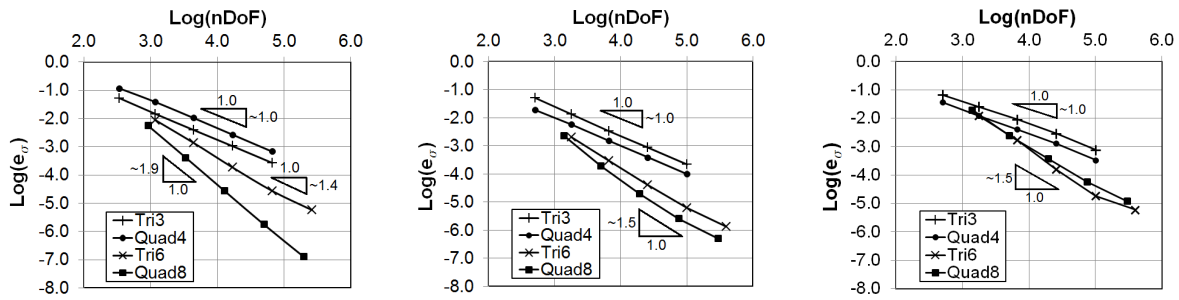
Fig. 5.11. Stress error versus nDoF for plain cylindrical bars subject to uniaxial tensile load (left), pure bending (centre) and pure torsion (right), modelled with under-integrated bi-quadratic quadrilateral elements. The slope of the lines represents the convergence rate.
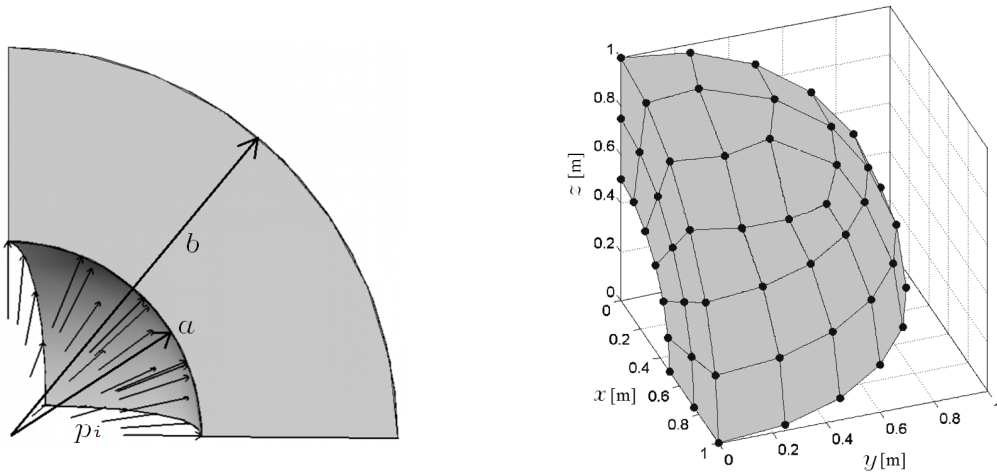
Fig. 5.12. Hollow sphere subject to an internal pressure: geometry and loading conditions (left), initial mesh (right).

The domain has been modelled with all four types of implemented 3D finite elements, starting from a coarse mesh, as shown in Fig. 5.12 for the tri-linear brick elements, and performing then a uniform mesh refinement.

The boundary conditions related to Eq. (5.7) are taken as *homogeneous essential* so that the circumferential displacements are null on the three planes of symmetry, while in what concerns Eq. (5.38) they are chosen as *homogeneous natural* throughout, like in the previous examples.

To define the error, the numerical solutions obtained using the new methodology have again been compared with the reference solution obtained by applying second-order Richardsons extrapolation.

Fig. 5.13 shows the convergence behaviour of all the implemented three-dimensional elements in the determination of both displacements and stresses. It can be observed that, overall, the numerical solutions converge to the associated exact solutions as theoretically expected, except for the quadratic tetrahedrons and the tri-quadratic bricks, which appear to be slightly slower than theoretically predicted, in the determination of
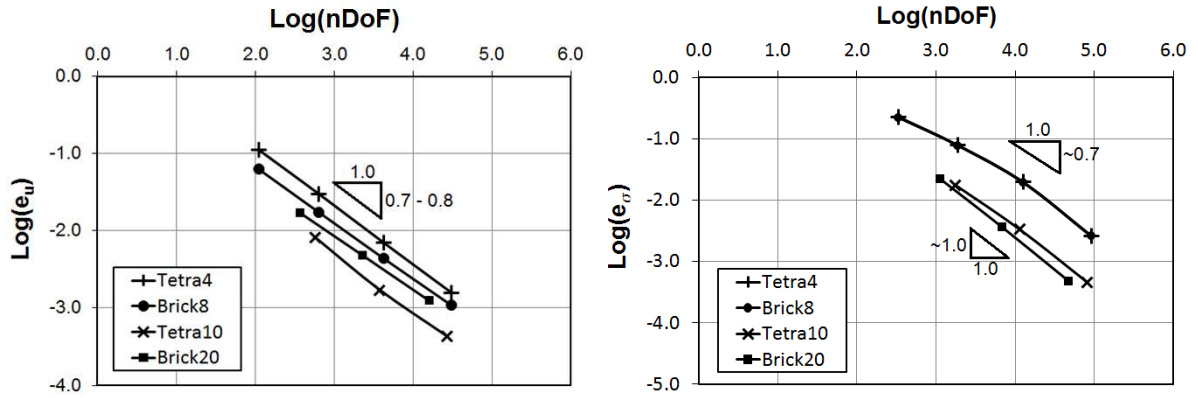
Fig. 5.13. Hollow sphere subject to an internal pressure: displacements error (left) and stresses error (right) versus number of Degrees of Freedom. The slope of the straight lines represent the convergence rate of the numerical solution to the exact solution.

the displacements.

5.6 Convergence in the presence of cracks

As mentioned in Chapter 3 one of the features of gradient elasticity is the ability to remove singularities from the stress and strain fields as those emerging in correspondence of crack tips. Problems characterised by the presence of cracks represent the most demanding case from the convergence point of view and, as a consequence of this, also in terms of element size in the vicinity of the crack tip. Hence, the study of the convergence behaviour of the implemented gradient-enriched finite elements in the presence of cracks is of prime importance.

The mode I fracture problem shown in Fig. 5.14 and presented in [14] has been analysed, using all the four implemented two-dimensional elements. The geometrical and material parameters of the problem are $L = 1$ mm, $E = 1000$ MPa, $\nu = 0.25$ and $\ell = 0.1$ mm. Prescribed displacements $\overline{u} = 0.01$ mm are applied at the top and bottom edges. Due to the symmetry only the top-right quarter has been modelled, with 4×4, 8×8, 16×16, 32×32 and 64×64 bi-linear and bi-quadratic quadrilateral elements and with the double of linear and quadratic triangular elements (where the triangular mesh is obtained by subdividing each quadrilateral element into two triangles).

Two different options are considered for the boundary conditions accompanying Eq. (5.12):

- **Option 1**: *essential*, that is the non-local stress components are prescribed so that $\boldsymbol{\sigma}^g = \boldsymbol{\sigma}^c$ on free boundaries. In the present example: $\sigma_{xx}^g = 0$ on the vertical edges, $\sigma_{yy}^g = 0$ on the face of the crack and $\sigma_{xy}^g = 0$ everywhere.

- **Option 2**: *homogeneous natural* throughout, that is $\mathbf{n} \cdot \nabla \boldsymbol{\sigma}^g = 0$.
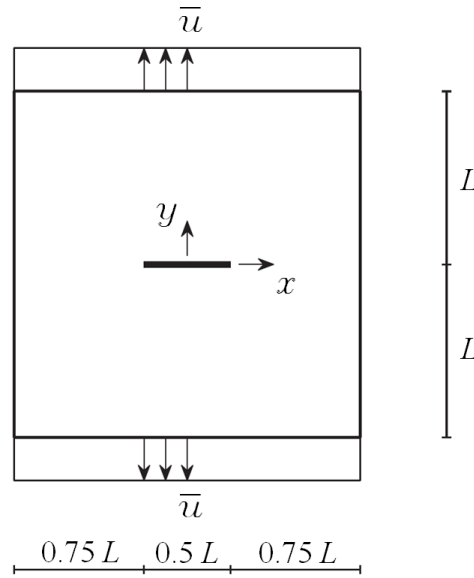
Fig. 5.14. Mode I fracture problem: geometry and boundary conditions. The crack is represented by the solid line.

To determine the convergence rate, the L2-norm error defined in §5.5 has been plotted against the number of degrees of freedom (nDoF), as shown in Fig. 5.15.

From the theory [164] it is well known that in problems with singularities the error on classical stresses is proportional to the nDoF as

$$e_\sigma \simeq O(\text{nDoF})^{-[\min(\lambda, \text{p})]/2} = O(\text{nDoF})^{\tilde{c}_\text{r}} \tag{5.45}$$

where $\lambda = 0.5$ for a nearly closed crack.

From Eq. (5.45), it is clear that the $\|e\|_2$ – nDoF curve in a bi-logarithmic system of axes is still a straight line, whose slope represents the convergence rate $\tilde{c}_r$ of the numerical solution to the exact solution, which in this case is $\tilde{c}_r = 0.25$ for both linear and quadratic elements.

To define the error, the numerical solutions obtained using the new methodology have been compared with the reference solution approximated using second-order Richardson's extrapolation.

Fig. 5.15 shows that, in presence of singularities, both linear and quadratic elements are characterised by approximatively the same convergence rate (in accordance with Eq. (5.45)), but higher than the correspondent theoretical value defined in Eq. (5.45), for what concerns the determination of the stresses. This higher convergence rate is due to two main causes:

- removal of singularities from the numerical solution;

- gradient-enriched stresses calculated as primary variables, instead of secondary variables (as in standard classical elasticity-based finite element methodologies).
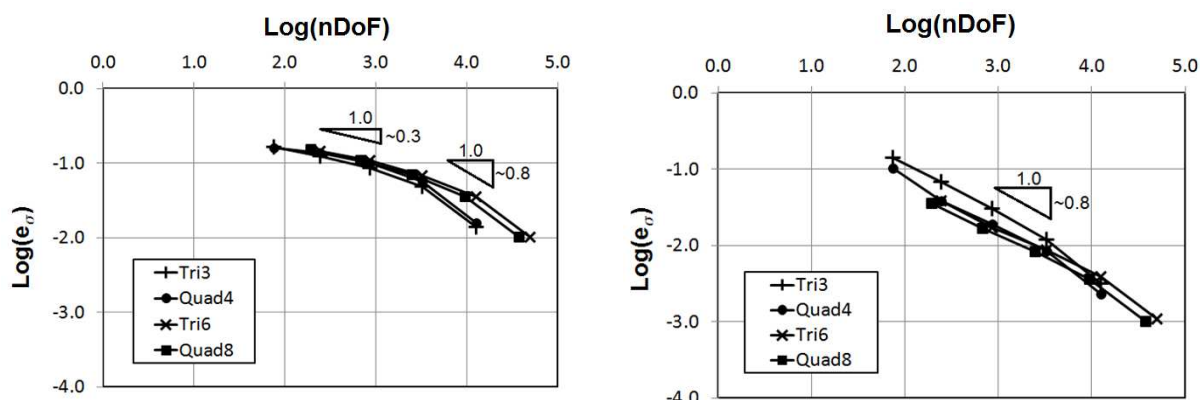
Fig. 5.15. Mode I fracture problem: stresses error versus number of Degrees of Freedom for the first (left) and the second (right) option of boundary conditions. The slope of the straight lines represent the convergence rate of the numerical solution to the reference solution.

Furthermore, it can be observed that, while the application of the second option of the boundary conditions leads to a uniform convergence rate equal to about 0.8, adopting the first option all the elements are characterised by an initial convergence rate of about 0.3, reaching the same convergence rate obtained using the option 2 only for more refined meshes.

In order to analyse the aforementioned aspects also for axisymmetric elements, three different problems (Fig. 5.16) consisting of a cylindrical bar characterised by the presence of a circumferential crack and subject, respectively, to axial load $F = 10^6$ N (axisymmetric), bending moment $M = 10^6$ Nm and torque $T = 10^6$ Nm (non-axisymmetric loads) have been studied. The cylinder has a radius $R = 1$ m, a length $L = 8$ m and the crack is 0.25 m deep. Material properties, boundary conditions and meshes are taken as in §5.5.3.

From Fig. 5.17 it is clear that also in the case of axisymmetric problems, when singularities are involved, both linear and quadratic elements show approximatively the same convergence rate in accordance with Eq. (5.45). Furthermore, the proposed gradient-enriched methodology produces a significant improvement in terms of convergence rate; in particular the solutions of the three analysed problems are all characterised by a convergence rate almost three times higher than the corresponding theoretical value (typical of standard finite element methodology based on classical elasticity). This higher convergence rate can be ascribed to the same previously described factors.

Since, as mentioned before, the case of a sharp crack represents the most demanding problem in terms of convergence, it is now possible to provide recommendations on optimal element size. In particular, in Table 5.4 the ratio between the element size and the length scale ℓ, necessary to guarantee an error of about 5% or lower, is summarised for the different elements.

The recommendations provided in Table 5.4 have a very important meaning from the commercial point of view, because they show that, applying the proposed methodology, a relatively coarse mesh is enough to obtain a solution affected by an acceptable error, with evident benefits in terms of computational cost.
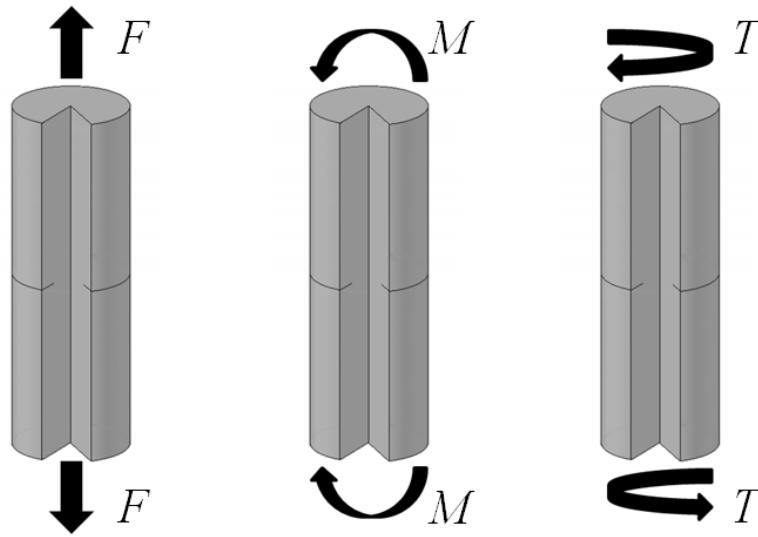
Fig. 5.16. Cracked cylindrical bars under uniaxial tensile load (left), pure bending (centre) and pure torsion (right).
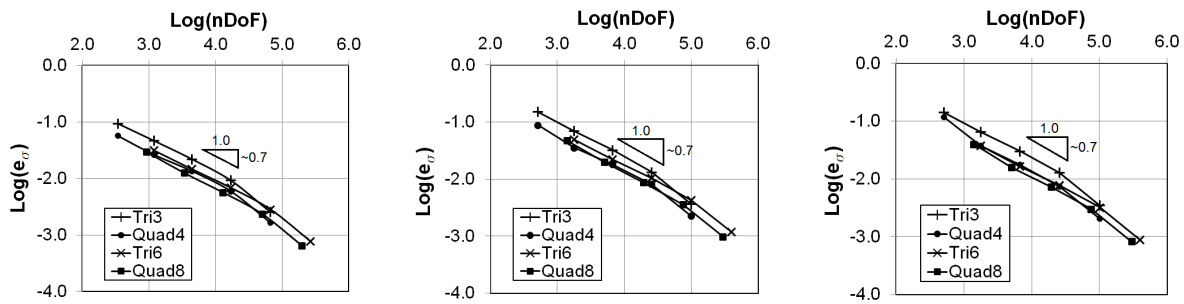
Fig. 5.17. Stress error versus nDoF for cracked cylindrical bars subject to uniaxial tensile load (left), pure bending (centre) and pure torsion (right), modelled with under-integrated bi-quadratic quadrilateral elements. The slope of the lines represents the convergence rate.

Table 5.4. Recommended optimal element size to guarantee an error of 5% or lower.

Boundary Conditions	Elements	Order	Element size/ℓ
Option 1 (essential b.c.)	Triangles	Linear	1/3
		Quadratic	1/4
	Quadrilaterals	Bi-linear	1/3
		Bi-quadratic	1/3
Option 2 (natural b.c.)	Triangles	Linear	1
		Quadratic	5/2
	Quadrilaterals	Bi-linear	3/2
		Bi-quadratic	5/2

5.7 Removal of singularities

Once the new methodology was fully implemented, it has been applied to plane, axisymmetric and three-dimensional problems, in order to show the ability of the methodology in removing singularities.

5.7.1 Mode I fracture

The mode I fracture problem described in §5.6 has been analysed, using all the four implemented two-dimensional elements, in order to check the quality of the results.

In Fig. 5.18 σ_{xx} and σ_{yy} profiles along the x-axis, obtained applying both the options on the boundaries conditions described in §5.6, are plotted and compared. It can be seen that the application of the different boundary conditions produces almost no variations for σ_{xx} and moderate effects on σ_{yy} in terms of maximum values. To explain this, it must be realised that along the face of the crack ($y = 0$), no boundary conditions are applied on σ_{xx}^g in both Option 1 and 2; σ_{yy}^g, instead, is forced to be null in Option 1, while it is left free in Option 2. At this point it is worth reminding that, in the proposed methodology, gradient enriched stresses are not determined by solving equilibrium equations but reaction-diffusivity equations (5.8) and therefore they are not meant to be equilibrated. Furthermore, as already discussed at the end of §5.1, the boundary conditions accompanying the proposed methodology cannot exactly replicate those accompanying the original fourth-order Aifantis theory (Eqs. (3.32) and (3.33)). At the light of these aspects, both Option 1 and Option 2 are appropriate. However, while Option 2 represents the most convenient choice for the boundary conditions, Option 1 by equilibrating the non-local stresses with externally applied tractions (σ_{yy}^g are forced to be zero on the crack faces) produces more realistic and easy to interpret results.

The aforementioned differences can be also observed from the stress fields reported in Figs. 5.19, 5.20, 5.21 and 5.22 (top and middle rows). From the bottom row of the same figures, instead, it can be noticed that also the non-local shear stress σ_{xy}^g is affected by the different options on the boundary conditions (in particular in the neighbourhood of the crack), since Option 1 forces σ_{xy}^g to be zero along the whole boundary, while σ_{xy}^g is free everywhere according to Option 2.

Comparing Figs. 5.19, 5.20, 5.21 and 5.22, it is also possible to observe that the corresponding gradient-enriched stress fields obtained by using the different types of implemented finite elements (under the same boundary conditions) match perfectly.

However, the most significant aspect is that, introducing a gradient enrichment, the singularities in the stress field are removed. In fact, as shown in Fig. 5.23, applying classical elasticity the solution does not converge to a finite value upon mesh refinement and an unbounded peak is detected at the crack tip, while by introducing a gradient enrichment in the governing equations and refining the mesh, the solution converges towards a unique and finite value.
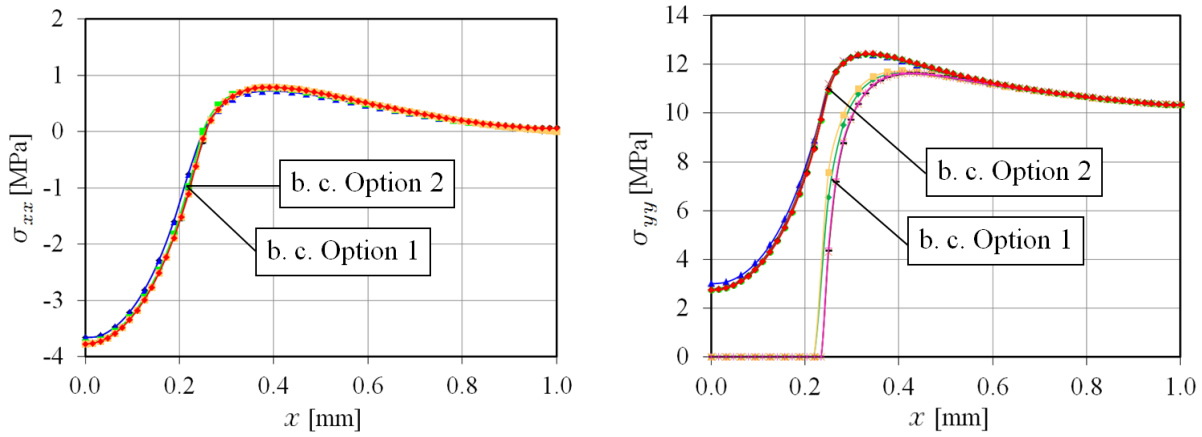
Fig. 5.18. Mode I fracture problem: comparison of the σ_{xx} (left) and σ_{yy} (right) values for $y = 0$, obtained employing the different kind of finite elements and both the options for the boundary conditions.

5.7.2   Cracked cylindrical bars

The singularity removal can be easily shown also for the axisymmetric elements by considering the problems presented in §5.6 and comparing the stress profiles obtained by applying the proposed methodology with those produced by classical elasticity. Fig. 5.24, in fact, shows that while the classical elastic stress fields are characterised by an unbounded peak in correspondence of the crack tip, the gradient-enriched ones converge to a unique finite solution upon mesh refinement (the stress profiles presented in Fig. 5.24 were obtained by using bi-quadratic quadrilateral elements, similar results are produced by all the other implemented elements).

5.7.3   Beams-column joint

Finally, in order to show the ability of the proposed methodology to remove the singularities also in three-dimensional problems, the problem shown in Fig. 5.25 has been studied. The geometrical and material properties of the problem are $L = 2.4$ m, $a = 0.4$ m, $E = 1000$ MPa, $\nu = 0.25$ and $\ell = 0.03$ m. Prescribed surface distributed loads $q = 10^5$ N/m^2 are applied at the free end of the two beams, while the column is fully restrained at its base. The boundary conditions associated to Eq. (5.38) are chosen as *homogeneous natural* throughout, that is $\mathbf{n} \cdot \nabla \boldsymbol{\sigma}^g = 0$. The domain has been modelled using 128 (Fig. 5.25), 1024, 8192 and 65536 linear brick elements.

In Fig. 5.26 the normal stress σ_{xx} and the shear stress σ_{xy} obtained by applying both classical elasticity ($\ell = 0.00$ m) and gradient elasticity ($\ell = 0.03$ m) are plotted along a vertical edge of the column ($x = 0.4$ m, $y = 0.4$ m, 0.0 m $\leq z \leq 2.4$ m, red solid line in Fig. 5.25), while in Fig. 5.27 the normal stress σ_{xx} is plotted along the beam in y-direction ($x = 0.2$ m, 0.0 m $\leq y \leq 2.4$ m, $z = 2.0$ m, red dashed line in Fig. 5.25).

Both figures clearly show the ability of the proposed methodology to remove singularities from the stress fields. In fact while the use of classical elasticity leads to singular
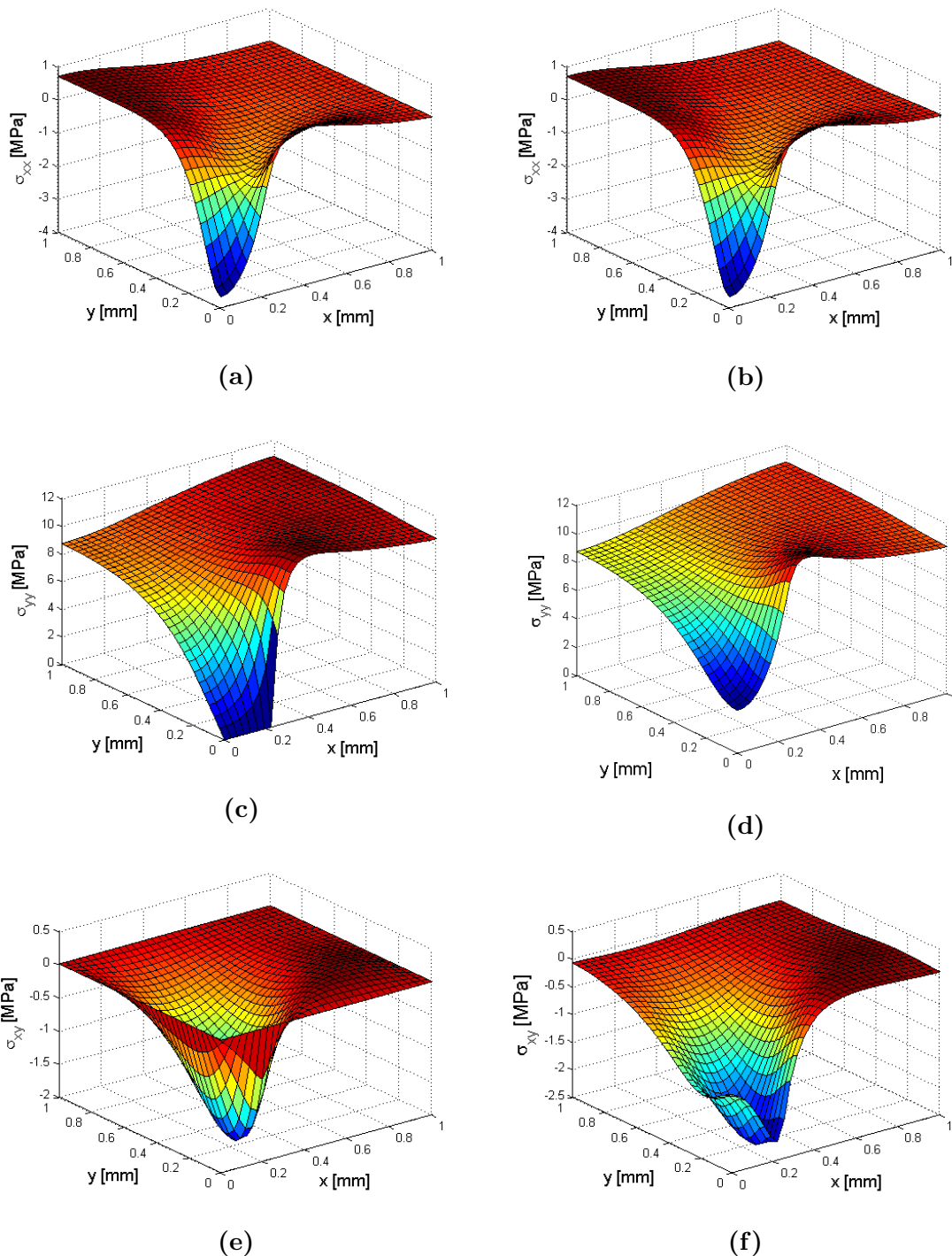
Fig. 5.19. Mode I fracture problem: surface plot of stress components σ_{xx} (top row), σ_{yy} (middle row), σ_{xy} (bottom row), obtained using linear triangular elements with *homogeneous natural* (left column) and *homogeneous essential* (right column) boundary conditions.
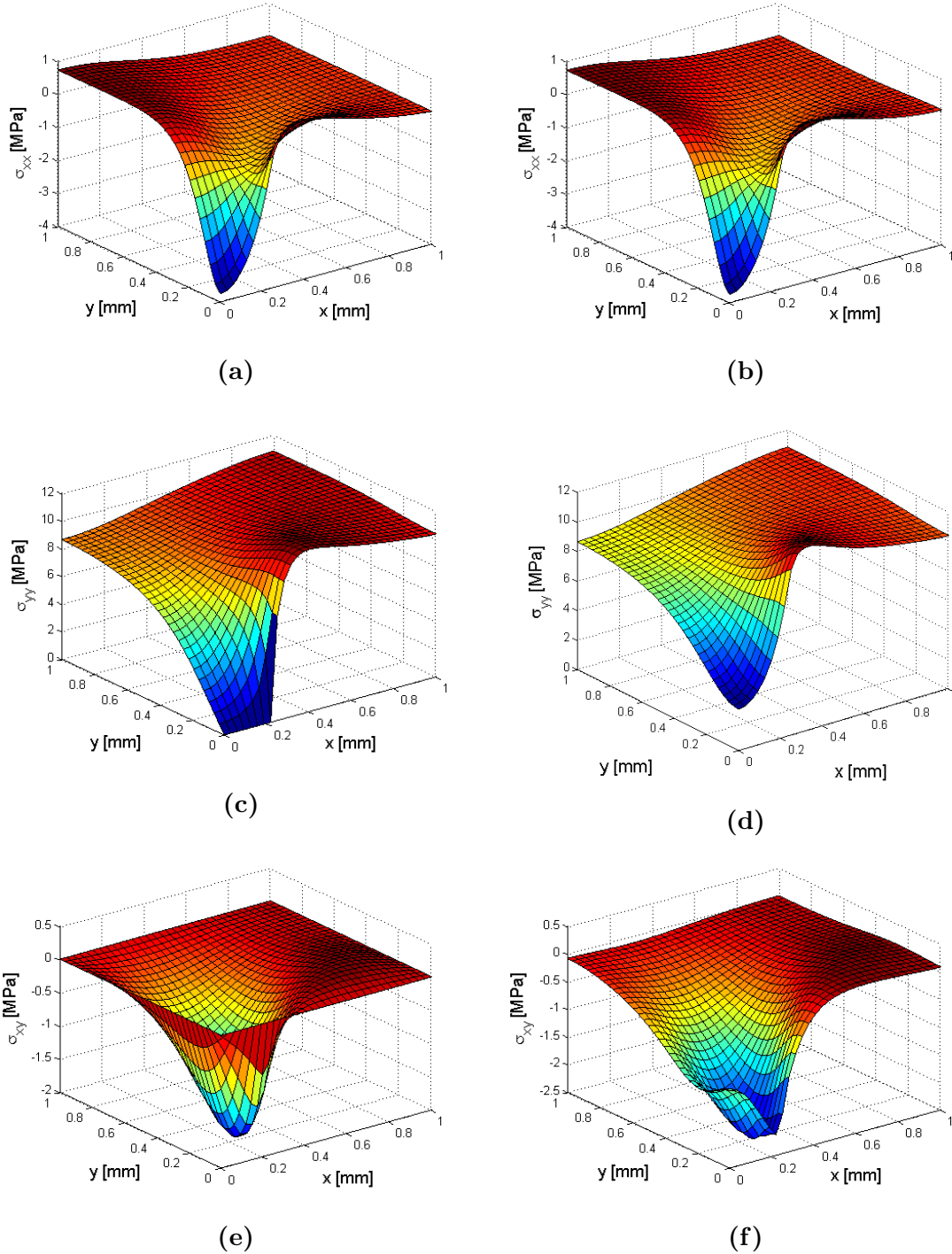
Fig. 5.20. Mode I fracture problem: surface plot of stress components σ_{xx} (top row), σ_{yy} (middle row), σ_{xy} (bottom row), obtained using bi-linear quadrilateral elements with *homogeneous natural* (left column) and *homogeneous essential* (right column) boundary conditions.
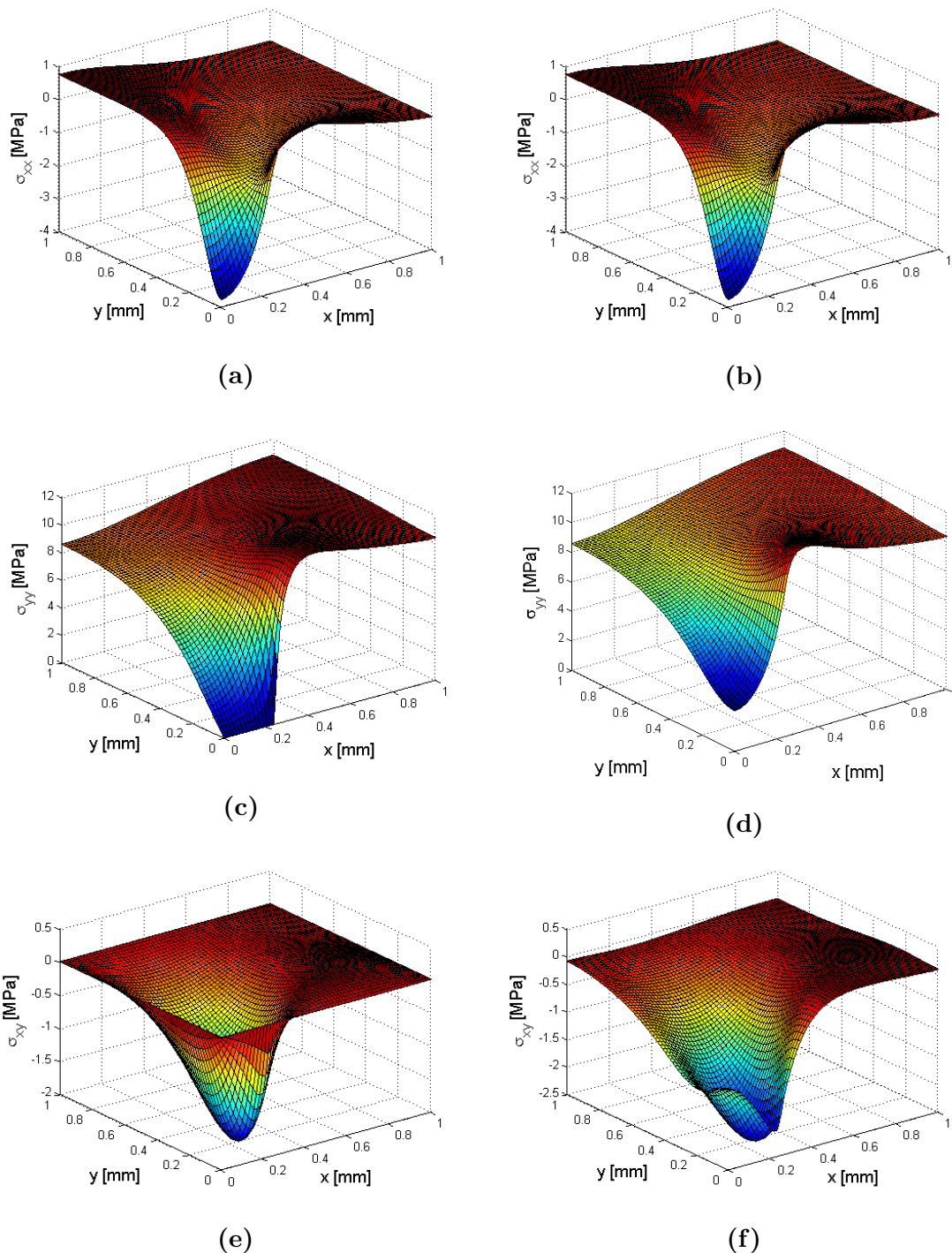
Fig. 5.21. Mode I fracture problem: surface plot of stress components σ_{xx} (top row), σ_{yy} (middle row), σ_{xy} (bottom row), obtained using quadratic triangular elements with *homogeneous natural* (left column) and *homogeneous essential* (right column) boundary conditions.
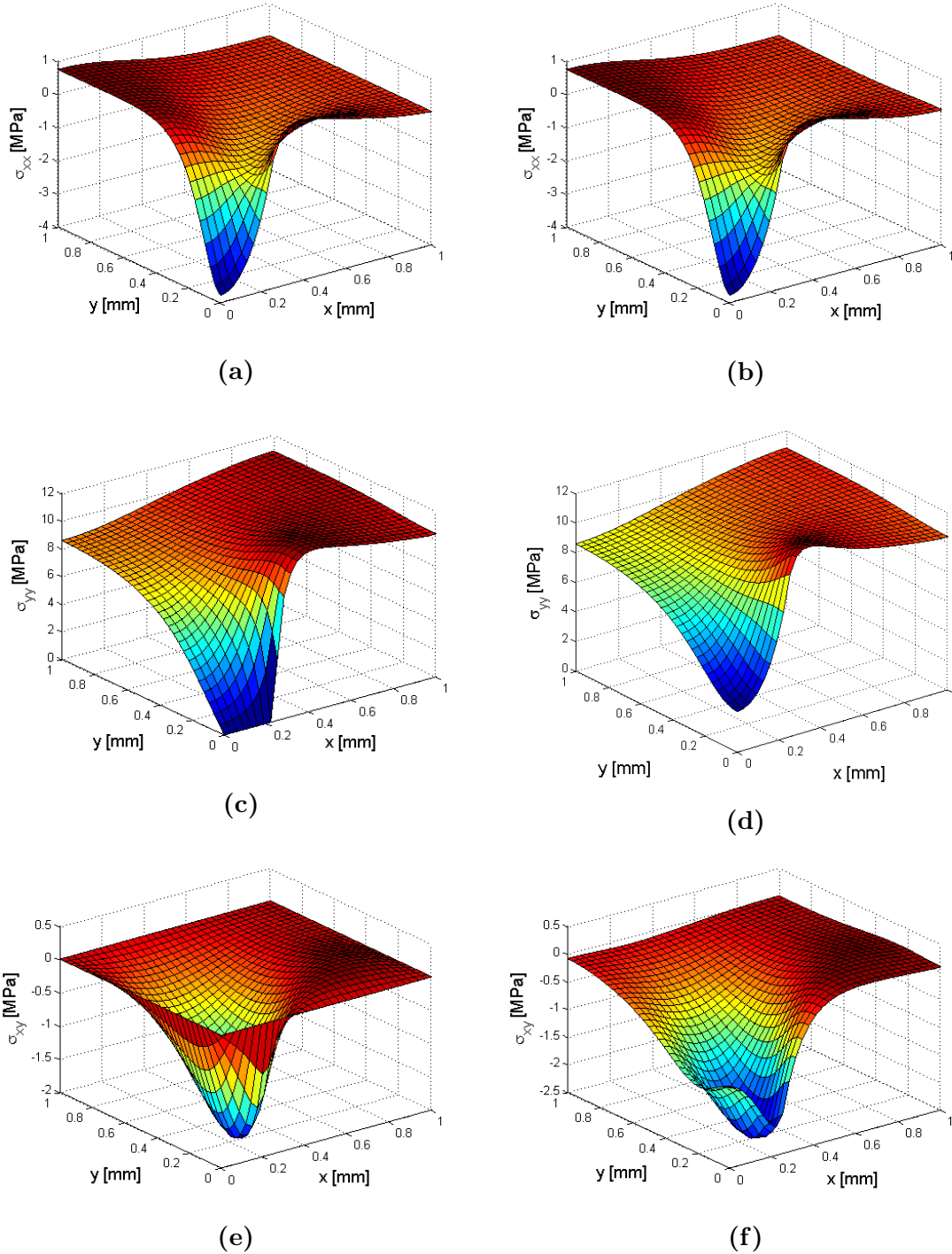
Fig. 5.22. Mode I fracture problem: surface plot of stress components σ_{xx} (top row), σ_{yy} (middle row), σ_{xy} (bottom row), obtained using bi-quadratic quadrilateral elements with *homogeneous natural* (left column) and *homogeneous essential* (right column) boundary conditions.
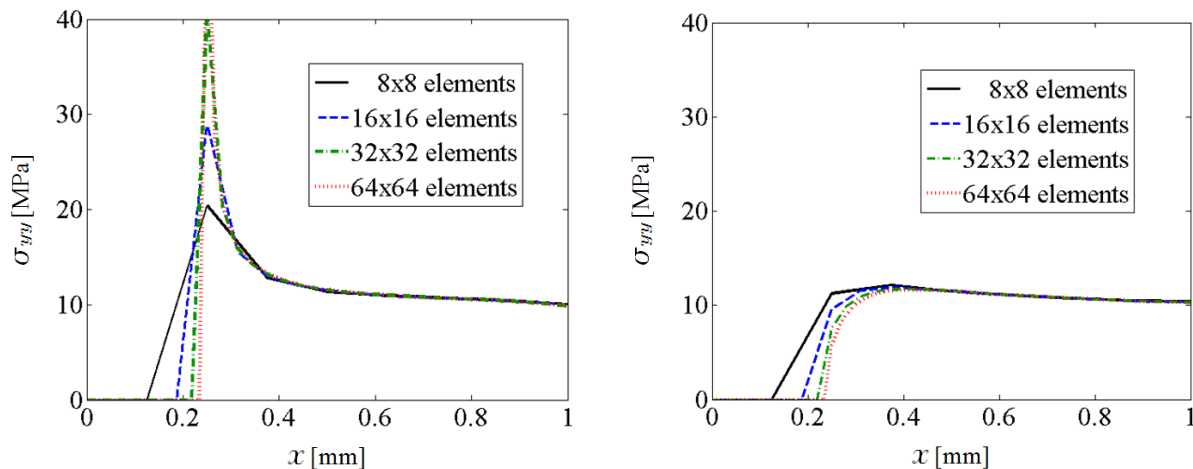
Fig. 5.23. Mode I fracture problem: σ_{yy} profiles along x-axis obtained by applying classical elasticity (left) and gradient elasticity (right) and the first option on the boundary condition, upon mesh refinement.

solutions in correspondence of the stress concentrators, if a gradient enrichment is introduced in the governing equations of the problem, the solutions are not singular anymore, converging to a unique finite solution. Hence, the ability of the proposed methodology to remove the singularities is confirmed also for three dimensional problems.

5.8 Conclusions

In this chapter a unified gradient-elastic FE methodology for plane, axisymmetric and three-dimensional problems has been developed.

The proposed methodology has been applied to plane, axisymmetric and three-dimensional simple problems without singularities and it has been found that, overall, the numerically obtained convergence rates are well in line with theoretical predictions. Furthermore, in what concerns axisymmetric problems it has been found that, while for the displacements all the implemented elements produce results coincident with the analytical solution, for the stresses the numerical estimates differ from the analytical counterparts proposed by Gao and Park [58]. These differences can be ascribed to the fact that while the proposed methodology is a stress-gradient elastic methodology, the one used by Gao and Park represents a displacement-based formulation, this leading in particular to different higher-order boundary conditions and different relationship amongst the stress components (while in the analytical solution proposed by Gao and Park the stress components are coupled, in the developed methodology they are uncoupled).

The convergence rate of the proposed methodology has also been analysed in presence of singularities, showing that both linear and quadratic elements are characterised by a convergence rate higher than the theoretical value typical of standard finite element methodologies based on classical elasticity. The cause of this faster convergence has been mainly attributed to two aspects:
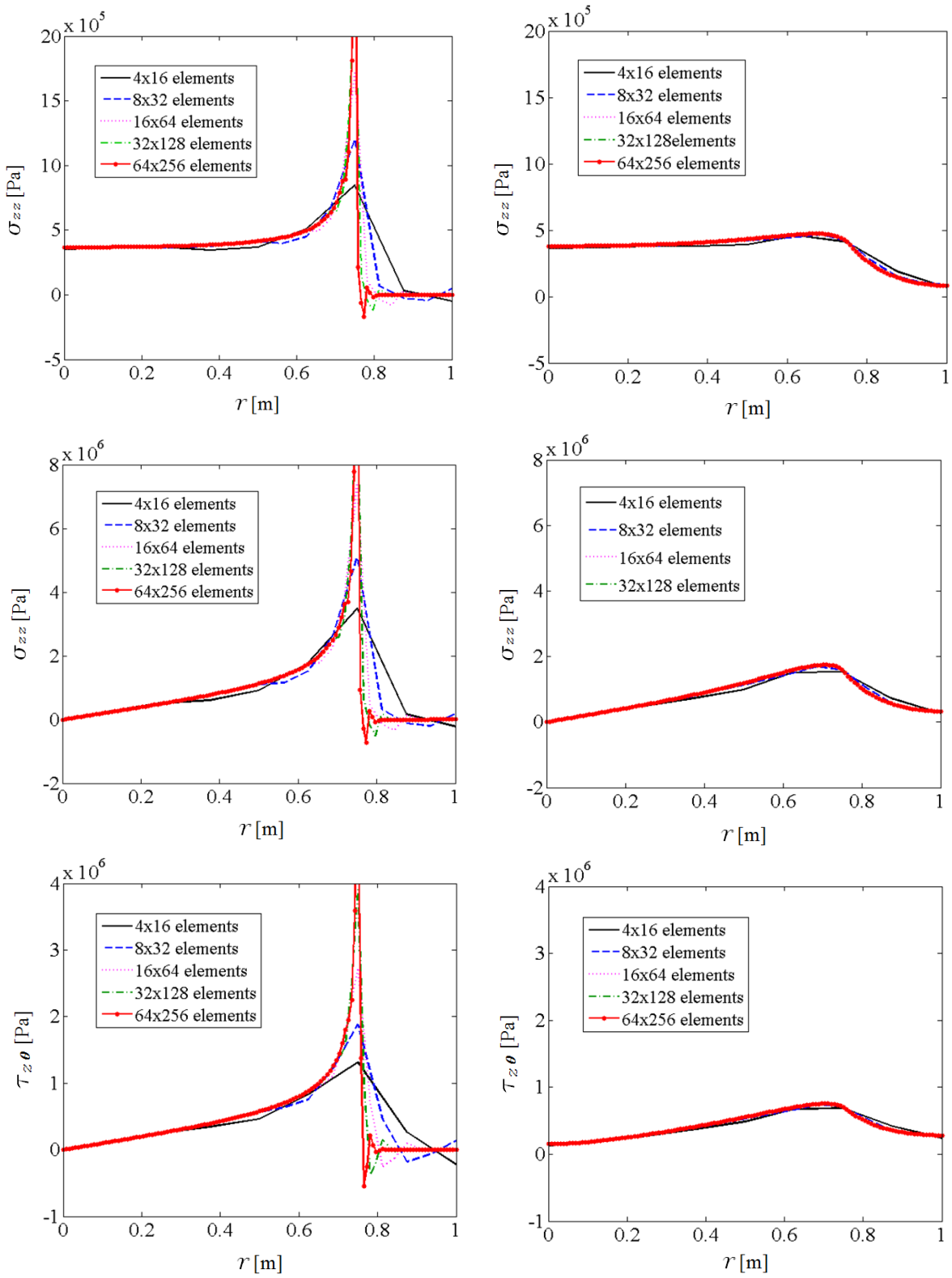
Fig. 5.24. Stress profiles obtained by applying classical (left) and gradient (right) elasticity, for uniaxial tensile loading (top), pure bending (centre) and pure torsion (bottom).
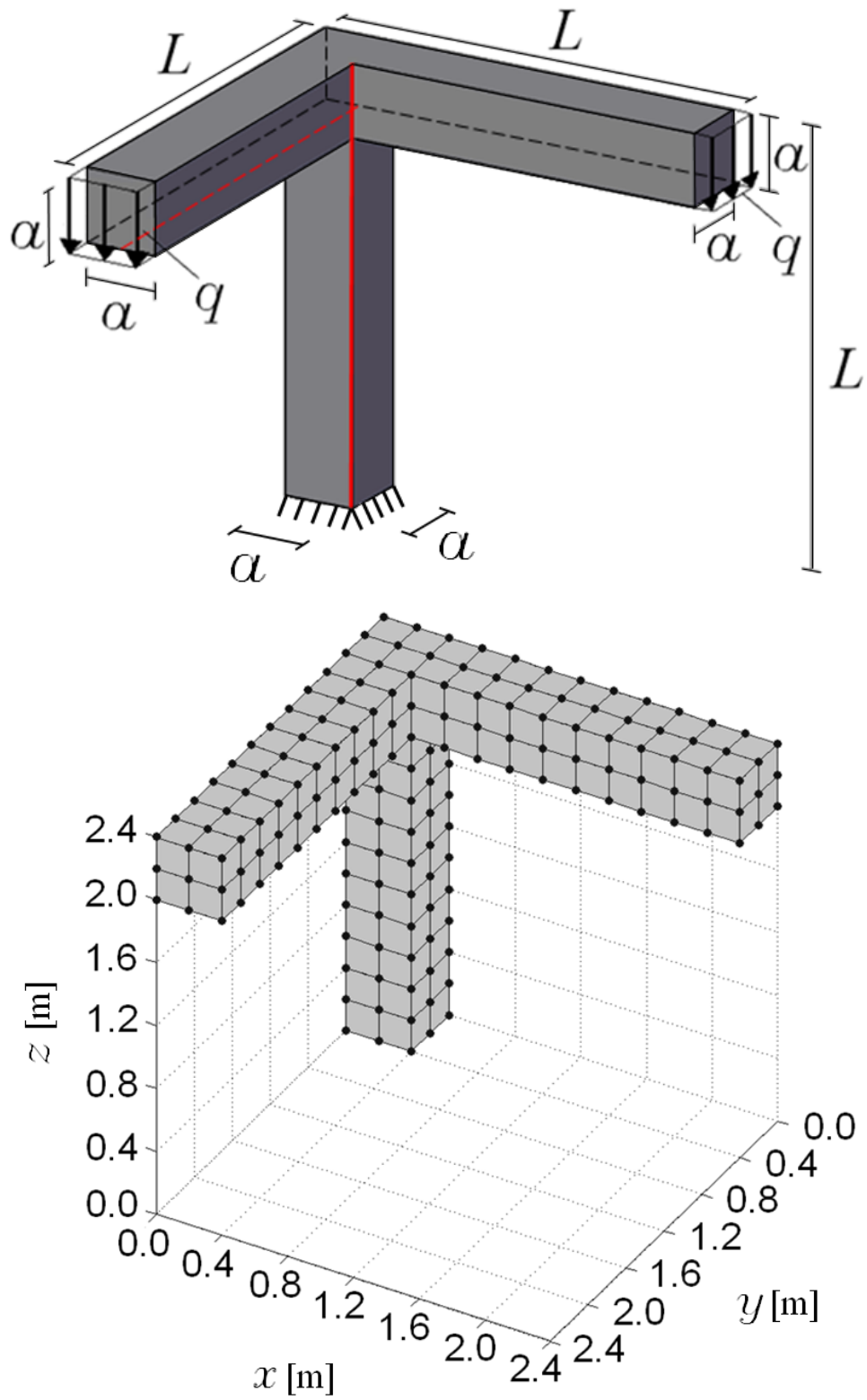
Fig. 5.25. Beams-column joint: geometry and loading conditions (top), coarsest mesh (bottom).
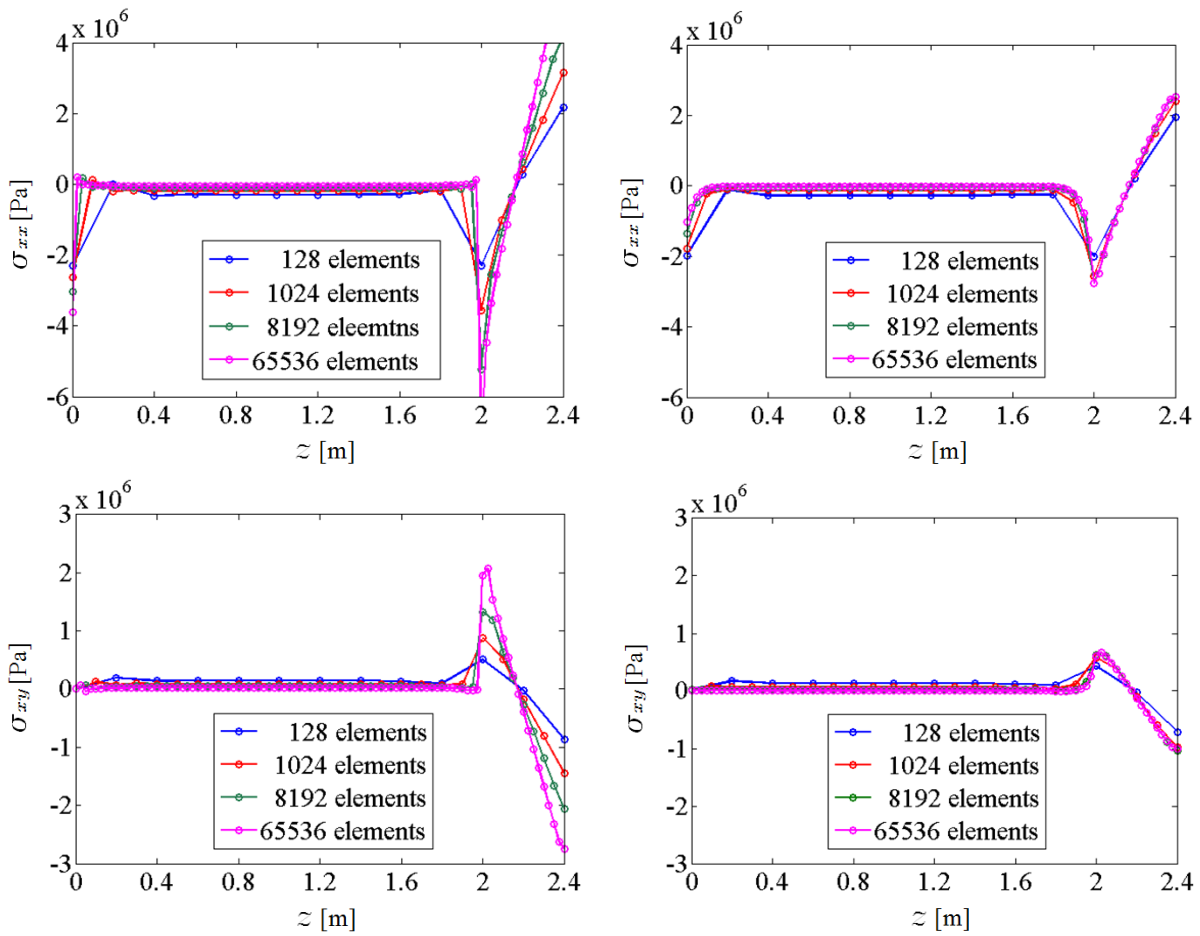
Fig. 5.26. Beams-column joint: profiles of σ_{xx} (top row) and σ_{xy} (bottom row), along a column vertical edge ($x = 0.4$ m, $y = 0.4$ m, 0.0 m $\leq z \leq 2.4$ m), for both classical (left column) and gradient (right column) elasticity, over mesh refinement.
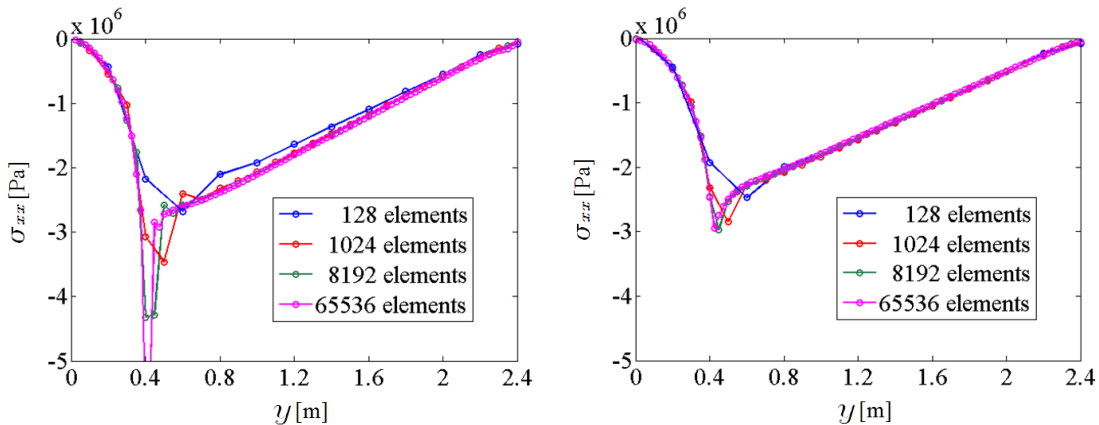
Fig. 5.27. Beams-column joint: profiles of σ_{xx}, along the beam in y-direction ($x = 0.2$ m, 0.0 m $\leq y \leq 2.4$ m, $z = 2.0$ m), for both classical (left column) and gradient (right column) elasticity, over mesh refinement.

- the removal of singularities, characteristic of gradient elasticity theories;

- the non-local stresses determined as primary variables, instead of secondary variables as in traditional finite element methodologies.

Moreover, a guideline on optimal element size have been suggested, highlighting that relatively coarse meshes can produce sufficiently accurate solutions, with consequent advantages in terms of computational cost.

Finally, the ability of the proposed methodology to remove singularities from the stress fields has been shown by analysing several plane, axisymmetric and three-dimensional problems characterised by singularities.

Chapter 6

Static and fatigue assessment of notched components

6.1 Static assessment of notched components

The accurate evaluation of the static strength of notched components is not an easy task since, as described in [137], the presence of stress risers can significantly affect the failure behaviour of components subject to static loading. In particular, Susmel and co-workers [137] found that components presenting sharp notches may show brittle failure even if they are made of ductile materials.

The accuracy of the TCD in estimating the static strength of notched components has been widely demonstrated in several works investigating a wide range of both notches and materials (from brittle to ductile) [133, 135, 138, 147, 150]. However, the estimation of the critical distance L through Eq. (2.76) requires the knowledge of the material inherent strength σ_0, which is not always feasible due to time and economic reasons, since it must be obtained experimentally by testing specimens with notches of different sharpness (see for example [88, 148]).

To overcome this problem, Louks and co-workers [88] proposed a simplified reformulation of the TCD that has demonstrated to be a very accurate and practical tool for the design of notched components subject to static loading. In particular, they hypothesised that $\sigma_0 = \sigma_{UTS}$ for any material, from brittle to ductile, leading to the following definition of the critical distance:

$$L^* = \frac{1}{\pi} \left(\frac{K_{IC}}{\sigma_{UTS}} \right)^2 \tag{6.1}$$

This definition, even if very similar to Eq. (2.76), presents the great advantage of requiring the knowledge of K_{IC} and σ_{UTS} that are typically provided by manufacturers, avoiding the need to run expensive and time consuming experimental tests.

In this section, following the encouraging results presented by Louks and co-workers [88], the gradient-enriched methodology developed in Chapter 5, where ℓ is estimated through Eq. (4.2) but with L defined according to Eq. (6.1), is validated against a wide range of experimental data found in the literature [33, 62, 63, 142]. In particular, both brittle and

Table 6.1. Mechanical properties of the analysed materials.

Material	Ref.	E [MPa]	ν	σ_{UTS} [MPa]	K_{IC} [Nm$^{-3/2}$]	L^* [mm]	ℓ [mm]
PMMA (-60°C)	[62, 63]	5050	0.40	128.4	1.7	0.056	0.020
Al-15%SiC	[33]	82500	0.33	230	6.0	0.217	0.077
Ferritic-pearlitic steel (-40°C)	[33]	203000	0.30	502	12.3	0.191	0.068
Martensitic steel	[142]	203000	0.30	1482	6.1	0.005	0.002

metallic materials subject to Mode I and mixed-Mode I and II are analysed.

6.1.1   Validation through static experimental results

To assess the accuracy of the proposed gradient-enriched methodology in the estimation of the static strength of notched components, several experimental results obtained by testing notched plane specimens under different loading conditions have been analysed. In particular, Mode I loading conditions were obtained by testing double edge notch specimens (DENS) under tensile loading [63] (Fig. 6.1a) and single edge notch specimens (SENS) under three-point bending [33] (Fig. 6.1b). Mixed-Mode I and II loading conditions, instead were reproduced by testing SENS under eccentric three-point bending [62, 142] (Figs. 6.1c and d). As previously mentioned both brittle materials (polymethyl-metacrylate (PMMA) at -60°C) and metals (Al-15%SiC, martensitic steel and ferritic-pearlitic steel at -40°C) have been considered. In Table 6.1 the relevant mechanical properties of the considered materials are listed, while Table 6.2 summarises the geometrical parameters of the analysed specimens as well as the various experimental static failure loads F_u used in the present validation exercise.

The accuracy of the proposed methodology to estimate the static strength of notched components was evaluated by calculating the following error:

$$E_S[\%] = \frac{\sigma^g_{\text{eff}} - \sigma_{UTS}}{\sigma_{UTS}} \cdot 100 \qquad (6.2)$$

where, σ^g_{eff} is the gradient-enriched effective stress at the hot-spot on the surface of the specimen. In particular, as suggested in [88], σ^g_{eff} was considered equal to the first principal stress, σ_1, for brittle materials and to the von Mises equivalent stress, σ_{VM}, defined by Eq. (2.6), for metallic materials.

It is important to note that, according to Eq. (6.2), positive errors correspond to conservative evaluations of the static strength, while negative values of E_S indicates non-conservative estimates.

In what concerns Mode I loading, given the symmetry of the problem (Figs. 6.1a and b) the gradient-enriched FE analyses were carried out by modelling only a quarter or half of the samples, respectively for DENS and SENS specimens. On the contrary, the whole domain had to be modelled for mixed-Mode I and II problems (Fig. 6.1c and d). Independently of the analysed problem, instead, under-integrated bi-quadratic quadrilateral

Table 6.2. Geometrical parameters and experimental static failure loads F_u.

Material	Ref.	Load Mode	Load type[a]	W [mm]	H [mm]	B [mm]	b [mm]	a [mm]	r_n [mm]	F_u [N]
PMMA (−60°C)	[63]	I	T (Fig. 6.1a)	—	28	14	—	7.95	0.53	6400
								8.07	0.97	7600
								7.95	1.46	8940
								7.93	1.91	9890
Al-15%SiC	[33]	I	TPB (Fig. 6.1b)	140	30	15	—	10	0.5	2248*
									1.0	2510*
									1.5	2785*
								15	0.5	1405*
									1.0	1723*
									1.5	2075*
Ferritic-pearlitic steel (−40°C)	[33]	I	TPB (Fig. 6.1b)	220	40	20	—	10	0.5	7730*
									1.0	9140*
									1.5	10800*
									2.0	11690*
								20	0.5	4010*
									1.0	4450*
									1.5	5570*
									2.0	5830*
PMMA (−60°C)	[62]	I+II	E-TPB (Fig. 6.1c)	126	28	14	9	14	0.2	1308*
									0.5	2188*
									1.0	2729*
									2.0	3589*
								18	14	0.2	1548*
									0.5	2561*
									1.0	3511*
									2.0	4081*
								27	14	0.2	2127*
									0.5	3458*
									1.0	4391*
									2.0	5052*
								36	14	0.2	3289*
									0.5	4716*
									1.0	6064*
									2.0	7786*
Martensitic steel	[142]	I+II	E-TPB (Fig. 6.1d)	120	20	10	10	10	0.2	9240
										8630
										8290
									0.5	12830
										13585
										12120
									1.0	18940
										18210
										17840

[a] T = Tension; TPB = Three Point Bending; E-TPB = Eccentric Three Point Bending.
(*) Average of three experimental tests.
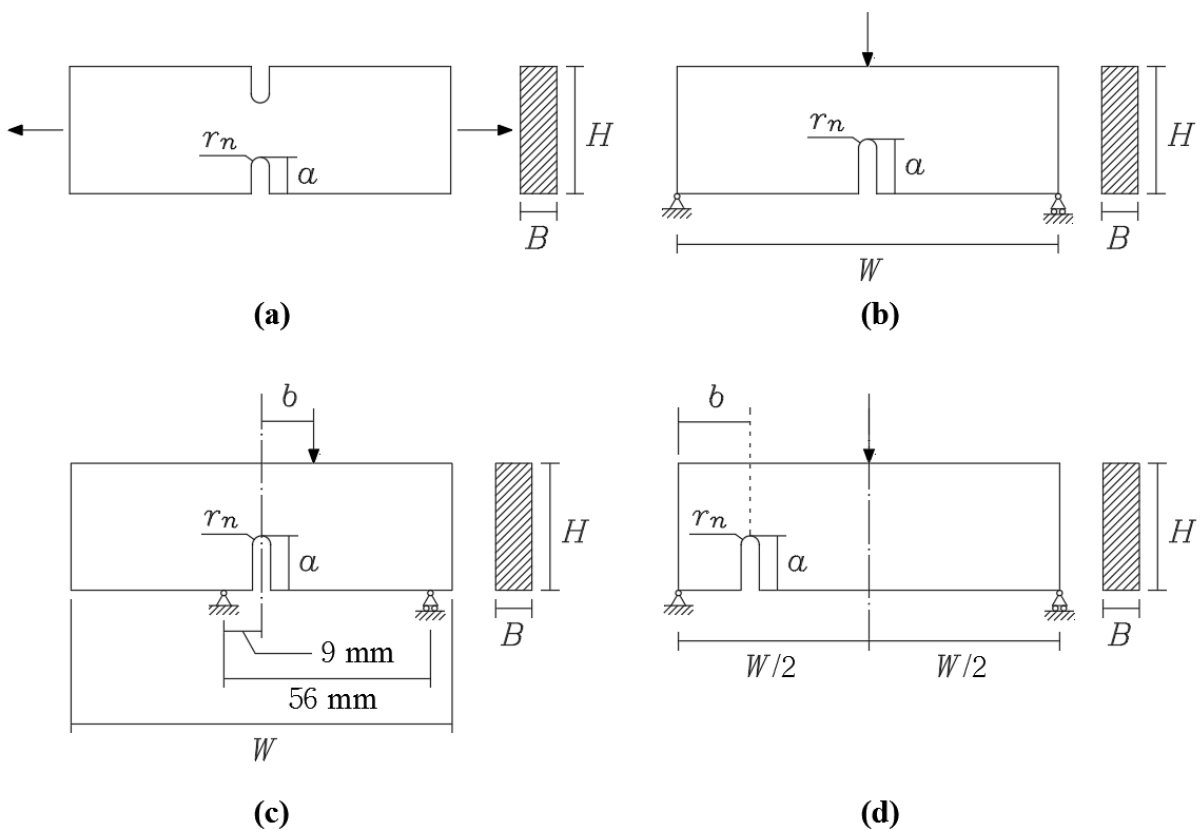
Fig. 6.1. Geometries and loading conditions of the analysed static problems.
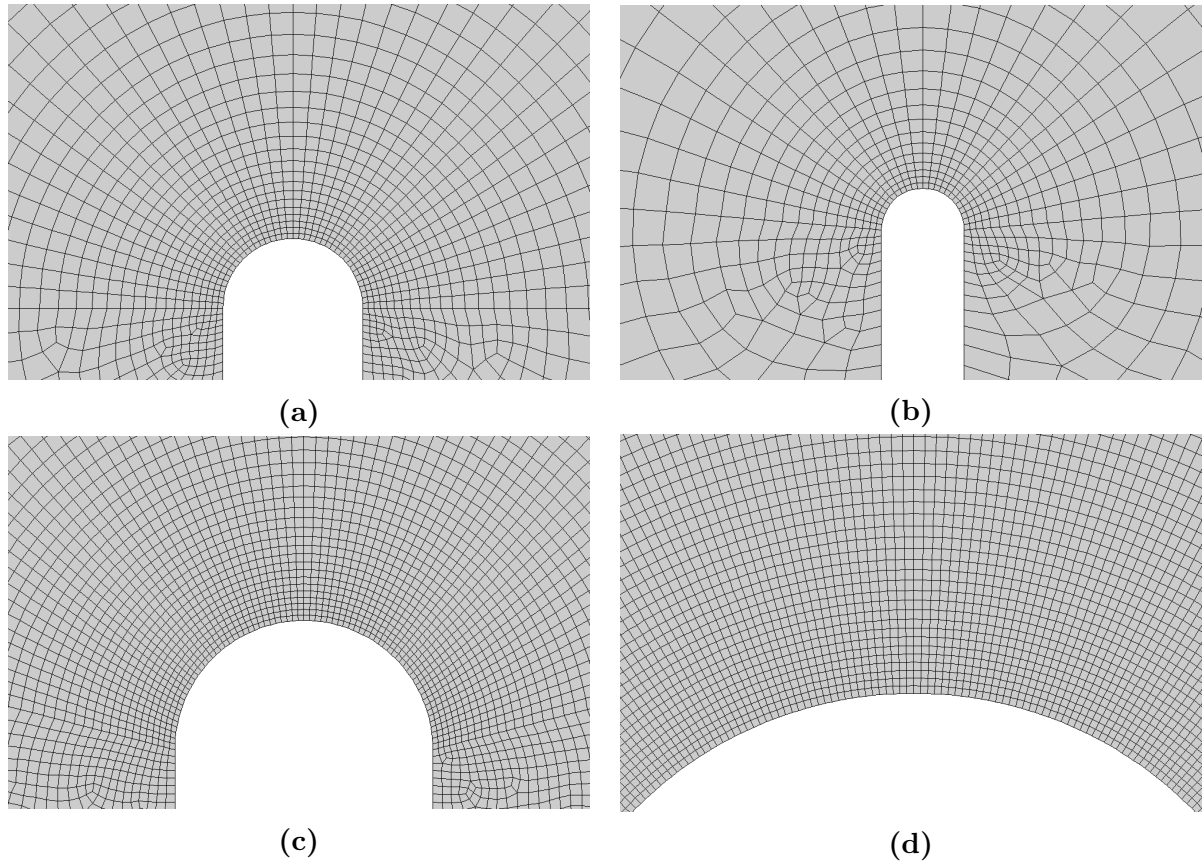
Fig. 6.2. Typical meshes used to model specimens of PMMA (a), Al-15%SiC (b), Ferritic-pearlitic steel (c) and Martensitic steel (d).

elements were used, gradually refining the mesh in the neighbourhood of the notch according to the recommendations on optimal element size suggested in Chapter 5 (see also [26]). Fig. 6.2 shows some examples of the meshes adopted to model the area around the notch tip. Regarding the boundary conditions, to solve the first step of the proposed methodology (Eq. (5.7)) the standard homogeneous essential boundary conditions of classical elasticity were applied. On the other hand, for the second step (Eq. (5.12)) homogeneous natural boundary conditions were chosen throughout, that is $\mathbf{n} \cdot \nabla \boldsymbol{\sigma}^g = 0$ (where $\mathbf{n}$ is the outward normal to the boundary).

The error graph of Fig. 6.3, summarising the accuracy of the proposed gradient-enriched methodology in the evaluation of the static strength of notched components, shows that the obtained predictions are affected by errors mainly falling within a scatter band of $\pm 20\%$, independently of the assessed material and loading conditions (note that a $\pm 20\%$ error band is considered acceptable due to all the uncertainties introduced both during testing and numerical analyses). Only in the case of brittle materials (PMMA at $-60°$C) with high degree of mode mixity ($b = 36$ mm) the proposed methodology produced slightly more non-conservative results (on average -25%). This can be ascribed to the fact that, as found by Susmel and Taylor [135], in notched brittle material (such as
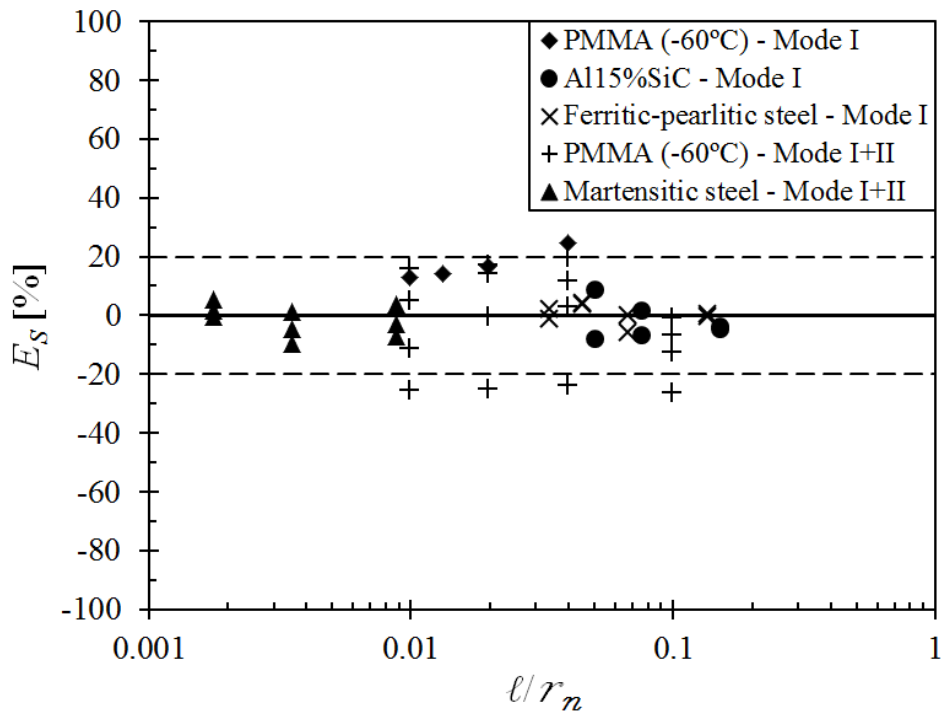
Fig. 6.3. Accuracy of the proposed gradient-enriched methodology in evaluating the static strength of notched components under Mode I and mixed-Mode I and II static loading.

PMMA) subject to static mixed-mode loading the value of the critical distance changes with the degree of multiaxiality of the stress field damaging the material process zone. This phenomenon, that becomes stronger for high degree of mode mixity, is due to the fact that as the degree of multiaxiality changes also the cracking behaviour of the material changes.

6.2 Uniaxial and multiaxial high-cycle fatigue assessment of notched components

Given the encouraging results obtained in the previous section for the static assessment of notched components, the gradient-enriched methodology developed in Chapter 5 is applied in this section to evaluate the high-cycle fatigue strength of notched components. In order to check the accuracy and reliability of the proposed methodology in the high-cycle fatigue assessment of notched components, it was used to analyse a large number of experimental data taken from the literature. The considered results were generated by testing, under both uniaxial and multiaxial cyclic loading, metallic specimens containing different geometrical features. Tables 6.3 and 6.4 summarise the experimental results used to perform the validation exercise that will be discussed in this section. The reader is also referred to [25, 120, 123, 134] for a detailed summary of the data sets listed in Tables 6.3 and 6.4.

Table 6.3. Summary of the experimental results generated under uniaxial fatigue loading.

Material	Ref.	R	$\Delta\sigma_0$ [MPa]	$\Delta\sigma_0^g$ [MPa]	ΔK_{th} [MPa m$^{1/2}$]	L [mm]	ℓ [mm]	Specimen type[a]	Load type[b]	r_n [mm]
SAE 1045	[45]	-1	608	608	13.6	0.159	0.056	CNP	Ax	0.12-2.5
Al-2024-T351	[45]	-1	248	248	5.0	0.129	0.046	CNP	Ax	0.12-1.5
G40.11	[46]	-1	464	464	15.9	0.374	0.132	CNP	Ax	0.2-4.8
SM41B	[143, 144]	-1	326	326	12.4	0.458	0.162	CNP	Ax	0.16-3.0
Mild steel	[54, 73]	-1	420	420	12.8	0.296	0.105	DENP/CNB	Ax	0.05-7.62
NiCr steel	[55]	-1	1000	1000	12.8	0.085	0.030	CNB	Ax	0.05-0.13
Steel 15313	[89]	-1	440	440	12.0	0.237	0.084	CNB	Ax	0.03-0.76
AISI 304	[73, 156]	-1	720	720	12.0	0.110	0.039	CNB	Ax	0.04
0.45 C steel	[100]	-1	582	575.5	8.1	0.061	0.022	CNB	RB	0.01-0.6
0.36 C steel	[100]	-1	446	442	7.6	0.092	0.033	CNB	RB	0.2

[a] CNP = Center Notch in flat Plate; DENP = Double Edge Notch in flat Plate; CNB = Circumferential Notch in cylindrical Bar.
[b] Ax = Axial loading; RB = Rotating Bending.

Table 6.4. Summary of the experimental results generated under multiaxial fatigue loading.

Material	Ref.	R	σ_0 [MPa]	σ_0^g [MPa]	τ_0 [MPa]	τ_0^g [MPa]	m	L [mm]	ℓ [mm]	Specimen type[a]	Load type[b]	r_n [mm]
SAE 1045	[82]	-1	304	303.1	176	175.5	—	0.159	0.056	SSF	B-T	5
Ck45	[113]	-1	304	303.1	176	175.5	—	0.159	0.056	SSF	B-T	5
S65A	[65]	-1	584	581.6	371	369.7	0.37	0.056	0.020	SSF	B-T	0.838
0.4% C Steel	[65]	-1	332	325.1	207	203.1	—	0.178	0.063	CNB	B-T	0.005
3% Ni Steel	[65]	-1	343	337.2	205	201.9	—	0.144	0.051	CNB	B-T	0.005
3/3.5% Ni Steel	[65]	-1	352	330.6	267	252.6	—	0.516	0.182	CNB	B-T	0.010
Cr-Va Steel	[151]	-1	429	423.9	258	255.2	—	0.101	0.036	CNB	B-T	0.011
3.5%NiCr Steel (normal impact)	[151]	-1	540	530.5	352	346.4	—	0.150	0.053	CNB	B-T	0.022
3.5%NiCr Steel (low impact)	[151]	-1	509	502.5	324	320.2	—	0.109	0.039	CNB	B-T	0.022
NiCrMo Steel	[151]	-1	594	586.6	343	339.1	—	0.106	0.037	CNB	B-T	0.031
En3B	[134]	-1,0	346	346	268	266.5	0.22	0.048	0.017	CNB	Ax-T	0.2, 1.25, 4.0

[a] SSF = cylindrical Shaft with Shoulder Fillet; CNB = Circumferential Notch in cylindrical Bar.
[b] Ax = Axial loading; R = Bending; T = Torsion.

6.2.1 Mode I fatigue loading

The accuracy of the proposed approach in estimating high-cycle fatigue strength of notched components was initially checked by considering a number of experimental results generated by testing flat and cylindrical notched specimens subject to uniaxial cyclic loading. For the Mode I loading case, the error was calculated as follows:

$$E_\sigma[\%] = \frac{\Delta\sigma_y^g - \Delta\sigma_0^g}{\Delta\sigma_0^g} \cdot 100 \tag{6.3}$$

where $\Delta\sigma_y^g$ is the range of the gradient-enriched stress at the notch tip (see Fig. 4.2a). According to Eq. (6.3), a positive value of E_σ indicates a conservative estimate, whereas a negative value of this error index denotes a non-conservative prediction.

The specimens being analysed were subdivided into three groups (Fig. 6.4): flat plates with central notch (CNP), flat plates with double edge notch (DENP) and cylindrical bars with circumferential notch (CNB). For any considered data set, Table 1 lists the relevant material fatigue properties, the maximum and minimum length of the investigated root

(a)   (b)   (c)
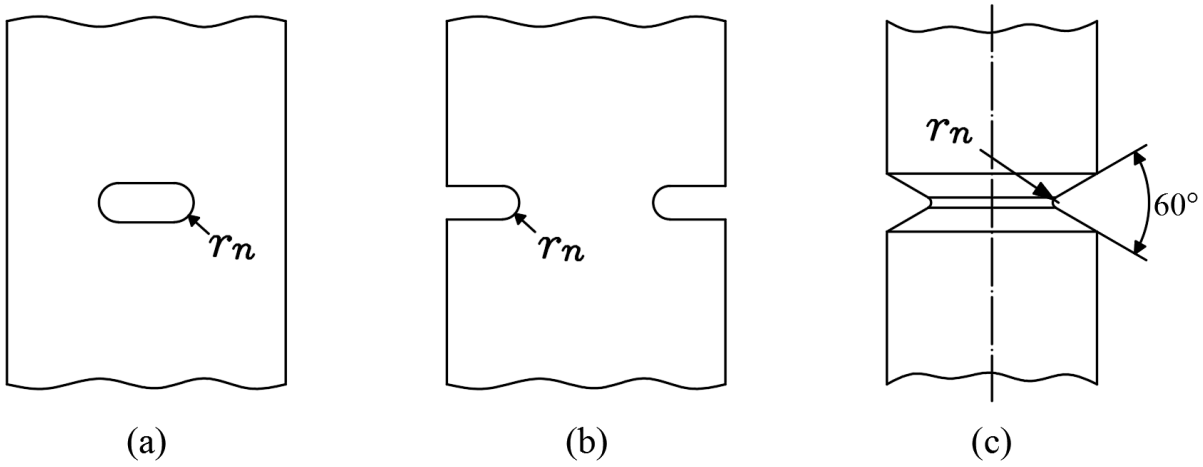
Fig. 6.4. Analysed specimens under uniaxial fatigue loadings: plate with central notch (a), plate with double edge notch (b) and cylindrical bar with circumferential V-shaped notch (c).

radii, r_n, the geometry of the tested notched specimens, and the type of applied loading.

Turning to the gradient elasticity FE analyses, since the considered notched flat specimens were symmetrical about two axes, only a quarter of the CNP and DENP samples was modelled. Similarly, in the case of the CNB specimens only half of the longitudinal section was modelled by using axisymmetric elements. Independently of the specific geometry, under-integrated bi-quadratic quadrilateral elements were used. The mesh in the vicinity of the stress concentrators was gradually refined according to the recommendations on optimal element size given in Chapter 5 (see also [26, 27]). In particular, in the highly stressed regions the average mesh size was equal to about 0.025 mm, with the minimum size approaching 0.002 mm (Fig. 6.5). To apply the Ru-Aifantis theory, two sets of boundary conditions were employed as follows. For the first step, the usual homogeneous essential boundary conditions of classic elasticity were used to preserve the symmetry of the problem. In the second step, homogeneous natural boundary conditions were applied throughout, so that $\mathbf{n} \cdot \nabla \boldsymbol{\sigma}^g = 0$ (where $\mathbf{n}$ is the outward normal to the boundary).

The charts of Fig. 6.5 show some examples of the linear-elastic stress fields obtained by using gradient elasticity according to the numerical procedure described in Chapter 4. In particular, the diagrams of Fig. 6.5a were determined by considering CNP specimens of SM41B [143, 144] with central hole having radius, r_n, equal to 0.16 mm ($K_t = 9.8$) and 3 mm ($K_t = 3$), respectively. The stress fields reported in Fig. 6.5b were calculated instead by modelling the DENP samples of mild steel [54, 73] with notch root radius, r_n, equal to 0.1 mm ($K_t = 14.9$) as well as to 1.27 mm ($K_t = 4.75$). In both cases length scale parameter ℓ was directly estimated from $\Delta\sigma_0$ and ΔK_{th} via Eq 4.1. These four diagrams clearly show gradient-elasticity smoothing effect, this resulting in stress fields having, in the vicinity of the notch tip, magnitude lower than the corresponding ones calculated according to continuum mechanics.

As mentioned in §2.4, Neuber proposed to calculate an effective stress to be used to design notched components against high-cycle fatigue by considering finite volumes and
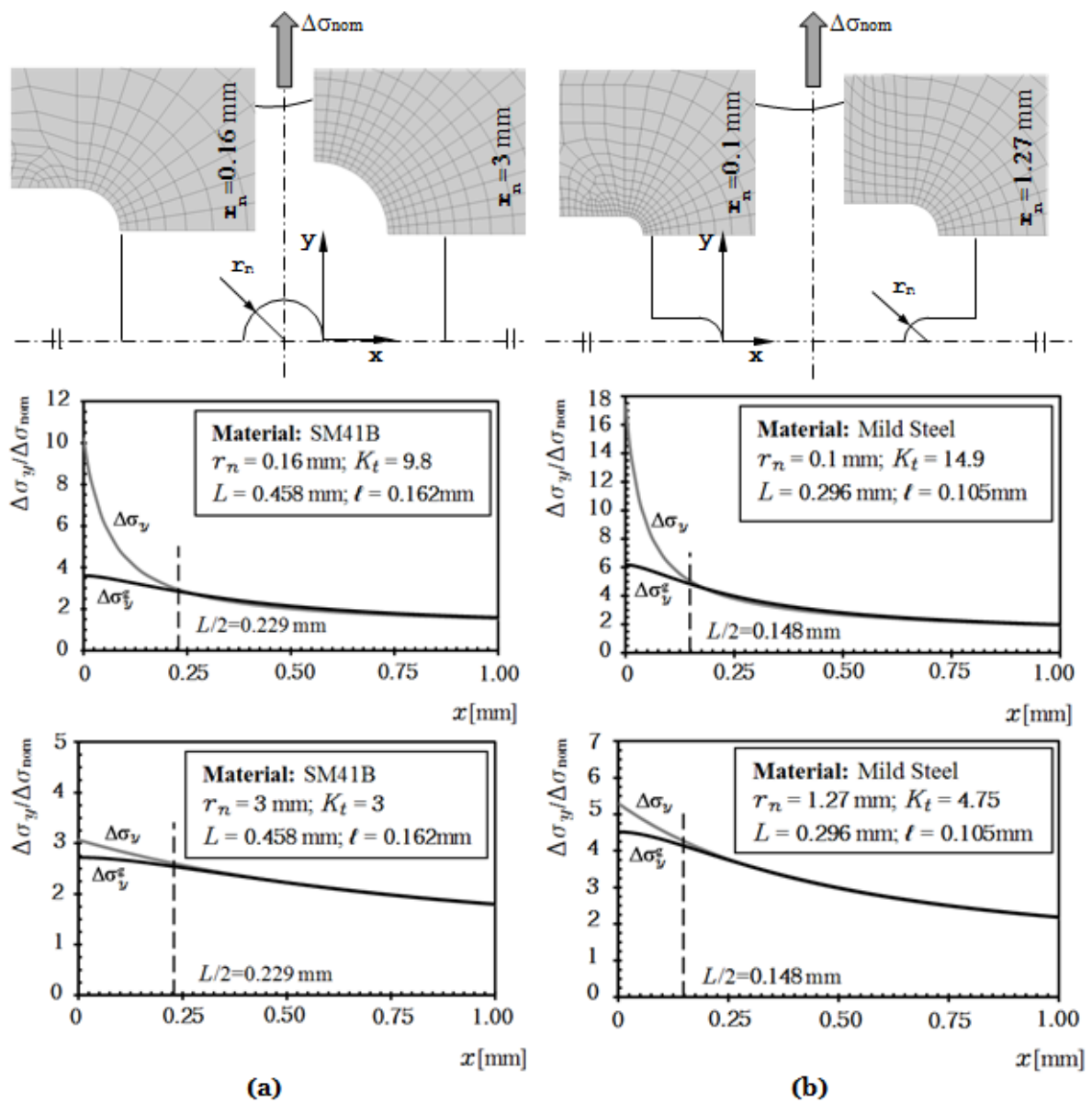
Fig. 6.5. Stress distributions along the notch bisector in CNP [143, 144] (a) and DENP [54, 73] (b) specimens subject to cyclic axial loading.

not infinitesimal volumes as postulated by classic continuum mechanics. The charts of Fig. 6.5 make it evident that gradient elasticity is a powerful numerical tool allowing Neuber's idea to be implemented efficiently, where the size of the finite volumes used to determine the relevant stress fields is related to characteristic length ℓ.

The error diagram of Fig. 6.6 summarises the overall accuracy obtained by using gradient elasticity according to the procedure described in Fig. 4.2a. This diagram makes it evident that the estimates are characterised by errors falling mainly within an interval ranging between -10% and $+30\%$. It is worth remembering here that the use of the conventional TCD is seen to result in predictions falling within an error interval of $\pm 20\%$ [130, 151]. This error level is considered to be acceptable because, in general, it is not possible to distinguish between an error of $\pm 20\%$ and an error of 0% because of those problems which are usually encountered during testing as well as during the numerical analyses [151]. Hence, the systematic usage of the proposed approach resulted in predictions falling within an error range of 40%, with the average value of the error being shifted by 10% toward the conservative side compared to the conventional TCD.

Regarding the predictions summarised in Fig. 6.6, it is worth pointing out that these estimates were obtained by using $\Delta\sigma_0^g$ as reference un-notched fatigue limit. Obviously, under axial loading, the same level of accuracy would be reached by using $\Delta\sigma_0$ instead of $\Delta\sigma_0^g$, as described in Chapter 4 (see Fig. 4.1b). In what concerns the notched specimens tested under rotating bending, Table 6.3 shows that for 0.45C steel and 0.36C steel the difference between $\Delta\sigma_0^g$ and $\Delta\sigma_0$ approaches 1%. This implies that using $\Delta\sigma_0$ as reference plain fatigue limit to assess these notched samples would result in the same overall level of accuracy as the one that was obtained by employing the gradient-enriched fatigue limits, $\Delta\sigma_0^g$. This confirms that gradient elasticity can be safely used to predict high-cycle fatigue strength by also employing the conventional un-notched fatigue limit as reference material strength.

6.2.2   Multiaxial fatigue loading

After investigating the accuracy of the Mode I formalisation of the proposed approach, the subsequent step was checking whether gradient elasticity applied with the MWCM (Fig. 4.2b) is successful also in estimating high-cycle fatigue strength under multiaxial fatigue loading. The experimental results summarised in Table 6.4 were generated by testing shafts with shoulder fillet (SSF) (Figs. 6.7a, b and c) and circumferentially notched cylindrical bars (CNB) (Fig. 6.7d) under in-phase and out-of-phase fully-reversed bending (or tension) and torsion. In order to check its accuracy in modelling the mean stress effect in fatigue, the proposed design approach was also employed to estimate the high-cycle fatigue strength of notched samples of both S65A [65] and En3B [134] subject to biaxial cyclic loading with superimposed static stresses. For the re-analysed experimental results, Table 6.4 summarises the relevant material fatigue properties, the length of the assessed notch root radii, r_n, the geometry of the notched specimens and the type of applied loading. As to the L values listed in this table, it is worth observing that they were estimated [120, 134] by following a procedure based on the combined use of plain
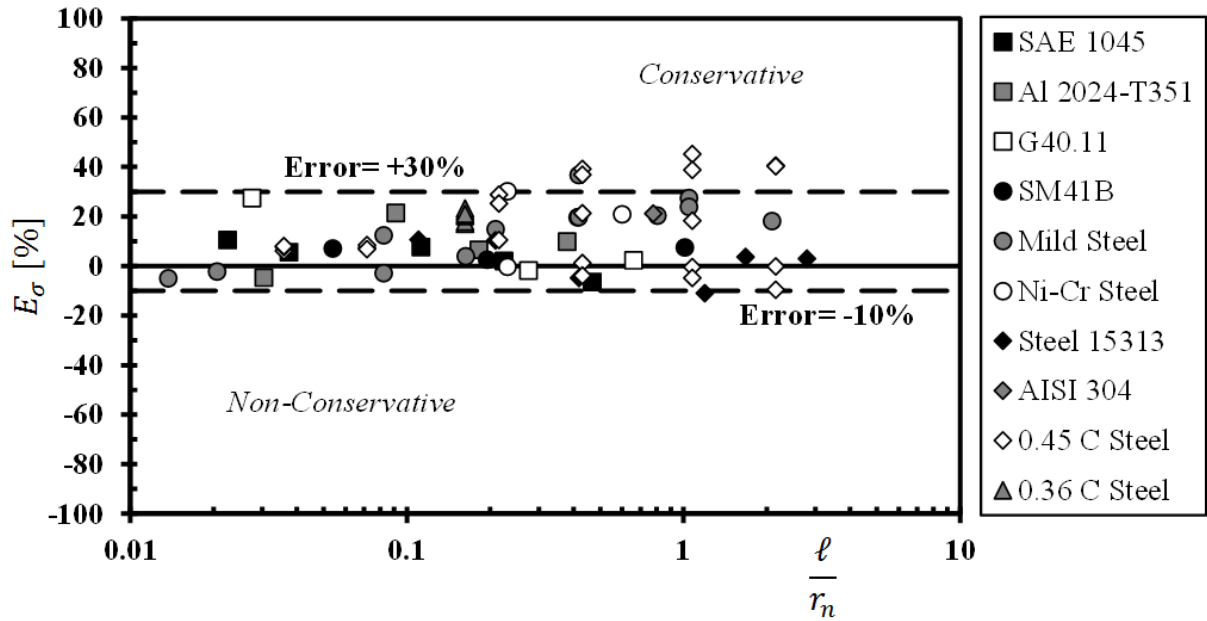
Fig. 6.6. Accuracy of the proposed design method (Fig. 4.2a) in estimating high-cycle fatigue strength of notched specimens subject to fully-reversed Mode I cyclic loading.

and notch fatigue limits [136]. Both SSF and CBN specimens were modelled by using under-integrated axisymmetric bi-quadratic quadrilateral elements refining the mesh in the vicinity of the stress riser being assessed, according to the recommendations on optimal element size presented in Chapter 5 and in [27]. Figs. 6.8, 6.9, 6.10 and 6.11 shows typical meshes used to model the aforementioned SSF and CBN specimens.

Other than the results summarised in Table 6.4 and generated under multiaxial fatigue loading, the accuracy of gradient elasticity applied in conjunction with the MWCM was also checked against a number of experimental results generated by testing CNP and DENP specimens under uniaxial loading (refer to Table 6.3). The goal of this validation exercise was to investigate whether this design approach is successful in taking into account the actual degree of multiaxiality of the gradient-enriched stress fields.

The gradient-enriched stress tensors at the hot-spots (Fig. 4.2b) were determined via 2D and 3D gradient elasticity FE models solved by using the developed FE code. In the CNP and DENP samples, the gradient enriched stress distributions across the thickness were determined by solving three-dimensional FE models obtained by considering one eighth of the specimens. These 3D solutions were obtained by discretising the domain with 10-noded (quadratic) tetrahedrons and using four Gauss points integration rule to solve both the steps of the numerical problem, i.e. Eqs. (5.7) and (5.38). In the 3D models, the average mesh size in the vicinity of the notch tips was equal to about 0.045 mm, with the minimum size approaching 0.008 mm (Fig. 6.12).

Turning to the notched cylindrical samples, only half of the longitudinal section of the investigated specimens was modelled by using under-integrated axisymmetric bi-quadratic quadrilateral elements, the mesh in the vicinity of the assessed stress concentrators being
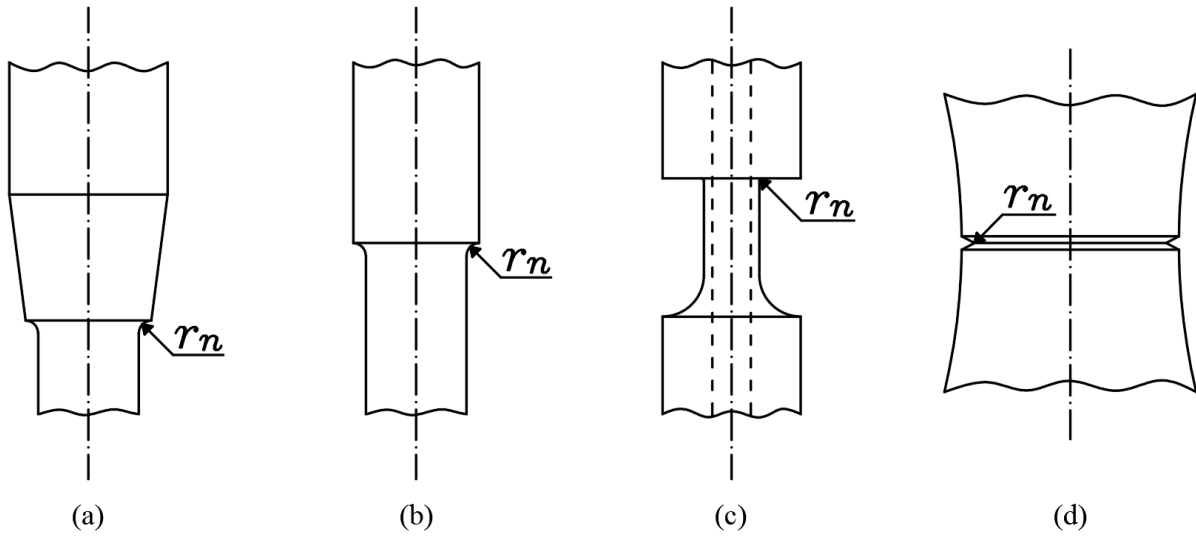
Fig. 6.7. Analysed specimens under multiaxial fatigue loadings: shafts with shoulder fillet (a, b, c) and cylindrical bar with circumferential V-shaped notch (d).
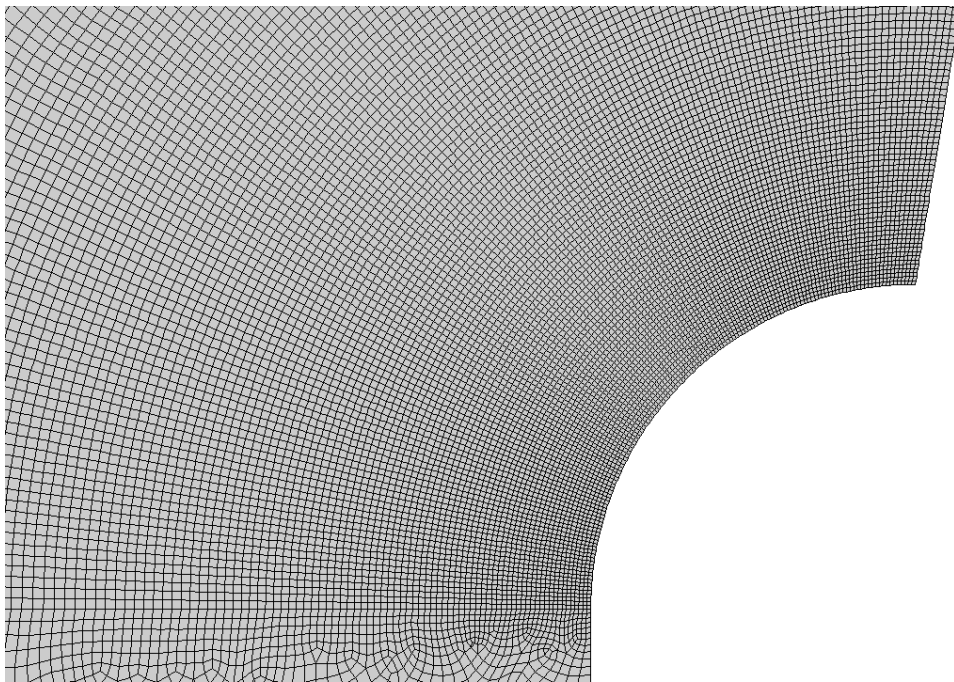
Fig. 6.8. Typical mesh used to model shafts with shoulder fillet of SAE 1045.
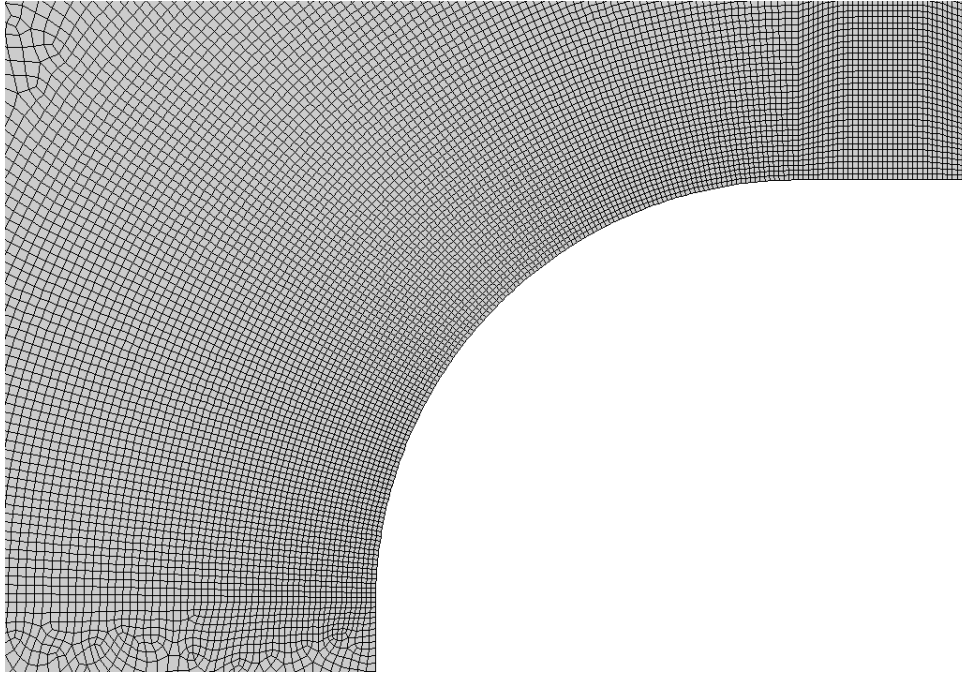
Fig. 6.9. Typical mesh used to model shafts with shoulder fillet of Ck45.
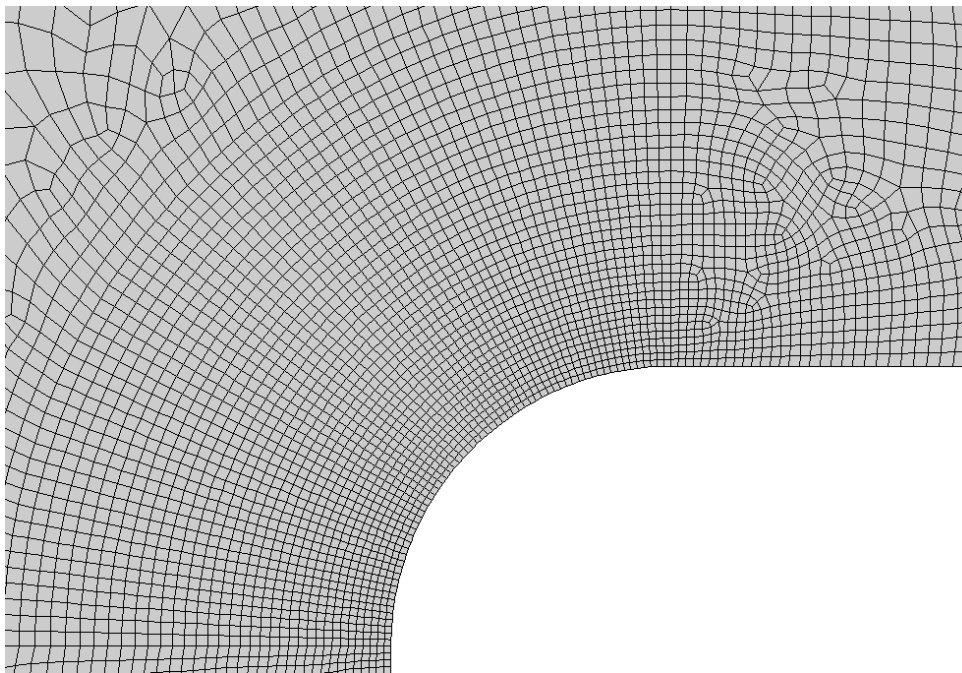
Fig. 6.10. Typical mesh used to model shafts with shoulder fillet of S65A.
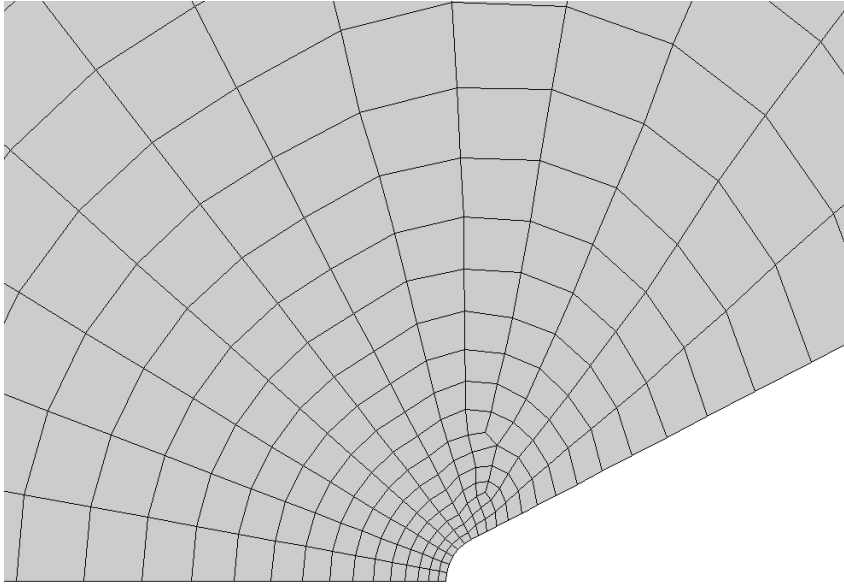
Fig. 6.11. Typical mesh used to model cylindrical bars with circumferential notch.

gradually refined until convergence occurred (see Chapter 5 and [27]). For these axisymmetric models the average mesh size in the highly stressed regions was equal to 0.015 mm, the minimum size being equal to about 0.001 mm (Fig. 6.13). As done for the Mode I loading specimens, also in this case the boundary conditions were taken as homogeneous essential to calculate the first step of the solution and homogeneous natural throughout to solve the second step of the numerical process. Finally, since the relevant stress states were calculated by solving linear gradient elasticity axisymmetric models, the total stress tensors at the hot-spots were determined for any considered multiaxial loading case by simply using the superposition principle.

As to the SSF specimens, the hot-spot was positioned, within the fillet, in a material region close to the junction between the fillet itself and the net section of the samples. This is in agreement with the cracking behaviour observed by Gough [65]. In fact, nearly all the SSF samples he tested were seen to fail by a crack initiating at the junction of the fillet with the central portion of the specimens or slightly removed from that region and within the fillet.

The diagrams reported in Fig. 6.12 show the through-thickness distribution of the gradient enriched stress components at the tip of the notch in the CNP specimens of SM41B [143, 144] loaded in cyclic tension-compression. The reported stress distributions (Figs. 6.12b and 6.12d) confirm that in three-dimensional bodies the gradient-enriched stress states at the tip of the notch (i.e. on the surface) are always multiaxial, even if the nominal loading being applied is uniaxial. This is a consequence of the fact that, as schematically shown in Fig. 4.1a, gradient elasticity acts as a numerical operator transferring the sub-surface stresses (which are, in the most general case, triaxial) onto the surface. In terms of fatigue assessment, this results in the fact that the hot-spots tend to move from the main surface toward the mid-section of the specimens (i.e. along axis z
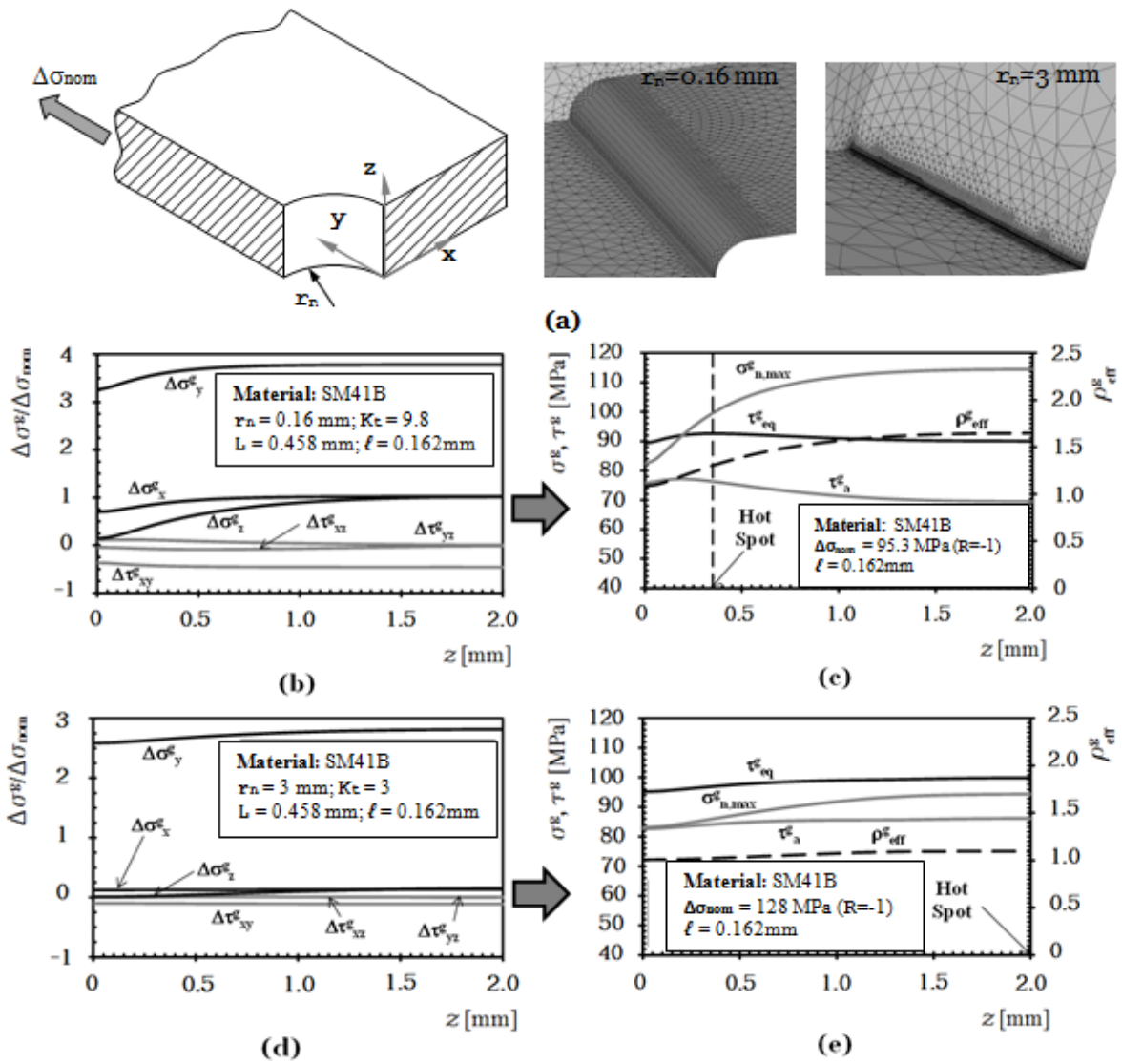
Fig. 6.12. Stress distributions along the notch edge in CNP specimens [143, 144] subject to cyclic axial loading.

in Fig. 6.12a). This is confirmed by the charts reported in Figs. 6.12c and 6.12e: for the specimens with $r_n = 0.16$ mm the hot-spot is at a distance from the main surface equal to 0.35 mm, whereas for the samples with $r_n = 3$ mm it is positioned at the mid-section of the notched plate. A similar situation was also observed in the DENP specimens.

The charts reported in Fig. 6.13 show the stress distributions along the notch bisector in CNB specimens loaded in bending, tension, and torsion. As to the stress analysis problem, it is interesting to observe here that, according to the way gradient elasticity manipulates the local stress fields, with $\ell > 0$ the gradient enriched stress state at the tip of a circumferential notch in a cylindrical bar loaded either in bending, in tension, or in torsion is always multiaxial. In other words, in the investigated axisymmetric notched specimens, the gradient-enriched stress fields acting on the material in the vicinity of the hot-spots were always multiaxial, this holding true independently from the degree of multiaxiality characterising the nominal load history.

Once the relevant gradient-enriched stress tensors at the hot-spots (Fig. 4.2b) were determined, the stress components relative to the critical plane (i.e. τ_a^g, $\sigma_{n,m}^g$ and $\sigma_{n,a}^g$) were calculated by using software Multi-FEAST (www.multi-feast.com). Multi-FEAST is a software designed to estimate fatigue damage under constant and variable amplitude uniaxial and multiaxial fatigue loading. Multi-FEAST is based on the Modified Wöhler Curve Method described in §2.2.5. In particular, provided the time histories of the stress components in the point of interest (respect to the global system of axes), Multi-FEAST considers several potential orientations of the critical plane (by varying the three Euler angles) and calculates for each of them the time history of the shear stress amplitude τ_a produced by the aforementioned stress components. The critical plane is then identified as the plane where the shear stress amplitude shows the maximum variance (Shear Stress Maximum Variance Method). Once the critical plane is determined, Multi-FEAST calculates the amplitude $\sigma_{n,a}$ and mean value $\sigma_{n,m}$ of the stress normal to the critical plane as well as the effective stress ratio ρ_{eff} and perform the assessment expressed by Eq. (2.51).

The error diagrams of Fig. 6.14 summarise the overall accuracy obtained by using gradient elasticity in conjunction with the MWCM to estimate the high-cycle fatigue strength, with the error being defined as follows:

$$E_\tau[\%] = \frac{\tau_{eq}^g - \tau_0^g}{\tau_0^g} \cdot 100 \qquad (6.4)$$

with τ_{eq}^g defined by Eq. (4.6).

According to Eq. (6.4), a positive value of this error index indicates a conservative estimate, whereas a negative value implies a non-conservative prediction.

Regarding the accuracy of the proposed approach (Fig. 4.2b), attention is initially focused on those experimental results generated by testing CNP and DENP specimens under nominal uniaxial fatigue loading. As mentioned earlier, for these specimens the relevant gradient enriched stress fields were determined by solving 3D FE models. As shown in Figs 6.12c and 6.12e for two samples of SM41B [143, 144], the fatigue damage extent in CNP and DENP specimens loaded in cyclic tension-compression was estimated
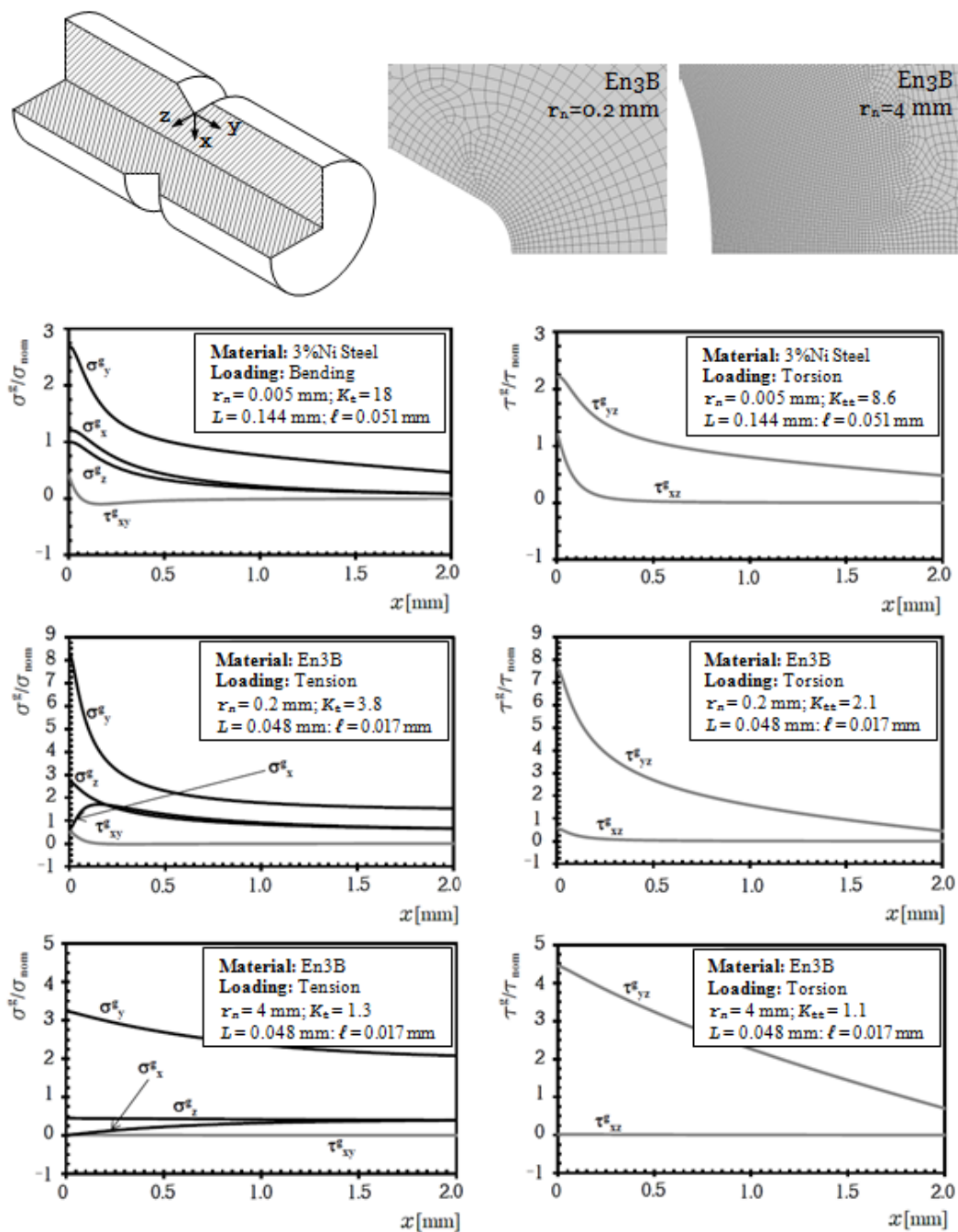
Fig. 6.13. Stress distributions along the notch edge in CNB specimens made of 3%Ni Steel [65] and En3B [134], loaded in bending, tension and torsion.

by considering that material point in the thickness experiencing the largest value of the equivalent shear stress amplitude, τ_{eq}^g, calculated according to Eq. (4.6). It is worth observing that, to calculate τ_{eq}^g, the gradient enriched plain torsional fatigue limits, τ_0^g, were estimated from the corresponding uniaxial ones according to von Mises hypothesis. The error diagram reported in Fig. 6.14a confirms that gradient elasticity applied along with the MWCM was successful in assessing the highcycle fatigue strength of CNP and DENP specimens, the estimates falling within an error interval of $\pm 20\%$.

Subsequently, attention was focused on the experimental results generated by testing notched cylindrical specimens under uniaxial fatigue loading (i.e. either bending or tension-compression). The error chart of Fig. 6.14b confirms that the use of the multiaxial formulation of the proposed approach resulted in estimates characterised by acceptable accuracy also when applied to axisymmetric problems. In particular, it is worth observing that accurate predictions were made not only under fully-reversed uniaxial loading (UA,ZMS), but also in the presence of superimposed static stresses (UA,N-ZMS).

For what concerns multiaxial load histories, the error chart of Fig. 6.14b confirms that the use of the proposed approach resulted in estimates mainly falling within an error interval of $\pm 20\%$, not only in the presence of out-of-phase loading, but also under non-zero mean stresses. The fact that a relatively small number of estimates fall outside the acceptable $\pm 20\%$ scatter band can be ascribed to two main factors:

- physiological scatter of experimental results: by testing several specimens of a given material, with same geometry and under the same loading conditions, significantly different values of the fatigue strength can be obtained;

- the TCD critical distance under torsion is seen to be larger than the corresponding value determined under uniaxial loading [131, 139]. However, in the proposed approach, also in the cases where torsional loading are involved (T,ZMS, T,N-ZMS, IPh,ZMS, IPh,N-ZMS, OoPh,ZMS and OoPh,N-ZMS) the material characteristic length ℓ is directly derived from the TCD critical distance, L, determined under uniaxial fatigue loading. This might lead is some instances to less accurate estimations.

Furthermore, it is worth observing that almost all the estimates with errors falling outside the acceptable $\pm 20\%$ scatter band are conservative. This aspect is usually well accepted by the industry.

As to the prediction reported in the charts of Fig. 6.14b, they were obtained by using σ_0^g and τ_0^g as reference fatigue strengths. However, according to Table 6.4, the difference between conventional and gradient-enriched fatigue limits was always lower than about 6% (with the average value approaching 1.5%). This makes it evident that using σ_0 and τ_0 would result in an overall accuracy similar to the one obtained by employing σ_0^g and τ_0^g. This further confirms that, in situations of practical interest, the proposed multiaxial fatigue design approach can safely be used by simply employing σ_0 and τ_0 as material reference strengths.
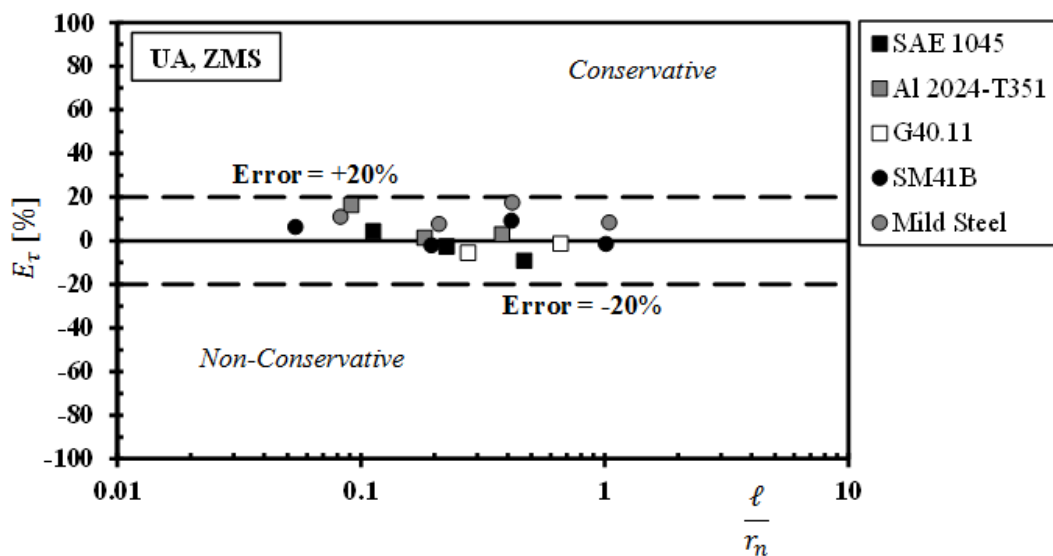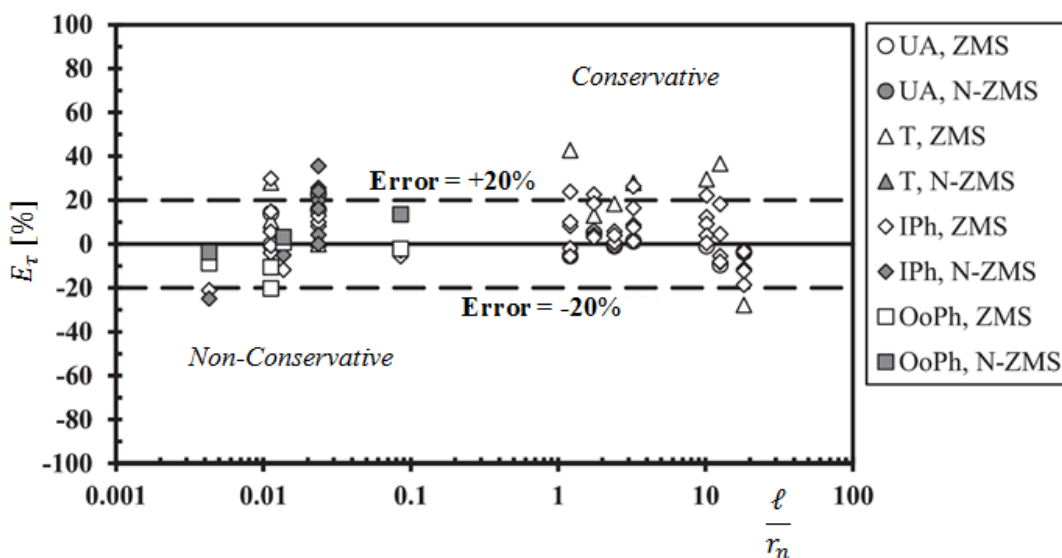
Fig. 6.14. Accuracy of gradient elasticity applied along with the MWCM (Fig. 4.2b) in estimating high-cycle fatigue strength of notched specimens subject to uniaxial/multiaxial fatigue loading (UA=uniaxial loading; T=torsional loading; IPh=In-Phase loading; OoPh=Out-of-Phase loading; ZMS=Zero Mean Stress; N-ZMS=Non-Zero Mean Stress).

6.2.3 Conclusions

In the present chapter, the gradient elasticity-based methodology developed in Chapter 5 has been used to estimate the static and high-cycle fatigue strength of different types of notched samples subject to various loading conditions; both brittle and metallic materials have been considered.

The encouraging results of the aforementioned validation exercise revealed that the proposed gradient-enriched methodology, combined with the TCD for the definition of the intrinsic length parameter ℓ, can potentially become a powerful tool for the static and high-cycle fatigue assessments of notched components. In fact, the ability of gradient elasticity to smooth the stress field in the neighbourhood of stress risers allows sufficiently accurate static and fatigue assessment of notched components by simply considering the relevant non-local stress at the hot-spot on the surface of the specimen. This significantly simplifies the assessment procedure, avoiding the need to define the failure location inside the body a priori.

In what concerns static problems, the definition of ℓ according to Eqs. (4.1) and (6.1) leads to further advantages, since ℓ can be estimated by knowing just two mechanical properties of the assessed material (namely K_{IC} and σ_{UTS}) that can be easily obtained from the manufacturers, with significant benefits in terms of time and costs.

Regarding fatigue problems, instead, it has been shown that, under Mode I cyclic loading, the gradient-enriched stress experienced at the hot-spot and perpendicular to the notch bisector can directly be used to estimate the extent of the high-cycle fatigue damage. Furthermore, gradient elasticity applied together with the MWCM resulted in estimations of the high-cycle fatigue strength of notched components characterised by acceptable levels of accuracy in both uniaxial and multiaxial fatigue loading conditions.

This brings significant simplifications with respect to many existing fatigue assessment approaches. In fact, the proposed methodology allows to perform the fatigue assessment of notched components by considering them as simple plain specimens, avoiding the non-trivial identification of the failure location into the assessed body a priori. Furthermore, these results have also the important implication that, as soon as the length scale ℓ is clearly identified, notched components can be assessed against fatigue by simply using the proposed gradient-enriched FE methodology without considering any linear elastic fracture mechanics (LEFM) concept. However, it has been shown that, in the absence of a clear identification of the length scale ℓ, Eq. (4.1), based on well-known LEFM concepts, represents a reliable and practical approximation of the length scale parameter.

These results, although encouraging, represent only the starting point and a more extensive research work would be extremely beneficial. In particular, a wider range of geometries and materials needs to be analysed (including metals, ceramics, polymers and concrete) as well as more loading conditions (both uniaxial and multiaxial).

Chapter 7

Estimation of the high-cycle fatigue strength of notched plain concrete

The continuous development of the civil engineering infrastructure sector makes concrete the most widely used structural material. In particular, as reported by the International Energy Agency (IEA) and the World Business Council for Sustainable Development (WBCSD) [77], 5% of the annual global CO_2 produced by human activities is due to the world cement production with an even worse future outlook, passing from a global concrete production of 2.55 billion tons in 2006 to an estimated global production ranging between 3.69 and 4.40 billion tons in 2050. Furthermore, in [77] is stated that the cement industry CO_2 emissions saw an increase of about 42% from 2000 to 2006 and, of course, this trend cannot continue indefinitely, on the contrary, it should be inverted. In 2008 G8 leaders asked the IEA to develop a series of roadmap with the aim of halving the global industrial CO_2 production by 2050. In particular, the cement roadmap [77] estimates that the cement industry could contribute to the aforementioned global reduction with an 18% abatement of its direct emissions, compared to the current levels, by 2050.

It is clear, then, that one of the most urgent issues to be addressed is the improvement of the in-service performance of concrete structures by simultaneously reducing the CO_2 emissions as well as the production, maintenance and energy costs. In this context, the static assessment of concrete structures has been investigated for decades by the international scientific community, and nowadays the design of concrete structures against static loading can be effectively performed by adopting relatively low safety factors. This results in slender structures, contributing to a significant reduction in the use of concrete and consequently of natural resources with positive consequences on the environmental impact, in particular from the carbon emissions point of view.

However, the aforementioned size reduction of concrete structural components makes concrete structures more vulnerable to fatigue, due to the inevitable increase of the magnitude of in-service local stresses. In a recent investigation [125], it has been shown that the effect of time-variable loading can no longer be ignored if the design, of both plain and short-fibre/particle reinforced concrete structures, is performed by using safety factors lower than 2.5. This is a crucial aspect since several key concrete structures such as, for instance, runways subject to repeated loads due to passing aircraft, asphalt concretes

subject to cyclic local pressures due to the action of tyres, bridges fatigued by travelling vehicles, and concrete foundations of wind turbines, are subject to in-service time-variable loading. Moreover, in 2012 fatigue has been recognised, by a British working group [10] operating under the auspices of both the Department of Energy and Climate Change and the Office for Nuclear Development, as one of the key structural issues to be assessed when designing concrete structures for the nuclear sector. In this scenario, the fatigue assessment of concrete infrastructures is complicated by stress/strain concentration phenomena produced by local stress risers characterising their structural parts.

Hence, from now on, structural engineers will have to deal with two main challenges:

- rationalise the usage of natural resources;

- minimise carbon emissions.

These two goals can be achieved by designing structural components, minimising the amount of material needed to reach an adequate level of safety. To achieve this, concrete structural parts/details characterised by complex shapes could be required, with the possible introduction of stress/strain risers, making the fatigue behaviour of notched concrete a research topic of central importance in the near future. Despite this, apart from three isolated investigations [101, 105, 154], the fatigue assessment of concrete notched components has not received the due consideration until now and, unfortunately, despite the wide availability of experimental studies and results (see [125] for an up-to-date summary of the data available in the literature), universally recognised design techniques have still to be defined.

In plain concrete the possible locations for crack initiation can typically be in the cement paste, inside the aggregates, or at the interface between matrix and aggregates [67, 162]. In case of fatigue loadings, the crack initiation has been seen to take place predominantly at the interface between the cement paste and the aggregates. Hence, fatigue cracks can be considered as the result of an increasing weakening of the bonds under local tensile/shear cyclic stresses and strains [97]. According to this fatigue damage model, the aggregates can be considered as hard inclusions leading to localised stress/strain concentration phenomena, suggesting that the overall fatigue strength of plain concrete is highly influenced by the material microstructural features. Thus, it is of primary importance to ensure that such microstructural features are properly taken into account, when continuum mechanics theories are used to predict the fatigue behaviour of concrete structures or components. In this chapter, the applicability and accuracy of the gradient elasticity-based methodology presented in Chapter 5 and of the Theory of Critical Distances in modelling the high-cycle fatigue behaviour of notched plain concrete, are investigated.

7.1   Preliminary definitions and assumptions

The fatigue strength of plain concrete depends on several variables which include surface roughness, extreme environmental conditions, temperature, type of loading, load history's degree of multiaxiality, water-to-cement ratio, ageing, and presence of shrinkage stresses.

Given the material and the environmental conditions, from a design point of view, the overall fatigue strength of a concrete structure is strongly affected also by the presence of non-zero mean stresses [125]. This implies that the stress quantities to be used to apply both the TCD and gradient elasticity must be defined so that the mean stress effect in concrete fatigue is taken into account effectively.

Consider the beam sketched in Fig. 7.1 which is hypothesised to be damaged either by a cyclic bending moment $M(t)$ (Fig. 7.1a) or by a cyclic axial force $P(t)$ (Fig. 7.1b), t being time. Point O is the location where a fatigue crack is expected to initiate, so that this material point is used also to define a convenient system of coordinates (see Figs. 7.1a and 7.1b). Time-variable force $P(t)$ and bending moment $M(t)$ result in a local stress at point O that varies cyclically as shown in the σ_y vs. t charts reported in Figs. 7.1c and d, respectively. As soon as the amplitude, σ_a, the mean value, σ_m, the maximum stress, $\sigma_{\max}$, and the minimum stress, $\sigma_{\min}$, characterising the loading cycle are known (see Figs. 7.1c and d), the corresponding load ratio, R, can directly be defined through Eq. (2.13).

Eq. (2.13) suggests that, as long as the maximum stress is positive (Fig. 7.1c), the load ratio takes on a value which is always lower than unity, a negative minimum stress resulting in a negative value for R. On the contrary, when the concrete component being assessed is subject to cyclic compression (Fig. 7.1d), R takes on a value which is always larger than unity, R diverging to infinity as $\sigma_{\max}$ approaches zero.

By re-analysing about 1500 experimental results taken from the literature and generated by testing both plain and short-fibre/particle reinforced concretes [125], it has been proven that the mean stress effect in concrete fatigue can efficiently be modelled by defining the design stress, σ_{Design}, as follows:

$$\sigma_{\text{Design}} = \sigma_{\max} \qquad \text{when} \qquad \sigma_{\max} > 0 \tag{7.1}$$

$$\sigma_{\text{Design}} = |\sigma_{\min}| \qquad \text{when} \qquad \sigma_{\max} \leq 0 \tag{7.2}$$

The fatigue strength of concrete can then be summarised in conventional log-log S-N diagrams, where the design stress, σ_{Design}, is plotted against the number of cycles to failure, N_f (Fig. 7.1e). According to this schematisation, fatigue results can directly be post-processed through appropriate statistical tools [116, 123] to determine the corresponding fatigue curve for the targeted probability of survival, P_S. Irrespective of the adopted value for P_S, as already explained in Chapter 2, fatigue curves can be mathematically described as follows:

$$\sigma_{\text{Design}}^k \cdot N_f = \sigma_A^k \cdot N_A \tag{7.3}$$

where k is the negative inverse slope and σ_A is the design endurance limit, i.e. a reference strength extrapolated at a reference number of cycles to failure, N_A (see Fig. 7.1e).

The level of scattering associated with the investigated data set can concisely be quantified by using the following ratio [123]:
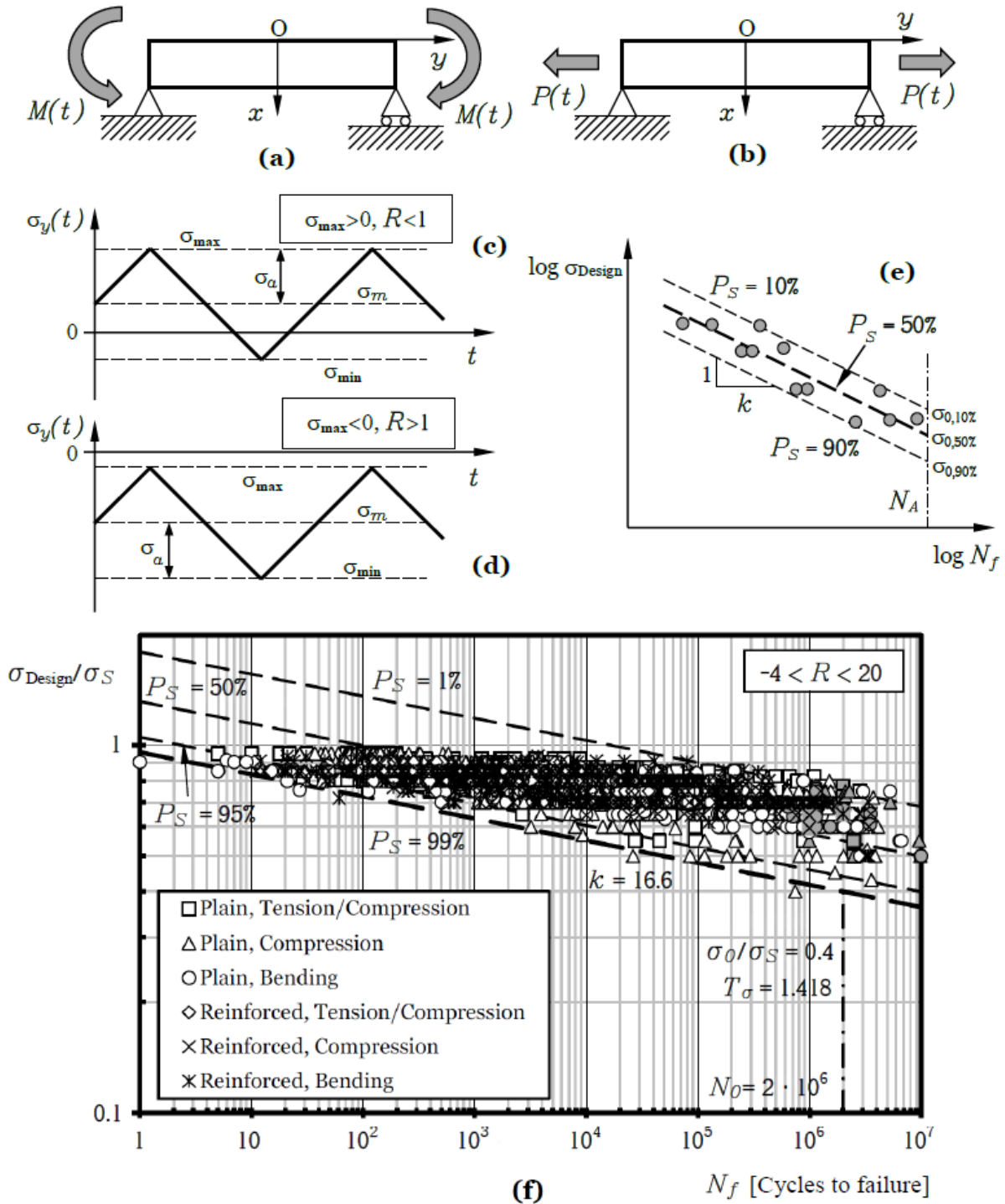
Fig. 7.1. Concrete beam loaded in cyclic bending (a) and subject to cyclic axial loading (b); load histories characterised by different values of the load ratio (c and d); Wöhler diagram and fatigue curves for different values of P_S (e); unifying Wöhler diagram to perform the fatigue assessment of un-notched plain and short fibre/particle reinforced concretes (grey markers = run outs) [125] (f).

$$T_\sigma = \frac{\sigma_{0,10\%}}{\sigma_{0,90\%}} \tag{7.4}$$

where $\sigma_{0,10\%}$ and $\sigma_{0,90\%}$ are the endurance limits determined, at N_A cycles to failure, for 10% and 90% probabilities of survival, respectively. According to Eqs. (7.1) and (7.2), design endurance limits, σ_A, are then suggested to be defined as [125]:

$$\sigma_A = \sigma_{\mathrm{MAX}} \qquad \text{when} \qquad \sigma_{\max} > 0 \tag{7.5}$$

$$\sigma_A = |\sigma_{\mathrm{MIN}}| \qquad \text{when} \qquad \sigma_{\max} \leq 0 \tag{7.6}$$

In the above definitions σ_{MAX} and $|\sigma_{\mathrm{MIN}}|$ are determined at N_A cycles to failure (note that σ_{MAX} and σ_{MIN} are different from $\sigma_{\max}$ and $\sigma_{\min}$ previously defined).

As demonstrated in the fatigue diagram reported in Fig. 7.1f, the assumptions discussed above allow a unifying scatter band suitable for designing un-notched concretes against fatigue to be determined. In more detail, this scatter band was determined by post-processing about 1500 experimental data taken from the literature and generated by testing both plain and short-fibre/particle reinforced concretes cyclically loaded either in tension, in tension-compression, in compression, or in bending [125]. Such a high level of unification was reached by normalising the design stress, σ_{Design}, via the pertinent reference static strength, σ_{S}, defined as follows:

- under cyclic tension-tension/compression $\Rightarrow \sigma_{\mathrm{S}} = f_T$

- under cyclic compression $\Rightarrow \sigma_{\mathrm{S}} = f_C$

- under cyclic bending $\Rightarrow \sigma_{\mathrm{S}} = f_B$

In the above definitions f_T, f_C, and f_B are the material static strengths determined under tension, compression, and bending, respectively. The fatigue curve reported in Fig. 7.1f was determined under the hypothesis of a log-normal distribution of the number of cycles to failure for each stress level by assuming a confidence level equal to 95% [116].

It is worth observing here that, according to the available design codes [9, 75], the reference fatigue curves recommended to perform the fatigue assessment of welded joints are characterised by a T_σ value equal to 1.5 [72]. As shown in Fig. 7.1f, the T_σ value associated with the reported unifying scatter band is equal to 1.418, which confirms the validity of the formed hypotheses. Therefore, according to Fig. 7.1f, the fatigue lifetime of un-notched plain and short-fibre/particle reinforced concrete can directly be estimated by using solely the pertinent material static strength, σ_{S}, as calibration information independently from the actual value of the mean stress characterising the load history being assessed.

Since the schematisation summarised in the present section has proven to be capable of accurately taking into account the mean stress effect in concrete fatigue, the same strategy

— i.e., Eqs. (7.5) and (7.6) — will be used in what follows not only to reformulate both the TCD and gradient elasticity to make them suitable for modelling the highcycle fatigue behaviour of notched plain concretes, but also to post-process the generated experimental results.

7.2   Experimental details

The accuracy of both the TCD and gradient elasticity in estimating high-cycle fatigue strength of notched plain concrete has been investigated by testing, under cyclic four-point bending, prismatic beams containing notches characterised by three different sharpness levels, as shown in Fig. 7.2. In particular, the investigated beams were 500 mm long with 100 mm × 100 mm cross sections, while the notch depth was equal to 50 mm. The investigated notches had root radius equal to 25 mm (Fig. 7.2b), 12.5 mm (Fig. 7.2c), and 1.4 mm (Fig. 7.2d), corresponding to a net stress concentration factor, K_t, of 1.47, 1.84, and 4.32, respectively. The un-notched specimens, as shown in Fig. 7.2a, were designed so that, during the tests the portion of material subject to cyclic uniform bending moment had the same net width (i.e., 50 mm) as the notched specimens, in order to avoid any size effects, independently from the geometry of the investigated specimens.

The samples were manufactured by using a concrete mix designed [153] using PFA Portland Cement with strength class equal to 32.5N/mm^2, natural round gravel with 10 mm grading, and grade M concrete sand (cement content = 450 kg/m^3; fine aggregate content = 825 kg/m^3; coarse aggregate content = 825 kg/m^3). Two batches of specimens, characterised by two different water-to-cement (w/c) ratios, were cast in order to investigate specimens having the same material morphology but different strengths. In particular, Batch A was produced by choosing a w/c ratio equal to 0.5, while in Batch B the w/c ratio was equal to 0.4. According to the ASTM recommendations [22], all the samples were removed from the moulds 24 h after casting and subsequently cured in a moist room at 23°C for 28 days. Whereas the sharp notches (root radius equal to 1.4 mm) were created by using a circular saw with thickness equal to 2.8 mm, all the other notched specimens, as well as the un-notched samples, were produced by casting the required geometrical features directly into the bulk material by using specific moulds having plastic inserts attached to their bottom.

Fig. 7.3 shows two examples of the macroscopic morphology of the concrete used to manufacture the two batches of samples, the average inter-aggregate distance being equal to about 4 mm.

The static properties were determined under three-point bending as the average of five different tests for each batch, resulting in a flexural strength $f_B = 4.9$ MPa for Batch A and $f_B = 6.5$ MPa for Batch B.

The fatigue results were generated by using a bespoke electric testing table which was modified and developed for this specific experimental investigation (Fig. 7.2e). Two independent loading cells were used to gather and record the load histories applied during the tests and the deflection at the mid-section of the samples was measured via a Linear Variable Displacement Transducer (LVDT). The force-controlled experiments were run
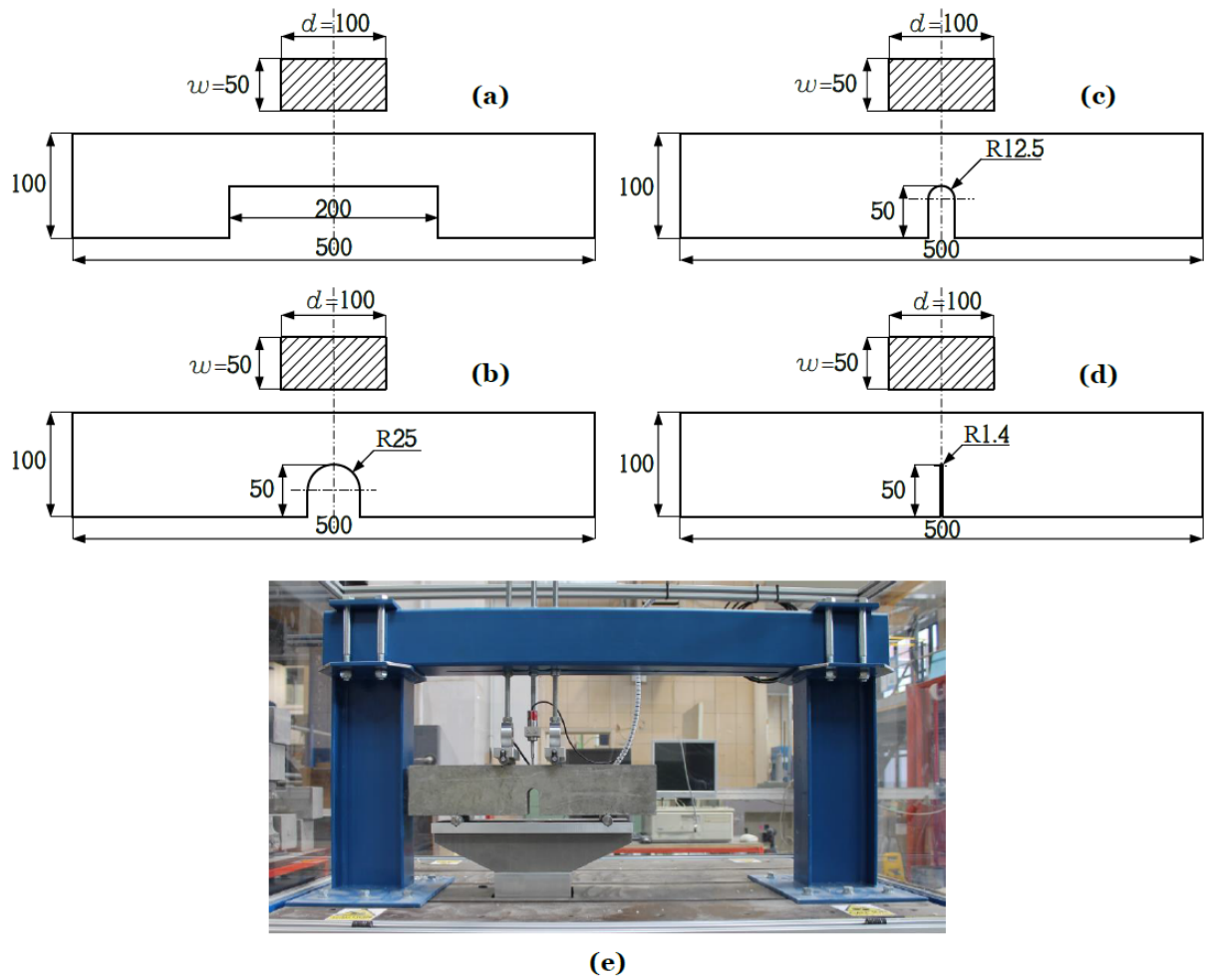
Fig. 7.2. Geometry of the investigated specimens (dimensions in millimetres) and fatigue testing apparatus.
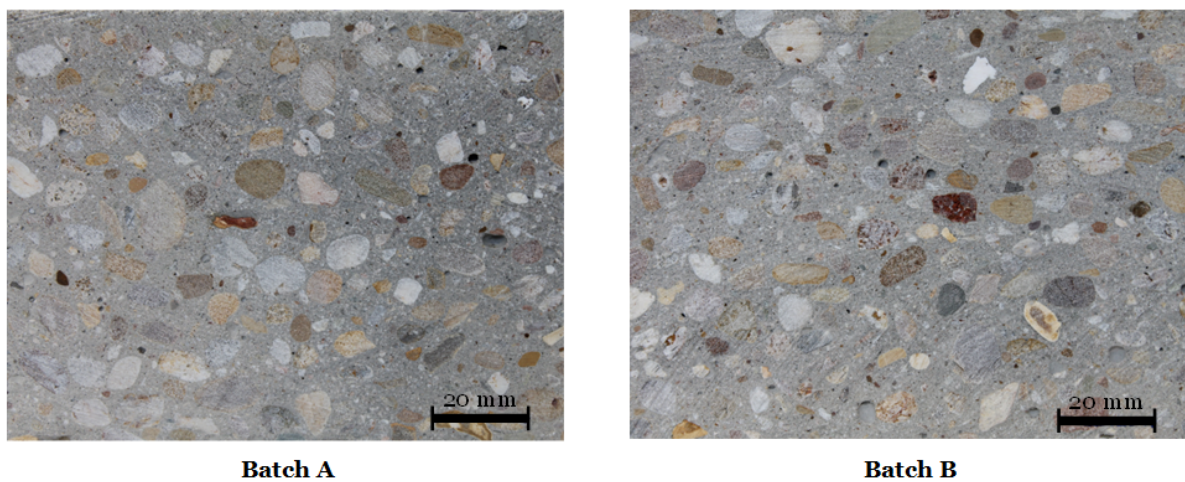
Fig. 7.3. Macroscopic morphology of the tested concrete.

Table 7.1. Batch A: summary of the geometrical dimensions of the tested specimens and corresponding fatigue results.

Code	d [mm]	w [mm]	r_n [mm]	σ_{max} [MPa]	R	N_f [Cycles]	Run out
P-A-1	101.6	53.1	—	3.4	0.16	132300	
P-A-2	101.6	52.9	—	3.2	0.11	2000000	•
P-A-3	99.6	53.4	—	3.4	0.09	175600	
P-A-4	99.6	53.2	—	3.2	0.06	2000000	•
B-A-1	101.0	50.5	25	3.7	0.05	500	
B-A-2	101.3	49.6	25	3.5	0.05	3800	
B-A-3	100.0	50.0	25	3.3	0.06	2000000	•
B-A-4	101.4	51.0	25	3.5	0.10	1890800	
B-A-5	100.8	49.4	25	3.3	0.08	36600	
B-A-6	101.4	51.0	25	3.1	0.08	2000000	•
B-A-7	100.0	50.0	25	3.3	0.05	2000000	•
I-A-1	100.4	49.3	12.5	3.5	0.06	147100	
I-A-2	100.0	50.0	12.5	3.3	0.06	551000	
I-A-3	100.0	50.2	12.5	3.2	0.10	312900	
I-A-4	100.4	52.8	12.5	2.9	0.07	2000000	•
I-A-5	100.4	49.3	12.5	3.2	0.12	2000000	•
S-A-1	101.7	50.4	1.4	3.4	0.12	855200	
S-A-2	101.7	49.7	1.4	3.2	0.06	2000000	•
S-A-3	100.3	46.1	1.4	3.4	0.14	22200	
S-A-4	100.6	49.8	1.4	3.1	0.07	523600	
S-A-5	101.7	50.4	1.4	2.9	0.15	2000000	•

at room temperature at a frequency of 10 Hz, adopting as failure criterion the complete breakage of the specimens and the run out tests were stopped at $2 \cdot 10^6$ cycles.

Tables 7.1 and 7.2 summarise the results obtained by testing under cyclic bending the specimens belonging to Batch A and Batch B, respectively. These tables report the code of the specimens, the measured depth, d, and width, w, of the net cross sectional area (see Fig. 7.2), the notch root radius, r_n, the maximum nominal net stress in the cycle during testing, σ_{max}, the applied load ratio, R, and the experimental number of cycles to failure, N_f.

Examining carefully the fracture surfaces of the investigated specimens, as those shown in Fig. 7.4, it was possible to notice that the fatigue cracks initiated mainly at the interfaces between cementitious matrix and aggregates, with the subsequent propagation taking place in the cement paste. The complete failure of the samples was reached through a fast fracture process, preceded by the formation of relatively short fatigue cracks. According to the observed cracking behaviour, it is possible to state that, in the highly stressed region, the cement paste represents the weakest link in the fatigue strength of the microstructural chain, with the interfaces between matrix and aggregate playing the

Table 7.2. Batch B: summary of the geometrical dimensions of the tested specimens and corresponding fatigue results.

Code	d [mm]	w [mm]	r_n [mm]	$\sigma_{\max}$ [MPa]	R	N_f [Cycles]	Run out
P-B-1	101.4	49.0	—	5.0	0.31	2000000	●
P-B-2	101.6	49.3	—	5.4	0.37	700	
P-B-3	100.7	48.7	—	5.1	0.31	2000000	●
P-B-4	99.2	48.5	—	5.4	0.34	71500	
P-B-5	101.0	49.0	—	5.0	0.32	468900	
B-B-1	101.1	50.8	25	5.0	0.44	2600	
B-B-2	101.2	51.0	25	4.8	0.40	180200	
B-B-3	100.9	51.5	25	4.6	0.36	2000000	●
B-B-4	101.4	51.7	25	4.8	0.37	226300	
B-B-5	101.0	51.8	25	4.6	0.38	2000000	●
I-B-1	100.3	53.3	12.5	4.7	0.37	2000000	●
I-B-2	101.8	51.6	12.5	4.9	0.37	1070200	
I-B-3	100.8	52.3	12.5	4.7	0.36	225600	
I-B-4	101.0	47.0	12.5	4.5	0.32	2000000	●
I-B-5	100.2	51.0	12.5	4.7	0.32	159700	
I-B-6	101.0	48.8	12.5	4.5	0.33	3100	
S-B-1	101.0	51.2	1.4	4.5	0.37	2000000	●
S-B-2	101.0	49.2	1.4	4.7	0.34	1935400	
S-B-3	101.7	49.8	1.4	4.5	0.33	2000000	●
S-B-4	100.7	49.9	1.4	4.7	0.36	75200	
S-B-5	101.1	49.8	1.4	4.5	0.32	2000000	●
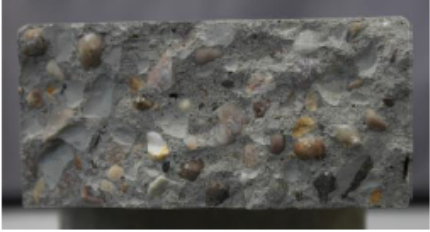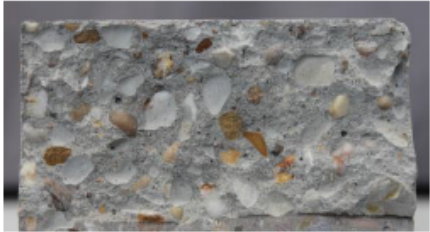
	Batch A	Batch B
$K_t=1$	Crack initiation surface P-A-3, σ_{max}=3.4 MPa, R=0.09	Crack initiation surface P-B-4, σ_{max}=5.4 MPa, R=0.34
$K_t=1.47$	Notch Tip B-A-5, σ_{max}=3.3 MPa, R=0.08	Notch Tip B-B-4, σ_{max}=4.8 MPa, R=0.37
$K_t=1.84$	Notch Tip I-A-1, σ_{max}=3.5 MPa, R=0.06	Notch Tip I-B-5, σ_{max}=4.7 MPa, R=0.32
$K_t=4.32$	Notch Tip S-A-1, σ_{max}=3.4 MPa, R=0.12	Notch Tip S-B-2, σ_{max}=4.7 MPa, R=0.34

Fig. 7.4. Macroscopic cracking behaviour under fatigue loading displayed by the tested concrete.

Table 7.3. Endurance limits determined through Dixon's procedure at $N_A = 2 \cdot 10^6$ cycles to failure.

Batch	f_b [MPa]	N. of tests	r_n [mm]	K_t	R_m	δ	K	σ_{MAX} [MPa]
A	4.9	4	—	1.00	0.11	0.20	0.500	3.3
		7	25	1.47	0.07	0.20	0.169	3.3
		5	12.5	1.84	0.09	0.23	−0.026	3.2
		5	1.4	4.36	0.11	0.22	0.878	3.1
B	6.5	5	—	1.00	0.33	0.36	0.084	5.1
		5	25	1.47	0.40	0.25	0.439	4.7
		6	12.5	1.84	0.35	0.20	0.296	4.6
		5	1.4	4.36	0.34	0.20	0.701	4.6

role of preferential crack initiation locations.

The endurance limits were determined by assuming $N_A = 2 \cdot 10^6$ as reference number of cycles to failure, according to the strategy adopted in [125] to investigate the fatigue behaviour of un-notched plain and short fibre/particle reinforced concrete. The experimental data summarised in Tables 7.1 and 7.2, used to determine the required endurance limits, were generated according to Dixons up-and-down procedure [43]. In particular this method consists in assuming an initial tentative endurance limit, running the first fatigue test at a stress level higher than the estimated value. If the specimen fails at reference number of cycles to failure lower than N_A, the following test has to be run at a lower stress level. Otherwise, if the specimen survives to a number of cycles equal to N_A, then the following test has to be run at a higher stress level. By so doing, the stress level characterising each test depends on the previous experimental results, such a procedure being applied iteratively by increasing or decreasing the magnitude of the applied cyclic loading. For each data set, the endurance limit for a probability of survival $\mathrm{P_S} = 50\%$ was estimated from the tests according to the following formula:

$$\sigma_{\mathrm{MAX}} = \sigma_{LT} + K \cdot \delta \tag{7.7}$$

where σ_{MAX} is the maximum nominal net stress in the fatigue cycle at the endurance limit, δ is the interval between two adjacent stress levels and σ_{LT} is the stress at the last test run for any material/geometry configuration, while K is a constant which can directly be extracted from the table supplied by Dixon himself in [43] and compiled by performing a rigorous statistical analysis. The results obtained by post-processing the experimental tests (listed in Tables 7.1 and 7.2) thorough Dixon's procedure are graphically presented in the diagrams of Fig. 7.5, as well as concisely summarised in Table 7.3. In both Fig. 7.5 and Table 7.3, R_m is the average value of the nominal load ratio, R, for each data set.
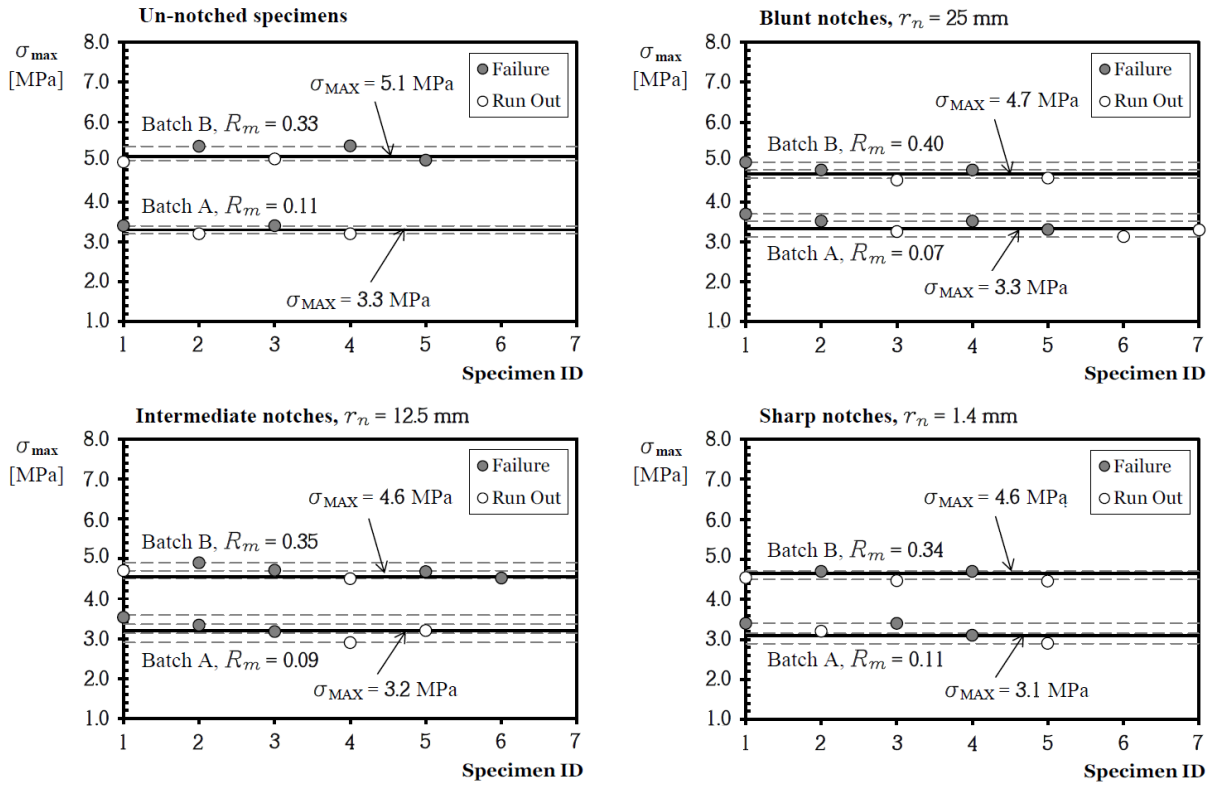
Fig. 7.5. Endurance limits determined according to the up-and-down method.

7.3   Validation through experimental data

To investigate the importance of microstructural length scale parameters in describing the high-cycle fatigue behaviour of notched plain concrete, the accuracy and reliability of both gradient elasticity and the TCD have been checked against the experimental results obtained from the tests described in the previous paragraph.

As already explained in Chapter 2, the different formalisations of the TCD are all characterised by a common feature consisting in the fact that the extent of damage is determined through an effective stress depending not only on the magnitude of the local linear elastic stress fields, but also on a material length scale parameter L, whose value is not affected by the profile of the stress concentrator being assessed [123, 148]. Furthermore, depending on both the morphological features of the assessed material and the nature of the crack nucleation and propagation mechanisms, several experimental evidence demonstrates that length L can be associated to either the material micro-, meso- or macroscopic features [123, 148]. Similarly, gradient elasticity length scale parameter ℓ is representative of the underlying microstructure of the considered material, in particular its value has been shown to be directly related to the size of the dominant source of microstructural heterogeneity [59]. Therefore, under high-cycle fatigue loading, both L and ℓ can range from a few microns [21, 158] up to several millimetres [17, 123].

Coming back to the investigated concrete mixes, since from §7.2 it emerges quite clearly

the fact that, at a mesoscopic level, the cement paste represents the weakest feature in the investigated concrete mixes, it is reasonable to expect that L and ℓ are of the order of the average inter-aggregate distance. This means that both the TCD and gradient elasticity will be used to model the high-cycle fatigue behaviour of notched concrete by employing length scale parameters determined at a mesoscopic level. This aspect is very important since the investigated mixes had different water to cement ratios, this resulting in cement pastes characterised by different microstructural features.

As far as ductile materials are concerned, both the TCD and gradient elasticity are seen to be capable of accommodating any material non-linearities into a linear-elastic constitutive law [17, 21, 123, 127, 148]. In particular, via length L, the magnitude of the effective stress used by the TCD to evaluate the extent of damage is lower than the value of the linear-elastic stress in the neighbourhood of the tip of the geometrical feature being assessed (see Figs. 2.25b and c). Similarly, giving the boundary conditions, the use of gradient elasticity produces, in the vicinity of the stress concentrator being assessed, gradient-enriched stress values lower than the correspondent stress values determined according to classical elasticity. This allows the TCD and gradient elasticity, in case of ductile materials, to simulate the smoothing effect of plasticity on the local stress fields without renouncing to the advantages of linear stress/strain analyses. Furthermore, since in notched/cracked ductile materials in the endurance limit condition the magnitude of the cyclic nominal loading is relatively small, the amount of material experiencing large scale plastic deformations is usually very limited [148], allowing local plasticity to be neglected with little loss of accuracy [123]. This explains why both the linear-elastic TCD and gradient elasticity show high accuracy in predicting the high-cycle fatigue strength of cracked [17, 21, 127, 146], notched [17, 122, 127, 130, 132, 146] and welded ductile metals [86, 87, 124, 126, 134, 149, 157].

Concrete, unfortunately, is a completely different and much more complex material, showing a quasi-brittle mechanical behaviour with various types of non-linearities, mainly influenced by the microstructural features of the mix. However, due to their accuracy in modelling the high-cycle fatigue behaviour of ductile materials, both the TCD and gradient elasticity are expected to be able to fit the aforementioned local non-linearities into a simple linear-elastic framework. As a consequence, in the following of this chapter TCD and gradient elasticity will be applied under the assumption that the stress-stain relation of the analysed concrete mixes can adequately be described, at a mesoscopic scale, through a simple linear-elastic constitutive law.

It is worth observing here also that the use of the TCD and gradient elasticity to model the high-cycle fatigue behaviour of notched concrete is based on the assumption that L and ℓ are independent parameters whose value is related solely to the material morphology. According to this assumption, the required length scale parameters can be defined without addressing the fracture energy problem a priori.

Much experimental evidence suggests that the frequency of the applied loading has a quite limited effect up to about 20 Hz [106]. Accordingly, it is possible to presume that lengths L and ℓ as well are not influenced by the frequency of the applied loading as long as the frequency itself does not affect the overall fatigue strength of the concrete being

investigated. On the contrary, owing to the viscous behaviour characterising the mechanical behaviour of concrete, frequency is expected to become more and more important as the rate of the cyclic loading increases, this possibly affecting not only the strength of the investigated concrete, but also the related length scale parameters [84]. As mentioned in §7.2, the experimental results used to assess the accuracy of both the TCD and gradient elasticity were generated at a frequency of 10 Hz. Therefore, owing to the fact that the applied frequency was lower than 20 Hz [106], the hypothesis was formed that its effect could be neglected with little loss of accuracy. However, in light of the complexity of this problem, it is evident that more theoretical and experimental work needs to be done in this area in order to accurately study the frequency effect in concrete fatigue, this being out of the scope of the present study.

7.3.1   Finite Element analyses

In order to apply the TCD, the continuum mechanics linear elastic stress fields ahead of the investigated notches were determined by using commercial FE software ANSYS®. The tested concrete was modelled as a homogeneous and isotropic material. The notched beams were meshed using 2D element Plane 183, an 8-node element with quadratic displacement behaviour. The required linear elastic stress-distance curves were obtained by gradually increasing the mesh density in the notch tip regions until convergence occurred (meaning that the stresses at the notch tip obtained from two consecutive mesh refinements are equal at the second decimal digit).

The gradient elasticity FE models were solved by using the finite element framework developed in Chapter 5. Both the un-notched and notched specimens were modelled by using quadrilateral four-noded bilinear elements. Also in this case, the mesh density in the regions of interest was gradually refined until convergence occurred (see Fig. 7.6). Finally, the numerical solutions were calculated by taking the boundary conditions as homogeneous essential for the first step of the Ru-Aifantis theory (Eq.(5.7)) and homogeneous natural throughout for the second step (Eq. (5.12)).

7.3.2   Theory of Critical Distances

Since the maximum stress in the cycle allows the mean stress effect in concrete fatigue to be modelled effectively, the Point Method (PM), Line Method (LM), and Area Method (AM) were reformulated as follows:

$$\sigma_{\text{eff,max}} = \sigma_{y,\text{max}} \left(\theta = 0°, \ r = \frac{L}{2} \right) \tag{7.8}$$

$$\sigma_{\text{eff,max}} = \frac{1}{2L} \int_0^{2L} \sigma_{y,\text{max}} \left(\theta = 0°, \ r \right) dr \tag{7.9}$$

$$\sigma_{\text{eff,max}} = \frac{4}{\pi L^2} \int_0^{\pi/2} \int_0^L \sigma_{1,\text{max}} \left(\theta, \ r \right) r \ dr \ d\theta \tag{7.10}$$
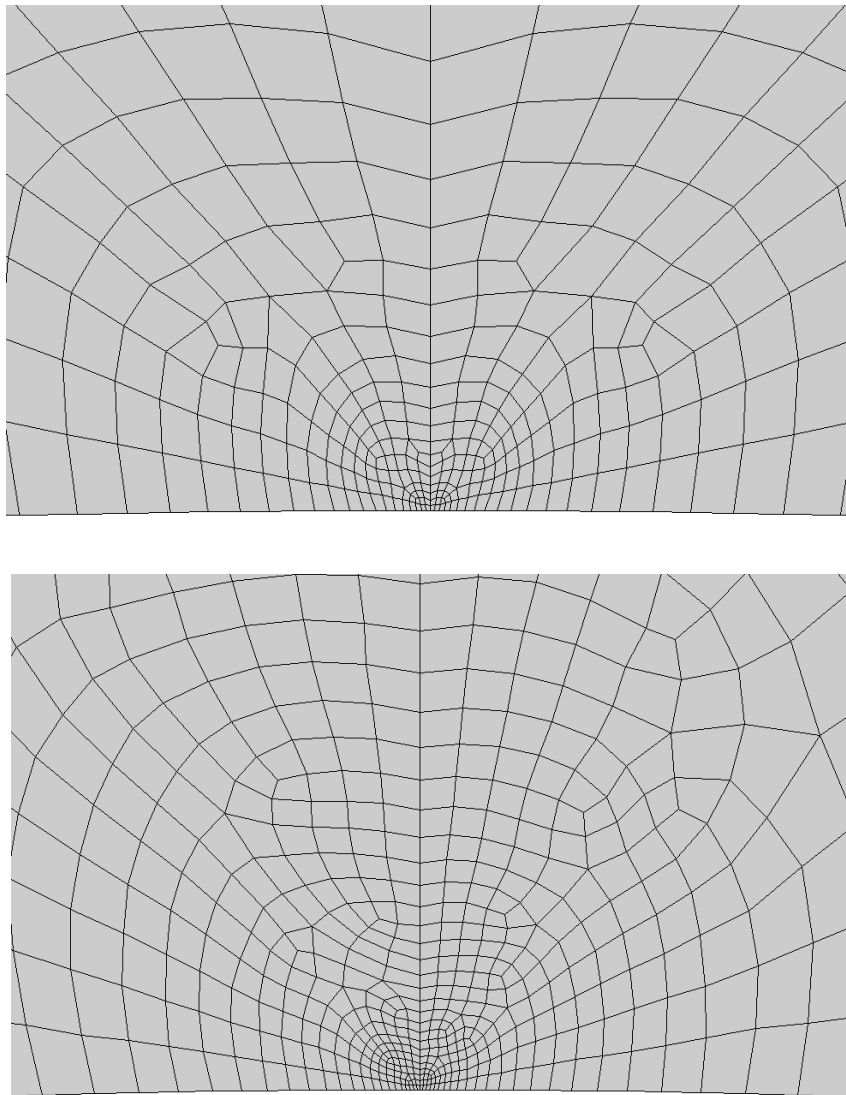
Fig. 7.6. Typical meshes used to model the area around the notch tip of the analysed concrete beams.

In the above definitions, $\sigma_{\text{eff,max}}$ is the maximum value of the effective stress, whereas $\sigma_{y,\text{max}}$ and $\sigma_{1,\text{max}}$ are the maximum values of local stress components σ_y and σ_1, respectively.

Given Eqs. (7.8), (7.9) and (7.10), according to the TCD philosophy [123, 148] a notched concrete component is within the endurance limit condition as long as the maximum effective stress, $\sigma_{\text{eff,max}}$, is lower than (or, at least, equal to) the maximum endurance limit of the un-notched material, $\sigma_{0,\text{MAX}}$.

In order to apply the TCD to estimate the notch endurance limits summarised in Table 7.3, the critical distance value, L, for the investigated concrete was determined by following the procedure schematically summarised in Fig. 2.26, the stress quantities of interest being obviously expressed in terms of maximum values. As shown in the charts of Fig. 7.7, the use of $\sigma_{0,\text{MAX}}$ and the linear-elastic stress-distance curve determined, in the endurance limit condition, from the sharply notched specimens led to a critical distance value, L, for Batch A and Batch B of 5.8 mm. Since the material mesoscopic morphology was the same for both batches (see Fig. 7.3), this result strongly supports the idea that length scale parameter L depends solely on those morphological features affecting the overall strength of the material being assessed. In particular, as mentioned earlier, in the investigated concrete the initiation process was seen to take place mainly at the interfaces between matrix and aggregates, the subsequent propagation occurring in the cement paste. Accordingly, the value for critical distance L estimated via the simplified procedure summarised in Fig. 2.26 resulted in a length approaching the average inter-aggregate distance of 4 mm.

Turning to the accuracy of the different formalisation of the TCD, the stress-distance curves plotted, at the endurance limit, in the charts of Fig. 7.7 prove that the PM was accurate in estimating the high-cycle fatigue strength of the beams containing blunt ($K_t = 1.47$), intermediate ($K_t = 1.84$) and sharp ($K_t = 4.32$) notches (i.e. the values of the linear elastic stress at a distance $L/2$ from the notch tip are close to the un-notched material endurance limit, $\sigma_{0,\text{MAX}}$). The error bands reported in Fig. 7.7 were determined by defining the error as follows:

$$\text{Error} = \frac{\sigma_{\text{eff,max}} - \sigma_{0,\text{MAX}}}{\sigma_{0,\text{MAX}}} \, [\%] \tag{7.11}$$

According to the above definition, an error larger than zero denotes a conservative prediction, whereas a negative error indicates a non-conservative estimate.

Table 7.4 confirms that the TCD used in the form of the PM and AM was capable of estimates falling within an error interval of about $\pm 10\%$ independently of the sharpness of the assessed notch. On the contrary, the predictions made using the LM were seen to fall on the non-conservative side, within an error interval of about $\pm 20\%$.

To conclude, the obtained level of accuracy is certainly encouraging since, as far as notches are concerned, it is not possible to distinguish between an error of $\pm 20\%$ and an error of 0% as a consequence of those problems that are usually encountered when performing the testing as well as the numerical analyses [151].
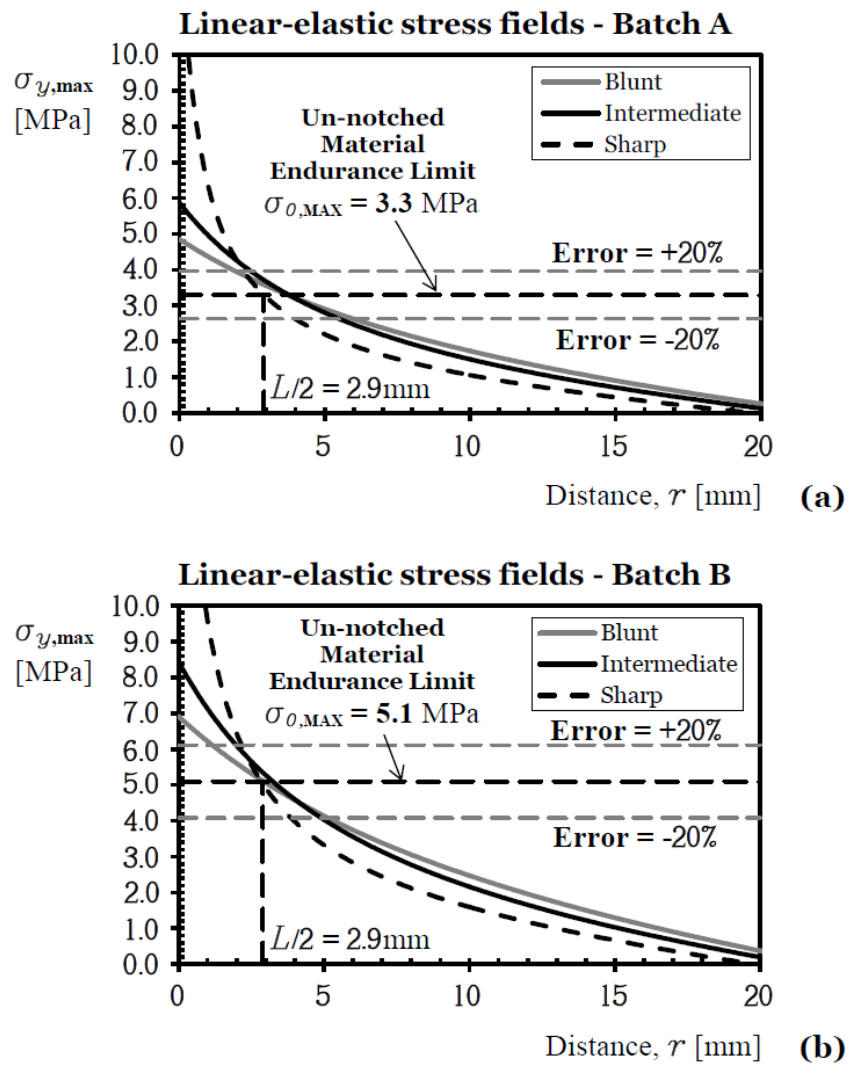
Fig. 7.7. Local linear-elastic stress fields in the endurance limit condition and accuracy of the PM in estimating the high-cycle fatigue strength of the tested notched concrete.

Table 7.4. Overall accuracy in the estimation of the high-cycle fatigue strength of the tested specimens through the TCD and gradient elasticity (GE).

Batch	K_t	Error [%]				
		PM	LM	AM	GE ($\ell = 2.05$ mm)	GE ($\ell = 4$ mm)
A	1.47	8.8	-14.1	12.6	18.5	15.4
	1.84	12.7	-13.9	16.6	27.6	15.7
	4.32	0.0	-15.3	10.8	29.4	-3.6
B	1.47	0.4	-20.8	3.7	9.2	7.0
	1.84	4.9	-19.9	8.5	18.8	8.4
	4.32	0.0	-18.7	6.3	24.3	-7.0

7.3.3 Gradient elasticity applied according to the Theory of Critical Distances

In two recent investigations [20, 127], it has been proven that gradient-enriched crack tip stresses are capable of accurately modelling, at the threshold condition, the transition from the long- to the short-crack regime, both under high-cycle fatigue [127] and static loading [20]. Due to the high level of accuracy that was obtained by following such a strategy, also in the present investigation the hypothesis is formed that the high-cycle fatigue strength of notched plain concrete can directly be estimated through the linear-elastic gradient-enriched stress state determined at the notch tip. Furthermore, as discussed in §7.1, gradient elasticity has to be applied in terms of maximum values of the stresses in the fatigue cycle in order to efficiently take into account the mean stress effect in concrete fatigue. According to the above considerations, the maximum value of the gradient-enriched effective stress is as follows:

$$\sigma^g_{\text{eff,max}} = \sigma^g_{y,\text{max}} \, (\theta = 0°, \ r = 0) \tag{7.12}$$

where in this case, $\sigma^g_{y,\text{max}}$ denotes the gradient-enriched stress perpendicular to the x-axis (see Fig. 2.25a for the definition of the local frame of reference). Therefore, similarly to the TCD, the assumption can be made that the notched concrete being designed is at its endurance limit (i.e., in the threshold condition) when $\sigma^g_{\text{eff,max}}$ equals the maximum endurance limit of the un-notched material, $\sigma_{0,MAX}$.

The second information which is needed to calculate the effective stress via Eq. (7.12) is the microstructural length scale parameter ℓ. As previously mentioned in Chapter 4, it was proven in [127] that ℓ can directly be estimated from the TCD critical distance value, L, through Eq. (4.1).

Therefore, gradient elasticity was applied in accordance with the TCD to estimate the notch endurance limits of the tested concrete by taking the length scale parameter, ℓ, equal to 2.05 mm, L being equal to 5.8 mm. The diagrams reported in Fig. 7.8 show the gradient-enriched stress fields determined, at the endurance limit, for $\ell = 2.05$ mm,

the error being calculated via Eq. (7.11). These diagrams together with Table 7.4 make it evident that the use of gradient elasticity applied according to the TCD resulted in conservative estimates, the level of conservatism increasing with the increase of the notch sharpness.

To conclude, since L can be easily derived, either via Eq. (2.80) re-arranged in terms of maximum values or through the simplified procedure summarised in Fig. 2.26, the obtained results strongly support the idea that gradient elasticity can be safely used in conjunction with the TCD's philosophy by always reaching during the design process an appropriate level of safety.

7.3.4 Gradient elasticity and material microstructural features

By carefully observing the diagrams of Fig. 7.8, it is possible to notice that, in the endurance limit condition, the gradient-enriched stress at the surface of the un-notched specimens is lower than the corresponding endurance limit determined according to continuum mechanics. This apparent anomaly is a consequence of the fact that, as already explained in Chapter 4, in the presence of stress gradients, gradient elasticity manipulates the local stress fields by incorporating into the stress analysis the microstructural length scale parameter, ℓ (see Figs. 4.1b and c). Solely in the absence of gradients the stress fields determined via gradient elasticity coincide with those determined according to continuum mechanics. This is what happens, for instance, under axial loading (see Fig. 4.1a). Therefore, one may argue that the conventional un-notched endurance limit, $\sigma_{0,\mathrm{MAX}}$, determined under bending is not a strength quantity suitable for being used to employ gradient elasticity to estimate the high-cycle fatigue strength of notched materials. Having said that, the hypothesis can be formed that the maximum value of the gradient-enriched endurance limit, $\sigma_{0,\mathrm{MAX}}^{g}$, can directly be derived from the experimental results generated by testing un-notched specimens under cyclic bending provided that the value of the length scale parameter, ℓ, is set a priori. In order to choose an appropriate value for the microstructural length scale parameter, it is worth remembering here that length ℓ is seen to be directly related to the size of the dominant source of microstructural heterogeneity [59]. Therefore, the assumption can be made that ℓ equals the average inter-aggregate distance, i.e., $\ell = 4$ mm, since in the tested concrete the cement paste was seen to play the role of the weakest link in the fatigue strength of the microstructural chain (Fig. 7.4). As shown in the diagrams of Figs. 7.9a and 7.9b, taking the length scale parameter equal to 4 mm resulted in a maximum value of the gradient-enriched un-notched endurance limit, $\sigma_{0,\mathrm{MAX}}^{g} = 2.8$ MPa for Batch A and $\sigma_{0,\mathrm{MAX}}^{g} = 4.3$ MPa to for Batch B. The gradient-enriched stress-distance curves reported in the above charts make it evident that the use of such a strategy resulted in highly accurate predictions, with estimates falling within an error interval of $\pm 15\%$ (see Table 7.4). To conclude, it is worth observing that in Figs. 7.9 as well as in the last column of Table 7.4 the error was calculated as follows:

$$\text{Error} = \frac{\sigma_{\mathrm{eff,max}}^{g} - \sigma_{0,\mathrm{MAX}}^{g}}{\sigma_{0,\mathrm{MAX}}^{g}}\ [\%] \tag{7.13}$$
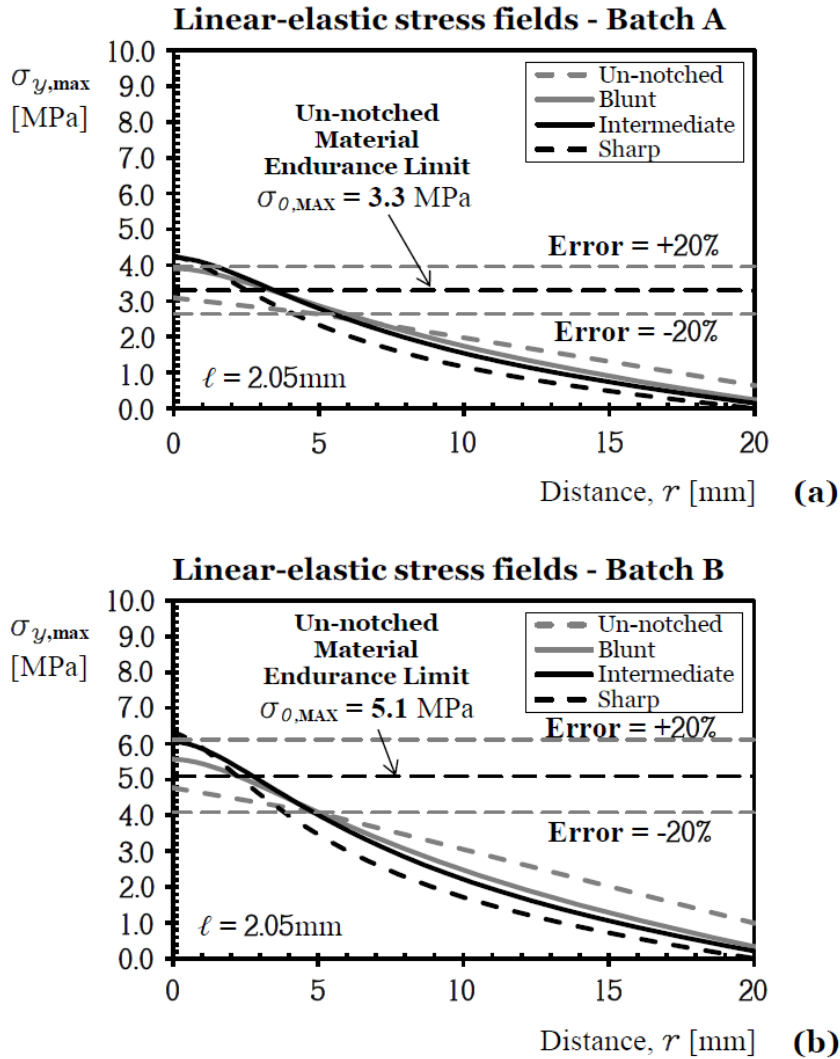
Fig. 7.8. Gradient-enriched stress fields in the endurance limit condition and accuracy of gradient elasticity applied according to the TCD in estimating the high-cycle fatigue strength of the tested notched concrete.
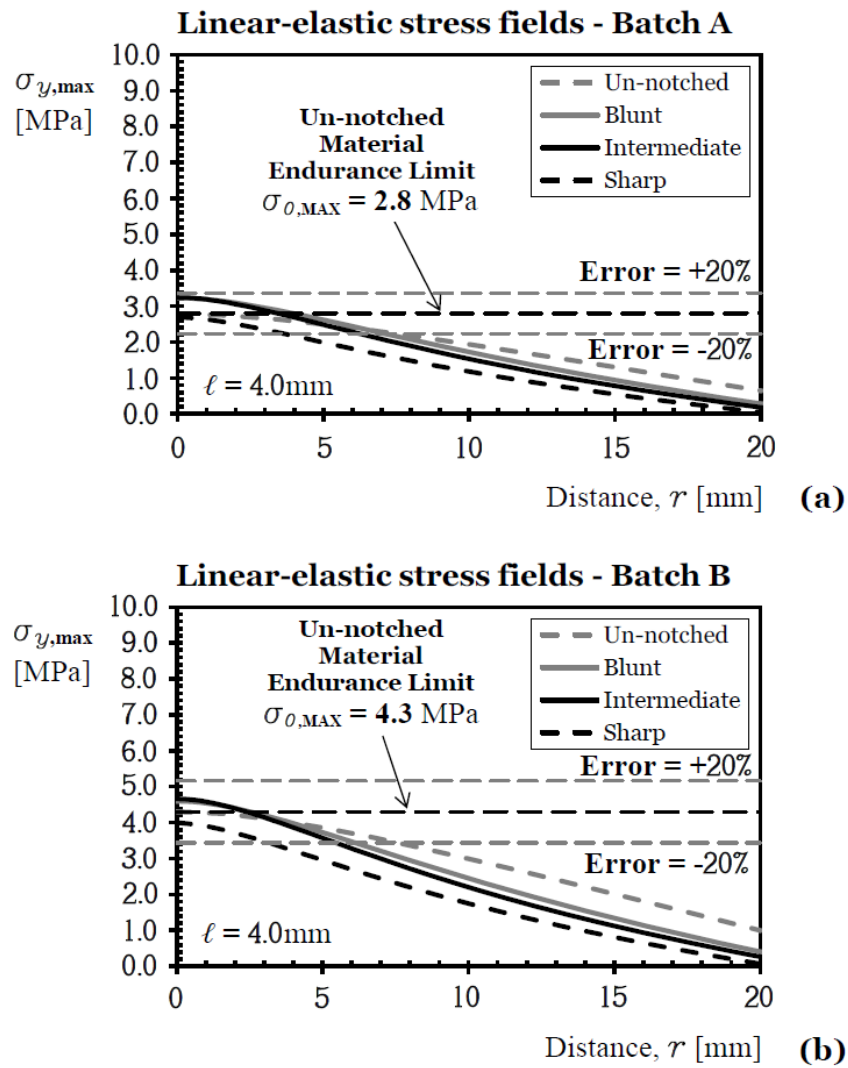
Fig. 7.9. Accuracy of gradient elasticity calibrated via the average inter-aggregate distance in estimating the high-cycle fatigue strength of the tested notched concrete.

where $\sigma_{\text{eff,max}}^{g}$ was determined according to Eq. (7.12).

Although the choice of taking the internal length $\ell = 4$ mm is reasonable, one could argue that it is to some extent arbitrary. Therefore, the sensitivity of the results with respect to a different choice of length scale has been investigated by analysing the same problems but with $\ell = 3$ mm (-25%) and $\ell = 5$ mm ($+25\%$). This investigation showed that a variation of $\pm 25\%$ on the length scale produced variations on the error included in the range $\pm 10\%$ with the errors falling anyway within the usual acceptable $\pm 20\%$ error scatter band. Hence, even if the accuracy of the results presents some sensitivity to the choice of the length scale, substantial variations of the length scale parameter result anyway in predictions with acceptable accuracy.

7.4   Conclusions

In this chapter the accuracy and reliability of using microstructural length scale parameters in modelling the high-cycle fatigue behaviour of notched plain concrete have been investigated against an appropriate set of experimental data. It is possible to conclude that, also for notched concrete under fatigue loading, the mean stress effect can be accurately taken into account by considering the maximum stress in the cycle.

Regarding the TCD, the use of both the PM and AM resulted in highly accurate estimates, proving that these two formalisations of the TCD are suitable for modelling the high-cycle fatigue behaviour of notched plain concrete. On the contrary, even though the obtained error level was acceptable, the use of the LM led to non-conservative estimates. Furthermore, the fact that the critical distance L was seen to be the same in both batches strongly supports the idea that L mainly depends on the morphological features affecting the overall strength of the considered material.

In what concerns gradient elasticity, instead, if applied according to the TCD it led to conservative estimates, the level of conservatism increasing with the sharpness of the notch. On the other hand, if gradient elasticity is applied by taking length scale parameter ℓ equal to the average inter-aggregate distance, it resulted in a remarkable level of accuracy. This strongly supports the idea that length ℓ is a parameter suitable for modelling the dominant source of microstructural heterogeneity.

Finally, more work needs to be done in this area to check the accuracy of the TCD and gradient elasticity, not only with other plain and short-fibre reinforced concrete containing different notches, but also under mixed mode loading.

Chapter 8

Gradient visco-elasticity

A material showing both elastic and viscous behaviour, when subject to deformation processes, is commonly defined *visco-elastic*. Visco-elastic materials are characterised by an intermediate behaviour between purely elastic and purely viscous materials; in particular the viscous component is responsible of the time-dependant behaviour of the material. For example, when the Maxwell model shown in Fig. 8.1a is used to describe the visco-elastic behaviour, a visco-elastic material subject to a constant strain experiences an instantaneous elastic stress which then decreases with time (relaxation). On the other hand, if the Kelvin-Voigt model shown in Fig. 8.1b is used, a material subject to a constant stress shows an instantaneous deformation (due to the elastic part) which increases with time until the material fails or the stress is removed (creep).

A large number of common materials like synthetic polymers, biopolymers, wood, human tissue, bituminous materials and metals at high temperature show strong visco-elastic behaviour, making the development of a continuum theory, capable of capturing micro-structural as well as time-dependent phenomena, of primary interest.

Despite the significant number of gradient-enriched theories for elasticity and plasticity, and the ability of gradient theories to take into account the effect of the microstructure on the global behaviour of a material in both static and dynamics, gradient visco-elasticity theories have received not great interest in the past. An attempt to describe visco-elastic materials has been made by Gudmundson [66] in 2006, who proposed a strain gradient visco-elastic model to describe length scale effects in such materials. However, as the author points himself further in [66], the proposed method is lacking a link between the length scale and the material's microstructure.

In this chapter a micro-inertia gradient visco-elasticity theory is proposed to study wave dispersion in periodic composites, allowing new insights into the effects of both gradient enrichment and viscosity on wave propagation as well as their interaction. The proposed theory is characterised by a direct link with the underlying microstructure as well as material properties. Moreover, an effective and straightforward finite element implementation of the presented theory is proposed. Some insight about the interaction between viscosity and inertia gradient, as well as the different effects they have on wave propagation and dispersion, are also given through an application of the new methodology to a one-dimensional wave propagation problem.
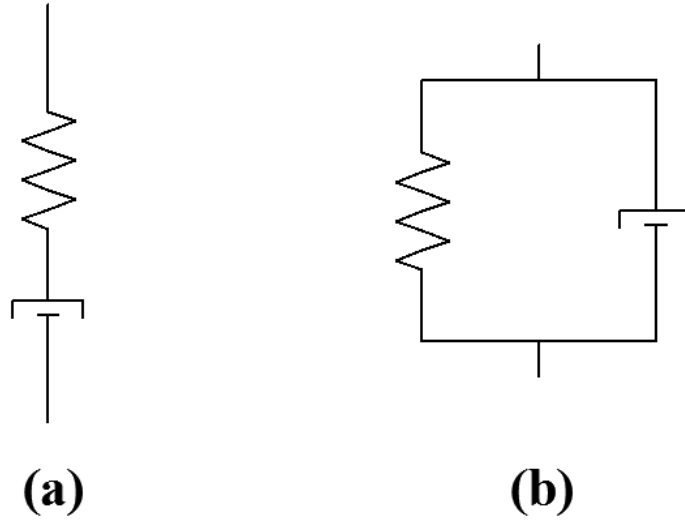
Fig. 8.1. Basic visco-elastic models: Maxwell (a) and Kelvin-Voigt (b).

8.1   Model derivation

Let us consider the Kelvin-Voigt model shown in Fig. 8.1b and represented by a purely viscous damper and a purely elastic spring connected in parallel. It can be expressed by the following equation:

$$f_{total} = f_{spring} + f_{damper} = su_{(t)} + \eta\dot{u}_{(t)} \tag{8.1}$$

where s is the stiffness of the spring and η is the viscosity of the damper, or analogously:

$$\sigma_{(t)} = E\varepsilon_{(t)} + \tilde{\gamma}\dot{\varepsilon}_{(t)} \tag{8.2}$$

where σ is the stress, ε the strain, E the Young's modulus, $\tilde{\gamma}$ the damping factor, t the time and the dot represents the time derivative.

Gradient visco-elasticity theory can be obtained through the continualisation of a discrete lattice (Fig. 8.2) as explained in [14], taking into account that now the particles of mass m are in series with Kelvin-Voigt models characterised by spring stiffness s and viscosity η; the distance between two consecutive particles is denoted d. The equation of the motion of the nth particle can be written as:

$$m\ddot{u}_n = s\left(u_{n+1} - 2u_n + u_{n-1}\right) + \eta\left(\dot{u}_{n+1} - 2\dot{u}_n + \dot{u}_{n-1}\right) \tag{8.3}$$

Passing now from the discrete to the continuum model, the displacements can be re-defined as

$$u(x,t) = u_n(t) \qquad \text{and} \qquad u(x \pm d, t) = u_{n\pm1}(t) \tag{8.4}$$
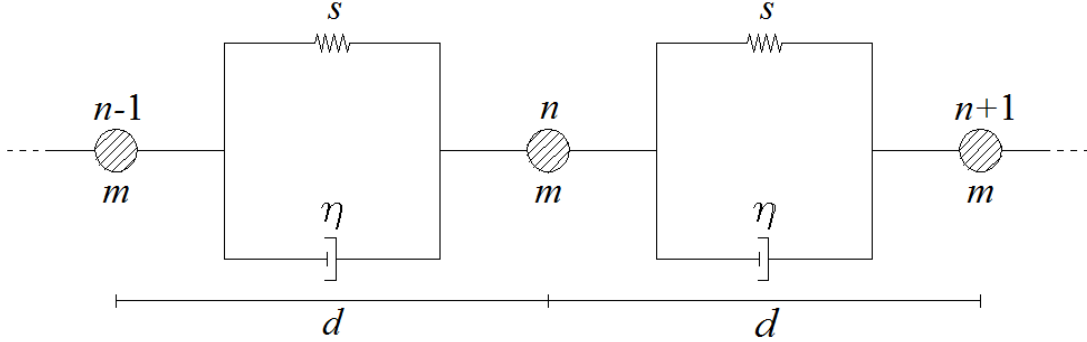
Fig. 8.2. Mono-dimensional discrete model consisting in particles and Kelvin-Voigt models.

Then, by using the Taylor series the generic displacement can be written as

$$u(x \pm d, t) \approx u(x, t) \pm du'(x, t) + \frac{1}{2}d^2 u''(x, t) \pm \frac{1}{6}d^3 u'''(x, t) + \frac{1}{24}d^4 u''''(x, t) \pm \cdots \quad (8.5)$$

and substituting Eq. (8.5) into Eq. (8.3), a new equation of the motion is obtained, in which an higher order term appears for both displacements and velocities:

$$m\ddot{u}(x, t) = sd^2 \left[u''(x, t) + \frac{1}{12}d^2 u''''(x, t) \right] + \eta d^2 \left[\dot{u}''(x, t) + \frac{1}{12}d^2 \dot{u}''''(x, t) \right] \quad (8.6)$$

or similarly, replacing the mass, the spring stiffness and the (stiffness-) proportional damping, respectively, with the following relations $m = \rho A d$, $s = EA/d$ and $\eta = \tau EA/d$

$$\rho\ddot{u}(x, t) = E \left[u''(x, t) + \frac{1}{12}d^2 u''''(x, t) + \tau \left(\dot{u}''(x, t) + \frac{1}{12}d^2 \dot{u}''''(x, t) \right) \right] \quad (8.7)$$

where ρ is the mass density and τ is the (stiffness-) proportional damping coefficient with unit of time. In Eqs. (8.6) and (8.7), truncation of the Taylor series has been applied such that only the next-highest order terms are maintained.

This results in an enriched-gradient model with positive sign, which unfortunately has been proved to produce unstable results [19]. Stabilisation can be obtained through a simple mathematical manipulation that consists in taking the Laplacian of the original equation of the motion (8.7), that is (ignoring the spatial and temporal dependence for notational simplicity)

$$\rho\ddot{u}'' = E \left[u'''' + \frac{1}{12}d^2 u'''''' + \tau \left(\dot{u}'''' + \frac{1}{12}d^2 \dot{u}'''''' \right) \right] \quad (8.8)$$

multiplying Eq. (8.8) by $\frac{1}{12}d^2$, which leads to (neglecting higher-order terms)

$$\frac{1}{12}d^2\rho\ddot{u}'' = \frac{1}{12}d^2E\left(u'''' + \tau\dot{u}''''\right) \tag{8.9}$$

and finally subtracting Eq. (8.9) from Eq. (8.7), which leads to:

$$\rho\left(\ddot{u} - \frac{1}{12}d^2\ddot{u}''\right) = E\left(u'' + \tau\dot{u}''\right) \tag{8.10}$$

or alternatively

$$\rho\left(\ddot{u} - \ell^2\ddot{u}''\right) = E\left(u'' + \tau\dot{u}''\right) \tag{8.11}$$

where the length scale ℓ is linked to the inter-particle distance d by the expression $\ell = \frac{1}{\sqrt{12}}d$.

This technique can also be applied in multi-dimensions, which in the isotropic case leads to the following equation of the motion:

$$\rho\left(\ddot{\mathbf{u}} - \ell^2\nabla^2\ddot{\mathbf{u}}\right) = \mathbf{L}^T\mathbf{C}\mathbf{L}\left(\mathbf{u} + \tau\dot{\mathbf{u}}\right) \tag{8.12}$$

Note 1. For non-isotropic materials the length scale ℓ is not a scalar anymore, but the length scale effects in each direction of anisotropy are collected in a tensor $\mathbf{L_s}$ (see for example [60]).

8.2   Dispersion analysis

8.2.1   Discrete model

To study the dispersive behaviour of the discrete model of Eq. (8.3), the general harmonic solution

$$u_n = U\exp(\mathrm{i}(\omega t - kx_n)) \tag{8.13}$$

is considered, where U is the amplitude, k is the wave number, t is the time, x_n the coordinate of the nth particle and ω is the angular frequency defined as a complex number as

$$\omega = \omega_h + \mathrm{i}\omega_d \tag{8.14}$$

with ω_h and ω_d the harmonic and damping component of ω, respectively.

Substituting Eqs. (8.13) and (8.14) into Eq. (8.3) and considering that $x_{n\pm1} = x_n \pm d$, the following expression for ω_d and ω_h are obtained

$$\omega_d = 2\frac{c_e^2}{d^2}\tau \sin^2\left(\frac{kd}{2}\right) \tag{8.15}$$

$$\omega_h = 2\frac{c_e}{d}\left|\sin\left(\frac{kd}{2}\right)\right|\sqrt{1 - \frac{c_e^2}{d^2}\tau^2 \sin^2\left(\frac{kd}{2}\right)} \tag{8.16}$$

where $c_e = \sqrt{E/\rho}$ is the elastic bar velocity. Sub-critical damping is identified via non-imaginary values of ω_h, which leads to the following condition:

$$1 - \frac{c_e^2}{d^2}\tau^2 \sin^2\left(\frac{kd}{2}\right) \geq 0 \tag{8.17}$$

or in terms of τ:

$$\tau \leq \frac{1}{\left|\sin\left(\frac{kd}{2}\right)\right|}\frac{d}{c_e} \tag{8.18}$$

Since $0 \leq \left|\sin\left(\frac{kd}{2}\right)\right| \leq 1$, Eq. (8.18) can be simplified as

$$\tau \leq \frac{d}{c_e} \tag{8.19}$$

which sets the threshold value of τ that separates sub-critical and super-critical damping.

8.2.2 Continuum model

In what concerns the continuum model, the following harmonic solution

$$u(x,t) = U\exp(i(\omega t - kx)) \tag{8.20}$$

is substituted into the one-dimensional continuum equation of the motion (8.10), leading to the following equation

$$\rho\omega^2\left(1 + \frac{1}{12}d^2k^2\right) = Ek^2\left(1 + i\omega\tau\right) \tag{8.21}$$

Introducing Eq. (8.14) in Eq. (8.21) the following expressions for ω_d and ω_h are obtained:

$$\omega_d = \frac{c_e^2 k^2 \tau}{2\left(1 + \frac{1}{12}d^2k^2\right)} \tag{8.22}$$

$$\omega_h = \frac{c_e k}{\sqrt{1 + \frac{1}{12}d^2k^2}}\sqrt{1 - \frac{c_e^2 k^2 \tau^2}{4\left(1 + \frac{1}{12}d^2k^2\right)}} \tag{8.23}$$
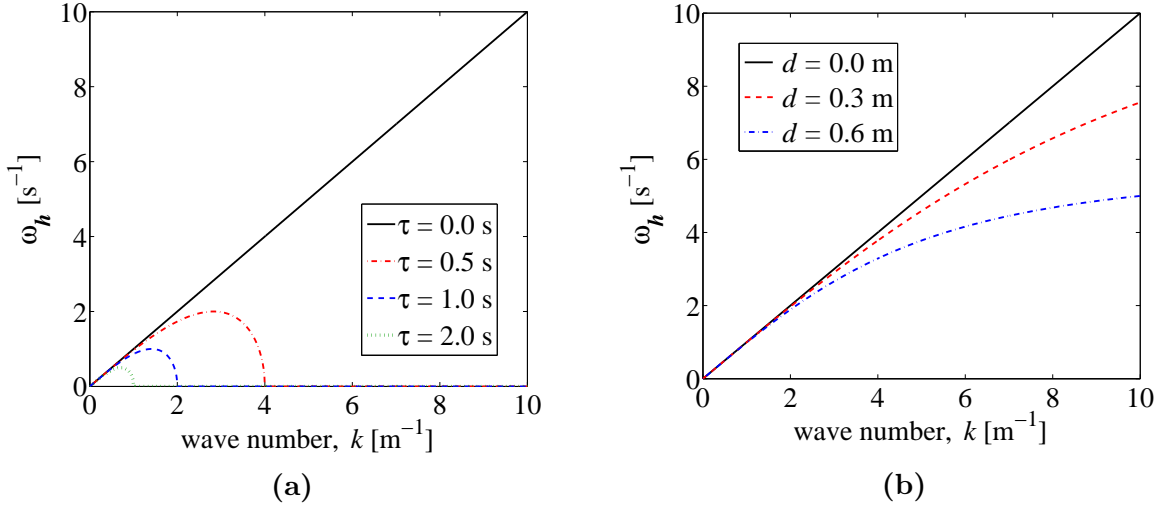
Fig. 8.3. Harmonic component of the angular frequency versus wave number when classical visco-elasticity theory is applied (a) and for the non-viscous micro-inertia theory (b).

Taking $d = 0$ m the continuum model for classical visco-elasticity is retrieved, obtaining the following expression for the harmonic component of the angular frequency

$$\omega_h = c_e k \sqrt{1 - \frac{c_e^2 k^2 \tau^2}{4}} \tag{8.24}$$

Thus,

$$\tau = 2 \frac{1}{c_e k_c} \tag{8.25}$$

is the condition for critical damping, from which can be easily determined the cut-off value k_c (i.e. the wave number associated with $\omega_h = 0$).

Similarly, the micro-inertia gradient elasticity model is found by setting the condition $\tau = 0$ s which yields

$$\omega_h = \frac{c_e k}{\sqrt{1 + \frac{1}{12} d^2 k^2}} \tag{8.26}$$

In Fig. 8.3a the harmonic component of the angular frequency ω_h is plotted against the wave number k, in the case the classical visco-elasticity theory is applied, for different values of τ, while in Fig. 8.3b the same graph is plotted for the non-viscous micro-inertia theory ($\tau = 0$ s), for different values of d.

Coming back to Eq. (8.23), it can be observed that positive values of the argument of the second square root lead to real values of ω_h, while if the considered argument is negative, ω_h becomes imaginary. Considering Eq. (8.20) together with Eq. (8.14) it can be easily found that real values of ω_h lead to the case of sub-critical damping, while imaginary values make the system super-critically damped (see Appendix B for a more

detailed discussion about the stability of this solution). Hence, summarising it can be stated that the condition

$$\tau_c = \frac{1}{\sqrt{3}} \frac{d}{c_e} \tag{8.27}$$

which makes the argument of the square root null for $k \to \infty$, represents the condition of critical damping and consequently if $\tau < \tau_c$ the system is under-damped, while for $\tau > \tau_c$ a range of higher wave numbers will be over-damped.

Thus, an important feature of the proposed theory can be found in the fact that varying τ (which depends on material properties) it is possible to have control on which wave numbers are over-damped. In particular, the lower bound of the over-damped wave numbers can be defined as the cut-off value k_c obtained by imposing

$$1 - \frac{c_e^2 k^2 \tau^2}{4 \left(1 + \frac{1}{12} d^2 k^2\right)} = 0 \tag{8.28}$$

which leads to

$$k_c = \frac{2}{\sqrt{c_e^2 \tau^2 - \frac{1}{3} d^2}} \tag{8.29}$$

that represents the wave number in correspondence of which ω_h is zero and beyond which imaginary frequencies ω_h are obtained.

In Fig. 8.4 the harmonic component of the angular frequency ω_h, obtained by applying the different models, is plotted versus the wave number k, for different values of the dimensionless parameter ξ, writing τ as

$$\tau = \xi \frac{d}{c_e} \tag{8.30}$$

It is worth clarifying that the results shown in Fig. 8.4 are physically of interest only for $0 \leq k \leq \pi$ (i.e. first Brillouin zone). However, for reasons of completeness and to allow further mathematical considerations, expressed below, a wider range of wave numbers has been considered.

From Fig. 8.4, considering wave numbers up to π, it is evident that the micro-inertia gradient visco-elastic model is able to describe with higher accuracy the dispersive behaviour of the discrete model, compared to the classical visco-elastic model, even if it must be observed that the improvement introduced by the gradient enrichment becomes weaker for high value of τ.

Note 2. It can also be noticed that, in the case of critical damping (Fig. 8.4b), the $\omega_h - k$ curve, resulting from the micro-inertia gradient model, can be split into two parts: a first part characterised by a negative second derivative (concave) and a second one convex. Through a more accurate study of the second derivative it has been found that for $\xi > 1/\sqrt{6}$ the curve shows an inflexion point.
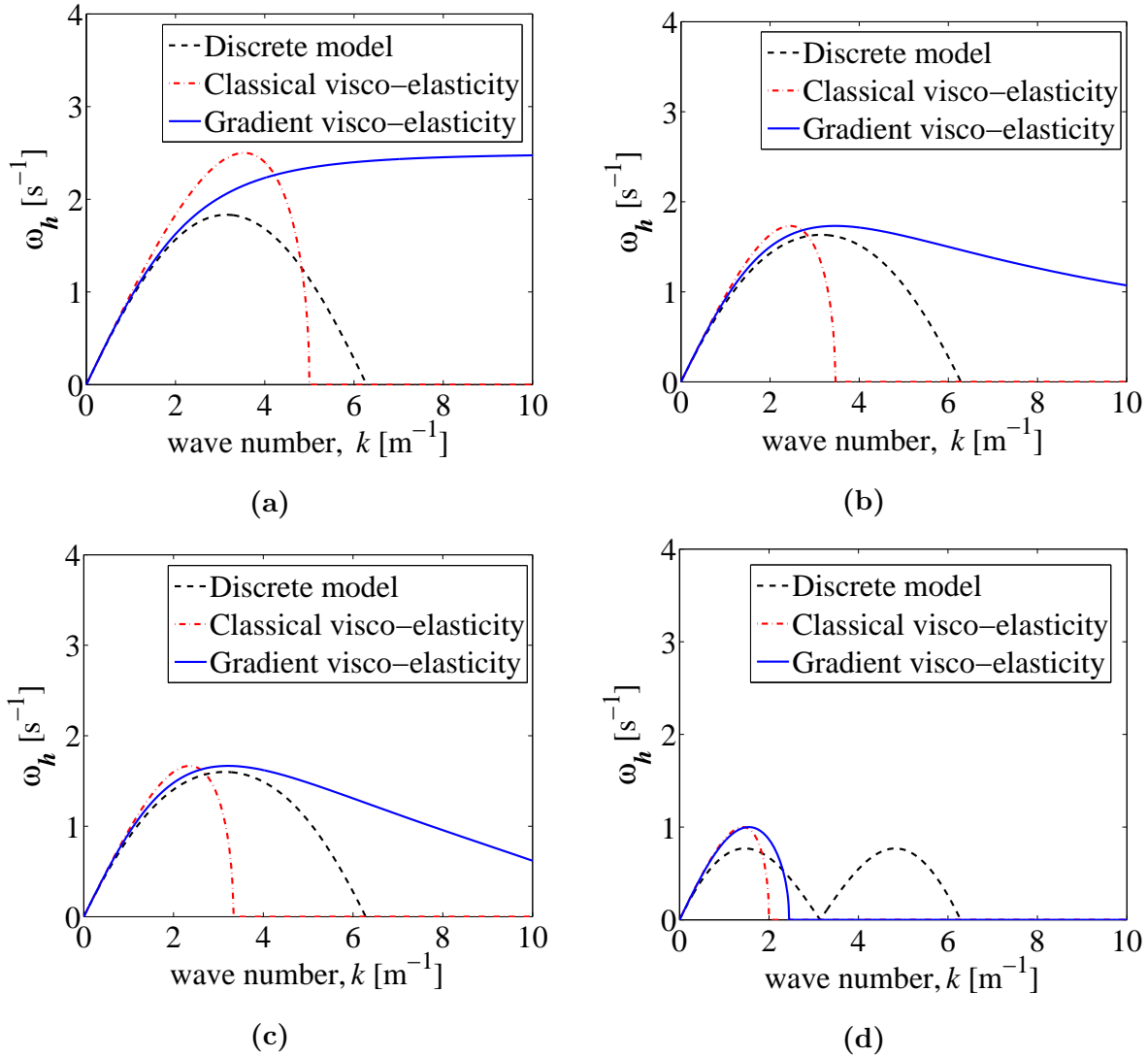
Fig. 8.4. Harmonic component of the angular frequency versus wave number for the discrete model (dashed line), classical visco-elastic model (dash-dotted line) and micro-inertia gradient visco-elastic model (solid line), for different values of ξ: $\xi = 0.4$ (a), $\xi = 1/\sqrt{3}$ (b), $\xi = 0.6$ (c), $\xi = 1.0$ (d).

Thus, we can summarise the results of the proposed micro-inertia gradient model as follows

- $0 \leq \xi \leq 1/\sqrt{6}$: the $\omega_h - k$ curve is always concave and it tends to the horizontal asymptote

$$\omega_h = 6\frac{c_e}{d}\sqrt{\frac{1}{3} - \xi^2} \tag{8.31}$$

- $1/\sqrt{6} < \xi \leq 1/\sqrt{3}$: the curve is characterised by a first concave part followed by a second convex one, but ω_h is real for every wave number;

- $\xi > 1/\sqrt{3}$: ω_h assumes imaginary values for a range of higher wave numbers.

Finally, comparing Fig. 8.4 with Fig. 8.3 it can be easily seen that both classical visco-elasticity and gradient elasticity (straight solid line in Fig. 8.3a, corresponding to $\tau = 0$ s) models alone are not able to accurately describe the dispersive behaviour of the discrete model, but introducing a micro-inertia gradient enrichment into the classical visco-elasticity theory a significant improvement of the results is obtained for $0 \leq k \leq \pi$.

8.3 Discretisation

Starting from Eq. (8.12) the finite element equations for the bi-dimensional case will be defined, while the equations for the three-dimensional case can be easily obtained, following a similar procedure. Some information about the time integration algorithm adopted in the proposed methodology to solve the equations of the motion will be also provided.

8.3.1 Finite element equations

The continuum displacement field is discretised by means of shape functions which, as usual, are collected in the matrix $\mathbf{N}_u$ defined by Eq. (5.2), which allows the continuum displacements $\mathbf{u} = [u_x, u_y]^T$ to be expressed in terms of the nodal displacements $\mathbf{d} = [d_{1x}, d_{1y}, d_{2x}, d_{2y}, \dots]^T$ through the relation $\mathbf{u} = \mathbf{N_u}\mathbf{d}$.

Taking the weak form of the equation of the motion (8.12), considering now also the body forces $\mathbf{b}$, with domain Ω and boundary Γ, followed by integration by parts, and considering the discretisation of the displacements described above, we obtain the following equation:

$$\int_\Omega \rho \left[\mathbf{N_u}^T \mathbf{N_u} + \ell^2 \left(\frac{\partial \mathbf{N_u}^T}{\partial x} \frac{\partial \mathbf{N_u}}{\partial x} + \frac{\partial \mathbf{N_u}^T}{\partial y} \frac{\partial \mathbf{N_u}}{\partial y} \right) \right] \mathrm{d}\Omega \, \ddot{\mathbf{d}} +$$
$$+ \int_\Omega \mathbf{B_u}^T \mathbf{C} \mathbf{B_u} \mathrm{d}\Omega \left(\mathbf{d} + \tau \dot{\mathbf{d}} \right) = \int_\Omega \mathbf{N_u}^T \mathbf{b} \mathrm{d}\Omega + \int_\Gamma \mathbf{N_u}^T \mathbf{t} \mathrm{d}\Gamma \tag{8.32}$$

where $\mathbf{t}$ is the vector of the prescribed traction on the Neumann part of the boundary and includes also the inertia effects.

Finally we obtain the discrete system of equation

$$[\mathbf{M} + \mathbf{H}]\,\ddot{\mathbf{d}} + \mathbf{K}\left(\mathbf{d} + \tau\dot{\mathbf{d}}\right) = \mathbf{f} \tag{8.33}$$

with

$$\mathbf{K} = \int_{\boldsymbol{\Omega}} \mathbf{B_u}^T \mathbf{C} \mathbf{B_u} d\Omega \tag{8.34}$$

the stiffness matrix,

$$\mathbf{M} = \int_{\boldsymbol{\Omega}} \rho \mathbf{N_u}^T \mathbf{N_u} d\Omega \tag{8.35}$$

the classic mass matrix,

$$\mathbf{H} = \int_{\boldsymbol{\Omega}} \rho \ell^2 \left(\frac{\partial \mathbf{N_u}^T}{\partial x} \frac{\partial \mathbf{N_u}}{\partial x} + \frac{\partial \mathbf{N_u}^T}{\partial y} \frac{\partial \mathbf{N_u}}{\partial y} \right) d\Omega \tag{8.36}$$

the gradient-enriched part of the mass matrix, and

$$\mathbf{f} = \int_{\boldsymbol{\Omega}} \mathbf{N_u}^T \mathbf{b} d\Omega + \int_{\Gamma} \mathbf{N_u}^T \mathbf{t} d\Gamma \tag{8.37}$$

the force vector. Note that the structure of $\mathbf{H}$ resembles that of a diffusivity matrix.

8.3.2   Time integration

In dynamics the equations of the motion of discrete systems are solved in the time domain by using direct integration algorithms.

Here, the Crank-Nicolson method [41] has been used, obtained from the Newmark method [99] by setting the two parameters $\beta^* = 1/4$ and $\gamma^* = 1/2$, which makes the method unconditionally stable [64].

The fundamental relations of this method are:

$$\ddot{u}_{i+1} = \frac{4}{\Delta t^2}\left(u_{i+1} - u_i - \Delta t\ \dot{u}_i - \frac{1}{4}\Delta t^2 \ddot{u}_i \right) \tag{8.38}$$

$$\dot{u}_{i+1} = \dot{u}_i + \frac{1}{2}\Delta t\left(\ddot{u}_i + \ddot{u}_{i+1} \right) \tag{8.39}$$

where u_i, $\dot{u}_i$ and $\ddot{u}_i$ are, respectively, the displacement, velocity and acceleration at the ith time instant, while Δt is the chosen time step; that lead to the following time-discretisation of Eq. (8.33)
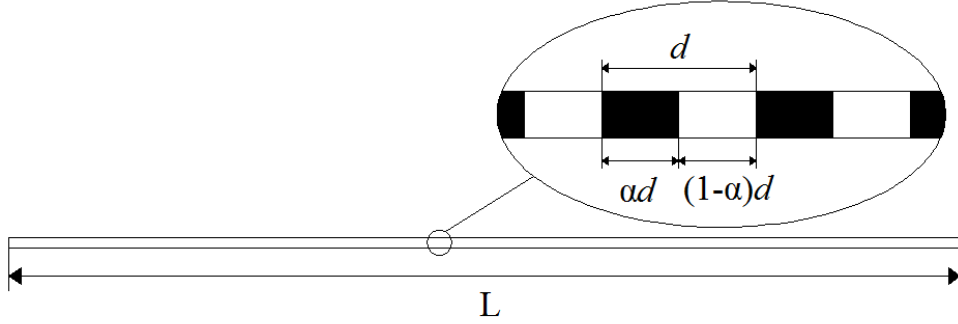
Fig. 8.5. Mono-dimensional representation of a periodic bi-component material.

$$\left[\frac{4\left[\mathbf{M}+\mathbf{H}\right]}{\Delta t^2} + \left(\frac{2\tau}{\Delta t}+1\right)\mathbf{K}\right]\mathbf{u}_{i+1} =$$

$$= \left[\mathbf{M}+\mathbf{H}\right]\left(\frac{4\mathbf{u}_i}{\Delta t^2}+\frac{4\dot{\mathbf{u}}_i}{\Delta t}+\ddot{\mathbf{u}}_i\right)+\tau\mathbf{K}\left(\frac{2\mathbf{u}_i}{\Delta t}+\dot{\mathbf{u}}_i\right)+\mathbf{f} \tag{8.40}$$

from which the nodal displacements at time i+1 can be determined, knowing the values of the nodal displacements, velocities and accelerations at the previous time step i.

8.4 Homogenisation approach and length scale identification for periodic composites

In the scope of this chapter, the periodic elastic composite analysed by Chen and Fish [39] will be considered. This periodic composite consists of two different materials (properties are denoted by the subscript 1 and 2 respectively), with volume fraction defined by the parameter α as shown in Fig. 8.5.

Now the constitutive relations can be presented as

$$\sigma = E\left(\varepsilon + \tau\dot{\varepsilon}\right) \tag{8.41}$$

where τ is the damping proportional factor.

Considering the homogeneous continuum model proposed by Chen and Fish [39], neglecting the multiple time scales and taking into account the constitutive relation (8.41), the leading order equation of the motion takes the following form:

$$\overline{\rho}\ddot{u} = \overline{E}\left(u'' + \tau\dot{u}''\right) \tag{8.42}$$

where

$$\overline{\rho} = \alpha\rho_1 + (1-\alpha)\rho_2 \tag{8.43}$$

$$\overline{E} = \frac{E_1 E_2}{(1 - \alpha) E_1 + \alpha E_2} \tag{8.44}$$

are, respectively, the homogenised mass density and Young's modulus.

Including the next high-order term, the equation of the motion reads:

$$\overline{\rho}\ddot{u} = \overline{E} \left(u'' + \tau \dot{u}'' \right) + \gamma d^2 \overline{E} \left(u'''' + \tau \dot{u}'''' \right) \tag{8.45}$$

where d is the size of the unit cell as shown in Fig. 8.5 and γ is expressed in the following way:

$$\gamma = \frac{1}{12} \left[\frac{\alpha(1 - \alpha)(\rho_1 E_1 - \rho_2 E_2)}{(1 - \alpha)\overline{\rho}E_1 + \alpha\overline{\rho}E_2} \right]^2 \tag{8.46}$$

Imposing the two conditions $0 < \alpha < 1$ and $\rho_1 E_1 \neq \rho_2 E_2$ we obtain $\gamma > 0$.

As it can be easily noticed, Eq. (8.45) represents an enriched-gradient equation of the motion in which the higher-gradient term is characterised by a positive sign, which, as previously mentioned, produces unstable results. However, with a mathematical procedure similar to the one previously explained, as also proposed in [39] for elastic materials, it is possible to replace the previous unstable model with a stable inertia-gradient model. This leads to the following stable inertia-gradient equation of the motion:

$$\overline{\rho} \left(\ddot{u} - \gamma d^2 \ddot{u}'' \right) = \overline{E} \left(u'' + \tau \dot{u}'' \right) \tag{8.47}$$

or equivalently

$$\overline{\rho} \left(\ddot{u} - \gamma d^2 \ddot{u}'' \right) = \overline{E} u'' + \overline{D} \dot{u}'' \tag{8.48}$$

where $\overline{D} = \tau \overline{E}$.

Comparing now Eq. (8.11) with Eq. (8.48), the length scale ℓ can be written in terms of geometry and material parameters only:

$$\ell = d\sqrt{\gamma} \tag{8.49}$$

Finally, it is worth highlighting that, since the governing partial differential equations (8.48) of the proposed micro-inertia gradient visco-elastic methodology are second-order in space, only one set of boundary conditions must be applied. In particular, either:

- essential boundary conditions: $u = \overline{u}$ or

- natural boundary conditions: $f_t = \overline{\rho}\ell^2\ddot{u}' + \overline{E}(u' + \tau\dot{u}') = \overline{f}_t$

where f_t are the tractions containing also inertia and damping effects, while $\overline{u}$ and $\overline{f}_t$ are, respectively, the prescribed values of displacements and tractions on the boundaries.

Furthermore, in addition to the aforementioned boundary conditions, the following initial conditions are also needed:

- $u_{(t=0)} = u_0$

- $\dot{u}_{(t=0)} = \dot{u}_0$

where u_0 and $\dot{u}_0$ are the prescribed initial values of, respectively, displacements and velocities.

8.5   Numerical tests

The proposed theory has been applied to the one-dimensional wave propagation problem consisting in a 100 m long periodic composite bar, similar to the one shown in Fig. 8.5, in which the first material is characterised by mass density ρ_1 and Young's modulus E_1, while in what concerns the second material, the properties are denoted as ρ_2 and E_2. Following Eqs. (8.43) and (8.44), the macroscopic effective material properties are $\overline{\rho} = 1$ kg m^{-3}, $\overline{E} = 1$ N m^{-2} and $\overline{c}_e = \sqrt{E/\overline{\rho}} = 1$ m/s. Both materials are characterised by the same damping proportional factor τ and the volume fraction is assumed to be $\alpha = 0.5$, while the unit cell size is taken $d = 1$ m.

   The bar has a square cross section A $= 1$ m^2, it is fully restrained at its right hand end and subject to a unit-pulse at its left hand end.

   The two problems presented in [32] denoted as Case a (large contrast) and Case b (moderate contrast) are considered. The length scales for the two problems are determined through Eqs. (8.46) and (8.49), which leads to $\ell = d\sqrt{\gamma} = 0.289$ m for Case a and $\ell = d\sqrt{\gamma} = 0.159$ m for Case b. Following the same procedure presented in §8.2.2 and considering that now $\ell = \sqrt{\gamma}d$ instead of $\ell = \frac{1}{12}d$ the critical value of the damping coefficient is found to be $\tau_c = 2\ell/\overline{c}_e = 0.578$ s for Case a and $\tau_c = 2\ell/\overline{c}_e = 0.318$ s for Case b. The two problems have been analysed for four different values of τ, from $\tau = 0.000$ s (corresponding to the case of rate independent elastic material discussed in [32]) up to a value of the same order of magnitude of τ_c (i.e. $\tau = 0.002$ s, $\tau = 0.02$ s and $\tau = 0.2$ s).

   The problems have been modelled using linear elements, where the elastic/viscoelastic heterogeneous solution has been obtained by explicitly modelling the microstructural heterogeneity of the bar, through alternating groups of elements, characterised by the properties of material 1 and 2, so that the unit cell size $d = 1$ m. A time step of $\Delta t = 6.25\cdot10^{-2}$ s has been used for the heterogeneous solution, while for the classical and gradient simulations it has been assigned a value $\Delta t = 0.2$ s. The time step Δt has been determined as $\Delta t = \Delta x/\overline{c}_e$ [30, 163], where Δx is the minimum element size (in the present exercise uniform meshes have been used). In order to explicitly model the two materials with good accuracy, the heterogeneous solution required a finer mesh (1600 elements) respect to the classical and gradient models (200 elements) where the composite material has been modelled as a homogeneous continuum, leading to a smaller time step.

   In Fig. 8.6 the dynamic response of the composite bar after 90 s is shown for both Case a and b and for different values of viscosity, where Figs. 8.6a and 8.6b are the same presented in [32]. Comparing the wave fronts produced by the gradient and the explicit heterogeneous models, it can be observed that the proposed theory provide a good approximation of the heterogeneous model. On the contrary, it is possible to notice that
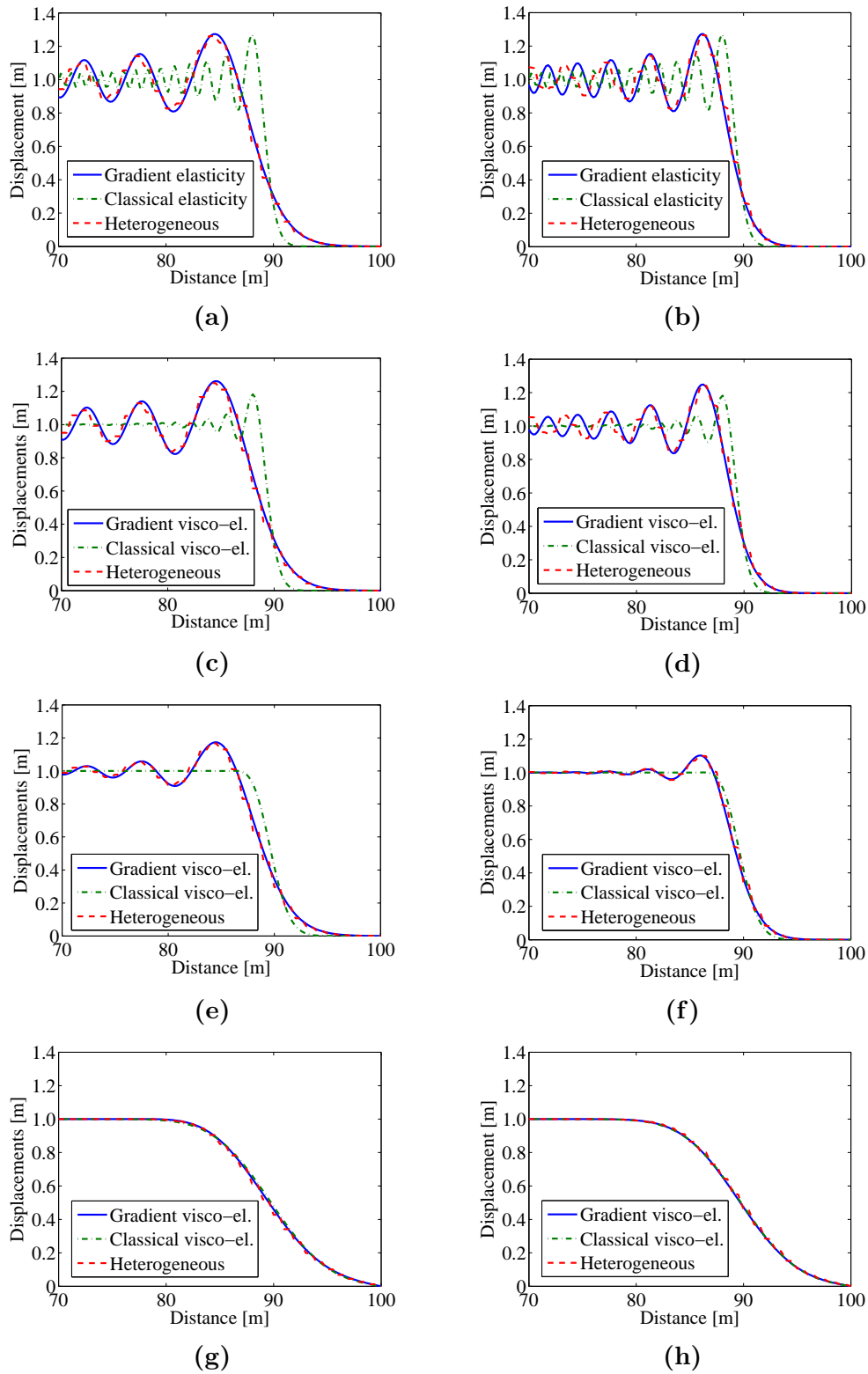
Fig. 8.6. Dynamic response of the one-dimensional periodic composite bar for Case a (a, c, e) and Case b (b, d, f) and for different value of the (stiffness-)proportional damping coefficient: $\tau = 0.000$ s (a, b), $\tau = 0.002$ s (c, d), $\tau = 0.02$ s (e, f), $\tau = 0.2$ s (g, h), at $t = 90$ s.

classical elasticity, for a given value of τ, produce the same dynamic response for both Case a and Case b, highlighting the inability of classical elasticity to take into account the effect of heterogeneity on the dynamic behaviour of a composite material.

Before further analysing Fig. 8.6, it is worth highlighting that the slope of the plotted wave fronts represents the wave propagation speed. For example, considering Fig. 8.6a and Fig. 8.6b, corresponding to the elastic case ($\tau = 0$ s), it is possible to observe that the response produced by the gradient model after 90 s from the application of the unit-pulse load (in good agreement with the response of the heterogeneous model) is characterised by a lower propagation speed (shallower wave front) if compared to the response produced by classical elasticity, that neglecting numerical dispersion can still be considered a Heaviside function as just after the application of the load. This aspect, valid also for visco-elastic problems with damping coefficient τ at least one order of magnitude smaller than the critical value τ_c (Figs. 8.6c-f), shows that the proposed methodology is able to properly describe the dispersive behaviour (reduction of the wave propagation speed with time) of a heterogeneous material regardless the viscosity. In fact from Fig. 8.7 it can be noticed that for values of τ up to one order of magnitude lower than the critical value, viscosity does not produce any significant reduction in the propagation speed of the wave front, while a significant reduction in the amplitude of the high-frequency components is observed. This attenuation of the high-frequency components is stronger in materials with low level of heterogeneity (Case b).

From Figs. 8.6a-f it is also possible to observe that the difference between the slope of the wave front produced by the classical theory and the one produced by the gradient model is smaller for Case b (lower heterogeneity) than for Case a (higher heterogeneity), meaning that materials with higher level of heterogeneity present stronger dispersive behaviour. For damping approaching the critical value (same order of magnitude), instead, the dispersion due to viscosity becomes predominant over the one due to the heterogeneity and the three models produce comparable results (Fig. 8.6g and Fig. 8.6h).

The ability of the proposed gradient-enriched visco-elastic methodology to describe the dispersive behaviour of heterogeneous materials, in contrast with classical visco-elasticity, is clearly shown in Fig. 8.8 where the wave fronts produced by both classical and gradient visco-elasticity are plotted at three different time instants. In fact it can be noticed that, while the propagation speed (slope of the wave front) obtained through classical elasticity does not vary in time (neglecting numerical dispersions), the propagation speed produced by the proposed gradient-enriched methodology decreases as time increases, with this phenomenon more pronounced for higher level of heterogeneity (Case a).

Summarising, for values of the damping coefficient τ up to one order of magnitude lower than the critical value, the introduction of a gradient enrichment has a significant effect on the propagation speed of the wave front, allowing a more accurate description of the dispersive behaviour of both elastic and visco-elastic heterogeneous materials, while the viscosity has a damping effect on the high frequency components and negligible effects on the propagation speed of the wave front. For values of τ approaching the critical value τ_c, instead, the dispersive effect due to the heterogeneity of the material becomes negligible compared to the one due to the viscosity and the responses produced by both
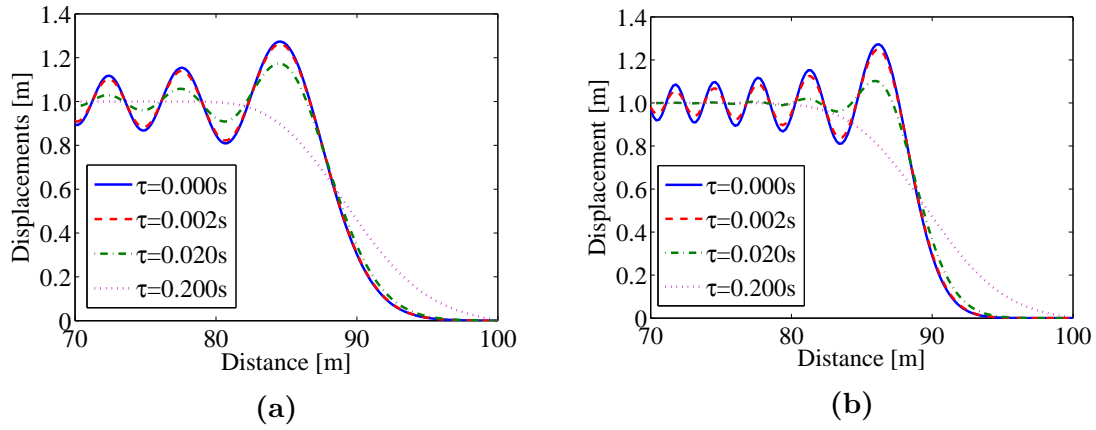
Fig. 8.7. Effect of viscosity on the dynamic response of the bar: gradient elastic/visco-elastic solutions for Case a (a) and Case b (b).
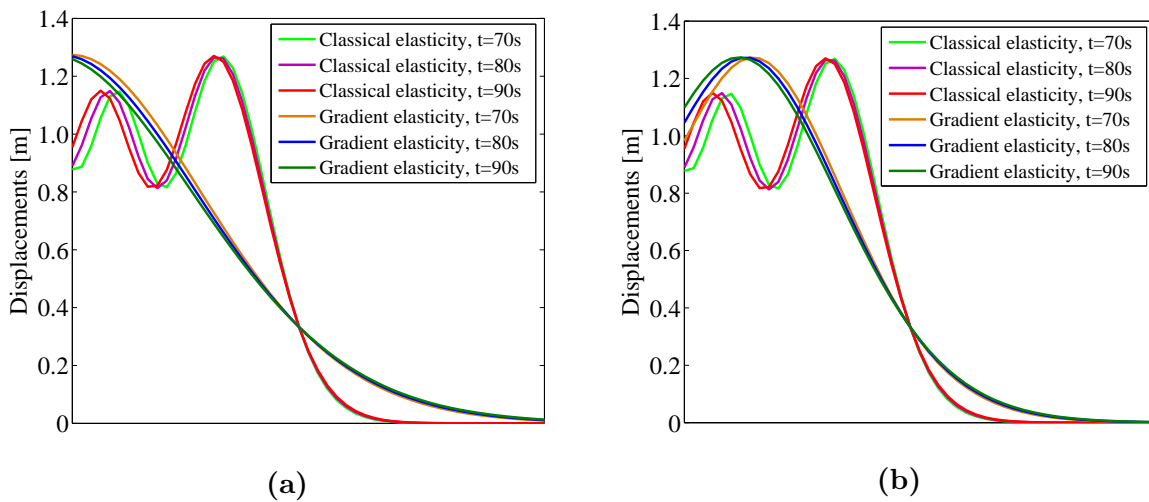
Fig. 8.8. Wave fronts produced by classical and gradient visco-elastic ($\tau = 0.002$ s) models after 70, 80 and 90 s for Case a (a) and Case b (b).

classical and gradient visco-elasticity coincides.

8.6 Conclusions

The proposed inertia-gradient visco-elastic theory represents a first attempt to extend and generalise gradient theories to the class of visco-elastic problems, and provides a more accurate tool to describe the dispersive behaviour of periodic visco-elastic composites.

The performed dispersion analysis has shown that the introduction of a micro-inertia gradient enrichment in the governing equations, helps capturing with higher accuracy the dispersive behaviour of the discrete model. Furthermore, from the mentioned analysis it has been also found that by changing the value of the (stiffness-)proportional damping coefficient, τ, it is possible to introduce super-critical damping and, in this case, control which wave numbers are super-critically damped.

The ability of the proposed theory to adequately describe dispersive wave propagation phenomena has been shown. Moreover, it has been observed that, for values of the damping coefficient at least one order of magnitude lower than the corresponding critical value, viscosity and gradient enrichment have two complementary effects, which makes essential the use of a gradient visco-elastic theory, for an accurate description of the overall dynamic behaviour of a visco-elastic material. In particular, while viscosity attenuates the high frequency components, gradient enrichment reduces the propagation speed of the wave front. For values of the damping coefficient approaching the corresponding critical value, instead, the viscosity becomes dominant over the heterogeneity of the material and both classical and gradient visco-elastic models produce comparable solutions. Additionally, the proposed methodology shows a very good agreement, in terms of displacements, with the correspondent heterogeneous model, where the microstructural heterogeneity of the material is explicitly modelled.

Since the proposed theory represents the first attempt to introduce viscosity in a gradient elasticity theory, the main goal of the present study was to explore and understand the interaction between viscosity and inertia-gradient, as well as their effects on wave dispersion rather than propose a complete gradient visco-elasticity theory.

Therefore, some issues remain open for future studies, in particular:

- extension of the proposed theory to periodic composites, whose constitutive materials are characterised by either proportional damping with different factor of proportionality or non proportional damping;

- extension of the one-dimensional theory to multi-dimensional problems.

Chapter 9

Conclusions and future directions

9.1   Conclusions

In this thesis, a unified finite element methodology based on the combination of gradient elasticity and the Theory of Critical Distances has been developed, implemented and validated against a wide range of problems, in particular for the static and high-cycle fatigue assessment of notched components subject to in-service complex systems of loads. The proposed methodology takes full advantage of the TCD's accuracy in estimating static and high-cycle fatigue strength of notched/cracked components and, on the other hand, of the ability of gradient elasticity to remove stress singularities or smooth stress concentrations such as those emerging at the tips of cracks or notches, respectively, when classical linear-elastic analyses are adopted.

The proposed methodology, devised to address plane, axisymmetric and three-dimensional problems, develops the stress-based Ru-Aifantis theory of gradient elasticity into an effective $\mathcal{C}^0$ finite element framework, making it readily implementable in commercial finite element software and therefore easily accessible to engineers for practical applications. In particular, the main advantage from a practical point of view, respect to existing approaches, is that it allows both static and high-cycle fatigue assessment of notched components by directly considering the relevant gradient-enriched stresses at the hot-spot on the surface of the component being assessed. This significantly simplifies the static and fatigue assessment of components containing stress risers by avoiding the need to know the failure location a priori, typical of the existing approaches.

Once the developed gradient-based methodology was implemented, the most suitable integration rules were identified for each implemented element. In particular, when $\ell \neq 0$ the same integration rule can be used to solve both the first and second step of the proposed methodology.

Furthermore, an extensive convergence study has been also carried out for problems with and without cracks, showing that:

- in the **absence of cracks**, the proposed methodology produces numerical solutions that converge to the exact solution with a rate in good agreement with theoretical predictions;

- in the **presence of cracks**, the proposed methodology shows a higher convergence rate compared to the theoretical value typical of standard finite element methodologies.

This faster convergence in the presence of cracks can be attributed to two main causes: the removal of singularities, characteristic of gradient elasticity theories and the fact that gradient-enriched stresses are determined as primary and not as secondary variables like in conventional finite element methodologies.

Moreover, the error study in the presence of cracks allowed the formulation of optimal element size guideline, showing that accurate solutions can be obtained by using relatively coarse meshes, significantly reducing the computational effort.

Through the study of several plane, axisymmetric and three-dimensional problems, the ability of the proposed gradient-based methodology to remove stress singularities was also confirmed.

Furthermore, the proposed methodology demonstrated to have the potential to become a powerful tool in the static and high-cycle fatigue assessment of notched components, showing its accuracy and reliability for a wide range of:

- **benchmark geometries**: plates with central notch, plates with double edge notch, cylindrical bars with circumferential notch, cylindrical shafts with shoulder fillet, notched beams;

- **notch geometries**: sharp, intermediate and blunt U-notches, V-notches, shoulder fillets;

- **materials**: from brittle to ductile materials. In particular, 19 different types of steel, aluminium alloys, PMMA, plain concrete;

- **loading conditions**: cyclic Mode I, cyclic mixed-Mode I and III, in-phase and out-of-phase cyclic loading, fully-reversed loading and also in presence of superimposed static stresses.

In all the analysed scenarios (under both static and high-cycle fatigue loading), the proposed methodology produced accurate estimates of the static and fatigue strength with errors mainly falling within an error band of $\pm 20\%$.

An interesting aspect emerged applying the proposed methodology to model the high-cycle fatigue behaviour of notched plain concrete. When the proposed methodology was applied according to the TCD, or in other words calculating ℓ according to Eq. (4.1), slightly too conservative estimations of the fatigue strength were obtained, while defining ℓ as the average inter-aggregate distance a higher level of accuracy was reached. This finding further supports the idea that the length scale of gradient elasticity ℓ must be somehow related to the dominant microstructural feature of the considered material.

Finally, the proposed gradient elastic methodology has also been extended to the study of visco-elastic problems, allowing a more accurate description of the dispersive behaviour of periodic visco-elastic composites. The proposed gradient visco-elastic theory resulted to be very accurate in the description of dispersive wave propagation phenomena. It also

highlighted that, to properly describe the dynamic behaviour of a visco-elastic material, a gradient visco-elastic theory must be used. In fact, it has been found that gradient enrichment and viscosity provide two complementary contributions for values of the damping coefficient at least one order of magnitude lower than the corresponding critical value: the first reduces the propagation speed of the wave front, while the second damps the high frequency components. For values of the damping coefficient approaching the corresponding critical value, instead, the viscosity becomes dominant over the heterogeneity of the material and both classical and gradient visco-elastic models produce comparable solutions.

9.2 Future directions

The work presented in this thesis represents an important step forward respect to the state of the art for two main reasons:

- the Ru-Aifantis theory of gradient elasticity has been implemented for the first time in a comprehensive and effective finite element methodology, easily implementable in commercial FE software and usable by engineers to study plane, axisymmetric and three-dimensional problems;

- accuracy and versatility of the proposed methodology, allowing accurate and straightforward (compared to existing approaches) static and fatigue assessments of notched components made of a wide range of materials, as well as a precise description of size effects and dispersive wave propagation phenomena.

Nevertheless, some problems need still to be addressed and others can now be explored thanks to the gradient-based methodology proposed in this thesis. In particular:

- a fundamental unresolved problem that needs to be addressed is undoubtedly the clear identification of the length scale parameter ℓ. Although several evidence supports the idea that ℓ is related to the dominant microstructural feature of the material being assessed, more research work needs to be done in order to give ℓ a clear physical meaning;

- passing to more applicative aspects, regarding the static assessment of notched components, more research work needs to be done in order to validate the gradient-based methodology developed in Chapter 5 against a wider range of geometries, materials and loading conditions. In what concerns the uni/multiaxial fatigue assessment of notched components, instead, further studies are needed to extend the proposed methodology to the finite lifetime regime. Furthermore, it would be of great interest to apply the proposed methodology to other new materials as well as more complex structures such as welded or bolted joints;

- another interesting study would be to test the accuracy of the proposed methodology against different type of plain and short-fibre reinforced concrete as well as different notch geometries and loading conditions;

- given the ability of the proposed gradient-enriched methodology to accurately describe size effects, a relatively straightforward but extremely useful research work would be to apply the proposed methodology to investigate both external and internal geometric size effects in components presenting one or more holes.

   Consider, for instance, the case of a plate with one or more holes, commonly used in practical engineering applications. In this case it is possible to encounter both external (due to the size of the whole component) and internal (due to size of the holes and distances amongst them) size effects.

   While the problem with a single hole is characterised by three length quantities (considering a square plate): the size of the plate D, the radius of the hole r_n and the internal length ℓ, representative of the underlying microstructure; the problem with two holes is characterised by an additional length, that is the distance d between the two holes. Finally in the more generic case with four or more holes, two further length parameters appear respect to the first case with just one hole: the horizontal d_x (x-direction) and vertical d_y (y-direction) distances between two consecutive holes. In first instance, it is possible to assume the condition $d_x = d_y = d$, reducing the additional length parameters to one.

   Whilst solving the problem with a single hole just the size effects due to the external geometry can be described, the solution of the other problems with two, four or more holes will allow to determine not only the size effects related to the external geometry, but also those due to internal geometry aspects (such as the radius of the holes and the distance among them) and in particular the effects that one or more holes induce in the stress field around a nearby hole.

   Different analysis can be performed, varying the specimen size (keeping constant the ratio between the radius of the hole and the size of the plate), the radius of the holes and their distances. Furthermore, the more complex scenario of plates with cracks departing from the holes could also be analysed;

- finally, regarding the proposed gradient visco-elastic methodology, further research efforts have to be spent in extending the aforementioned methodology to multi-dimensional problems and to materials showing non proportional damping. This would make this methodology applicable to several important problems, such as the study of regeneration phenomena in bones subject to vibrations for the treatment of osteoporosis.

Appendix A

Richardson's extrapolation

Richardson's extrapolation is a technique used to generate high-accuracy results while using low order formulas. Extrapolation can be applied whenever it is known that an approximation technique has an error term with a predictable form.

Let us consider a problem for which an analytical solution is not available but an accurate estimation of the exact solution is needed. Solving the problem through a numerical procedure characterised by a step Δt, the solution $f_{\Delta t}$ is obtained. If the same problem is then solved by regularly reducing the step size n-times (e.g. $\frac{\Delta t}{2}$, $\frac{\Delta t}{4}$, $\frac{\Delta t}{8}$, ..., $\frac{\Delta t}{2^n}$), the exact solution, F_{exact}, can be extrapolated by solving the following system of equations:

$$
\begin{cases}
F_{\text{exact}} \approx f_{\Delta t} + C_1 \Delta t + C_2 \Delta t^2 + C_3 \Delta t^3 + \ldots + C_n \Delta t^n \\[2mm]
F_{\text{exact}} \approx f_{\frac{\Delta t}{2}} + C_1 \frac{\Delta t}{2} + C_2 (\frac{\Delta t}{2})^2 + C_3 (\frac{\Delta t}{2})^3 + \ldots + C_n (\frac{\Delta t}{2})^n \\[2mm]
F_{\text{exact}} \approx f_{\frac{\Delta t}{4}} + C_1 \frac{\Delta t}{4} + C_2 (\frac{\Delta t}{4})^2 + C_3 (\frac{\Delta t}{4})^3 + \ldots + C_n (\frac{\Delta t}{4})^n \\[2mm]
F_{\text{exact}} \approx f_{\frac{\Delta t}{8}} + C_1 \frac{\Delta t}{8} + C_2 (\frac{\Delta t}{8})^2 + C_3 (\frac{\Delta t}{8})^3 + \ldots + C_n (\frac{\Delta t}{8})^n \\[2mm]
\vdots \\[2mm]
F_{\text{exact}} \approx f_{\frac{\Delta t}{2^n}} + C_1 \frac{\Delta t}{2^n} + C_2 (\frac{\Delta t}{2^n})^2 + C_3 (\frac{\Delta t}{2^n})^3 + \ldots + C_n (\frac{\Delta t}{2^n})^n
\end{cases}
\tag{A.1}
$$

where $f_{\frac{\Delta t}{2}}, \ldots, f_{\frac{\Delta t}{2^n}}$ are the solutions correspondent to the step sizes indicated by the subscripts, while $C_1, \ldots, C_n$ are coefficients.

Depending on the number of refinements used to extrapolate the exact solution, system A.1 can be significantly reduced and different orders of Richardson's extrapolation can be identified:

- **First-order**: when only one refinement of the original step Δt is used. In this case, system A.1 reduces to the first two equations in the two unknowns F_{exact} and C_1, leading to the following expression for the exact solution:

$$
F_{\text{exact}} \approx -f_{\Delta t} + 2 f_{\frac{\Delta t}{2}}
\tag{A.2}
$$

- **Second-order**: when two refinements of the original step Δt are used. In this case, system A.1 reduces to the first three equations with F_{exact}, C_1 and C_2 as unknowns, leading to the following expression for the exact solution:

$$F_{\text{exact}} \approx -\frac{1}{3}f_{\Delta t} - 2f_{\frac{\Delta t}{2}} + \frac{8}{3}f_{\frac{\Delta t}{4}} \tag{A.3}$$

- **Third-order**: when three refinements of the original step Δt are used. System A.1 reduces to the first four equations with F_{exact}, C_1, C_2 and C_3 as unknowns. The exact solution for the third-order extrapolation is approximated by the following polynomial:

$$F_{\text{exact}} \approx -\frac{1}{21}f_{\Delta t} + \frac{2}{3}f_{\frac{\Delta t}{2}} - \frac{8}{3}f_{\frac{\Delta t}{4}} + \frac{64}{21}f_{\frac{\Delta t}{8}} \tag{A.4}$$

- **Higher-order**: in a similar fashion, higher-order extrapolations can be obtained by considering more refinements. However, the accuracy increase could not justify the higher computational effort.

Appendix B

Stability of the harmonic solution when ω_h assumes imaginary values

When the argument of the square root in Eq. (8.23) is negative, ω_h takes the following form

$$\omega_h = \pm i \frac{c_e k}{\sqrt{1 + \frac{1}{12} d^2 k^2}} \sqrt{\frac{c_e^2 k^2 \tau^2}{4 \left(1 + \frac{1}{12} d^2 k^2\right)} - 1} \tag{B.1}$$

Considering Eq. (8.14), Eq. (8.20) can then be re-written as

$$u(x, t) = U \exp((i\omega_h - \omega_d) t) \exp(-ikx) \tag{B.2}$$

and substituting Eqs. (8.22) and (B.1) into Eq. (B.2), the following expression is obtained

$$u(x, t) = U \exp\left[\left(\pm \frac{c_e k}{\sqrt{1 + \frac{1}{12} d^2 k^2}} \sqrt{\frac{c_e^2 k^2 \tau^2}{4 \left(1 + \frac{1}{12} d^2 k^2\right)} - 1} - \right.\right.$$
$$\left.\left. - \frac{c_e^2 k^2 \tau}{2 \left(1 + \frac{1}{12} d^2 k^2\right)}\right) t\right] \exp(-ikx) \tag{B.3}$$

Focusing the attention on the argument of the first exponential term, it can be observed that negative values produce stable results and represent the condition of supercritical damping, while positive values would lead to unstable results (amplification of the response). However, it can be easily shown that the considered argument is always negative; hence there are no risks to incur in instabilities of the solution.

Bibliography

[1] AIFANTIS, E. C. On the microstructural origin of certain inelastic models. *ASME Journal of Engineering Materials and Technology 106*, 4 (1984), 326–330.

[2] AIFANTIS, E. C. The physics of plastic deformation. *International Journal of Plasticity 3*, 3 (1987), 211–247.

[3] AIFANTIS, E. C. On the role of gradients in the localization of deformation and fracture. *International Journal of Engineering Science 30*, 10 (1992), 1279–1299.

[4] AIFANTIS, E. C. Gradient effects at macro, micro, and nano scales. *Journal of the Mechanical Behavior of Materials 5* (1994), 355–375.

[5] AIFANTIS, E. C. Gradient deformation models at nano, micro, and macro scales. *ASME Journal of Engineering Materials and Technology 121* (1999), 189–202.

[6] ALTAN, S. B., AND AIFANTIS, E. C. On the structure of the mode III crack-tip in gradient elasticity. *Scripta Metallurgica et Materialia 26* (1992), 319–324.

[7] AMANATIDOU, E., AND ARAVAS, N. Mixed finite element formulations of strain-gradient elasticity problems. *Computer Methods in Applied Mechanics and Engineering 191* (2002), 1723–1751.

[8] ANDERSON, T. L. *Fracture Mechanics - Fundamentals and Applications*. CRC Press, 1991.

[9] ANON. *ENV 1993-1-1, EUROCODE 3 – design of steel structures*. 1988.

[10] ANON. *Nuclear construction lesson learned – guidance on best practice: concrete*. London: The Royal Academy of Engineering, 2012.

[11] ARNOLD, D., AND WINTHER, R. Mixed finite elements for elasticity. *Numerische Mathematik 92* (2002), 401–419.

[12] ASHBY, M. F., AND JONES, D. R. H. *Engineering Materials*, 2nd ed., vol. 1 – An Introduction to their Properties and Applications. Butterworth-Heinemann, UK, 1996.

[13] ASKES, H., AND AIFANTIS, E. C. Numerical modelling of size effects with gradient elasticity - formulation, meshless discretization and examples. *International Journal of Fracture 117* (2002), 347–358.

[14] ASKES, H., AND AIFANTIS, E. C. Gradient elasticity in statics and dynamics: An overview of formulations, length scale identification procedures, finite element implementations and new results. *International Journal of Solids and Structures 48*, 13 (2011), 1962–1990.

[15] ASKES, H., AND GITMAN, I. Non-singular stresses in gradient elasticity at bi-material interface with transverse crack. *International Journal of Fracture 156* (2009), 217–222.

[16] ASKES, H., AND GUTIÉRREZ, M. Implicit gradient elasticity. *International Journal for Numerical Methods in Engineering 67*, 3 (2006), 400–416.

[17] ASKES, H., LIVIERI, P., SUSMEL, L., TAYLOR, D., AND TOVO, R. Intrinsic material length, Theory of Critical Distances and Gradient Mechanics: analogies and differences in processing linear-elastic crack tip stress fields. *Fatigue & Fracture of Engineering Materials & Structures 36* (2013), 39–55.

[18] ASKES, H., MORATA, I., AND AIFANTIS, E. C. Finite element analysis with staggered gradient elasticity. *Computers & Structures 86* (2008), 1266–1279.

[19] ASKES, H., SUIKER, A., AND SLUYS, L. J. A classification of higher-order strain-gradient models - linear analysis. *Archive of Applied Mechanics 72* (2002), 171–188.

[20] ASKES, H., AND SUSMEL, L. Gradient enriched linear-elastic crack tip stresses to estimate the static strength of cracked engineering ceramics. *Frattura ed Integrita Strutturale 7*, 25 (2013), 87–93.

[21] ASKES, H., AND SUSMEL, L. Understanding cracked materials: is linear fracture mechanics obsolete? *Fatigue & Fracture of Engineering Materials & Structures 38* (2015), 154–160.

[22] ASTM C192/C192M. *Standard practice for making and curing concrete test specimens in the laboratory.* ASTM International, West Conshohocken (PA), 2007.

[23] ASTM E647-00. *Standard Test Method for Measurement of Fatigue Crack Growth Rates.* 2000.

[24] ATZORI, B. *Appunti di Costruzione di Macchine.* Edizioni Libreria Cortina, Padova, 2000. In italian.

[25] ATZORI, B., LAZZARIN, P., AND MENEGHETTI, G. Fracture mechanics and notch sensitivity. *Fatigue and Fracture of Engineering Materials and Structures 26* (2003), 257–267.

[26] BAGNI, C., AND ASKES, H. Unified finite element methodology for gradient elasticity. *Computers and Structures 160* (2015), 100–110.

[27] BAGNI, C., ASKES, H., AND AIFANTIS, E. C. Gradient-enriched finite element methodology for axisymmetric problems. *Acta Mechanica* (2017).

[28] BAGNI, C., ASKES, H., AND SUSMEL, L. Gradient elasticity: a transformative stress analysis tool to design notched components against uniaxial/multiaxial high-cycle fatigue. *Fatigue and Fracture of Engineering Materials and Structures* (2016).

[29] BAGNI, C., GITMAN, I., AND ASKES, H. A micro-inertia gradient visco-elastic motivation for proportional damping. *Journal of Sound and Vibration 347* (2015), 115–125.

[30] BATHE, K.-J. *Finite Element Procedures.* Prentice-Hall, New Jersey, 1996.

[31] BELLETT, D., TAYLOR, D., MARCO, S., MAZZEO, E., GUILLOIS, J., AND PIRCHER, T. The fatigue behaviour of three-dimensional stress concentrations. *International Journal of Fatigue 27*, 3 (2005), 207–221.

[32] BENNETT, T., GITMAN, I. M., AND ASKES, H. Elasticity Theories with Higher-order Gradients of Inertia and Stiffness for the Modelling of Wave Dispersion in Laminates. *International Journal of Fracture 148*, 2 (2007), 185–193.

[33] BERTO, F., AND BARATI, E. Fracture assessment of U-notches under three point bending by means of local energy density. *Materials and Design 32* (2011), 822–830.

[34] CARSTENSEN, C., GÜNTHER, D., REININGHAUS, J., AND THIELE, J. The Arnold-Winther mixed FEM in linear elasticity. Part I: implementation and numerical verification. *Computer Methods in Applied Mechanics and Engineering 197* (2008), 3014–3023.

[35] CAUCHY, A. Mémoire sur les vibrations d'un double système de molécules et de l'éther continu dans un corps cristallisé. *In: Oeuvres complètes, 1re Série – Tome II. Gauthier-Villars (reprint 1908), Paris* (1850a), 338–350.

[36] CAUCHY, A. Mémoire sur les systèmes isotorpes de points matériels. *In: Oeuvres complètes, 1re Série – Tome II. Gauthier-Villars (reprint 1908), Paris* (1850b), 351–386.

[37] CAUCHY, A. Note sur l'équilibre et les mouvements vibratoires des corps solides. *In: Oeuvres complètes, 1re Série – Tome XI. Gauthier-Villars (reprint 1899), Paris* (1851), 341–346.

[38] CHANG, C., AND GAO, J. Second-gradient constitutive theory for granular material with random packing structure. *International Journal of Solids and Structures 32* (1995), 2279–2293.

[39] CHEN, W., AND FISH, J. A Dispersive Model for Wave Propagation in Periodic Heterogeneous Media Based on Homogenization With Multiple Spatial and Temporal Scales. *Journal of Applied Mechanics 68*, 2 (2001), 153–161.

[40] COSSERAT, E., AND COSSERAT, F. *Théorie des corps déformables.* Librairie Scientifique A. Hermann et Fils, Paris, 1909.

[41] CRANK, J., AND NICOLSON, P. A practical method for numerical evaluation of solutions of partial differential equations of the heat conduction type. *Proceedings of the Cambridge Philosophical Society 43*, 1 (1947), 50–67.

[42] DAVOLI, P., BERNASCONI, A., FILIPPINI, M., FOLETTI, S., AND PAPADOPOU-LOS, I. V. Independence of the torsional fatigue limit upon a mean shear stress. *International Journal of Fatigue 25* (2003), 471–480.

[43] DIXON, W. J. The up-and-down method for small samples. *Journal of the American Statistical Association 60*, 312 (1965), 967–978.

[44] DOWLING, N. E. *Mechanical Behaviour of Materials*, 2nd ed. Prentice-Hall Inc., New Jersey, USA, 1998.

[45] DUQUESNAY, D. L., YU, M., AND TOPPER, T. H. An analysis of notch size effect on the fatigue limit. *Journal of Testing and Evaluation 4* (1988), 375–385.

[46] EL HADDAD, M. H. *A study of the growth of short fatigue cracks based on fracture mechanics.* Ph. D. Thesis, University of Waterloo, Waterloo, Ontario, 1978.

[47] EL HADDAD, M. H., TOPPER, T. H., AND SMITH, K. N. Prediction of non propagating cracks. *Engineering Fracture Mechanics 11*, 3 (1979), 573–584.

[48] ERINGEN, A. C. Linear theory of nonlocal elasticity and dispersion of plane waves. *International Journal of Engineering Science 10*, 5 (1972), 425–435.

[49] ERINGEN, A. C. Nonlocal polarelastic continua. *International Journal of Engineering Science 10*, 1 (1972), 1–16.

[50] ERINGEN, A. C. On differential equations of nonlocal elasticity and solutions of screw dislocation and surface waves. *Journal of Applyed Physics 54*, 9 (1983), 4703–4710.

[51] FINDLEY, W. N. *A theory for the effect of mean stress on fatigue of metals under combined torsion and axial load or bending.* Engineering Materials Research Laboratory, Division of Engineering, Brown University, 1958.

[52] FISH, J., CHEN, W., AND NAGAI, G. Non-local dispersive model for wave propagation in heterogeneous media: multi-dimensional case. *International Journal for Numerical Methods in Engineering 54* (2002), 347–363.

[53] FISH, J., CHEN, W., AND NAGAI, G. Non-local dispersive model for wave propagation in heterogeneous media: one-dimensional case. *International Journal for Numerical Methods in Engineering 54* (2002), 331–346.

[54] FROST, N. E. A relation between the critical alternating propagation stress and crack length for mild steel. In *Proceedings of the Institution of Mechanical Engineers* (1957), vol. 173, pp. 811–834.

[55] FROST, N. E. Non-propagating cracks in vee-notched specimens subjected to fatigue loadingsl. *Aeronautical Quarterly VIII* (1957), 1–20.

[56] FROST, N. E., MARSH, K. J., AND POOK, L. P. *Metal fatigue*. Clarendon Press, Oxford, 1974.

[57] FUKUDA, T., AND NISITANI, H. The background of fatigue limit ratio of torsional fatigue to rotating bending fatigue in isotropic materials and materials with clear-banded structures. In *Biaxial and Multiaxial Fatigue and Fracture*, A. Carpinteri, M. de Freitas, and A. Spagnoli, Eds. Elsevier and ESIS, 2003, pp. 285–302.

[58] GAO, X.-L., AND PARK, S. K. Variational formulation of a simplified strain gradient elasticity theory and its application to a pressurized thick-walled cylinder problem. *International Journal of Solids and Structures 44* (2007), 7486–7499.

[59] GITMAN, I. M., ASKES, H., AND AIFANTIS, E. C. The representative volume size in static and dynamic micro-macro transitions. *International Journal of Fracture 135* (2005), L3–L9.

[60] GITMAN, I. M., ASKES, H., KUHL, E., AND AIFANTIS, E. C. Stress concentrations in fractured compact bone simulated with a special class of anisotropic gradient elasticity. *International Journal of Solids and Structures 47* (2010), 1099–1107.

[61] GITMAN, I. M., ASKES, H., AND SLUYS, L. Representative Volume size as a macroscopic length scale parameter. In *Proceedings of FraMCoS-5, Vail (USA)*. IA-FraMCoS, 2004, pp. 483–489.

[62] GÓMEZ, F. J., ELICES, M., BERTO, F., AND P., L. Local strain energy to assess the static failure of U-notches in plates under mixed mode loading. *International Journal of Fracture 145* (2007), 29–45.

[63] GÓMEZ, F. J., ELICES, M., AND PLANAS, J. The cohesive crack concept: application to PMMA at −60°C. *Engineering Fracture Mechanics 72* (2005), 1268–1285.

[64] GOUDREAU, G. L., AND TAYLOR, R. L. Evaluation of numerical integration methods in elastodynamics. *Computer Methods in Applied Mechanics and Engineering 2* (1972), 69–97.

[65] GOUGH, H. J. Engineering steels under combined cyclic and static stresses. *Proceedings of the Institution of Mechanical Engineers 160* (1949), 417–440.

[66] GUDMUNDSON, P. Modelling of length scale effects in viscoelastic materials. *European Journal of Mechanics - A/Solids 25* (2006), 379–388.

[67] GUO, L. P., SUN, W., R., Z. K., CHEN, H. J., AND LIU, B. Study on the flexural fatigue performance and fractal mechanism of concrete with high proportions of ground granulated blast-furnace slag. *Cement and Concrete Research 37*, 2 (2007), 242–250.

[68] GUTKIN, M. Nanoscopics of dislocations and disclinations in gradient elasticity. *Reviews on Advanced Materials Science 1* (2000), 27–60.

[69] GUTKIN, M., AND AIFANTIS, E. C. Edge dislocation in gradient elasticity. *Scripta Materialia 36* (1997), 129–135.

[70] GUTKIN, M., AND AIFANTIS, E. C. Dislocations in the theory of gradient elasticity. *Scripta Materialia 40* (1999), 559–566.

[71] GUTKIN, M. Y., AND AIFANTIS, E. C. Dislocations and disclinations in gradient elasticity. *Physica Status Solidi (b) 214* (1999), 245–284.

[72] HAIBACH, E. *Service fatigue-strength methods and data for structural analysis.* Düsseldorf, Germany: VDI, 1992.

[73] HARKEGARD, G. An effective stress intensity factor and the determination of the notched fatigue limit. In *Fatigue Thresholds: Fundamentals and Engineering Applications*, J. Backlund, A. F. Blom, and C. J. Beevers, Eds., vol. II. Chameleon Press Ltd: London, UK, 1981, pp. 867–879.

[74] HARTMANN, F. The discrete Babuška-Brezzi condition. *Ingenieur-Archiv 56* (1986), 221–228.

[75] HOBBACHER, A. Recommendations for fatigue design of welded joints and components. *IIW document XIII-2151-07/XV-1254-07* (May 2007).

[76] IHLENBURG, F., AND BABUŠKA, I. Finite Element Solution of the Helmholtz Equation with High Wave Number Part I: The h-Version of the FEM. *Computers & Mathematics with Applications 30*, 9 (1995), 9–37.

[77] INTERNATIONAL ENERGY AGENCY AND WORLD BUSINESS COUNCIL FOR SUSTAINABLE DEVELOPMENT. *Cement Technology Roadmap 2009 – Carbon emissions reductions up to 2050.* 2009.

[78] IRWIN, G. R. Analysis of Stresses and Strains Near the End of a Crack Traversing a Plate. *Journal of Applied Mechanics 24* (1957), 361–364.

[79] JADALLAH, O., BAGNI, C., ASKES, H., AND SUSMEL, L. Microstructural length scale parameters to model the high-cycle fatigue behaviour of notched plain concrete. *International Journal of Fatigue 82* (2016), 708–720.

[80] KAUFMAN, R. P., AND TOPPER, T. The influence of static mean stresses applied normal to the maximum shear planes in multiaxial fatigue. In *Biaxial and Multiaxial Fatigue and Fracture*, A. Carpinteri, M. de Freitas, and A. Spagnoli, Eds. Elsevier and ESIS, 2003, pp. 123–143.

[81] KOUZNETSOVA, V., GEERS, M., AND BREKELMANS, W. Size of a representative volume element in a second-order computational homogenization framework. *International Journal for Multiscale Computational Engineering 2*, 4 (2004), 575–598.

[82] KURATH, P., DOWNING, S. D., AND GALLIART, D. R. Summary of non-hardened notched shaft round robin program. In *Multiaxial Fatigue*, G. E. Leese and D. F. Socie, Eds., vol. II. Society of Automotive Engineers, AE-14, Philadelphia, USA, 1989, pp. 13–32.

[83] LAZZARIN, P., AND SUSMEL, L. A stress-based method to predict lifetime under multiaxial fatigue loadings. *Fatigue and Fracture of Engineering Materials and Structures 26* (2003), 1171–1187.

[84] LEE, M. K., AND BARR, B. I. G. An overview of the fatigue behaviour of plain and fibre reinforced concrete. *Cement and Concrete Composites 26* (2004), 209–305.

[85] LEE, Y. L., PAN, J., HATHAWAY, R. B., AND BARKEY, M. E. *Fatigue Testing and Analysis*, 1st ed., vol. Theory and Practice. Elsevier Butterworth-Heinemann, 2005.

[86] LIVIERI, P., AND TOVO, R. The effect of throat underflushing on the fatigue strength of fillet weldments. *Fatigue & Fracture of Engineering Materials & Structures 36*, 9 (2013), 884–892.

[87] LIVIERI, P., AND TOVO, R. Numerical methods for calculating the structural reliability of fatigue-loaded welds. *Welding International 28*, 11 (2014), 865–872.

[88] LOUKS, R., ASKES, H., AND SUSMEL, L. A generalised approach to rapid finite element design of notched materials against static loading using the Theory of Critical Distances. *Materials and Design 108* (2016), 769–779.

[89] LUKAS, P., KUNZ, L., WEISS, B., AND STICKLER, R. Non-damaging notches in fatigue. *Fatigue and Fracture of Engineering Materials and Structures 9* (1986), 195–204.

[90] MARIN, J. Interpretation of fatigue strength for combined stresses. In *Proceedings of International Conference on Fatigue of Metals* (London, 1956), pp. 184–194.

[91] MATAKE, T. An Explanation on Fatigue Limit under Combined Stress. *Bulletin of JSME 20*, 141 (1977), 257–263.

[92] METRIKINE, A. V., AND ASKES, H. One-dimensional dynamically consistent gradient elasticity models derived from a discrete microstructure. Part 1: Generic formulation. *European Journal of Mechanics - A/Solids 21* (2002), 555–572.

[93] METRIKINE, A. V., AND ASKES, H. An isotropic dynamically consistent gradient elasticity model derived from a 2D lattice. *Philosophical Magazine 86* (2006), 3259–3286.

[94] MILLER, K. J. The short crack problem. *Fatigue & Fracture of Engineering Materials & Structures 5* (1982), 223–232.

[95] MINDLIN, R. Micro-structure in linear elasticity. *Archive for Rational Mechanics and Analysis 16* (1964), 52–78.

[96] MÜHLHAUS, H.-B., AND OKA, F. Dispersion and wave propagation in discrete and continuous models for granular materials. *International Journal of Solids and Structures 33* (1996), 2841–2858.

[97] MURDOCK, J., AND KESLER, C. *The mechanism of fatigue in concrete. Report No. 587.* University of Illinois, August 1960.

[98] NEUBER, H. *Theory of notch stresses: principles for exact calculation of strength with reference to structural form and material*, 2nd ed. Springer Verlag, Berlin, 1958.

[99] NEWMARK, N. M. A method of computation for structural dynamics. *Journal of the Engineering Mechanics Division ASCE 85* (1959), 67–94.

[100] NISITANI, H., AND ENDO, M. Unified treatment of deep and shallow notches in rotating bending fatigue. In *Basic Questions in Fatigue*, vol. I. ASTM STP 924, Philadelphia, USA, 1988, pp. 136–153.

[101] OHLSSON, U., DAERGA, P. A., AND ELFGREN, L. Fracture energy and fatigue strength of unreinforced concrete beams at normal and low temperatures. *Engineering Fracture Mechanics 35*, 1–3 (1990), 195–203.

[102] PAPANICOLOPULOS, S. A., ZERVOS, A., AND VARDOULAKIS, I. A three-dimensional C^1 finite element for gradient elasticity. *International Journal for Numerical Methods in Engineering 77* (2009), 1396–1415.

[103] PETERSON, R. E. Notch-sensitivity. In *Metal Fatigue*, G. Sines and J. L. Waisman, Eds. McGraw Hill, New York, 1959, pp. 293–306.

[104] PETERSON, R. E. *Stress Concentration Factors.* John Wiley & Sons, New York, USA, 1974.

[105] PLIZZARI, G. A., CANGIANO, S., AND ALLERUZZO, S. The fatigue behaviour of cracked concrete. *Fatigue & Fracture of Engineering Materials & Structures 20*, 8 (1997), 1195–1206.

[106] RAITHBY, K. D. Flexural fatigue behaviour of plain concrete. *Fatigue & Fracture of Engineering Materials & Structures 2*, 3 (1979), 269–278.

[107] RICHARDSON, L. F. The approximate arithmetical solution by finite differences of physical problems involving differential equations, with an application to the stresses in a masonry dam. *Philosophical Transactions of the Royal Society of London A: Mathematical, Physical and Engineering Sciences 210*, 459-470 (1911), 307–357.

[108] RU, C. Q., AND AIFANTIS, E. C. A simple approach to solve boundary-value problems in gradient elasticity. *Acta Mechanica 101* (1993), 59–68.

[109] SHU, J. Y., KING, W. E., AND FLECK, N. A. Finite elements for materials with strain gradient effects. *International Journal for Numerical Methods in Engineering 44* (1999), 373–391.

[110] SINCLAIR, G. M., AND DOLAN, T. J. Effect of stress amplitudes on statistical variability in fatigue life of 75S-T6 Aluminium Alloy. *Transaction of the ASME 75* (1953), 867–872.

[111] SINES, G. Behaviour of metals under complex static and alternating stresses. In *Metal Fatigue*, G. Sines and J. L. Waisman, Eds. McGraw Hill, New York, 1959, pp. 145–169.

[112] SOCIE, D. F. Multiaxial Fatigue Damage Models. *Journal of Engineering Materials and Technology 109*, 4 (1987), 293–298.

[113] SONSINO, C. M. Fatigue behaviour of welded components under complex elasto-plastic multiaxial deformation. *LBF-Bericht, Nr. 6078* (1994).

[114] SONSINO, C. M. Multiaxial fatigue of welded joints under in-phase and out-of-phase local strains and stresses. *International Journal of Fatigue 17* (1995), 55–70.

[115] SONSINO, C. M., AND KUEPPERS, M. Multiaxial fatigue of welded joints under constant and variable amplitude loadings. *Fatigue and Fracture of Engineering Materials and Structures 24* (2001), 309–327.

[116] SPINDEL, J. E., AND HAIBACH, E. Some considerations in the statistical determination of the shape of S–N curves. In *Statistical analysis of fatigue data*, R. E. Little and J. C. Ekvall, Eds., ASTM STP 744. 1981, pp. 89–113.

[117] SUIKER, A. S. J., DE BORST, R., AND CHANG, C. S. Micro-mechanical modelling of granular material. Part 1: Derivation of a second-gradient micro-polar constitutive theory. *Acta Mechanica 149*, 1 (2001), 161–180.

[118] SUIKER, A. S. J., DE BORST, R., AND CHANG, C. S. Micro-mechanical modelling of granular material. Part 2: Plane wave propagation in infinite media. *Acta Mechanica 149*, 1 (2001), 181–200.

[119] SUSMEL, L. Validazione di un criterio di resistenza a fatica multiassiale fondato sullindividuazione di un piano di verifica. In *Proceedings of IGF National Conference* (Bari, Italy, 2000), pp. 167–174. (In italian).

[120] SUSMEL, L. A unifying approach to estimate the highcycle fatigue strength of notched components subjected to both uniaxial and multiaxial cyclic loadings. *Fatigue and Fracture of Engineering Materials and Structures 27* (2004), 391–411.

[121] SUSMEL, L. Multiaxial fatigue limits and material sensitivity to non-zero mean stresses normal to the critical planes. *Fatigue and Fracture of Engineering Materials and Structures 31* (2008), 295–309.

[122] SUSMEL, L. The Theory of Critical Distances: a review of its applications in fatigue. *Engineering Fracture Mechanics 75* (2008), 1706–1724.

[123] SUSMEL, L. *Multiaxial Notch Fatigue: from nominal to local stress-strain quantities.* Woodhead & CRC, Cambridge, UK, 2009.

[124] SUSMEL, L. The Modified Wöhler Curve Method calibrated by using standard fatigue curves and applied in conjunction with the Theory of Critical Distances to estimate fatigue lifetime of aluminium weldments. *International Journal of Fatigue 31* (2009), 197–212.

[125] SUSMEL, L. A unifying methodology to design un-notched plain and short fibre/particle reinforced concretes against fatigue. *International Journal of Fatigue 61* (2014), 226–243.

[126] SUSMEL, L. Four stress analysis strategies to use the Modified Wöhler Curve Method to perform the fatigue assessment of weldments subjected to constant and variable amplitude multiaxial fatigue loading. *International Journal of Fatigue 64* (2014), 38–54.

[127] SUSMEL, L., ASKES, H., BENNETT, T., AND TAYLOR, D. Theory of Critical Distances versus Gradient Mechanics in modelling the transition from the short to long crack regime at the fatigue limit. *Fatigue and Fracture of Engineering Materials and Structures 36* (2013), 861–869.

[128] SUSMEL, L., AND LAZZARIN, P. A bi-parametric modifi ed Whler curve for high cycle multiaxial fatigue assessment. *Fatigue and Fracture of Engineering Materials and Structures 25* (2002), 63–78.

[129] SUSMEL, L., AND PETRONE, N. Multiaxial fatigue life estimations for 6082-T6 cylindrical specimens under in-phase and out-of-phase biaxial loadings. In *Biaxial and Multiaxial Fatigue and Fracture*, A. Carpinteri, M. de Freitas, and A. Spagnoli, Eds. Elsevier and ESIS, 2003, pp. 83–104.

[130] SUSMEL, L., AND TAYLOR, D. Fatigue design in the presence of stress concentrations. *Journal of Strain Analysis for Engineering Design 38* (2003), 443–452.

[131] SUSMEL, L., AND TAYLOR, D. A simplified approach to apply the theory of critical distances to notched components under torsional fatigue loading. *International Journal of Fatigue 28* (2006), 417–430.

[132] SUSMEL, L., AND TAYLOR, D. A novel formulation of the Theory of Critical Distances to estimate lifetime of notched components in the medium-cycle fatigue regime. *Fatigue & Fracture of Engineering Materials & Structures 30*, 7 (2007), 567–581.

[133] SUSMEL, L., AND TAYLOR, D. On the use of the Theory of Critical Distances to predict static failures in ductile metallic materials containing different geometrical features. *Engineering Fracture Mechanics 75* (2008), 4410–4421.

[134] SUSMEL, L., AND TAYLOR, D. The Modified Wöhler Curve Method applied along with the Theory of Critical Distances to estimate finite life of notched components subjected to complex multiaxial loading paths. *Fatigue and Fracture of Engineering Materials and Structures 31* (2008), 1047–1064.

[135] SUSMEL, L., AND TAYLOR, D. The theory of critical distances to predict static strength of notched brittle components subjected to mixed-mode loading. *Engineering Fracture Mechanics 75* (2008), 534–550.

[136] SUSMEL, L., AND TAYLOR, D. The Theory of Critical Distances as an alternative experimental strategy for the determination of K_{IC} and ΔK_{th}. *Engineering Fracture Mechanics 77* (2010), 1492–1501.

[137] SUSMEL, L., AND TAYLOR, D. The Theory of Critical Distances to estimate the static strength of notched samples of Al6082 loaded in combined tension and torsion. Part I: Material cracking behaviour. *Engineering Fracture Mechanics 77* (2010), 452–469.

[138] SUSMEL, L., AND TAYLOR, D. The Theory of Critical Distances to estimate the static strength of notched samples of Al6082 loaded in combined tension and torsion. Part II: Multiaxial static assessment. *Engineering Fracture Mechanics 77* (2010), 470–478.

[139] SUSMEL, L., AND TAYLOR, D. The Theory of Critical Distances to estimate finite lifetime of notched components subjected to constant and variable amplitude torsional loading. *Engineering Fracture Mechanics 98* (2013), 64–79.

[140] SUSMEL, L., TOVO, R., AND LAZZARIN, P. The mean stress effect on the high-cycle fatigue strength from a multiaxial fatigue point of view. *International Journal of Fatigue 27* (2005), 928–943.

[141] TADA, H., PARIS, P. C., AND R., I. G. *Stress Analysis of Cracks Handbook*, 3rd ed. ASME, New York, 2000.

[142] TAGHIZADEH, K., BERTO, F., AND E., B. Local strain energy density applied to martensitic steel plates weakened by U-notches under mixed mode loading. *Theoretical and Applied Fracture Mechanics 59* (2012), 21–28.

[143] TANAKA, K., AND AKINIWA, Y. Notch geometry effect on propagation threshold of short fatigue cracks in notched components. In *Fatigue '87*, R. O. Ritchie and E. A. Starke Jr., Eds., vol. II, 3th Int. Conf. on Fatigue and Fracture Thresholds. EMAS, London, UK, 1987, pp. 739–748.

[144] TANAKA, K., AND NAKAI, Y. Propagation and nonpropagation of short fatigue cracks at a sharp notch. *Fatigue and Fracture of Engineering Materials and Structures 6* (1983), 315–327.

[145] TANG, Z., SHEN, S., AND ATLURI, S. Analysis of materials with strain-gradient effects: a meshless local Petrov-Galerkin (MLPG) approach, with nodal displacements only. *Computer Modeling in Engineering & Sciences 4* (2003), 177–196.

[146] TAYLOR, D. Geometrical effects in fatigue: a unifying theoretical model. *International Journal of Fatigue 21* (1999), 413–420.

[147] TAYLOR, D. Predicting the fracture strength of ceramic materials using the theory of critical distances. *Engineering Fracture Mechanics 71* (2004), 2407–2416.

[148] TAYLOR, D. *The Theory of Critical Distances: A New Perspective in Fracture Mechanics.* Elsevier, Oxford, UK, 2007.

[149] TAYLOR, D., BARRETT, N., AND LUCANO, G. Some new methods for predicting fatigue in welded joints. *International Journal of Fatigue 24*, 5 (2002), 509–518.

[150] TAYLOR, D., MERLO, M., PEGLEY, R., AND CAVATORTA, M. P. The effect of stress concentrations on the fracture strength of polymethylmethacrylate. *Materials Science and Engineering A 382* (2004), 288–294.

[151] TAYLOR, D., AND WANG, G. The validation of some methods of notch fatigue analysis. *Fatigue and Fracture of Engineering Materials and Structures 23* (2000), 387–394.

[152] TENEK, L., AND AIFANTIS, E. C. A two-dimensional finite element implementation of a special form of gradient elasticity. *Computer Modeling in Engineering & Sciences 3* (2002), 731–741.

[153] TEYCHENNE, D., FRANKLIN, R. E., ERNTROY, H. C., HOBBS, D. W., AND MARSH, B. K. *Design of normal concrete mixes. Construction research communications, 2nd ed.* 2010.

[154] THUN, H., OHLSSON, U., AND ELFGREN, L. A deformation criterion for fatigue of concrete in tension. *Structural Concrete 12*, 3 (2011), 187–197.

[155] Timoshenko, S., and Goodier, J. *Theory of Elasticity*, 3rd ed. McGraw-Hill, New York, 1970.

[156] Ting, J. C., and Lawrence, F. V. A crack closure model for predicting the threshold stresses of notches. *Fatigue and Fracture of Engineering Materials and Structures 16* (1993), 93–114.

[157] Tovo, R., and Livieri, P. An implicit gradient application to fatigue of sharp notches and weldments. *Engineering Fracture Mechanics 74*, 4 (2007), 515–526.

[158] Wiersma, S., and Taylor, D. Fatigue of materials used in microscopic components. *Fatigue & Fracture of Engineering Materials & Structures 28*, 12 (2005), 1153–1160.

[159] Wilson, E. L. Structural Analysis of Axisymmetric Solids. *AIAA Journal 3* (1965), 2269–2274.

[160] Zenner, H., Simbürger, A., and Liu, J. On the fatigue limit of ductile metals under complex multiaxial loading. *International Journal of Fatigue 18* (2000), 235–244.

[161] Zervos, A. Finite elements for elasticity with microstructure and gradient elasticity. *International Journal for Numerical Methods in Engineering 73*, 4 (2008), 564–595.

[162] Zhang, B. Relationship between pore structure and mechanical properties of ordinary concrete under bending fatigue. *Cement and Concrete Research 28*, 5 (1998), 699–711.

[163] Zhang, Z., and Paulino, G. Wave propagation and dynamic analysis of smoothly graded heterogeneous continua using graded finite elements. *International Journal of Solids and Structures 44* (2007), 3601–3626.

[164] Zienkiewicz, O., and Taylor, R. *The Finite Element Method*, 5th ed., vol. 1 – The Basis. Butterworth-Heinemann, 2000.

[165] Zienkiewicz, O., and Taylor, R. *The Finite Element Method*, 5th ed., vol. 2 – Solid Mechanics. Butterworth-Heinemann, 2000.